

論文 / 著書情報
Article / Book Information

題目(和文)	122型鉄ニクタイド超伝導体のヘテロエピタキシャル成長と電子輸送特性
Title(English)	Heteroepitaxial Growth and Electron Transport Properties of 122-type Iron-Pnictide Superconductors
著者(和文)	佐藤光
Author(English)	Hikaru Sato
出典(和文)	学位:博士(工学), 学位授与機関:東京工業大学, 報告番号:甲第10194号, 授与年月日:2016年3月26日, 学位の種別:課程博士, 審査員:細野 秀雄,平松 秀典,須崎 友文,阿藤 敏行,松石 聡,神谷 利夫
Citation(English)	Degree:., Conferring organization: Tokyo Institute of Technology, Report number:甲第10194号, Conferred date:2016/3/26, Degree Type:Course doctor, Examiner:,,,,,
学位種別(和文)	博士論文
Type(English)	Doctoral Thesis

**Heteroepitaxial Growth and Electron Transport Properties of
122-type Iron-Pnictide Superconductors**

Hikaru Sato

2016

**Department of Materials Science and Engineering
Interdisciplinary Graduate School of Science and Engineering
Tokyo Institute of Technology**

Contents

Chapter 1: General introduction	1
1.1. Background of present study	1
1.1.1. <i>History of superconductors and the discovery of new high-T_c superconductor: “Iron-based superconductor”</i>	1
1.1.2. <i>Crystal structures of iron-based superconductors</i>	2
1.1.3. <i>Doping variations and pressure effects</i>	3
1.1.4. <i>High upper critical magnetic field and small anisotropy</i>	5
1.1.5. <i>Heteroepitaxial growth and superconducting properties of iron pnictide thin films: Advantageous properties for application</i>	6
1.1.6. <i>Comparison with other superconductors: toward future applications</i>	9
1.2. Objectives and outline of this study	10
References	13
Chapter 2: Critical factor for heteroepitaxial growth of cobalt-doped BaFe₂As₂ thin films	31
2.1. Introduction	31
2.2. Experimental procedure	32
2.2.1. <i>Thin film fabrication</i>	32
2.2.2. <i>Characterization</i>	33
2.3. Results and discussion	34
2.3.1. <i>Optical properties and pulse-energy dependence of deposition rate</i>	34
2.3.2. <i>Relationship between crystallinity of the films and pulse energies</i>	35
2.3.3. <i>Microstructure analysis: defects and reaction layer between film and LSAT</i>	37
2.3.4. <i>J_c properties of the epitaxial films grown by several lasers at the optimal growth rate</i>	38
2.4. Discussion	39
2.5. Conclusion	40
References	42
Chapter 3: Anomalous scaling behavior in mixed-state Hall effect of a cobalt-doped BaFe₂As₂ epitaxial film	50
3.1. Introduction	50
3.2. Experimental procedure	51
3.2.1. <i>Thin film fabrication</i>	51
3.2.2. <i>Mixed-state Hall effect measurements</i>	52

3.3. Results	53
3.3.1. <i>Mixed-state Hall effect measurements with T sweep and H sweep</i>	53
3.3.2. <i>Summary of anomalous Hall scaling with large vortex phase diagram</i>	54
3.4. Discussion.....	56
3.5. Conclusion	59
References.....	61
Chapter 4: Anisotropic pressure effects on superconducting properties of cobalt-doped BaFe₂As₂ epitaxial films	69
4.1. Introduction.....	69
4.2. Experimental procedure	72
4.2.1. <i>Thin film fabrication and structure characterization</i>	72
4.2.2. <i>Electrical transport measurements under ambient and high pressure</i>	73
4.3. Results	74
4.3.1. <i>Structural parameters of the films</i>	74
4.3.2. <i>Investigations on strain effects using high temperature XRD</i>	76
4.3.3. <i>Electrical transport properties under ambient pressure: the unique characteristics of strained films on CaF₂</i>	76
4.3.4. <i>Electrical transport properties under high pressures</i>	78
4.4. Discussion.....	79
4.5. Conclusion	81
References.....	83
Chapter 5: Unusual pressure effects on the superconductivity of indirectly electron-doped (Ba_{1-x}La_x)Fe₂As₂ epitaxial films	99
5.1. Introduction.....	99
5.2. Experimental procedure	101
5.2.1. <i>Thin film fabrication and patterning of the films</i>	101
5.2.2. <i>Electrical transport measurements under high pressures</i>	101
5.3. Results and discussion	102
5.3.1. <i>Electron transport properties under ambient pressure</i>	102
5.3.2. <i>Electron transport properties under high pressures</i>	103
5.4. Conclusion	107
References.....	108
Chapter 6: Heteroepitaxial growth of phosphorus-doped BaFe₂As₂ thin films	117

6.1. Introduction	117
6.2. Experimental procedure	119
6.2.1. Thin film fabrication	119
6.2.2. Characterization	120
6.3. Results and discussion	121
6.3.1. Optimization of growth temperature	121
6.3.2. Fabrication on LSAT substrates and characterization	122
6.3.3. Electron transport properties of the films on MgO and LSAT	127
6.4. Conclusion	127
References	129
Chapter 7: High critical-current density with less anisotropy in phosphorus-doped BaFe₂As₂ epitaxial thin films	135
7.1. Introduction	135
7.2. Experimental procedure	135
7.2.1. Thin film fabrication	135
7.2.2. Characterization of microstructure and transport J_c	136
7.3. Results and discussion	136
7.3.1. Comparison of the J_c properties of the films on MgO with those on LSAT	136
7.3.2. Growth rate dependence of vortex pinning properties	138
7.3.3. J_c properties of optimized epitaxial films and comparison with other films	139
7.3.4. Microstructure analysis and mechanism of isotropic vortex pinning	140
7.4. Conclusion	142
References	143
Chapter 8: Isotropic J_c properties of phosphorus-doped BaFe₂As₂ films on practical tape-substrates: Toward future applications to coated conductors	150
8.1. Introduction	150
8.2. Experimental procedure	151
8.2.1. Thin film fabrication on IBAD substrates	151
8.2.2. Characterization	151
8.3. Results and discussion	152
8.3.1. Optimization of growth temperature and structural characterization	152
8.3.2. Comparison of the electron transport properties between BaFe₂(As_{0.78}P_{0.22})₂ films on IBAD-substrate and those on MgO single-crystal substrates	154
8.3.3. Optimization of the phosphorous concentration	156

8.3.4. *Fabrication and characterization of “roughly aligned” $BaFe_2(As_{1-x}P_x)_2$ films : Attractive properties for the practical application*.....157

8.4. **Conclusion**159

References.....160

Chapter 9: General conclusion170

Acknowledgments176

Publication List177

Papers included in this thesis177

Other Papers.....177

Presentation List179

International Presentations179

Domestic Presentations180

Award181

Biography181

Chapter 1: General introduction

1.1. Background of present study

1.1.1. History of superconductors and the discovery of new high- T_c superconductor: “Iron-based superconductor”

In 1911, Heike Kamerlingh Onnes discovered that the resistivity of the mercury becomes completely “zero” at 4.2 K. This is the first discovery of superconductor¹. Since the first discovery of the superconductors, many kinds of superconductors were discovered. Figure 1 - 1 shows the history of superconductors and improvements of superconducting transition critical temperature (T_c) in the representative categories¹⁻¹⁷. Superconductors have been mainly categorized into BCS (Bardeen, Cooper and Schrieffer)¹⁸ type metals, organics, and cuprates. In the case of the BCS type superconductivity, electron-phonon interaction mediates the formation of electron-pair (cooper-pair). The highest T_c of BCS metals is 39 K of MgB_2 ⁷. For organic-based superconductors, $(TMTSF)_2PF_6$ (TMTSF = tetramethyltetraselenafulvalene) is firstly reported as an organic-based superconductor¹⁷. However, their T_c had been much lower than those of the BCS type metals and the cuprates. While, in 1991, dramatic improvement was observed in an alkali metal intercalated C_{60} which exhibited superconductivity at 18 K¹⁴. Tuning the alkali metal dopants, maximum T_c becomes 33 K for $(Cs_2Rb)C_{60}$ ¹⁵.

In 1986, the first “high- T_c ” superconductor was discovered. Bednorz and Müller¹⁶ reported that $(La,Ba)_2CuO_4$ exhibits superconductivity at $T_c \sim 20$ K. This report is the first report of the cuprate superconductor. After this report, many kinds of superconductors with various crystal structures containing CuO_2 planes were discovered

and many kinds of doping variation were examined comprehensively⁸⁻¹¹. The T_c increased drastically up to 133 K in $\text{HgBa}_2\text{Ca}_2\text{Cu}_3\text{O}_x$ ¹¹ and the highest T_c record of superconductors is reported under high pressure (164 K at 31 GPa)¹⁹. Cuprates became the first superconductors which have the higher T_c than the boiling point of liquid nitrogen and they are stable in the air. Therefore, the discovery of the cuprate superconductors promotes not only the research of fundamental science but also the development of the superconducting wire and tapes.

After the discovery of the cuprates, perovskite type oxide and various layered structure materials have attracted attention. 20 years later from the discovery of the cuprates, Kamihara *et al.*²⁰ discovered the new layered superconductor LaFePO in 2006 through their researches to explore new type of magnetic semiconductors in oxypnictide $\text{RETM}Pn\text{O}$ (RE = rare earth, TM = transition metal, Pn = pnictogen). LaFePO exhibits the paramagnetic metal state and the superconducting transition at 5 K. However, when Pn site is substituted from P to As along with doping of F^- at O site, T_c increases up to 26 K²¹ and the T_c drastically increased up to 55 K²² by changing RE site from La to Sm, which is much higher than T_c of BCS metals and other kinds of superconductor except those of the cuprates. These findings rekindled enthusiastic material researches on the new superconductors based on $\text{Fe}Pn_4$ or $\text{Fe}Ch_4$ tetrahedra because it had been thought that magnetic elements such as Fe disturb superconductivity. These compounds are now categorized into “iron-based” superconductors and many kinds of parent materials containing $\text{Fe}Pn_4$ or $\text{Fe}Ch_4$ tetrahedral layer were discovered²³⁻³⁰.

1.1.2. Crystal structures of iron-based superconductors

At the early stage of discovery of the cuprates, many kinds of related

superconductors containing “CuO₂ planes” were discovered. In the same way, one of the significant characteristic of the iron-based superconductors is “FePn₄ or FeCh₄ tetrahedral layer”

Figure 1 - 2 summarizes representative crystal structures of iron-based superconductors. The firstly discovered system is REFeAsO as I mentioned above. This system has the chemical composition of 1:1:1:1 for each element. Thus, it is abbreviated as 1111-type [Figure 1 - 2 (a)]. After the discovery of 1111-type, AEF₂As₂ (AE = alkaline earth and Eu) was rapidly dicovered. This family is called “122-type” with the ThCr₂Si₂-type structure³¹. Then, AFeAs (A = alkali. This family is called “111-type”) with the CeFeSi-type structure²⁴ and FeCh (Ch = chalcogen) with the anti-PbO type structure (This family is called “11-type”)²⁵ were discovered in the same year. As shown in Figure 1 - 2, FePn₄ or FeCh₄ tetrahedral layer exists between blocking layers except for 11-type (i.e., 11-type does not have blocking layer.). In the case of iron-pnictide superconductors, the space between FePn₄ tetrahedral layers can be controlled by changing the blocking layer from simple atoms or square net to skuttrudite-^{29,30} and perovskites-types^{27,32}. Moreover, intercalation between FeSe₄ tetrahedral layers are also reported²⁶ and unique Fermi surface was reported³³.

1.1.3. Doping variations and pressure effects

In an analogous way to the cuprates, iron-based superconductors have many variations of doping methods. In the case of cuprates, the parent materials are antiferromagnetic (AFM) Mott insulator but insulator-superconductor transition occurs when carriers are doped by chemical substitution and/or controlling concentration of

oxygen vacancies. Undoped parent materials of the iron-based superconductors are also AFM metals. The AFM ordering occurs at 100–200 K along with structural phase transition from tetragonal to orthorhombic structures^{23,34–36}. However, the AFM long range order and the structural transition can be suppressed by doping carriers (electron and hole) or applying high pressures. After that, superconductivity is induced in iron-based layered parent materials.

Doping variation is categorized in “indirect” and “direct” dopings based on difference in its chemical substitution site. Indirect doping is the doping in blocking layer (e.g., doping to *AE* site in the case of *AFeFe₂As₂*). On the other hand, direct doping is the doping at Fe site of *FePn₄* or *FeCh₄* layer. Combining choices of carrier types with variation of the indirect or direct dopings, there are many variations of doping methods in iron-based superconductors. In Table 1 - 1, representative doping methods are summarized.

Another method to induce the superconductivity is to apply external high-pressures to parent materials (Table 1 - 2). Undoped parent phases of iron-based superconductors are AFM metals. The AFM ordering occurs along with the structural phase transition from tetragonal to orthorhombic lattices. While, external pressures can suppress the AFM transition by structural tuning. Moreover, external pressure works well to increase the T_c except for the 122 system (Table 1 - 3).

(i) 1111 system

$\text{LaFeAsO}_{0.89}\text{F}_{0.11}$ exhibits T_c at 26 K but T_c extremely enhanced up to 43 K. This report activated the research for the high pressure studies of iron-based superconductors. However, the application of external pressure in undoped LaFeAsO without intentional

impurity-doping induced onset $T_c = 21$ K at 12 GPa, although clear zero resistivity was not observed³⁷.

(ii) 122 system

In 122-type system, undoped parent phases under an external high pressure exhibits clear zero-resistivity at high T_c of 34 K for SrFe_2As_2 at 3.5 GPa³⁸ and 35 K for BaFe_2As_2 at 3.0 GPa³⁹. On the other hand, T_c of the 122 system does not increase by applying pressure. This point is an exception among the iron-based superconductors.

(iii) 111 system

In 111 system, parent material $\text{Li}_{0.8}\text{FeAs}$ shows the superconducting transition at 18 K at ambient pressure. However, T_c of $\text{Li}_{0.8}\text{FeAs}$ decreases with increasing pressure. On the other hand, T_c of $\text{Na}_{0.9}\text{FeAs}$ increases with increasing pressure. While, at higher pressures than 3 GPa, T_c gently decreases.⁴⁰

(iv) 11 system

In this system, parent $\text{Fe}_{1.01}\text{Se}$ is a superconductor but its T_c largely enhanced by an external pressure from 8 K to 37 K⁴¹.

1.1.4. High upper critical magnetic field and small anisotropy

One of attractive properties of the iron-based superconductors are large upper critical magnetic fields H_{c2} with small anisotropies ($\gamma = H_{c2}(0)//ab / H_{c2}(0)//c$) because the BCS-type superconductors have usually small $H_{c2}(0) < 30$ T. Although the cuprates have extremely large H_{c2} but their wires and tapes are still expensive due to the complicated fabrication process and/or components of precious elements such as silver. Soon after the discovery of the iron-based superconductors, H_{c2} measurement of polycrystalline $\text{LaFeAs}(\text{O}_{1-x}\text{F}_x)$ revealed its quite high $H_{c2}(0) > 60$ T [Figure 1 - 3 (a)]⁴².

After that, it is also reported that $(\text{Ba}_{1-x}\text{K}_x)\text{Fe}_2\text{As}_2$ [Figure 1 - 3 (b)]⁴³ and $\text{Ba}(\text{Fe},\text{Co})_2\text{As}_2$ [Figure 1 - 3 (c)]⁴⁴ have the large $H_{c2}(0)$ over 60 T with small anisotropies. Reflecting its three-dimensional Fermi surface structure of 122-type materials, they exhibit isotropic H_{c2} properties. Therefore, isotropic J_c properties are also expected because anisotropy of J_c is also affected by anisotropy of coherent length and penetration depth, which are directly related to its electronic structure.

1.1.5. Heteroepitaxial growth and superconducting properties of iron pnictide thin films: Advantageous properties for application

Since the discovery of the iron-based superconductors, much effort has been invested in thin film growth and their characterizations. Hiramatsu et al. first reported 1111-type iron-pnictide epitaxial films in Aug. 2008. They attempted to grow epitaxial films of LaFeAsO (La-1111) using several techniques, including conventional laser ablation, post-deposition thermal annealing in evacuated ampoules, and reactive solid-phase epitaxy method, which are effective for the fabrication of epitaxial films of the other ZrCuSiAs type compounds. However, not even a polycrystalline film of the target La-1111 phase was obtained, even when a single-crystal substrate was used. Hence, they reoptimized the preparation conditions of bulk La-1111 samples and obtained a pure-phase laser ablation target free from wide-gap impurity phases such as La_2O_3 and LaOF . Moreover, they also changed the excitation source of laser ablation from an ArF excimer laser to the second harmonics ($\lambda = 532$ nm) of a neodymium-doped yttrium aluminum garnet (Nd:YAG) laser.^{45,46} These improvements along with further optimization of the substrate temperature to 780 °C under a vacuum

of $\sim 10^{-5}$ Pa led to the successful growth of epitaxial La1111 thin films [Figure 1 - 5 (a)]. However, the resulting LaFeAsO epitaxial films did not show superconducting transition owing to severe deficiency of F dopant in the films [Figure 1 - 5 (b)].

Then, the dopant was changed from F to Co with lower vapor pressure, and the $A\text{E}(\text{Fe},\text{Co})_2\text{As}_2$ epitaxial films exhibited clear superconducting transitions at $T_c = \sim 20$ K. These are the first fabrication of superconducting epitaxial films of the iron-based superconductors. [Figure 1 - 5 (c)]⁴⁷

To apply this high- T_c superconductor film for application, enhancement of critical current density (J_c) was absolutely necessary. Katase et al. succeeded in fabrication of $\text{Ba}(\text{Fe},\text{Co})_2\text{As}_2$ epitaxial films exhibiting high $J_c > 1$ MA/cm² by precisely-optimized film-growth conditions and using high-purity targets. Impurities was eliminated in high quality (HQ) films [Figure 1 - 6 (a)(b)] and the HQ film exhibits a sharp superconducting transition [$\Delta T_c = 1.1$ K, Figure 1 - 6 (c)]. In addition, the HQ film has strong c -axis pinning centers that work even at high fields up to 15 T [Figure 1 - 6 (d)]. Origin of such a high J_c , which is much larger than J_c of $\sim 10^5$ A/cm² for single crystals with the same chemical composition, was clarified to be good crystalinities and strong c -axis pinning centers.

On the other hand, S. Lee et al⁴⁸. succeeded in fabricating $\text{Ba}(\text{Fe},\text{Co})_2\text{As}_2$ epitaxial films exhibiting $J_c > 1$ MA/cm² using perovskite-oxide buffer [Figure 1 - 7 (a)]. Moreover, SrTiO_3 (STO) buffer layer provides oxygen to the film, and BaFeO_2 nanorods⁴⁹ whose diameter is about 4nm are introduced during thin film growth [Figure 1 - 7 (b)]. These nanorods become high density pinning centers and the film on STO buffer layer exhibits such a high J_c , not only in self-field but also in high magnetic fields. [Figure 1 - 7 (c)]

Iida et al. also succeeded in fabricating high- J_c Ba(Fe,Co) $_2$ As $_2$ epitaxial films using thin Fe buffer layer between films and substrates. Figure 1 - 7 (d) shows cross-sectional HR-STEM and HR-TEM images between the Ba(Fe $_{1-x}$ Co $_x$) $_2$ As $_2$ film and the Fe buffer layer. The Ba(Fe,Co) $_2$ As $_2$ film is grown heteroepitaxially on the Fe (001) buffer layer with the epitaxial relationship of [001] Ba(Fe,Co) $_2$ As $_2$ // [001] Fe buffer layer for out-of-plane and [100] Ba(Fe,Co) $_2$ As $_2$ // [110] Fe buffer layer for in-plane. The Fe buffer layer improves crystallinity of the film and the film exhibits high- J_c [Figure 1 - 7 (b)]. Therefore, to achieve fabrication of the high- J_c epitaxial films, it was believed that these were necessary: (i) Nd:YAG laser as the excitation source for direct deposition (i.e., without any buffer layer) or (ii) buffer layer on single-crystal substrates.

After these achievements of the high- J_c films, an advantageous grain boundary (GB) nature of Ba(Fe,Co) $_2$ As $_2$ films for superconducting tapes was clarified using biaxially grain boundary (BGB) junctions with entire misorientation angle (θ_{GB}) range of 3–45°. ⁵⁰ The primary point is that the Ba(Fe,Co) $_2$ As $_2$ BGB junctions exhibit a transition from strong-link to weak-link at a critical θ_{GB} angle (θ_c) of 9° [Figure 1 - 8 (a)], which is much higher than that of cuprates ($\theta_c = 3\text{--}5^\circ$). No deterioration of J_c even at $\theta_c = 9^\circ$ makes it easier to produce high- J_c superconducting tapes [Figure 1 - 8 (b)] with lower-cost fabrication process because formation of a buffer layer with large in-plane mis-orientation ($\Delta\phi \leq 9^\circ$) is much easier than those ($\Delta\phi < 5^\circ$), which is used for cuprate-based superconducting tapes such as YBa $_2$ Cu $_3$ O $_{7-\delta}$. Figure 1 - 8 (c) shows $\rho - T$ curve of a Ba(Fe $_{1-x}$ Co $_x$) $_2$ As $_2$ film on IBAD-MgO substrate (red closed circles) and an epitaxial film on MgO single-crystal substrate (blue open circles) in temperature range 15–35 K. T_c of the film on IBAD-MgO substrate is almost the same as that on single crystal, and superconducting–normal transitions are sharp until $\Delta\phi_{MgO} = 7.3^\circ$. These

results are consistent with BGB junctions experiment data and clarify advantageous GB nature of Ba(Fe,Co)₂As₂ films for superconducting tapes.

1.1.6. Comparison with other superconductors: toward future applications

Table 1 - 4. summarizes superconducting properties and anisotropies of the iron-based superconductors⁵¹⁻⁵⁹ and representative other superconductors⁶⁰⁻⁶⁴. As I mentioned in section 1.1.4., the iron-based superconductors have extremely high H_{c2} with small γ and good GB properties. Compared with the cuprates, 122-type and 11-type iron-based superconductors are particularly superior to the cuprates. Although anisotropies of the BCS metals such as Nb-Ti, Nb₃Sn, and MgB₂ are almost negligible^{60,65}, H_{c2} of these materials are lower than 30 T. Therefore, the iron-based superconductors are promising for superconducting wires and tapes for high field applications.

Figure 1 - 9 summarizes the current state of the iron-based superconductor with other superconductors. Figure 1 - 9 (a) shows the magnetic field dependence of J_c of a Ba(Fe_{1-x}Co_x)₂As₂ epitaxial film on IBAD-MgO substrate⁶⁶. Reflecting the robustness for the misorientation, self-field J_c is over 1MA/cm² but the in-field J_c is lower than that of cuprates and conventional superconductors. These results indicate that the microstructure engineering is necessary to improve the in-field J_c . Figure 1 - 9 (b) shows temperature dependence of H_{c2} . As shown in Figure 1 - 9 (b), H_{c2} is enough for high-field application. Figure 1 - 9 (c) shows applicable conditions of the conventional superconductors and the cuprates. The low-temperature region area (magenta shaded area) can be covered by using the conventional superconductors and they are practically used in this region. As mentioned above, the iron-based superconductors have extremely

high H_{c2} and comparatively high T_c compared with the conventional superconductors. Compared with the conventional superconductors, the iron-based conductors have great potential not only for high magnetic field application but also for high temperature application (red shaded area). While, H_{c2} line is observed $\rho = 0.9\rho_0$. Therefore, how to disturb the deterioration of J_c is the key for the future application.

1.2. Objectives and outline of this study

Based on the above overview of the iron-based superconductors, the most noteworthy issues are the following three points:

1. Critical factor of the thin film fabrication process. 3 groups achieved the fabrication of the high performance $\text{Ba}(\text{Fe},\text{Co})_2\text{As}_2$, but the fabrication process and its properties are completely different.
2. T_c of 122 type superconductors. Because of the wide growth window, low anisotropy, and extremely high H_{c2} , 122-type superconductors are the most promising materials among the iron-based superconductors. However, the T_c of 122-type superconductor is still lower than that of MgB_2 . If it is not enhanced, application of the iron-based superconductor is very limited because of high fabrication cost.

3. Microstructure engineering and demonstration of the potential for future practical application. Because J_c of 122-type superconductors still lower than that of practical superconducting wires and tapes. $\text{Ba}(\text{Fe}_{1-x}\text{Co}_x)_2\text{As}_2$ exhibit the strong c -axis pinning, but it depends on the fabrication process.

In this study, the following three objectives were therefore established to examine the intrinsic/extrinsic properties and to demonstrate the superconductor tapes.

1. Clarification of the critical factor in the fabrication process of high-quality 122-type BaFe_2As_2 epitaxial films grown by pulsed laser deposition: High-quality epitaxial films are inevitable to clarify the intrinsic physical properties and to examine the potential for the practical applications.

2. Establishment of the way to enhance the T_c of 122-type superconductors utilizing the heterointerface structure and the investigation of the relationship among superconductivity, local structure and carrier density. In addition, the fabrication of the epitaxial film which exhibits higher T_c should be examined by changing the doping mode.

3. Evaluation of the vortex pinning properties and feedback to the demonstration of the fabrication of the thin film on the practical superconducting tape.

This thesis is summarized into the following 9 chapters.

Chapter 1 describes the general introduction and objectives of this study.

Chapter 2 describes how the excitation wavelength and pulse energy affected the growth of cobalt-doped BaFe_2As_2 films on $(\text{La,Sr})(\text{Al,Ta})\text{O}_3$ single-crystal substrates. I found that the optimal deposition rate, which could be tuned by pulse energy, was independent of laser wavelength.

Chapter 3 describes the mixed state Hall effects in a $\text{Ba}(\text{Fe}_{1-x}\text{Co}_x)_2\text{As}_2$ epitaxial film to examine the vortex pinning mechanism.

Chapter 4 describes the new approach to apply the anisotropic pressures utilizing the hetero-interface properties such as differences in thermal expansion coefficients and the compressibilities between optimally cobalt doped BaFe_2As_2 and various substrates.

Chapter 5 describes pressure effects on superconductivity of metastable indirect electron-doped BaFe_2As_2 films.

Chapter 6 and 7 describes the heteroepitaxial growth of phosphorous-doped BaFe_2As_2 film and characterization of its vortex pinning properties.

Chapter 8 demonstrates the fabrication and characterization of phosphorus-doped BaFe_2As_2 films on practical metal-tape substrates.

Chapter 9 summarizes this study.

References

- ¹ H. Kamerling Onnes, *Akad. Van Wet. Amst.* **14**, 113 (1911).
- ² H. Kamerling Onnes, *Akad. Van Wet. Amst.* **16**, 673 (1913).
- ³ W. Meissner and H. Fraxz, *Z. Für Phys.* **65**, 30 (1930).
- ⁴ G. Aschermann, E. Frmdrich, E. Justi, and J. Krame, *Phys. Z.* **42**, 349 (1941).
- ⁵ B.T. Matthias, T.H. Geballe, S. Geller, and E. Corenzwit, *Phys. Rev.* **95**, 1435 (1954).
- ⁶ J.R. Gavaler, *Appl. Phys. Lett.* **23**, 480 (1973).
- ⁷ J. Nagamatsu, N. Nakagawa, T. Muranaka, Y. Zenitani, and J. Akimitsu, *Nature* **410**, 63 (2001).
- ⁸ M.K. Wu, J.R. Ashburn, C.J. Torng, P.H. Hor, R.L. Meng, L. Gao, Z.J. Huang, Y.Q. Wang, and C.W. Chu, *Phys. Rev. Lett.* **58**, 908 (1987).
- ⁹ H. Maeda, Y. Tanaka, M. Fukutomi, and T. Asano, *Jpn. J. Appl. Phys.* **27**, L209 (1988).
- ¹⁰ Z.Z. Sheng and A.M. Hermann, *Nature* **332**, 138 (1988).
- ¹¹ A. Schilling, M. Cantoni, J.D. Guo, and H.R. Ott, *Nature* **363**, 56 (1993).
- ¹² K. Bechgaard, K. Carneiro, M. Olsen, F.B. Rasmussen, and C.S. Jacobsen, *Phys. Rev. Lett.* **46**, 852 (1981).
- ¹³ H.H. Wang, M.A. Beno, U. Geiser, M.A. Firestone, K.S. Webb, L. Nunez, G.W. Crabtree, K.D. Carlson, and J.M. Williams, *Inorg Chem* **24**, 2465 (1985).
- ¹⁴ A.F. Hebard, M.J. Rosseinsky, R.C. Haddon, D.W. Murphy, S.H. Glarum, T.T.M. Palstra, A.P. Ramirez, and A.R. Kortan, *Nature* **350**, 600 (1991).
- ¹⁵ K. Tanigaki, T.W. Ebbesen, S. Saito, J. Mizuki, J.S. Tsai, Y. Kubo, and S. Kuroshima, *Nature* **352**, 222 (1991).
- ¹⁶ J.G. Bednorz and K.A. Müller, *Z. Für Phys. B Condens. Matter* **64**, 189 (1986).
- ¹⁷ D. Jérôme, A. Mazaud, M. Ribault, and K. Bechgaard, *J. Phys. Lett.* **41**, 95 (1980).
- ¹⁸ J. Bardeen, L.N. Cooper, and J.R. Schrieffer, *Phys. Rev.* **108**, 1175 (1957).
- ¹⁹ L. Gao, Y.Y. Xue, F. Chen, Q. Xiong, R.L. Meng, D. Ramirez, C.W. Chu, J.H. Eggert, and H.K. Mao, *Phys. Rev. B* **50**, 4260 (1994).
- ²⁰ Y. Kamihara, H. Hiramatsu, M. Hirano, R. Kawamura, H. Yanagi, T. Kamiya, and H. Hosono, *J. Am. Chem. Soc.* **128**, 10012 (2006).
- ²¹ Y. Kamihara, T. Watanabe, M. Hirano, and H. Hosono, *J. American Chem. Soc.* **130**, 3296 (2008).
- ²² Z.-A. Ren, W. Lu, J. Yang, W. Yi, X.-L. Shen, Z.-C. Li, G.-C. Che, X.-L. Dong, L.-L. Sun, F. Zhou, and Z.-X. Zhao, *Chin Phys Lett* **25**, 2215 (2008).
- ²³ M. Rotter, M. Tegel, D. Johrendt, I. Schellenberg, W. Hermes, and R. Pöttgen, *Phys. Rev. B* **78**, 020503 (2008).
- ²⁴ X.C. Wang, Q.Q. Liu, Y.X. Lv, W.B. Gao, L.X. Yang, R.C. Yu, F.Y. Li, and C.Q. Jin, *Solid State Commun.* **148**, 538 (2008).

- ²⁵ F.-C. Hsu, J.-Y. Luo, K.-W. Yeh, T.-K. Chen, T.-W. Huang, P.M. Wu, Y.-C. Lee, Y.-L. Huang, Y.-Y. Chu, D.-C. Yan, and M.-K. Wu, *Proc Natl Acad Sci USA* **105**, 14262 (2008).
- ²⁶ J. Guo, S. Jin, G. Wang, S. Wang, K. Zhu, T. Zhou, M. He, and X. Chen, *Phys. Rev. B* **82**, 180520 (2010).
- ²⁷ H. Ogino, Y. Matsumura, Y. Katsura, K. Ushiyama, S. Horii, K. Kishio, and Jun-ichi Shimoyama, *Supercond. Sci. Technol.* **22**, 075008 (2009).
- ²⁸ X. Zhu, F. Han, G. Mu, P. Cheng, B. Shen, B. Zeng, and H.-H. Wen, *Phys. Rev. B* **79**, 220512 (2009).
- ²⁹ N. Ni, J.M. Allred, B.C. Chan, and R.J. Cava, *Proc. Natl. Acad. Sci.* **108**, E1019 (2011).
- ³⁰ S. Kakiya, K. Kudo, Y. Nishikubo, K. Oku, E. Nishibori, H. Sawa, T. Yamamoto, T. Nozaka, and M. Nohara, *J. Phys. Soc. Jpn.* **80**, 093704 (2011).
- ³¹ M. Rotter, M. Tegel, and D. Johrendt, *Phys. Rev. Lett.* **101**, 107006 (2008).
- ³² H. Ogino, Y. Katsura, S. Horii, K. Kishio, and J. Shimoyama, *Supercond. Sci. Technol.* **22**, 085001 (2009).
- ³³ T. Qian, X.-P. Wang, W.-C. Jin, P. Zhang, P. Richard, G. Xu, X. Dai, Z. Fang, J.-G. Guo, X.-L. Chen, and H. Ding, *Phys. Rev. Lett.* **106**, 187001 (2011).
- ³⁴ C. de la Cruz, Q. Huang, J.W. Lynn, J. Li, W.R. II, J.L. Zarestky, H.A. Mook, G.F. Chen, J.L. Luo, N.L. Wang, and P. Dai, *Nature* **453**, 899 (2008).
- ³⁵ T. Nomura, S.W. Kim, Y. Kamihara, M. Hirano, P.V. Sushko, K. Kato, M. Takata, A.L. Shluger, and H. Hosono, *Supercond. Sci. Technol.* **21**, 125028 (2008).
- ³⁶ Q. Huang, Y. Qiu, W. Bao, M.A. Green, J.W. Lynn, Y.C. Gasparovic, T. Wu, G. Wu, and X.H. Chen, *Phys. Rev. Lett.* **101**, 257003 (2008).
- ³⁷ H. Okada, K. Igawa, H. Takahashi, Y. Kamihara, M. Hirano, H. Hosono, K. Matsubayashi, and Y. Uwatoko, *J. Phys. Soc. Jpn.* **77**, 113712 (2008).
- ³⁸ H. Kotegawa, H. Sugawara, and H. Tou, *J. Phys. Soc. Jpn.* **78**, 013709 (2008).
- ³⁹ F. Ishikawa, N. Eguchi, M. Kodama, K. Fujimaki, M. Einaga, A. Ohmura, A. Nakayama, A. Mitsuda, and Y. Yamada, *Phys. Rev. B* **79**, 172506 (2009).
- ⁴⁰ X.C. Wang, S.J. Zhang, Q.Q. Liu, Z. Deng, Y.X. Lv, J.L. Zhu, S.M. Feng, and C.Q. Jin, *High Press. Res.* **31**, 7 (2011).
- ⁴¹ S. Medvedev, T.M. McQueen, I.A. Troyan, T. Palasyuk, M.I. Eremets, R.J. Cava, S. Naghavi, F. Casper, V. Ksenofontov, G. Wortmann, and C. Felser, *Nat Mater* **8**, 630 (2009).
- ⁴² F. Hunte, J. Jaroszynski, A. Gurevich, D.C. Larbalestier, R. Jin, A.S. Sefat, M.A. McGuire, B.C. Sales, D.K. Christen, and D. Mandrus, *Nature* **453**, 903 (2008).
- ⁴³ H.Q. Yuan, J. Singleton, F.F. Balakirev, S.A. Baily, G.F. Chen, J.L. Luo, and N.L. Wang, *Nature* **457**, 565 (2009).
- ⁴⁴ A. Yamamoto, J. Jaroszynski, C. Tarantini, L. Balicas, J. Jiang, A. Gurevich, D.C. Larbalestier, R.

Jin, A.S. Sefat, M.A. McGuire, B.C. Sales, D.K. Christen, and D. Mandrus, *Appl. Phys. Lett.* **94**, 062511 (2009).

⁴⁵ H. Hiramatsu, T. Katase, T. Kamiya, M. Hirano, and H. Hosono, *Appl. Phys. Lett.* **93**, 162504 (2008).

⁴⁶ H. Hiramatsu, T. Katase, T. Kamiya, and H. Hosono, *J. Phys. Soc. Jpn.* **81**, 011011 (2012).

⁴⁷ H. Hiramatsu, T. Katase, T. Kamiya, M. Hirano, and H. Hosono, *Appl. Phys. Express* **1**, 101702 (2008).

⁴⁸ S. Lee, J. Jiang, Y. Zhang, C.W. Bark, J.D. Weiss, C. Tarantini, C.T. Nelson, H.W. Jang, C.M. Folkman, S.H. Baek, A. Polyanskii, D. Abraimov, A. Yamamoto, J.W. Park, X.Q. Pan, E.E. Hellstrom, D.C. Larbalestier, and C.B. Eom, *Nat. Mater.* **9**, 397 (2010).

⁴⁹ Y. Zhang, C.T. Nelson, S. Lee, J. Jiang, C.W. Bark, J.D. Weiss, C. Tarantini, C.M. Folkman, S.-H. Baek, E.E. Hellstrom, D.C. Larbalestier, C.-B. Eom, and X. Pan, *Appl. Phys. Lett.* **98**, 042509 (2011).

⁵⁰ T. Katase, Y. Ishimaru, A. Tsukamoto, H. Hiramatsu, T. Kamiya, K. Tanabe, and H. Hosono, *Nat. Commun.* **2**, 409 (2011).

⁵¹ J. Jaroszynski, S.C. Riggs, F. Hunte, A. Gurevich, D.C. Larbalestier, G.S. Boebinger, F.F. Balakirev, A. Migliori, Z.A. Ren, W. Lu, J. Yang, X.L. Shen, X.L. Dong, Z.X. Zhao, R. Jin, A.S. Sefat, M.A. McGuire, B.C. Sales, D.K. Christen, and D. Mandrus, *Phys. Rev. B* **78**, 064511 (2008).

⁵² Y. Jia, P. Cheng, L. Fang, H. Luo, H. Yang, C. Ren, L. Shan, C. Gu, and H.-H. Wen, *Appl. Phys. Lett.* **93**, 032503 (2008).

⁵³ M. Kano, Y. Kohama, D. Graf, F. Balakirev, A.S. Sefat, M.A. McGuire, B.C. Sales, D. Mandrus, and S.W. Tozer, *J. Phys. Soc. Jpn.* **78**, 084719 (2009).

⁵⁴ M.M. Altarawneh, K. Collar, C.H. Mielke, N. Ni, S.L. Bud'ko, and P.C. Canfield, *Phys. Rev. B* **78**, 220505 (2008).

⁵⁵ D.L. Sun, Y. Liu, and C.T. Lin, *Phys. Rev. B* **80**, 144515 (2009).

⁵⁶ J.E. Sonier, W. Huang, C.V. Kaiser, C. Cochran, V. Pacradouni, S.A. Sabok-Sayr, M.D. Lumsden, B.C. Sales, M.A. McGuire, A.S. Sefat, and D. Mandrus, *Phys. Rev. Lett.* **106**, 127002 (2011).

⁵⁷ J. Kacmarcik, C. Marcenat, T. Klein, Z. Pribulova, C.J. van der Beek, M. Konczykowski, S.L. Budko, M. Tillman, N. Ni, and P.C. Canfield, *Phys. Rev. B* **80**, 014515 (2009).

⁵⁸ M. Bendele, S. Weyeneth, R. Puzniak, A. Maisuradze, E. Pomjakushina, K. Conder, V. Pomjakushin, H. Luetkens, S. Katrych, A. Wisniewski, R. Khasanov, and H. Keller, *Phys. Rev. B* **81**, 224520 (2010).

⁵⁹ R. Khasanov, H. Luetkens, A. Amato, H.-H. Klauss, Z.-A. Ren, J. Yang, W. Lu, and Z.-X. Zhao, *Phys. Rev. B* **78**, 092506 (2008).

⁶⁰ M. Zehetmayer, M. Eisterer, J. Jun, S.M. Kazakov, J. Karpinski, A. Wisniewski, and H.W. Weber, *Phys. Rev. B* **66**, 052505 (2002).

- ⁶¹ R. Prozorov and V.G. Kogan, Rep. Prog. Phys. **74**, 124505 (2011).
- ⁶² P. Zimmermann, H. Keller, S.L. Lee, I.M. Savić, M. Warden, D. Zech, R. Cubitt, E.M. Forgan, E. Kaldis, J. Karpinski, and C. Krüger, Phys. Rev. B **52**, 541 (1995).
- ⁶³ Y. Kopelevich, S. Moehlecke, and J.H.S. Torres, Phys. Rev. B **49**, 1495 (1994).
- ⁶⁴ JSAP school text, *High Temperature Superconductor Data Book* (2009).
- ⁶⁵ A. Godeke, Supercond. Sci. Technol. **19**, R68 (2006).
- ⁶⁶ T. Katase, H. Hiramatsu, V. Matias, C. Sheehan, Y. Ishimaru, T. Kamiya, K. Tanabe, and H. Hosono, Appl. Phys. Lett. **98**, 242510 (2011).
- ⁶⁷ L. Harnagea, S. Singh, G. Friemel, N. Leps, D. Bombor, M. Abdel-Hafiez, A.U.B. Wolter, C. Hess, R. Klingeler, G. Behr, S. Wurmehl, and B. Büchner, Phys. Rev. B **83**, 094523 (2011).
- ⁶⁸ K. Zhao, Q.Q. Liu, X.C. Wang, Z. Deng, Y.X. Lv, J.L. Zhu, F.Y. Li, and C.Q. Jin, Phys. Rev. B **84**, 184534 (2011).
- ⁶⁹ S. Kasahara, T. Shibauchi, K. Hashimoto, Y. Nakai, H. Ikeda, T. Terashima, and Y. Matsuda, Phys. Rev. B **83**, 060505 (2011).
- ⁷⁰ A. Leithe-Jasper, W. Schnelle, C. Geibel, and H. Rosner, Phys. Rev. Lett. **101**, 207004 (2008).
- ⁷¹ Y. Muraba, S. Matsuishi, S.-W. Kim, T. Atou, O. Fukunaga, and H. Hosono, Phys. Rev. B **82**, 180512 (2010).
- ⁷² K. Sasmal, B. Lv, B. Lorenz, A.M. Guloy, F. Chen, Y.-Y. Xue, and C.-W. Chu, Phys. Rev. Lett. **101**, 107007 (2008).
- ⁷³ T. Kobayashi, S. Miyasaka, S. Tajima, and N. Chikumoto, J. Phys. Soc. Jpn. **83**, 104702 (2014).
- ⁷⁴ A.S. Sefat, R. Jin, M.A. McGuire, B.C. Sales, D.J. Singh, and D. Mandrus, Phys. Rev. Lett. **101**, 117004 (2008).
- ⁷⁵ T. Katase, S. Iimura, H. Hiramatsu, T. Kamiya, and H. Hosono, Phys. Rev. B **85**, 140516 (2012).
- ⁷⁶ M. Rotter, M. Tegel, and D. Johrendt, Phys. Rev. Lett. **101**, 107006 (2008).
- ⁷⁷ S. Kasahara, T. Shibauchi, K. Hashimoto, K. Ikada, S. Tonegawa, R. Okazaki, H. Shishido, H. Ikeda, H. Takeya, K. Hirata, T. Terashima, and Y. Matsuda, Phys. Rev. B **81**, 184519 (2010).
- ⁷⁸ M. Matusiak, Z. Bukowski, and J. Karpinski, Phys. Rev. B **83**, 224505 (2011).
- ⁷⁹ Anupam, P.L. Paulose, S. Ramakrishnan, and Z. Hossain, J. Phys. Condens. Matter **23**, 455702 (2011).
- ⁸⁰ G. Cao, S. Xu, Z. Ren, S. Jiang, C. Feng, and Z. Xu, J. Phys. Condens. Matter **23**, 464204 (2011).
- ⁸¹ S. Matsuishi, Y. Inoue, T. Nomura, H. Yanagi, M. Hirano, and H. Hosono, J. Am. Chem. Soc. **130**, 14428 (2008).
- ⁸² S. Matsuishi, Y. Inoue, T. Nomura, M. Hirano, and H. Hosono, J. Phys. Soc. Jpn. **77**, 113709 (2008).
- ⁸³ C. Wang, Y.K. Li, Z.W. Zhu, S. Jiang, X. Lin, Y.K. Luo, S. Chi, L.J. Li, Z. Ren, M. He, H. Chen, Y.T. Wang, Q. Tao, G.H. Cao, and Z.A. Xu, Phys. Rev. B **79**, 054521 (2009).

- ⁸⁴ J. Prakash, S.J. Singh, S. Patnaik, and A.K. Ganguli, *J. Phys. Condens. Matter* **21**, 175705 (2009).
- ⁸⁵ G. Mu, L. Fang, H. Yang, X. Zhu, P. Cheng, and H.-H. Wen, *J. Phys. Soc. Jpn.* **77**, 15 (2008).
- ⁸⁶ C. Wang, S. Jiang, Q. Tao, Z. Ren, Y. Li, L. Li, C. Feng, J. Dai, G. Cao, and Zhu-an Xu, *EPL Europhys. Lett.* **86**, 47002 (2009).
- ⁸⁷ L.-D. Zhao, D. Berardan, C. Byl, L. Pinsard-Gaudart, and N. Dragoë, *J. Phys. Condens. Matter* **22**, 115701 (2010).
- ⁸⁸ G.F. Chen, Z. Li, D. Wu, G. Li, W.Z. Hu, J. Dong, P. Zheng, J.L. Luo, and N.L. Wang, *Phys. Rev. Lett.* **100**, 247002 (2008).
- ⁸⁹ Y. Luo, Y. Li, S. Jiang, J. Dai, G. Cao, and Z. Xu, *Phys. Rev. B* **81**, 134422 (2010).
- ⁹⁰ X. Lin, H.J. Guo, C.Y. Shen, Y.K. Luo, Q. Tao, G.H. Cao, and Z.A. Xu, *Phys. Rev. B* **83**, 014503 (2011).
- ⁹¹ C.R. Rotundu, D.T. Keane, B. Freelon, S.D. Wilson, A. Kim, P.N. Valdivia, E. Bourret-Courchesne, and R.J. Birgeneau, *Phys. Rev. B* **80**, 144517 (2009).
- ⁹² G. Mu, B. Zeng, X. Zhu, F. Han, P. Cheng, B. Shen, and H.-H. Wen, *Phys. Rev. B* **79**, 104501 (2009).
- ⁹³ A. Marcinkova, D.A.M. Grist, I. Margiolaki, T.C. Hansen, S. Margadonna, and J.-W.G. Bos, *Phys. Rev. B* **81**, 064511 (2010).
- ⁹⁴ L. Malavasi, G.A. Artioli, C. Ritter, M.C. Mozzati, B. Maroni, B. Pahari, and A. Caneschi, *J. Am. Chem. Soc.* **132**, 2417 (2010).
- ⁹⁵ M. Xu, F. Chen, C. He, H.-W. Ou, J.-F. Zhao, and D.-L. Feng, *Chem. Mater.* **20**, 7201 (2008).
- ⁹⁶ K. Kasperkiewicz, J.-W.G. Bos, A.N. Fitch, K. Prassides, and S. Margadonna, *Chem. Commun.* 707 (2009).
- ⁹⁷ Y. Qi, Z. Gao, L. Wang, D. Wang, X. Zhang, and Y. Ma, *Supercond. Sci. Technol.* **21**, 115016 (2008).
- ⁹⁸ N.D. Zhigadlo, S. Katrych, S. Weyeneth, R. Puzniak, P.J.W. Moll, Z. Bukowski, J. Karpinski, H. Keller, and B. Batlogg, *Phys. Rev. B* **82**, 064517 (2010).
- ⁹⁹ N.D. Zhigadlo, S. Katrych, M. Bendele, P.J.W. Moll, M. Tortello, S. Weyeneth, V.Y. Pomjakushin, J. Kanter, R. Puzniak, Z. Bukowski, H. Keller, R.S. Gonnelli, R. Khasanov, J. Karpinski, and B. Batlogg, *Phys. Rev. B* **84**, 134526 (2011).
- ¹⁰⁰ T. Shang, L. Yang, Y. Chen, N. Cornell, F. Ronning, J.L. Zhang, L. Jiao, Y.H. Chen, J. Chen, A. Howard, J. Dai, J.D. Thompson, A. Zakhidov, M.B. Salamon, and H.Q. Yuan, *Phys. Rev. B* **87**, 075148 (2013).
- ¹⁰¹ E.P. Khlybov, O.E. Omelyanovsky, A. Zaleski, A.V. Sadakov, D.R. Gizatulin, L.F. Kulikova, I.E. Kostuleva, and V.M. Pudalov, *JETP Lett.* **90**, 387 (2009).
- ¹⁰² C. Wang, L. Li, S. Chi, Z. Zhu, Z. Ren, Y. Li, Y. Wang, X. Lin, Y. Luo, S. Jiang, X. Xu, G. Cao, and Z. 'an Xu, *EPL Europhys. Lett.* **83**, 67006 (2008).

- ¹⁰³ J.-W.G. Bos, G.B.S. Penny, J.A. Rodgers, D.A. Sokolov, A.D. Huxley, and J.P. Attfield, *Chem. Commun.* 3634 (2008).
- ¹⁰⁴ L.-J. Li, Y.-K. Li, Z. Ren, Y.-K. Luo, X. Lin, M. He, Q. Tao, Z.-W. Zhu, G.-H. Cao, and Z.-A. Xu, *Phys. Rev. B* **78**, 132506 (2008).
- ¹⁰⁵ Y. Luo, X. Lin, Y. Li, Q. Tao, L. Li, Z. Zhu, G. Cao, and Z. 'an Xu, *Int. J. Mod. Phys. B* **26**, 1250207 (2012).
- ¹⁰⁶ S.V. Chong, T. Mochiji, and K. Kadowaki, *J. Phys. Conf. Ser.* **150**, 052036 (2009).
- ¹⁰⁷ S. Ghannadzadeh, J.D. Wright, F.R. Foronda, S.J. Blundell, S.J. Clarke, and P.A. Goddard, *Phys. Rev. B* **89**, 054502 (2014).
- ¹⁰⁸ B. Lee, S. Khim, B.-J. Jeon, J.-Y. Park, S.H. Lee, K.-Y. Choi, G.R. Stewart, and K.H. Kim, *Phys. C Supercond.* **495**, 130 (2013).
- ¹⁰⁹ J.H. Tapp, Z. Tang, B. Lv, K. Sasmal, B. Lorenz, P.C.W. Chu, and A.M. Guloy, *Phys. Rev. B* **78**, 060505 (2008).
- ¹¹⁰ M.H. Fang, H.M. Pham, B. Qian, T.J. Liu, E.K. Vehstedt, Y. Liu, L. Spinu, and Z.Q. Mao, *Phys. Rev. B* **78**, 224503 (2008).
- ¹¹¹ H. Okada, H. Takahashi, S. Matsuishi, M. Hirano, H. Hosono, K. Matsubayashi, Y. Uwatoko, and H. Takahashi, *Phys. Rev. B* **81**, 054507 (2010).
- ¹¹² H. Takahashi, H. Okada, K. Igawa, Y. Kamihara, M. Hirano, H. Hosono, K. Matsubayashi, and Y. Uwatoko, *J. Supercond. Nov. Magn.* **22**, 595 (2009).
- ¹¹³ H. Lee, E. Park, T. Park, V.A. Sidorov, F. Ronning, E.D. Bauer, and J.D. Thompson, *Phys. Rev. B* **80**, 024519 (2009).
- ¹¹⁴ M. Kumar, M. Nicklas, A. Jesche, N. Caroca-Canales, M. Schmitt, M. Hanfland, D. Kasinathan, U. Schwarz, H. Rosner, and C. Geibel, *Phys. Rev. B* **78**, 184516 (2008).
- ¹¹⁵ W. Uhoya, G. Tsoi, Y.K. Vohra, M.A. McGuire, A.S. Sefat, B.C. Sales, David Mandrus, and S.T. Weir, *J. Phys. Condens. Matter* **22**, 292202 (2010).
- ¹¹⁶ H. Takahashi, K. Igawa, K. Arii, Y. Kamihara, M. Hirano, and H. Hosono, *Nature* **453**, 376 (2008).
- ¹¹⁷ D.A. Zocco, J.J. Hamlin, R.E. Baumbach, M.B. Maple, M.A. McGuire, A.S. Sefat, B.C. Sales, R. Jin, D. Mandrus, J.R. Jeffries, S.T. Weir, and Y.K. Vohra, *Phys. C Supercond.* **468**, 2229 (2008).
- ¹¹⁸ W. Yi, L. Sun, Z. Ren, W. Lu, X. Dong, H. Zhang, X. Dai, Z. Fang, Z. Li, G. Che, J. Yang, X. Shen, F. Zhou, and Z. Zhao, *EPL Europhys. Lett.* **83**, 57002 (2008).
- ¹¹⁹ M.S. Torikachvili, S.L. Bud'ko, N. Ni, and P.C. Canfield, *Phys. Rev. B* **78**, 104527 (2008).
- ¹²⁰ K. Ahilan, F.L. Ning, T. Imai, A.S. Sefat, M.A. McGuire, B.C. Sales, and D. Mandrus, *Phys. Rev. B* **79**, 214520 (2009).
- ¹²¹ E. Colombier, M.S. Torikachvili, N. Ni, A. Thaler, S.L. Bud'ko, and P.C. Canfield, *Supercond. Sci. Technol.* **23**, 054003 (2010).

- ¹²² L. E. Klintberg, S. K. Goh, S. Kasahara, Y. Nakai, K. Ishida, M. Sutherland, T. Shibauchi, Y. Matsuda, and T. Terashima, *J. Phys. Soc. Jpn.* **79**, 123706 (2010).
- ¹²³ A.F. Wang, Z.J. Xiang, J.J. Ying, Y.J. Yan, P. Cheng, G.J. Ye, X.G. Luo, and X.H. Chen, *New J. Phys.* **14**, 113043 (2012).
- ¹²⁴ S.J. Zhang, X.C. Wang, R. Sammynaiken, J.S. Tse, L.X. Yang, Z. Li, Q.Q. Liu, S. Desgreniers, Y. Yao, H.Z. Liu, and C.Q. Jin, *Phys. Rev. B* **80**, 014506 (2009).
- ¹²⁵ R. Khasanov, H. Luetkens, A. Amato, H.-H. Klauss, Z.-A. Ren, J. Yang, W. Lu, and Z.-X. Zhao, *Phys. Rev. B* **78**, 092506 (2008).
- ¹²⁶ M. Kano, Y. Kohama, D. Graf, F. Balakirev, A. S. Sefat, M. A. Mcguire, B. C. Sales, D. Mandrus, and S. W. Tozer, *J. Phys. Soc. Jpn.* **78**, 084719 (2009).
- ¹²⁷ D.L. Sun, Y. Liu, and C.T. Lin, *Phys. Rev. B* **80**, 144515 (2009).
- ¹²⁸ D. Larbalestier, A. Gurevich, D.M. Feldmann, and A. Polyanskii, *Nature* **414**, 368 (2001).
- ¹²⁹ Y. Kopelevich, S. Moehlecke, and J.H.S. Torres, *Phys. Rev. B* **49**, 1495 (1994).
- ¹³⁰ Y. Kamihara, H. Hiramatsu, M. Hirano, R. Kawamura, H. Yanagi, T. Kamiya, and H. Hosono, *J. Am. Chem. Soc.* **128**, 10012 (2006).
- ¹³¹ X.H. Chen, T. Wu, G. Wu, R.H. Liu, H. Chen, and D.F. Fang, *Nature* **453**, 761 (2008).
- ¹³² K. Tanabe and H. Hosono, *Jpn. J. Appl. Phys.* **51**, 010005 (2012).
- ¹³³ T. Katase, H. Hiramatsu, T. Kamiya, and H. Hosono, *Appl. Phys. Express* **3**, 063101 (2010).
- ¹³⁴ B. Maiorov, T. Katase, S.A. Baily, H. Hiramatsu, T.G. Holesinger, H. Hosono, and L. Civale, *Supercond. Sci. Technol.* **24**, 055007 (2011).
- ¹³⁵ T. Thersleff, K. Iida, S. Haindl, M. Kitzun, D. Pohl, A. Hartmann, F. Kurth, J. Hänisch, R. Hühne, B. Rellinghaus, L. Schultz, and B. Holzapfel, *Appl. Phys. Lett.* **97**, 022506 (2010).
- ¹³⁶ D. Rall, K. Il'in, K. Iida, S. Haindl, F. Kurth, T. Thersleff, L. Schultz, B. Holzapfel, and M. Siegel, *Phys. Rev. B* **83**, 134514 (2011).
- ¹³⁷ A. Xu, J.J. Jaroszynski, F. Kametani, Z. Chen, D.C. Larbalestier, Y.L. Viouchkov, Y. Chen, Y. Xie, and V. Selvamanickam, *Supercond. Sci. Technol.* **23**, 014003 (2010).
- ¹³⁸ C.G. Zhuang, S. Meng, H. Yang, Y. Jia, H.H. Wen, X.X. Xi, Q.R. Feng, and Z.Z. Gan, *Supercond. Sci. Technol.* **21**, 082002 (2008).
- ¹³⁹ C. Tarantini, A. Gurevich, J. Jaroszynski, F. Balakirev, E. Bellingeri, I. Pallecchi, C. Ferdeghini, B. Shen, H.H. Wen, and D.C. Larbalestier, *Phys. Rev. B* **84**, 184522 (2011).
- ¹⁴⁰ J. Shimoyama, *Supercond. Sci. Technol.* **27**, 044002 (2014).

Table 1 - 1. Summary of the doping variation and T_c .

System	Parent	Dopant/site [doping mode]				
		Co(d7)/Fe(d6) [electron]	La ³⁺ /Ae ²⁺ [electron]	A ⁺ /Ae ²⁺ [hole]	P/As [isovalent]	
122	CaFe ₂ As ₂	20 ^[67]		34 ^[68]	15 ^[69]	
	SrFe ₂ As ₂	20 ^[70]	22 ^[71]	37 ^[72]	33 ^[73]	
	BaFe ₂ As ₂	22 ^[74]	22 ^[75]	37 ^[76]	31 ^[77]	
	EuFe ₂ As ₂	20.5 ^[78]		33 ^[79]	29 ^[80]	
		Co(d7)/Fe(d6) [electron]	F ⁻ /O ²⁻ [electron]	Th ⁴⁺ /RE ³⁺ [electron]	Sr ²⁺ /RE ³⁺ [hole]	P/As [isovalent]
1111	CaFeAsF	22 ^[81]				
	SrFeAsF	4 ^[82]				
	LaFeAsO	13 ^[83]	26 ^[21]	30.3 ^[84]	25 ^[85]	11 ^[86]
	CeFeAsO	12.5 ^[87]	41 ^[88]			NO-SC ^[89]
	PrFeAsO	16 ^[90]	47 ^[91]		16.3 ^[92]	
	NdFeAsO	16.5 ^[93]	45 ^[94]	38 ^[95]	13.5 ^[96]	
	SmFeAsO	17.2 ^[97]	55 ^[22]	51.5 ^[98]		NO-SC ^[99]
	GdFeAsO	20 ^[100]	53 ^[101]	56 ^[102]		
	TbFeAsO		45.5 ^[103]	52 ^[104]		
	DyFeAsO		45.3 ^[103]	49 ^[105]		
	HoFeAsO					
ErFeAsO						
YFeAsO		10.2 ^[106]				
		Co(d7)/Fe(d6) [electron]	Te/Se [isovalent]	Non-doped		
111 & 11	NaFeAs	21 ^[107]		10 ^[107]		
	LiFeAs	Continuously decrease ^[108]		18 ^[109]		
	FeSe		14 ^[110]	8 ^[25]		

Table 1 - 2. Summary of pressure induced superconductivity of parent materials of iron-based-superconductors. 111 type and 11 type superconductors are not listed because they exhibit superconductivity at ambient pressure.

System	Parent	T_c^{opt} (K)	P^{opt} (GPa)	Ref.
1111	CaFeAsF	29	5	[111]
	LaFeAsO	21	12	[112]
	SmFeAsO	11	9	[112]
122	CaFe ₂ As ₂	12	0.5	[113]
	SrFe ₂ As ₂	34	3.5	[114]
	BaFe ₂ As ₂	35	3.5	[39]
	EuFe ₂ As ₂	41	10	[115]

Table 1 - 3. Pressure effects on iron-based superconductors.

System	Superconductors	T_c (0GPa)	dT_c/dP (K/GPa)	T_c^{opt} (P)	Ref.
1111	CaFe _{0.9} Co _{0.1} AsF	23.8	+ 0.9	24.7	[111]
	LaFeAsO _{0.89} F _{0.11}	26	+ 5.7	43	[116]
	CeFeAsO _{0.88} F _{0.12}	44	- 1.6		[117]
	NdFeAsO _{0.85}	53	- 2.6		[118]
	SmFeAsO _{0.85}	55	- 2.0		[118]
122	Ba _{0.55} K _{0.45} Fe ₂ As ₂	30	- 0.2		[119]
	Ba(Fe _{0.926} Co _{0.074}) ₂ As ₂	22	- 2.2		[120,121]
	BaFe ₂ (As _{0.65} P _{0.35}) ₂	31	- 0.3		[122]
	EuFe ₂ (As _{0.81} P _{0.19}) ₂	23	- 2.6		[122]
111	NaFe _{0.972} Co _{0.028} As	20	+ 4.8	31	[123]
	NaFe _{0.99} Co _{0.01} As	22	+ 1.7	32.5	[123]
	LiFeAs	18	- 1.3		[124]
11	Fe _{1.01} Se	8	+ 3.2	36.7	[41]

Table 1 - 4. Summary of the superconducting properties of iron-based superconductors and other representative superconductors. T_c , ξ , H_{c2} , λ and γ are critical temperature, coherent length, upper critical magnetic field, penetration depth and anisotropy factor. Here, ξ is estimated from $H_{c2}(T)$ using the Ginzburg-Landau expression, $\xi = \Phi_0 / (2\pi\mu_0(dH_{c2}/dT)|_{T_c} T_c)^{1/2}$ and penetration depth λ is measured by muon spin relaxation and/or tunnel diode resonator techniques.

Material	T_c (K)	ξ_{ab} (nm)	ξ_c (nm)	$H_{c2}^{ab}(0)$ (T)	$H_{c2}^c(0)$ (T)	λ_{ab} (nm)	γ	Ref.
NdFeAsO _{1-x} F _x	55	1.8	0.45	70	304	195	5	[51,52,56,57,125,126]
Ba(Fe _{1-x} Co _x) ₂ As ₂	24	2.4	1.2	50	70	200	1.5	[56,61,126]
(Ba _{1-x} K _x)Fe ₂ As ₂	38	3.4	2.9	75	80	140	~1.2	[54]
FeSe _{1-x} Te _x	15	2.8	3	43	62	400	1-2	[58,127]
Nb-Ti	9.4		5.5		12	120	1	[128]
Nb ₃ Sn	18.3		3		30	85	1-3	[65]
MgB ₂	39	10.2	2.3	3.2	14.5	50	4.6	[60]
YBa ₂ Cu ₃ O _{7-δ}	93	2.1	0.4	72	350	140	5-7	[62,64]
Bi ₂ Sr ₂ Ca ₂ Cu ₃ O _{10+δ}	110	2.3	0.15	60	850	124	50-200	[129]

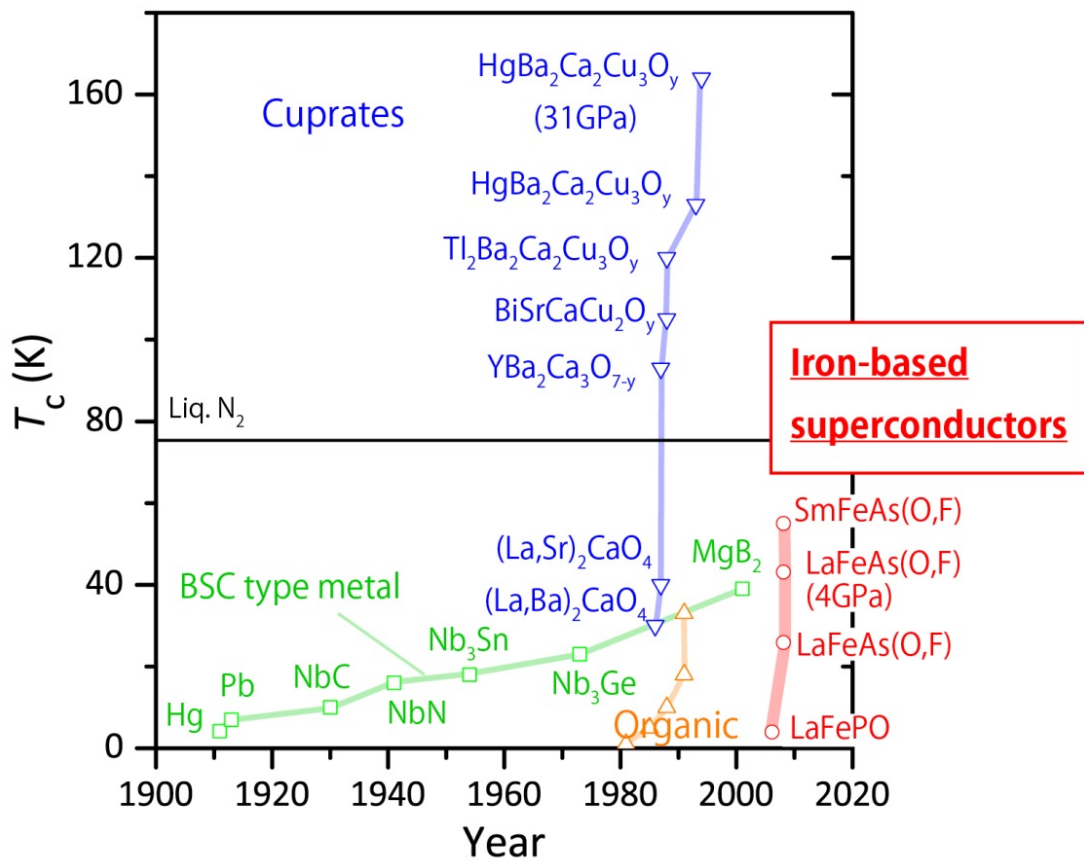


Figure 1 - 1. History of the superconductors. The square, reversed triangle, triangle and circle symbols indicate the critical temperature T_c of BCS metals¹⁻⁷, cuprates⁸⁻¹¹, organics^{12-15,17}, and iron-based superconductor^{21,116,130,131}, respectively.

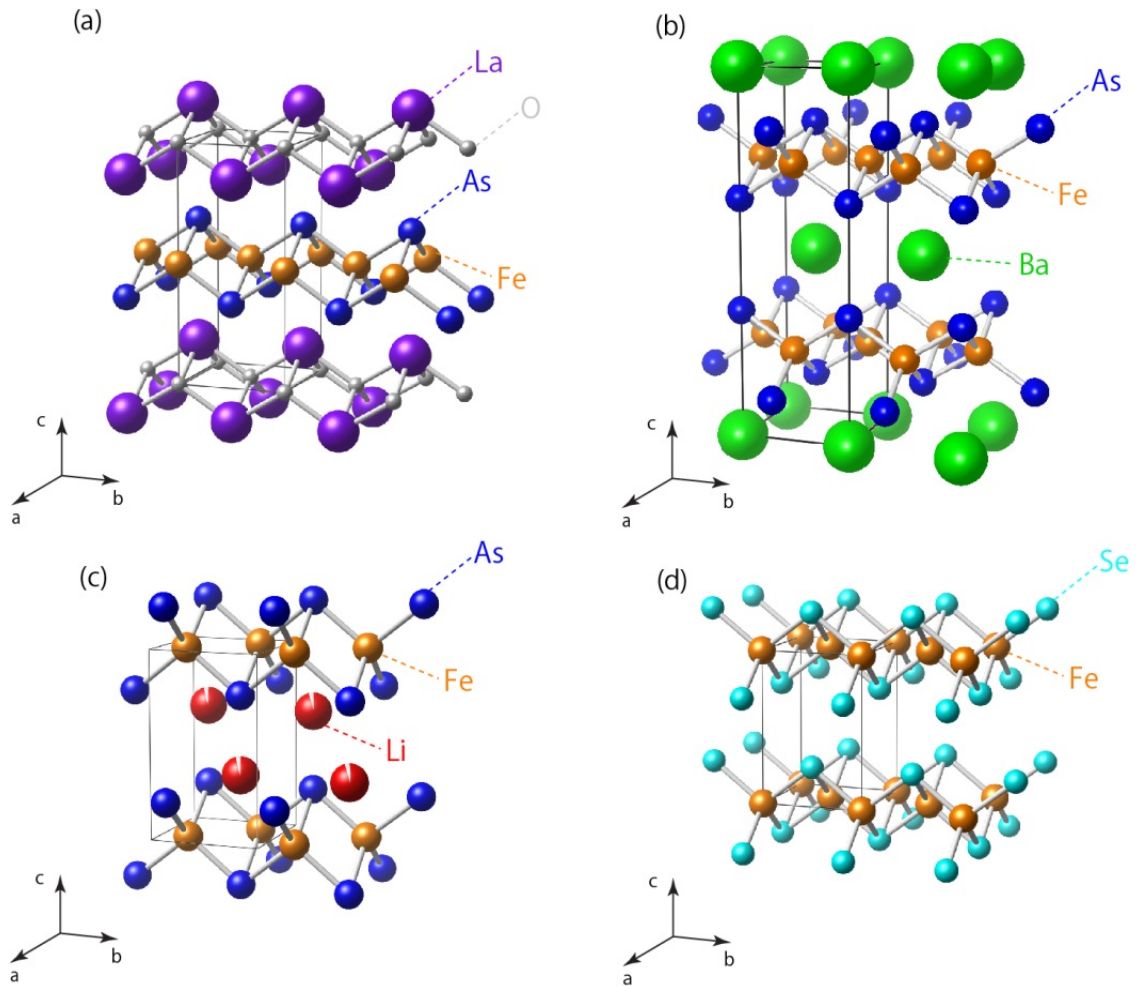


Figure 1 - 2. Crystal structures of iron-based superconductors. (a) 1111-type (represented by LaFeAsO), (b) 122-type (represented by BaFe_2As_2), (c) 111 (represented by $\text{Li}_{0.8}\text{FeAs}$) and (d) 11 (represented by FeSe)

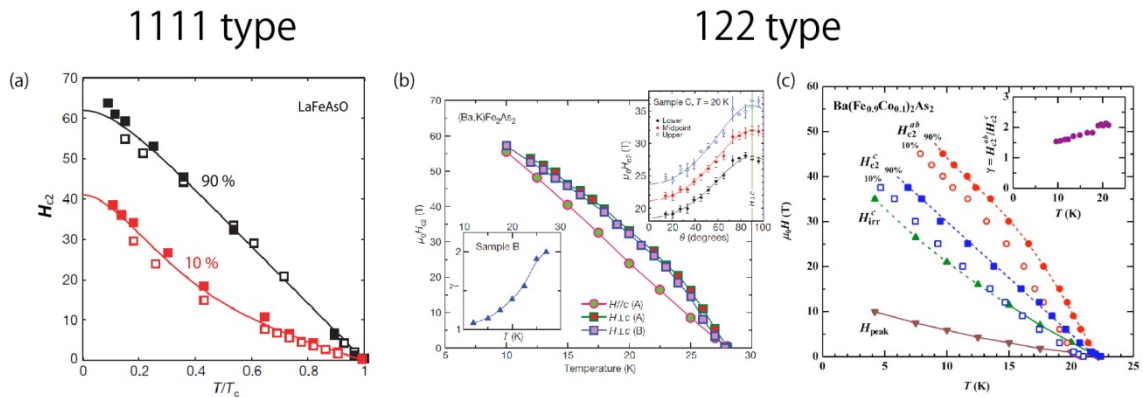


Figure 1 - 3. Upper critical magnetic fields H_{c2} of iron-based superconductors. (a) polycrystalline $\text{LaFeAsO}_{1-x}\text{F}_x$ ⁴², (b) $(\text{Ba,K})\text{Fe}_2\text{As}_2$ ⁴³ (c) $\text{Ba}(\text{Fe},\text{Co})_2\text{As}_2$ ⁴⁴.

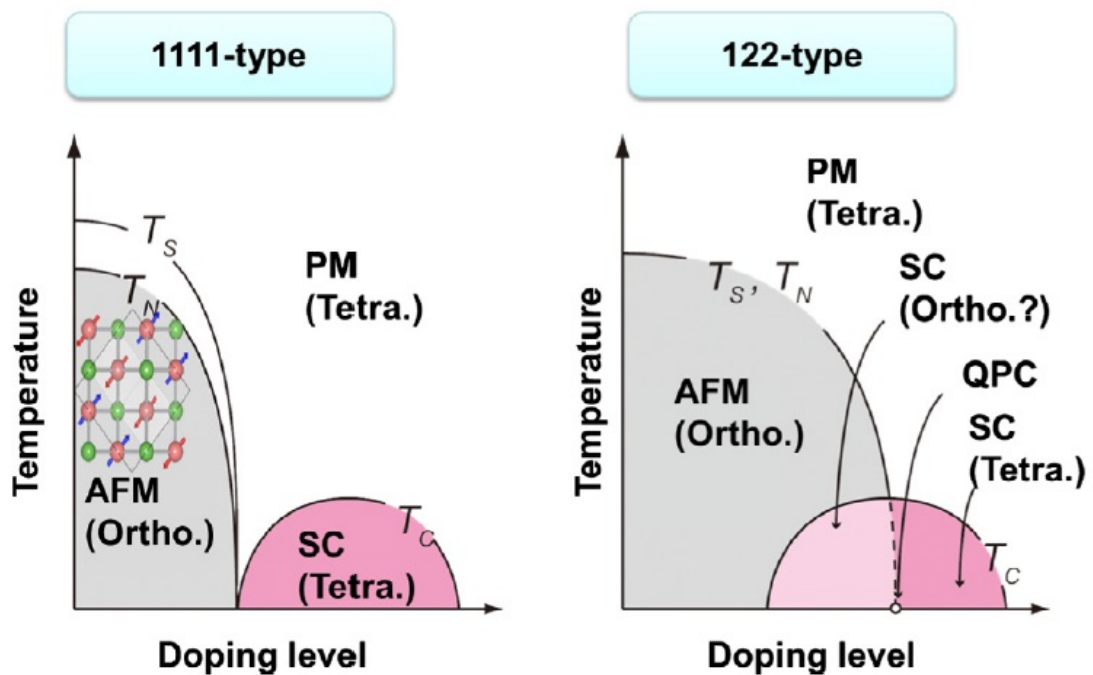


Figure 1 - 4. Phase diagrams of 1111-type (left) and 122-type (right) superconductors.¹³²

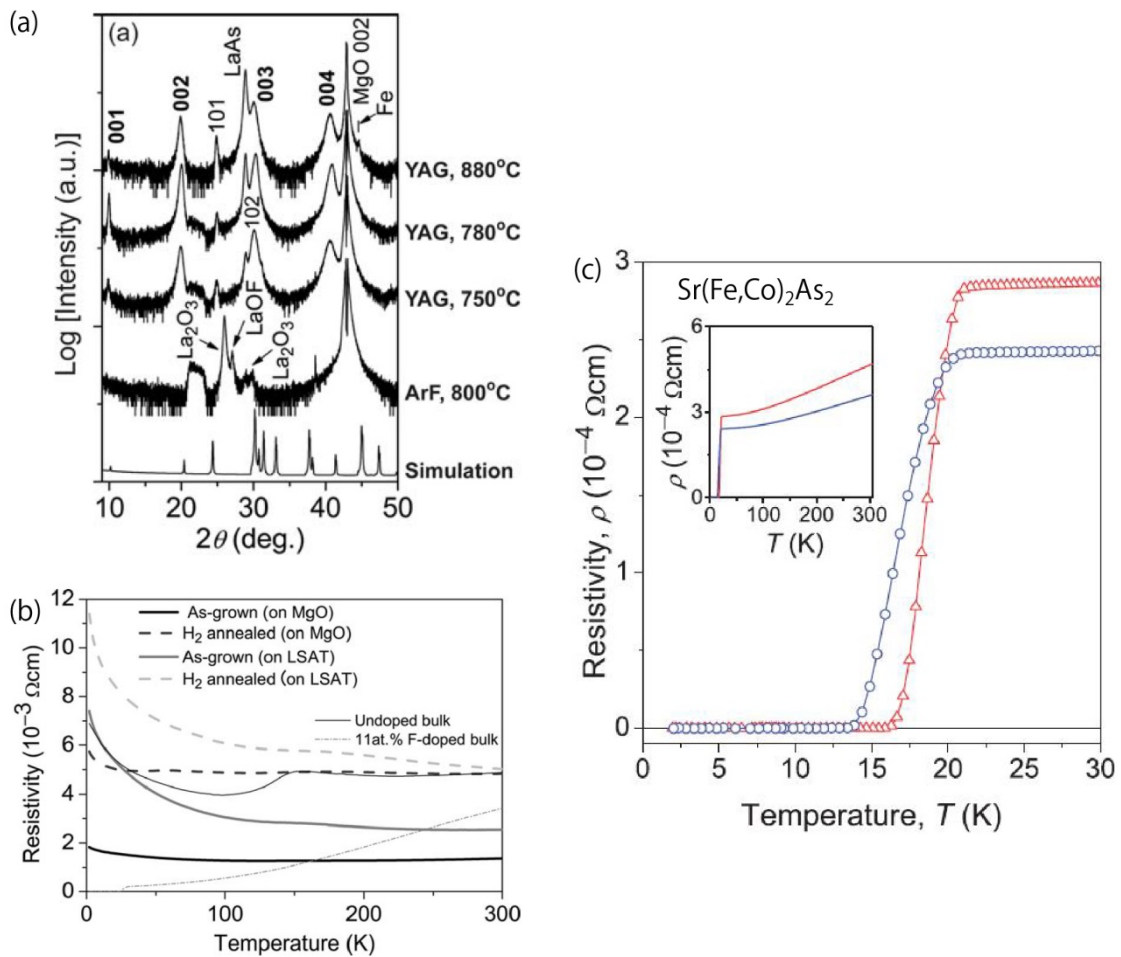


Figure 1 - 5. (a) XRD patterns of $\text{LaFeAsO}_{1-x}\text{F}_x$ epitaxial films. (b) $\rho - T$ curve of LaFeAsO epitaxial films which treated by annealing technique. (c) $\rho - T$ curve of $\text{Sr}(\text{Fe}_{1-x}\text{Co}_x)_2\text{As}_2$ film in temperature range 0–30 K⁴⁷.

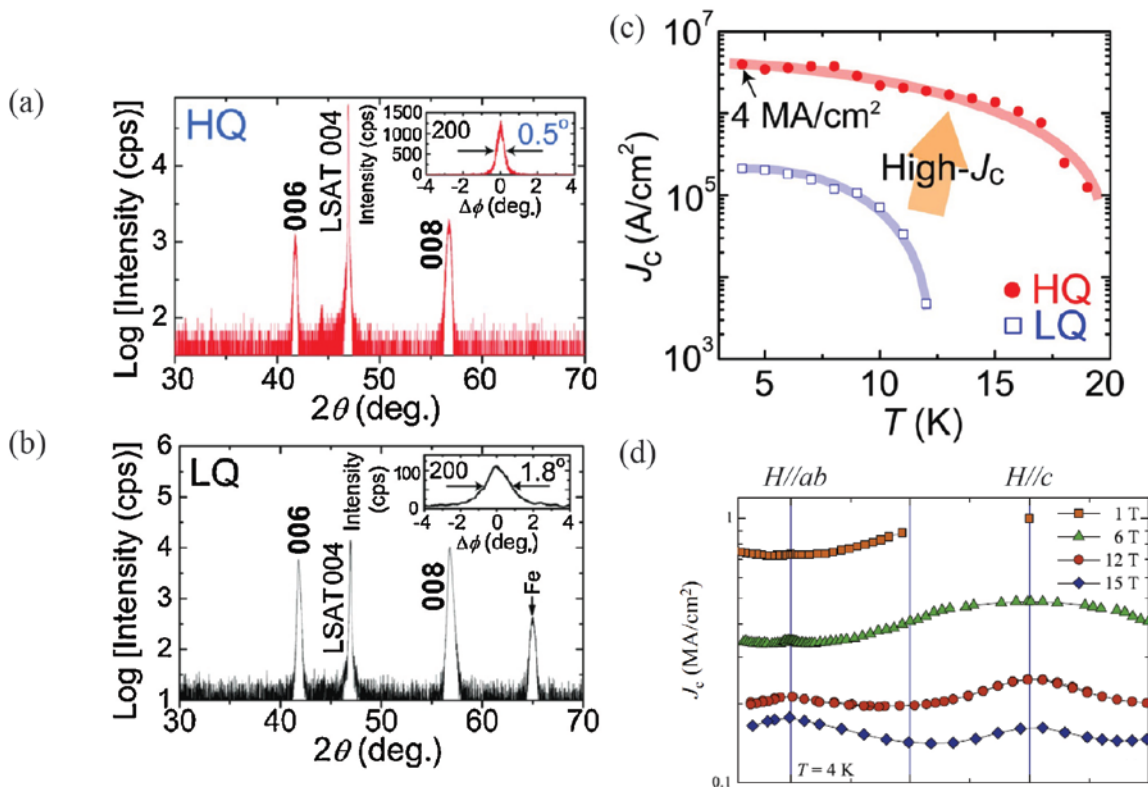


Figure 1 - 6. XRD patterns of (a) high quality (HQ) films and (b) low quality (LQ) films. Inset figures show rocking curve of 200 of HQ and LQ film, respectively¹³³ (c) J_c vs. T in temperature range 2–20 K. (d) Angular dependence of J_c at 1, 6, 12, 15 T at 4K.¹³⁴

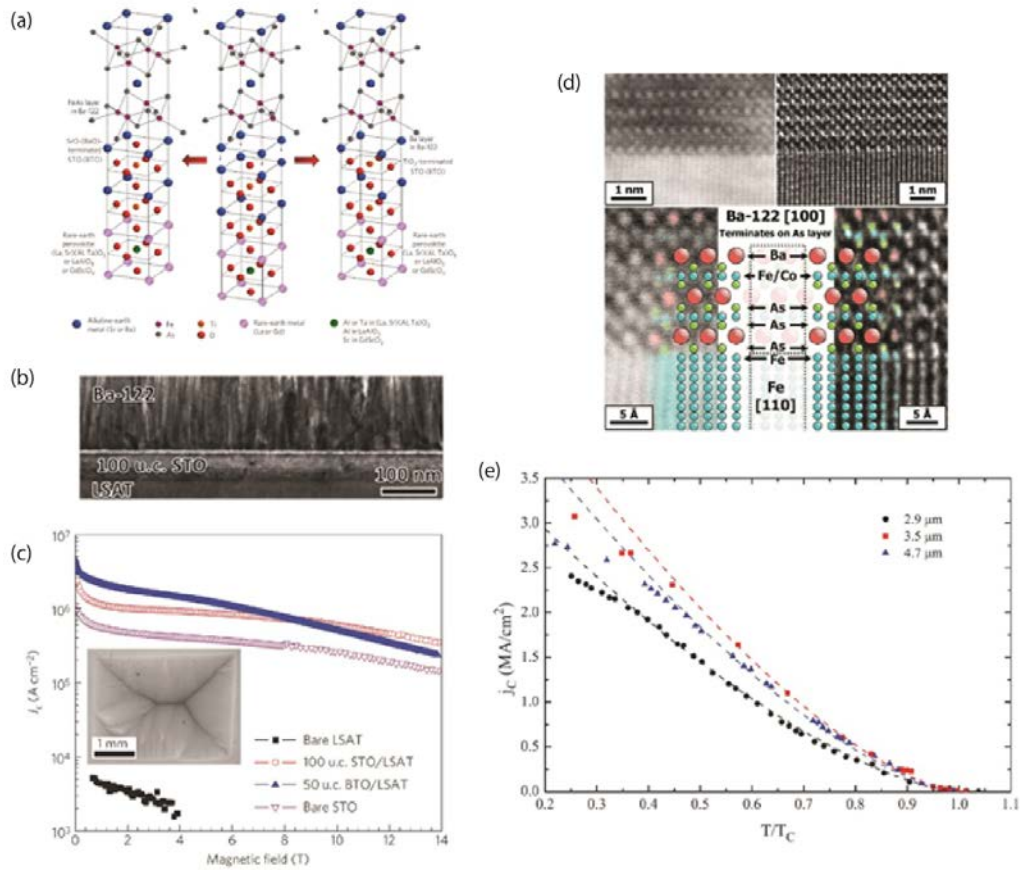


Figure 1 - 7. (a) Schematically illustrated concept of using perovskite-oxide buffer to obtain high-quality $\text{Ba}(\text{Fe}_{1-x}\text{Co}_x)_2\text{As}_2$ epitaxial films on LSAT, LAO etc.⁴⁸ (b) Cross-sectional TEM image on interface between $\text{Ba}(\text{Fe}_{1-x}\text{Co}_x)_2\text{As}_2$ and substrate. STO buffer layer introduced in the surface of substrate and large amount of columnar defects are observed. (c) J_c of samples on bare LSAT, 100 u.c. STO/LSAT, 50 u.c. BTO/LSAT and bare STO as a function of magnetic field. (d) Cross-sectional HR-STEM and HR-TEM images between $\text{Ba}(\text{Fe}_{1-x}\text{Co}_x)_2\text{As}_2$ and Fe buffer layer. (e) Transport- J_c as a function of normalized temperature T/T_c .^{135,136}

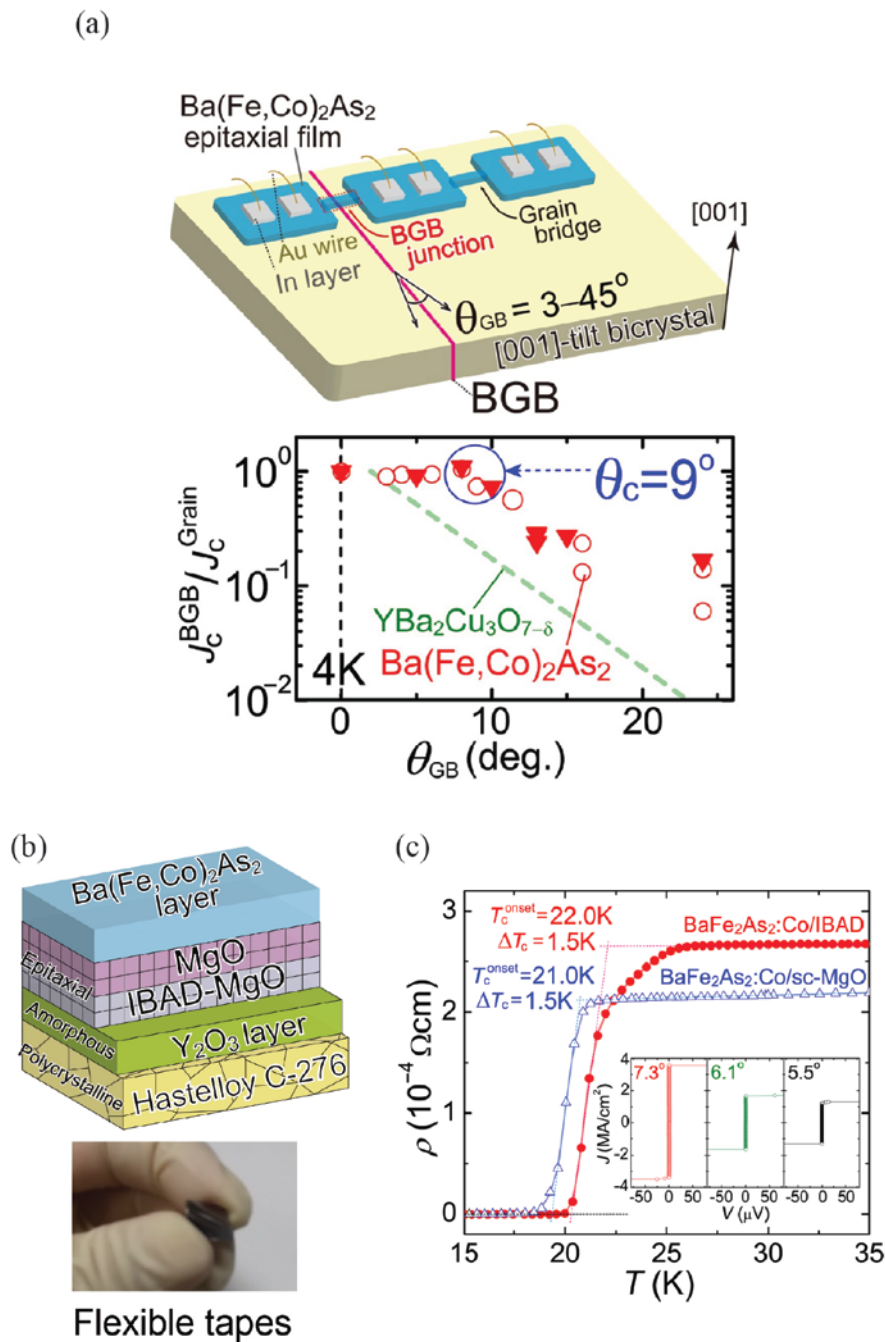


Figure 1 - 8. (a) Upper panel shows schematic device structures of the BGB junctions and Grain bridges rectangular solid is an enlargement at the BGB junction. Lower panel show the decreasing rate as function of misorientation angle θ_{GB} . (b) Upper panel shows the schematic multi-layered structure of $Ba(Fe_{1-x}Co_x)_2As_2$ superconducting tapes and lower panel is photograph of IBAD-MgO buffered metal tape substrate. (c) $\rho - T$ curve of $Ba(Fe_{1-x}Co_x)_2As_2$ film on IBAD-MgO substrate (red closed circles) and epitaxial film on MgO single crystal substrate (blue open circles) in temperature range 15-35 K Inset figures the $J-V$ characteristics at 2 K of Film/IBAD with $\Delta\phi_{MgO} = 7.3^\circ$ (left), 6.1° (middle) and 5.5° (right)

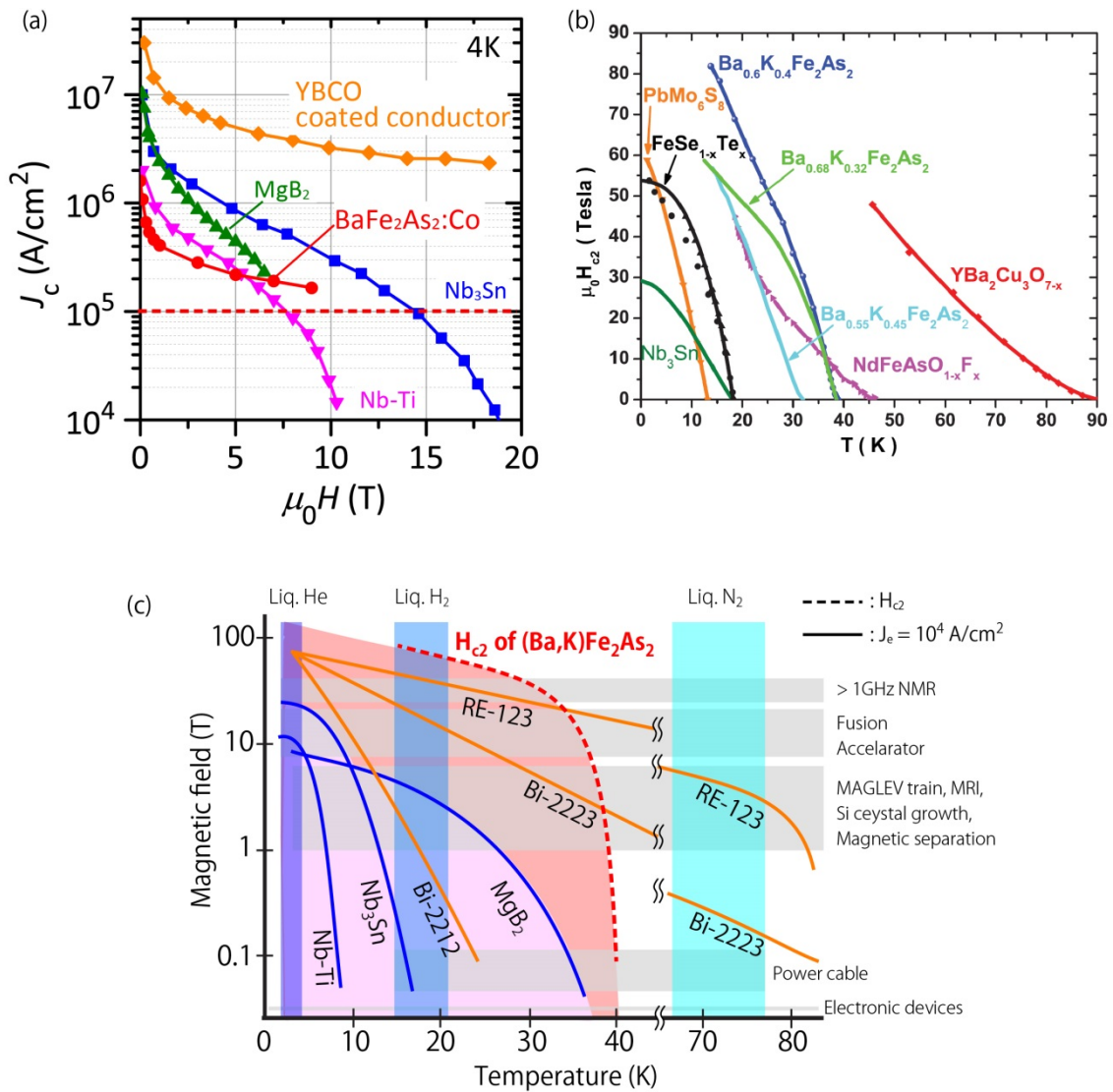


Figure 1 - 9. Comparison of superconducting properties with other superconductors. (a) magnetic field dependence of J_c . Also shown for comparison are the data for YBCO¹³⁷, MgB₂¹³⁸, Nb₃Sn⁶⁵ and Nb-Ti. Dashed lines indicate the J_c limits if it was operate in practical applications. (b) Temperature dependence of H_{c2} ¹³⁹. (c) Applicable conditions for engineering $J_c J_e > 10^4$ A cm² for various superconducting tapes and wires. The low temperature and low temperature region area (magenta shaded area) can be covered by using conventional superconductors. Compared with conventional superconductors¹⁴⁰, iron-based conductors have great potential not only in high magnetic field but also high temperature (red shaded area).

Chapter 2: Critical factor for heteroepitaxial growth of cobalt-doped BaFe₂As₂ thin films

2.1. Introduction

The report of an iron-based superconductor in 2008¹ soon provoked extensive research on growing thin films of the related materials.²⁻⁷ These materials are advantageous for high magnetic-field applications, such as superconducting wires and tapes, because they have high upper critical fields of > 50 T,⁸ small anisotropy factors,⁹ and good grain boundaries.¹⁰ Many researchers have reported superconducting wires¹¹⁻¹³ and tapes¹⁴⁻¹⁶ made from these materials that exhibit high critical current densities (J_c) under high magnetic fields. Among the iron-based superconductors, 122-type cobalt-doped BaFe₂As₂ [BaFe₂As₂:Co] has been extensively studied because of its chemical stability¹⁷ and its ease of epitaxial growth compared with other iron-based compounds such as LaFeAs(O,F) and (Ba,K)Fe₂As₂. These advantages originate from the lower vapor pressure of the Co dopant compared with those of F and K dopants. Researchers have been able to achieve high J_c (≥ 1 MA/cm²) in high-quality BaFe₂As₂:Co epitaxial films,¹⁸⁻²⁰ leading to demonstrations of Josephson junctions^{10,21,22} and superconducting quantum-interference devices²³ built from those films.

So far, BaFe₂As₂:Co epitaxial films with high J_c have been effectively grown on two kinds of buffer layers: perovskite-type oxides,¹⁸ such as SrTiO₃, and metallic Fe.²⁴ These buffer layers relax the in-plane lattice mismatch between the single-crystal substrate and the BaFe₂As₂:Co film. In contrast, I have grown these films with high J_c on single-crystal substrates without buffer layers by optimizing the growth conditions of

pulsed laser deposition (PLD).^{19,25} Other researchers^{18,24} employing buffer layers have used KrF excimer lasers as their PLD excitation source; in contrast, I used a neodymium-doped yttrium aluminum garnet (Nd:YAG) laser to produce high-performance BaFe₂As₂:Co epitaxial films ever since we epitaxially grew the iron-based superconductor LaFeAsO.² The reason why the laser choice mattered is not yet clear because PLD has many parameters such as the geometrical configuration, the base pressure of the growth chamber, the quality of the targets, and the excitation laser source. Among these parameters, we thought the important difference in our setup was the wavelength of the excitation laser used for PLD.

In this study, we grew BaFe₂As₂:Co epitaxial films by using four types of ns-pulsed lasers; by growing films over a variety of pulse energies, we found the film crystallinity depended on the growth rate (pulse energy), rather than the excitation laser wavelength.

2.2. Experimental procedure

2.2.1. Thin film fabrication

BaFe₂As₂:Co films were deposited on (001)-oriented (La,Sr)(Al,Ta)O₃ (LSAT) single-crystal substrates without buffer layers. I deposited these films by using PLD to ablate Ba(Fe_{0.92}Co_{0.08})₂As₂ target disks.^{19,25} I used the same deposition chamber for every growth. I used four excitation sources for the pulsed laser: (i) an ArF excimer laser (wavelength $\lambda = 193$ nm), (ii) a KrF excimer laser (248 nm), (iii) the second harmonic of a Nd:YAG laser (532 nm), and (iv) the fundamental harmonic of a Nd:YAG (1064 nm) laser. The COMPex 205 series (Lambda Physik, maximum pulse energies are 400 mJ for ArF and 700 mJ for KrF) was used for the excimer lasers, and the INDI-40 series (Spectra Physics, maximum pulse energies are 200 mJ for 532 nm and 450 mJ for

1064 nm) was used for the Q-switched Nd:YAG laser. The laser spots at the target surface were 1.5×2.0 mm rectangles for the excimer lasers and 2-mm-diameter circles for the Nd:YAG laser. The growth temperature was 850 °C.²⁵ In this study, we only varied the pulse energy. The pulse width and pulse energy were measured with a photodiode and an energy meter, respectively, which were calibrated for each wavelength. The repetition rate of each laser was 10 Hz. The distance between the substrate and the target was 30 mm. The base pressure of the PLD growth chamber was $\sim 5 \times 10^{-7}$ Pa.

2.2.2. Characterization

The film thicknesses were 200–300 nm, measured with a stylus surface profiler, while thickness of the thinner films (~ 90 nm) was determined by using X-ray reflectivity measurements. Using out-of-plane and in-plane X-ray diffraction (XRD), we confirmed that all the films grew heteroepitaxially on the LSAT (001) substrates.²⁵ Variations of the crystallite orientation were characterized by XRD rocking curves of the out-of-plane 004 diffraction (2θ -fixed ω scans, $\Delta\omega$ = tilting angle) and in-plane 200 diffraction (2θ -fixed ϕ scans, $\Delta\phi$ = twisting angle). These measurements used Cu K α 1 radiation with a Ge (220) monochromator. The samples' microstructures were observed by cross-sectional transmission electron microscopy (TEM). The chemical compositions of the films were analyzed with an energy dispersive X-ray (EDX) spectrometer with a spatial resolution of ~ 1 nm, attached to a scanning TEM. The magnetic J_c at 2 K up to 9 T was extracted using the Bean model from magnetization hysteresis loops, measured with a vibrating sample magnetometer. In these measurements, an external magnetic field (H) was applied normal to the substrate plane (i.e., parallel to the c-axis of the

films). Optical transmission (T_{obs}) and normal reflectance (R_{obs}) spectra were measured with a conventional spectrophotometer at room temperature in the ultraviolet to near-infrared region. The absorption coefficient (a) was evaluated from T_{obs} and R_{obs} by the following relationship: $T_{\text{obs}}/(1-R_{\text{obs}}) \approx \exp(-ad)$, where d is the film thickness (90nm).

2.3. Results and discussion

2.3.1. Optical properties and pulse-energy dependence of deposition rate

Figure 2 - 1 (a) shows the optical spectra of a 90-nm-thick BaFe₂As₂:Co epitaxial film. In the wavelength region of Nd:YAG, the a values were $4.3 \times 10^5 \text{ cm}^{-1}$ at $\lambda = 532$ nm and $3.0 \times 10^5 \text{ cm}^{-1}$ at 1064 nm, indicating that the pulse energy was absorbed down to several tens of nanometers below the surface (i.e., the penetration depth). These spectra are explained well by intraband transitions in the metallic band structure of BaFe₂As₂:Co.²⁶ In contrast, at the wavelength of the excimer lasers, the a values were $> 1 \times 10^6 \text{ cm}^{-1}$ and the penetration depths were a few nanometers. Figure 2 - 1 (b) shows the deposition rate (DR) of the BaFe₂As₂:Co film as a function of laser pulse energy. For Nd:YAG ablation at 1064 nm, the DR was extremely high compared with the other cases and grew linearly with pulse energy, but a distinct kink was present at a DR of $\sim 3 \text{ \AA/s}$. For Nd:YAG ablation at 532 nm, the DR was linear in the high-energy region, but a distinct kink was also present at $\sim 3 \text{ \AA/s}$ (see the inset of Figure 2 - 1 (b) for a magnified view). I found similar trends also for ablation using the KrF excimer laser. Although the ArF excimer laser provided a maximum output pulse energy of 400 mJ, the maximum pulse energy irradiating the target was reduced to 165 mJ, mostly because of absorption of the deep ultraviolet light by O₂ molecules in the ambient air. In addition, for this laser, it was hard to observe a visible plume from the surface of the target disk at pulse

energies less than 100 mJ, where the resulting thin films were very inhomogeneous and too thin. Therefore, for the ArF laser, we measured the DR between 115 and 165 mJ. A similar phenomenon occurred also for the KrF ablation, where the minimum pulse energy required to form a plume was 50–60 mJ. These results indicate that the ablation threshold energy is higher for shorter wavelengths. Because BaFe₂As₂:Co has a metallic band structure,²⁶ ablation should be dominated by the thermal effect, rather than electronic excitation such as multi-photon processes.²⁷ I believe that the high ablation threshold energy and low DR when using excimer laser excitation was caused by the very thin absorption layer.

2.3.2. Relationship between crystallinity of the films and pulse energies.

Next, we examined how the crystallinity of the BaFe₂As₂:Co film depended on pulse energy. Because all the films exhibited c-axis orientation in the out-of-plane XRD measurements and because they did not differ significantly in concentrations of impurities (e.g., Fe)²⁵ we examined in-plane ω -scans of the 200 diffraction to confirm the heteroepitaxy. Because BaFe₂As₂:Co has a tetragonal lattice, we expect a four-fold symmetry at 90° in this scan if the film lacks a rotational domain. However, for ArF ablation [(i) in Figure 2 - 2 (a)], we observed two kinds of domains rotated by 45° in all pulse-energy regions, indicating that ablation using the ArF excimer laser did not produce a high-quality epitaxial film. Also, for KrF ablation, we observed a similar rotational domain at a relatively low pulse energy [(ii) in Figure 2 - 2 (a)]. This result is similar to that without a buffer layer reported by Lee et al.¹⁸ employing the KrF excimer laser. However, we found that, by further increasing the pulse energy, BaFe₂As₂:Co films exhibiting four-fold symmetry grew directly on the LSAT substrates, as shown in

(iii) and iv) in Figure 2 - 2 (a). For Nd:YAG ablation [Figure 2 - 2 (b)], we did not observe any rotational domain over the entire pulse-energy region we examined. I also evaluated the full width at half maximums (FWHMs) of the rocking curves for the out-of-plane [Figure 2 - 2 (c)] and in-plane [Figure 2 - 2 (d)] measurements as functions of pulse energy. These data have inverted bell-like shapes, and the minimum FWHMs fall in a range of $\Delta\omega$, $\Delta\phi = 0.6 - 0.7^\circ$; the optimum pulse energy depended strongly on the wavelength, shifting to higher energy with decreasing wavelength.

From the above results, we discuss why the crystallinity takes the optimum values against pulse energy. I believe that the DR of this process was dominated by the density of deposition precursors adsorbed on the growing surface and their re-evaporation rate, we can reasonably assume that the re-evaporation rate was constant for the range of laser power we used. Thus, the low DR at pulse energies lower than the kinks in Figure 2 - 1 (b) can be explained by the re-evaporation rate being comparable to the adsorption rate in that regime. In fact, the DRs at low pulse energy were smaller than expected from extrapolating the linear relationship from the higher pulse energies, as seen in the inset of Figure 2 - 1 (b), supporting the dependence of DR on re-evaporation in the low-energy regime. In other words, we believe the kinks observed at a DR of $\sim 3 \text{ \AA/s}$ correspond to a transition to the supersaturation regime.³⁰ In contrast, at high pulse energy, the DR was too high to complete the surface reconstruction, leading to the increased FWHMs with increasing pulse energy, completing the inverted bell-like shape of the FWHM. Iida et al.^{28,29} also reported epitaxial growth of BaFe₂As₂:Co films using a KrF excimer laser, but they need to use a Fe buffer layer to obtain good epitaxial films. This would be because that their laser power was in the range of 3–5 Jcm², which is much lower than our optimum values (see Table 2 - 1), and their substrate-to target

distance was longer (50mm) than that of our PLD growth chamber (30mm); therefore, we speculate that the above-discussed supersaturation regime is not attained due to the low density and the low kinetic energies of the deposition precursors, and consequently the Fe buffer layer is required to assist improved epitaxial growth.

2.3.3. Microstructure analysis: defects and reaction layer between film and LSAT

Based on these results, the optimum range of pulse energy is 200–300 mJ (excitation density 6.7–10 J/cm²) for KrF, 70–100 mJ (2.2–3.2 J/cm²) for Nd:YAG at 532 nm, and 40–50 mJ (1.3–1.6 J/cm²) for Nd:YAG at 1064 nm.

Figure 2 - 3 (a) shows a cross-sectional TEM image of the BaFe₂As₂:Co epitaxial film, deposited using the KrF excimer laser at an optimum pulse energy. Similar to films grown by Nd:YAG ablation at 532 nm,^{30,31} we observed line defects along the c-axis, indicated by vertical white arrows, that act as vortex pinning centers. At the interface between the substrate and film, we observed a bright region with a thickness of a few nanometers, a feature more easily seen in Figure 2 - 3 (b). I found no differences from the KrF-deposited film in the defect structure or interface structure/contrast in the cross-sectional TEM images of the films deposited with the Nd:YAG laser at 532 and 1064 nm at optimal pulse energies (see Figure 2 - 3 (d) and (e)). Next, we show the interfacial chemical composition of the film deposited using the KrF excimer laser (Figure 2 - 3 (c)). The EDX intensities of Ba, Fe, Co, and As were almost constant in the deep film region, while they gradually decreased as the probing beam approached the interface, and elements from the substrate (La and Sr) were detected at the interface. The transition width was ~8 nm, much larger than the spatial resolution of this EDX measurement (~1nm), which we attribute to diffusion. However, we found no

segregation of specific elements, such as Fe, at the interface. This result differs from that reported by Iida et al.²⁹ they observed a biaxially textured thin Fe layer at the interface and claimed that the thin Fe buffer layer was important to heteroepitaxially growing their BaFe₂As₂:Co films.^{24,32} Our present result is more similar to that reported by Rall et al.²⁰ they reported a 2-nm-thick Fe-rich and Ba-poor reaction layer. I observed similar reaction layers also in the 532 and 1064nm laser ablations. In previous work on MgO substrates,³³ we did not observe a thin reacted interfacial layer. Thus, we believe this interfacial phenomenon will commonly occur when epitaxially growing BaFe₂As₂:Co films on LSAT substrates.

As seen in Figure 2 - 2 (a), our BaFe₂As₂:Co films possess rotational domain structures when the DRs were low. Also in these cases, we always observed reaction layers similarly to those observed in the optimal samples (Figure 2 - 3 (f) for TEM images and EDX spectrum), but we could not find clear difference in their structures and compositions. However, atomic structures of the growing surfaces of these reaction layers should play an important role for determining the epitaxial structures of the growing thin films, e.g., it is reported that *c*-plane α-Ga₂O₃ on *c*-plane α-Al₂O₃ (Ref. 34) exhibit similar rotational domains because α-Al₂O₃ (0001) surfaces have different atomic structures that are rotated by 180° with each other and the rotational domains are formed where a single-molecular layer step is formed at the substrate surface.

2.3.4. J_c properties of the epitaxial films grown by several lasers at the optimal growth rate.

Figure 2 - 4 shows the magnetic J_c at 2 K of the BaFe₂As₂:Co epitaxial films deposited with KrF and Nd:YAG lasers at optimum pulse energies. Irrespective of the excitation wavelength used during growth, the films exhibited high self-field J_c (>1

MA/cm²), comparable to those of films grown on SrTiO₃ buffer layers¹⁸ and higher than those of films grown on metallic Fe buffer layers.³⁵ The in-field properties of the film grown at 532 nm appeared slightly better than the others, implying a slightly higher defect density (i.e., density of pinning centers); however, the samples had similar decay ratios under magnetic fields. Thus, we conclude that high- J_c BaFe₂As₂:Co epitaxial films can be fabricated by using a variety of excitation wavelengths, assuming they are deposited at an optimum pulse energy.

2.4. Discussion

Next, we discuss how the laser excitation parameters affected crystallinity of BaFe₂As₂:Co films. Table 2 - 2 summarizes the optimum pulse energy for each laser to fabricate BaFe₂As₂:Co epitaxial films with high J_c as well as related optical parameters. Although the optimal pulse energy and pulse width for each laser were very different, the DRs produced by those optimum conditions were almost the same (3.3 ± 0.5 Å/s), indicating that the most important growth parameter was the DR. This finding explains why a high- J_c BaFe₂As₂:Co film with the ArF excimer laser could not be produced: its maximum pulse energy was limited to 165 mJ (5.5 Jcm²), producing a maximum DR (2.3 Å/s) far lower than the optimum value (3.3 Å/s). As explained before, the optimum pulse energies and thus the excitation energy densities differed significantly between the lasers; in contrast, the photon number, PN (10^{17}) and peak power density, PPD (108 W/cm²) were on the same order of magnitude for all the wavelengths used. To further discuss these parameters, we re-plot the data from Figure 2 - 2 (c) and Figure 2 - 2 (d) in Figure 2 - 5 with respect to $(1-R_{\text{obs}})PN$ and $(1-R_{\text{obs}})PPD$, where the PN and PPD are corrected with the actual photon count absorbed by the BaFe₂As₂:Co [R_{obs} values are

taken from Figure 2 - 1 (a)]. As for $(1-R_{\text{obs}})$ PN [Figure 2 - 5 (a) and Figure 2 - 5(b)], the optimum range is narrow, $(1.3-3) \times 10^{17}$, while the values for ablation at 248 nm are higher than those for ablation at longer wavelengths. As for $(1-R_{\text{obs}})$ PPD [Figure 2 - 5 (c) and (d)], the optimum range is again narrow, but the value for ablation at 1064nm deviates much from the others. These results suggest that $(1-R_{\text{obs}})$ PN is closely correlated with the DR. However, although this result implies that the DR (i.e., the ablation rate) was determined by a single-electron excitation process, this explanation is not consistent with previous research on the mechanisms of laser ablation. In the previous research, electron excitation processes become dominant at shorter pulse widths (larger energy densities) and are important for insulator and semiconductor films. In contrast, when ablating metallic materials like BaFe₂As₂:Co with nanosecond pulses, the thermal process should dominate.²⁷ Therefore, we tentatively believe that the DR is mostly determined by the absorbed PPD. The deviation observed for ablation at 1064 nm can be explained by its large penetration depth (33 nm) compared with ablation at 532 nm (23 nm) and 248 nm (~5 nm). The 1064nm laser ablated a larger amount of the PLD target, resulting in a high ablation efficiency and very high DR, as shown by Figure 2 - 1 (b); in contrast, the lasers with shorter wavelengths ablated thinner surfaces, resulting in lower DRs even at the same PPD.

2.5. Conclusion

In summary, we epitaxially grew BaFe₂As₂:Co films by using PLD and examined how the laser wavelength and pulse energy affected the growth by using four different excitation wavelengths. I found that the optimal DR, which could be tuned by pulse energy, does not depend on the type of laser (i.e., wavelength). This study also explains

why the Nd:YAG laser is better for producing high- J_c BaFe₂As₂:Co films with high crystallinity at a low laser power, and will help improve the fabrication of other iron-based superconductor films such as REFeAsO (RE = rare earth), BaFe₂(As,P)₂, and Fe(Se,Te).

References

- ¹ Y. Kamihara, T. Watanabe, M. Hirano, and H. Hosono, *J. Am. Chem. Soc.* **130**, 3296 (2008).
- ² H. Hiramatsu, T. Katase, T. Kamiya, M. Hirano, and H. Hosono, *Appl. Phys. Lett.* **93**, 162504 (2008).
- ³ E. Backen, S. Haindl, T. Niemeier, R. Hühne, T. Freudenberg, J. Werner, G. Behr, L. Schultz, and B. Holzapfel, *Supercond. Sci. Technol.* **21**, 122001 (2008).
- ⁴ H. Hiramatsu, T. Katase, T. Kamiya, M. Hirano, and H. Hosono, *Appl. Phys. Express* **1**, 101702 (2008).
- ⁵ Q. Li, W. Si, and I.K. Dimitrov, *Rep. Prog. Phys.* **74**, 124510 (2011).
- ⁶ H. Hiramatsu, T. Katase, T. Kamiya, and H. Hosono, *J. Phys. Soc. Jpn.* **81**, 011011 (2012).
- ⁷ S. Haindl, M. Kitzun, F. Onken, A. Mietke, and T. Thersleff, *Int. J. Mod. Phys. B* **27**, 1330001 (2012).
- ⁸ F. Hunte, J. Jaroszynski, A. Gurevich, D.C. Larbalestier, R. Jin, A.S. Sefat, M.A. McGuire, B.C. Sales, D.K. Christen, and D. Mandrus, *Nature* **453**, 903 (2008).
- ⁹ H.Q. Yuan, J. Singleton, F.F. Balakirev, S.A. Baily, G.F. Chen, J.L. Luo, and N.L. Wang, *Nature* **457**, 565 (2009).
- ¹⁰ T. Katase, Y. Ishimaru, A. Tsukamoto, H. Hiramatsu, T. Kamiya, K. Tanabe, and H. Hosono, *Nat. Commun.* **2**, 409 (2011).
- ¹¹ Y. Ma, *Supercond. Sci. Technol.* **25**, 113001 (2012).
- ¹² J.D. Weiss, C. Tarantini, J. Jiang, F. Kametani, A.A. Polyanskii, D.C. Larbalestier, and E.E. Hellstrom, *Nat. Mater.* **11**, 682 (2012).
- ¹³ Z. Gao, K. Togano, A. Matsumoto, and H. Kumakura, *Sci. Rep.* **4**, (2014).
- ¹⁴ K. Iida, J. Hänisch, S. Trommler, V. Matias, S. Haindl, F. Kurth, I.L. del Pozo, R. Hühne, M. Kitzun, J. Engelmann, L. Schultz, and B. Holzapfel, *Appl. Phys. Express* **4**, 013103 (2011).
- ¹⁵ T. Katase, H. Hiramatsu, V. Matias, C. Sheehan, Y. Ishimaru, T. Kamiya, K. Tanabe, and H. Hosono, *Appl. Phys. Lett.* **98**, 242510 (2011).
- ¹⁶ W. Si, S.J. Han, X. Shi, S.N. Ehrlich, J. Jaroszynski, A. Goyal, and Q. Li, *Nat. Commun.* **4**, 1347 (2013).
- ¹⁷ T. Katase, H. Hiramatsu, H. Yanagi, T. Kamiya, M. Hirano, and H. Hosono, *Solid State Commun.* **149**, 2121 (2009).
- ¹⁸ S. Lee, J. Jiang, Y. Zhang, C.W. Bark, J.D. Weiss, C. Tarantini, C.T. Nelson, H.W. Jang, C.M. Folkman, S.H. Baek, A. Polyanskii, D. Abaimov, A. Yamamoto, J.W. Park,

- X.Q. Pan, E.E. Hellstrom, D.C. Larbalestier, and C.B. Eom, *Nat. Mater.* **9**, 397 (2010).
- ¹⁹ T. Katase, H. Hiramatsu, T. Kamiya, and H. Hosono, *Appl. Phys. Express* **3**, 063101 (2010).
- ²⁰ D. Rall, K. Il'in, K. Iida, S. Haindl, F. Kurth, T. Thersleff, L. Schultz, B. Holzapfel, and M. Siegel, *Phys. Rev. B* **83**, 134514 (2011).
- ²¹ T. Katase, Y. Ishimaru, A. Tsukamoto, H. Hiramatsu, T. Kamiya, K. Tanabe, and H. Hosono, *Appl. Phys. Lett.* **96**, 142507 (2010).
- ²² S. Schmidt, S. Döring, F. Schmidl, V. Grosse, P. Seidel, K. Iida, F. Kurth, S. Haindl, I. Mönch, and B. Holzapfel, *Appl. Phys. Lett.* **97**, 172504 (2010).
- ²³ T. Katase, Y. Ishimaru, A. Tsukamoto, H. Hiramatsu, T. Kamiya, K. Tanabe, and H. Hosono, *Supercond. Sci. Technol.* **23**, 082001 (2010).
- ²⁴ T. Thersleff, K. Iida, S. Haindl, M. Kidszun, D. Pohl, A. Hartmann, F. Kurth, J. Hänisch, R. Hühne, B. Rellinghaus, L. Schultz, and B. Holzapfel, *Appl. Phys. Lett.* **97**, 022506 (2010).
- ²⁵ T. Katase, H. Hiramatsu, T. Kamiya, and H. Hosono, *Supercond. Sci. Technol.* **25**, 084015 (2012).
- ²⁶ C. Krellner, N. Caroca-Canales, A. Jesche, H. Rosner, A. Ormeci, and C. Geibel, *Phys. Rev. B* **78**, 100504 (2008).
- ²⁷ B.N. Chichkov, C. Momma, S. Nolte, F. von Alvensleben, and A. Tünnermann, *Appl. Phys. A* **63**, 109 (1996).
- ²⁸ K. Iida, J. Hänisch, R. Hühne, F. Kurth, M. Kidszun, S. Haindl, J. Werner, L. Schultz, and B. Holzapfel, *Appl. Phys. Lett.* **95**, 192501 (2009).
- ²⁹ K. Iida, J. Hänisch, T. Thersleff, F. Kurth, M. Kidszun, S. Haindl, R. Hühne, L. Schultz, and B. Holzapfel, *Phys. Rev. B* **81**, 100507 (2010).
- ³⁰ B. Maiorov, T. Katase, S.A. Baily, H. Hiramatsu, T.G. Holesinger, H. Hosono, and L. Civale, *Supercond. Sci. Technol.* **24**, 055007 (2011).
- ³¹ H. Sato, T. Katase, W.N. Kang, H. Hiramatsu, T. Kamiya, and H. Hosono, *Phys. Rev. B* **87**, 064504 (2013).
- ³² K. Iida, J. Hänisch, S. Trommler, S. Haindl, F. Kurth, R. Hühne, Ludwig Schultz, and B. Holzapfel, *Supercond. Sci. Technol.* **24**, 125009 (2011).
- ³³ H. Hiramatsu, T. Katase, Y. Ishimaru, A. Tsukamoto, T. Kamiya, K. Tanabe, and H. Hosono, *Mater. Sci. Eng. B* **177**, 515 (2012).
- ³⁴ D. Shinohara and S. Fujita, *Jpn. J. Appl. Phys.* **47**, 7311 (2008).
- ³⁵ K. Iida, S. Haindl, T. Thersleff, J. Hänisch, F. Kurth, M. Kidszun, R. Hühne, I. Mönch, L. Schultz, B. Holzapfel, and R. Heller, *Appl. Phys. Lett.* **97**, 172507 (2010).
- ³⁶ C.P. BEAN, *Rev. Mod. Phys.* **36**, 31 (1964).

Table 2 - 3. Optimum pulse energies and deposition rates for each laser to fabricate BaFe₂As₂:Co epitaxial films with high J_c as well as related optical parameters.

Laser wavelength (nm)	248	532	1064
R_{obs} (%) ^a	24	34	52
Pulse width (ns)	20	5	10
Spot area (10 ² cm ²)	3.0	3.1	3.1
Optimum pulse energy (mJ)	200–300	70–100	40–50
Deposition rate (Å/s)	3.1–3.6	2.8–3.3	3.5–3.8
Photon number per pulse, PN (10 ¹⁷) ^b	2.5–3.8	1.9–2.7	2.2–2.7
Excitation energy density (J/cm ²) ^c	6.7–10	2.2–3.2	1.3–1.6
Peak power density, PPD (10 ⁸ W/cm ²) ^d	3.3–5.0	4.5–6.4	1.3–1.6

^a Taked from Figure 2 - 1 (a)

^b Photon number per pulse.Pulse energy (J)/Photon energy (J).

^c Excitation energy density (J/cm²).Pulse energy (J)/Spot area (cm²).

^d Peak power density (W/cm²).Pulse energy (J)/Pulse width (s)/Spot area (cm²).

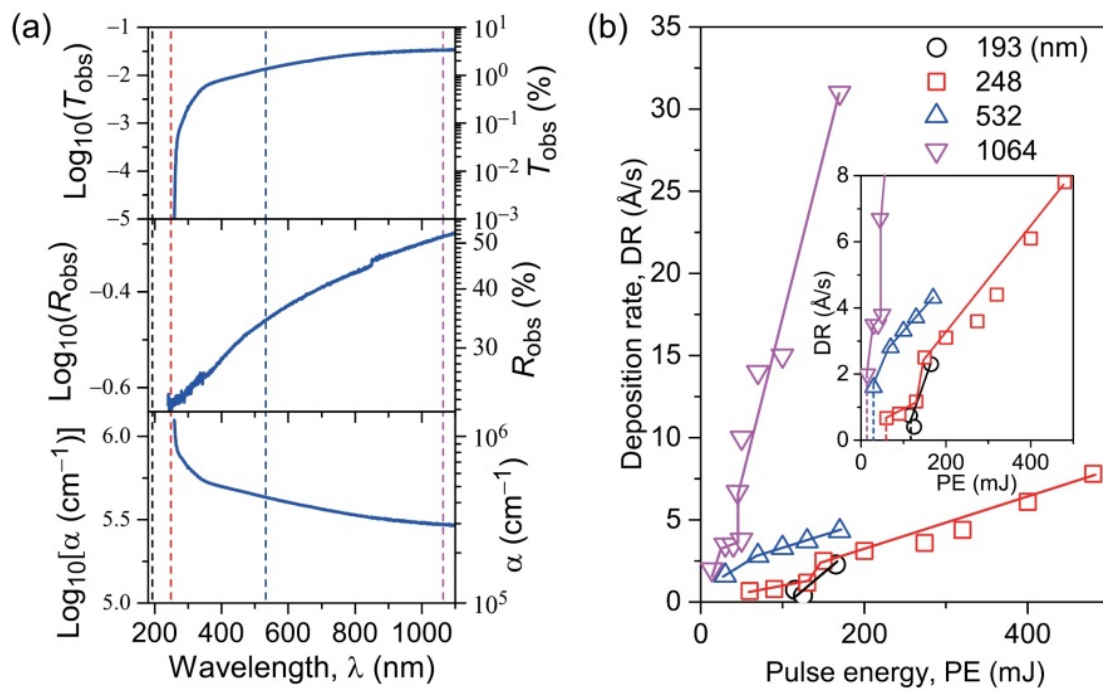


Figure 2 - 1. (a) Optical spectra (T_{obs} , R_{obs} , and α) of a 90-nm-thick BaFe₂As₂:Co epitaxial film at room temperature. The vertical dashed lines indicate the laser wavelengths used in this study. (b) Dependence of deposition rate of BaFe₂As₂:Co films on pulse energy. The PLD laser wavelengths are shown in the upper right. The inset shows an enlarged image from the region of deposition rates less than 8 \AA/s , more clearly showing the kinks.

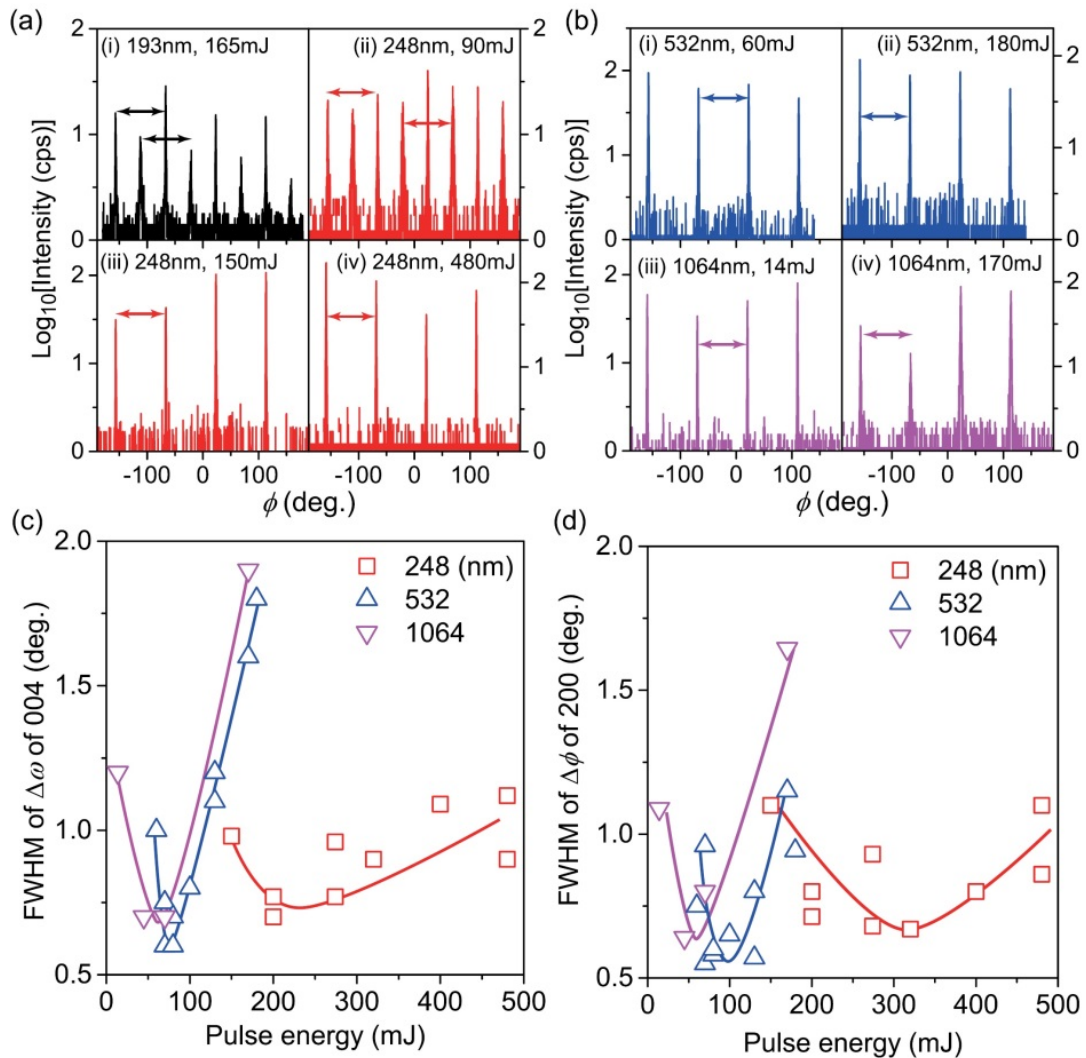


Figure 2 - 2. Relationship between thin film crystallinity and pulse laser energy. (a) and (b): XRD results from in-plane ϕ -scans of 200 diffraction of BaFe₂As₂:Co films grown by (a) excimer and (b) Nd:YAG lasers. The horizontal arrows show a 90° interval because of the film's tetragonal symmetry. (c) and (d): FWHMs of rocking curves of (c) outof-plane 004 diffraction and (d) in-plane 200 diffraction of BaFe₂As₂:Co epitaxial films without a rotational domain, grown by KrF and Nd:YAG lasers as a function of various pulse energies.

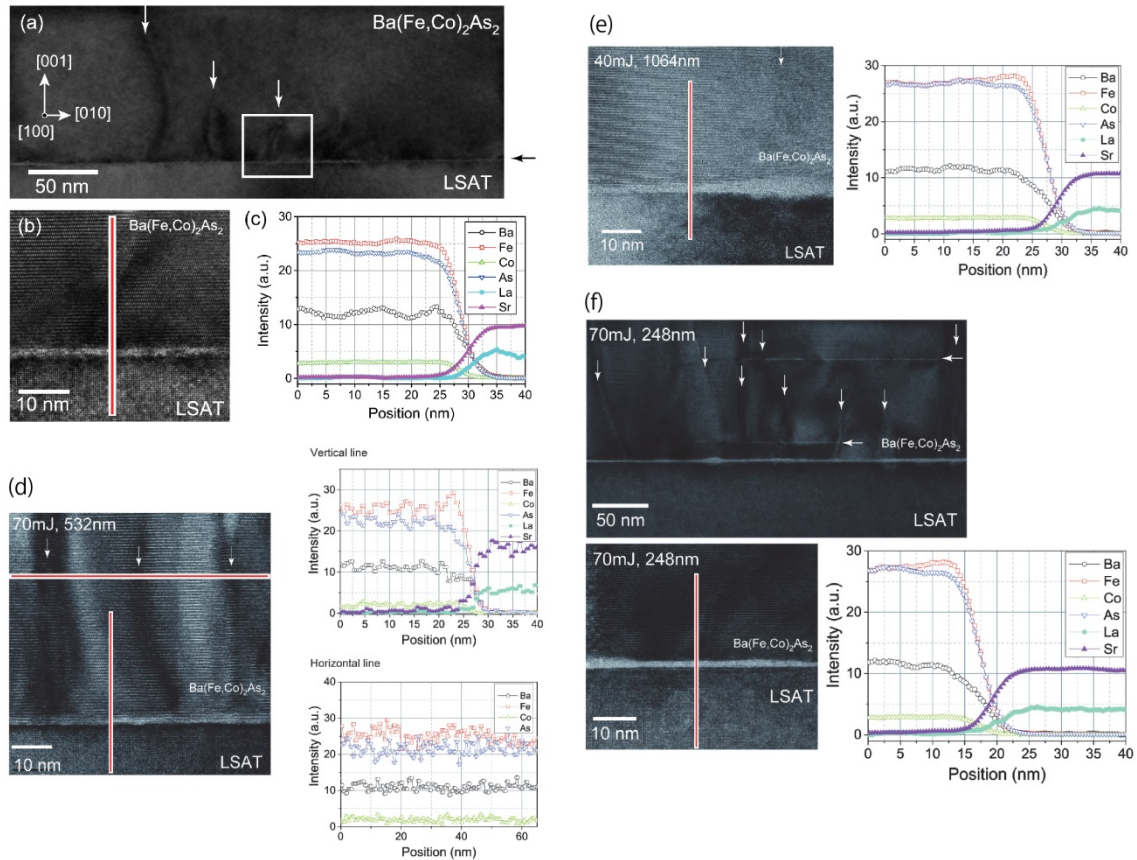


Figure 2 - 3. Examination of a $BaFe_2As_2:Co$ epitaxial film grown by several excitation sources. (a) Cross-sectional TEM image of a $BaFe_2As_2:Co$ epitaxial film grown by the KrF excimer laser at the optimum pulse energy. The vertical white arrows indicate defects along the c -axis. The horizontal black arrow on the right shows the position of the film/LSAT interface. (b) Magnified view of the white square shown in (a). (c) EDX line-scan spectra along the red vertical line shown in (b). Cross-sectional TEM images of $BaFe_2As_2:Co$ films grown by ablations at (d) optimum pulse energy (70 mJ) of 532 nm, (e) optimum pulse energy (40 mJ) of 1064 nm, and (f) low pulse energy (70 mJ) of 248 nm. The vertical and horizontal white arrows indicate the vertical defects along the c -axis and stacking faults, respectively. (right) EDX line-scans along the red lines in the TEM images.

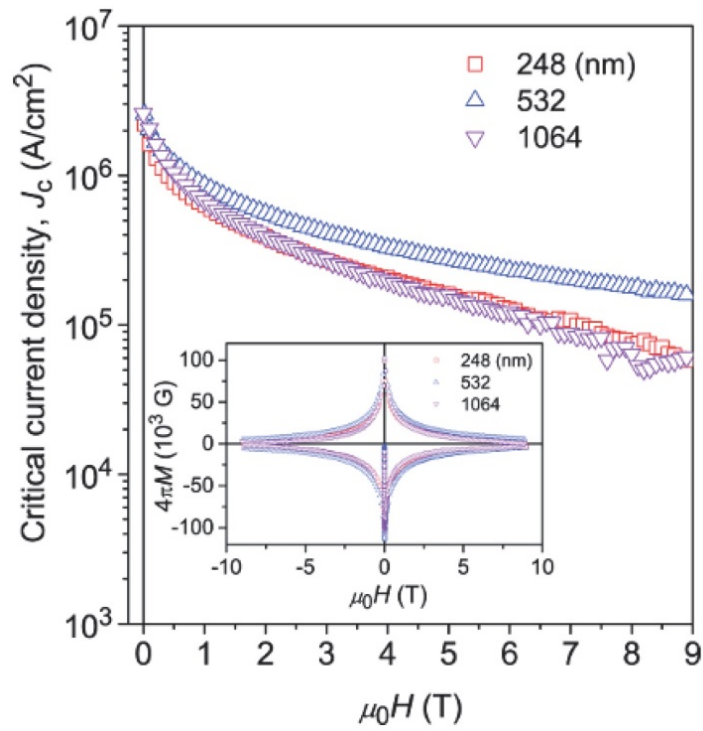


Figure 2 - 4. Magnetic J_c at 2 K of BaFe₂As₂:Co epitaxial films grown using three types of lasers, at their respective optimal pulse energies, as a function of magnetic field. The inset shows the magnetization (M) hysteresis loops measured at 2 K used to extract the magnetic J_c for each sample. J_c is calculated by Bean model³⁶.

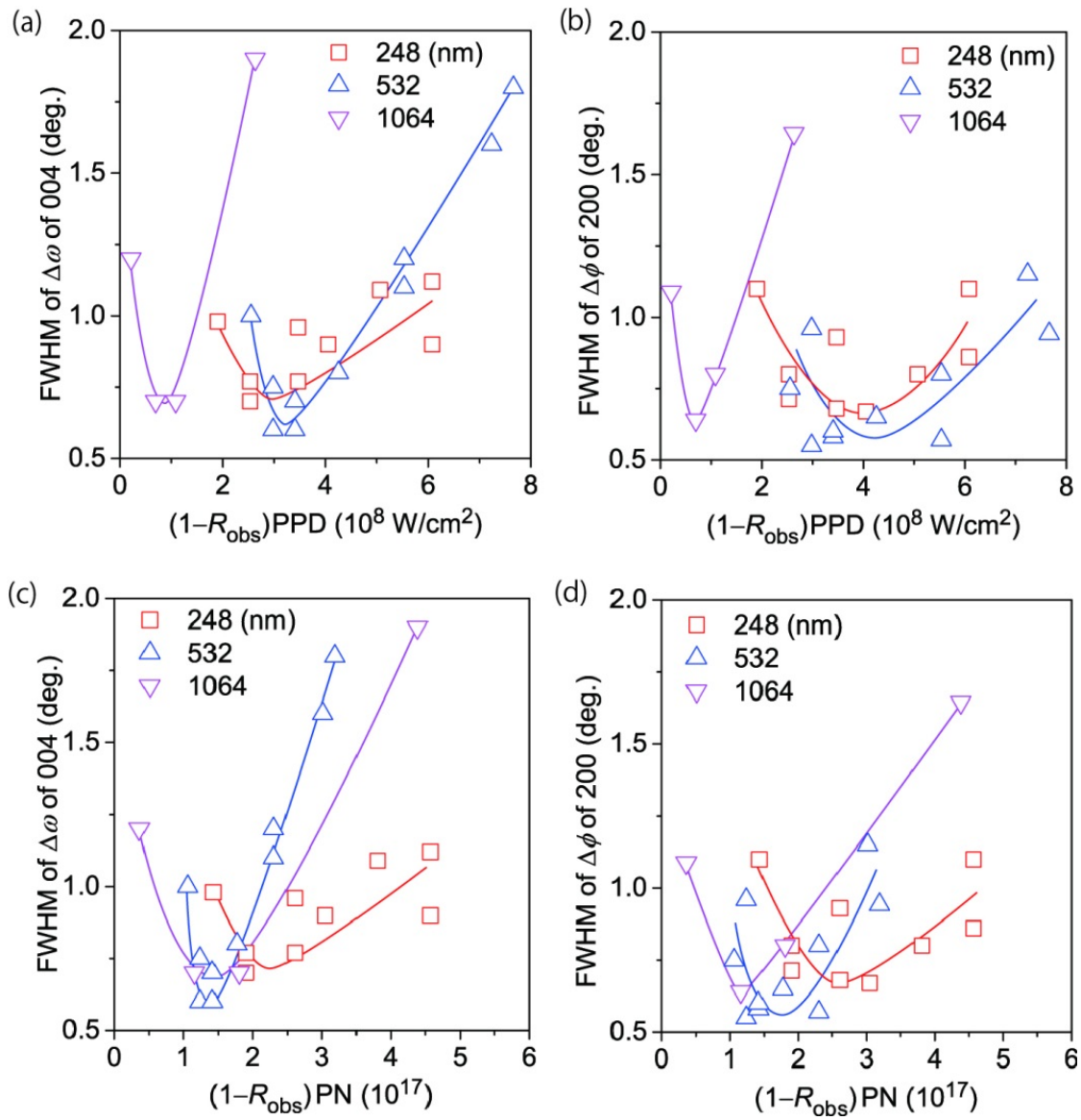


Figure 2 - 5. Re-plots of Figure 2 - 2(c) and (d) with respect to $(1-R_{\text{obs}})\text{PN}$ (a and b) and $(1-R_{\text{obs}})\text{PPD}$ (c and d). Each R_{obs} is taken from Figure 2 - 1(a).

Chapter3: Anomalous scaling behavior in mixed-state Hall effect of a cobalt-doped BaFe₂As₂ epitaxial film

3.1. Introduction

Compared to cuprates, the properties of iron-pnictide Josephson-junction devices remain inferior due largely to their metallic characters. However, their superior grain boundary properties¹ along with high upper critical magnetic fields (H_{c2}) ≥ 50 T and small anisotropic factors $\gamma = H_{c2}^{//ab} / H_{c2}^{//c} = 1-2$ ² are promising for wire³⁻⁵ and tape applications.^{6,7} Similar to cuprates, the extrinsic pinning centers largely control J_c in iron pnictides. Therefore, the vortex pinning mechanism for high- J_c BaFe₂As₂:Co epitaxial films is important to understand the ultimate potential of the iron pnictide superconducting wires and tapes. Although the pinning properties have been studied extensively on single crystals,^{8,9} there are few reports on high- J_c pnictide films, particularly about transport measurements.¹⁰

Because most high- J_c BaFe₂As₂:Co epitaxial films are grown on electrically conductive buffer layers such as Fe metal¹¹ and SrTiO₃,¹² it is difficult to extract reliable transport properties. On the other hand, BaFe₂As₂:Co epitaxial films with $J_c > 1$ MA/cm² have been successfully grown directly on insulating single-crystal substrates without a buffer layer,^{13,14} allowing the transport properties of iron-pnictide epitaxial films to be directly and reliably examined.

The Hall effect measurement in a normal–superconducting mixed-state is a representative probing technique of a vortex motion. High- T_c superconductors such as cuprates and MgB₂ follow a power law scaling of $\rho_{xy} = A\rho_{xx}^\beta$, where ρ_{xy} and ρ_{xx} are the transverse and longitudinal resistivities, respectively. The behavior of the β value has

actively been discussed in relation to the superconducting and vortex pinning mechanisms.^{15–20}

Although sign reversal of ρ_{xy} has been observed, its origin remains controversial.^{21–23} Vinokur *et al.* considered the momentum balance and proposed a model where a system of interacting vortices under quenched disorders and thermal noises follows a universal scaling law with a universal $\beta = 2.0$.²⁴ However, this model does not explain all the mixed-state Hall effects of high- T_c superconductors. Wang *et al.* considered both backflow currents and thermal fluctuations, and suggested that the β value varies from 2.0 to 1.5 as the pinning strength increases.²⁵ Comparison of the experimental results to theoretical models is important to understand the vortex dynamics in a mixed-state of high- J_c BaFe₂As₂:Co epitaxial films.

In this study, the transport properties were examined in a mixed-state high-quality BaFe₂As₂:Co epitaxial film with a high J_c over 1 MA/cm². The pinning mechanism is discussed based on the obtained β values < 2.0 and different behaviors observed during the temperature (T) sweeps and magnetic-field (H) sweeps. Furthermore, the comprehensive Hall effect measurements confirm that a BaFe₂As₂:Co epitaxial film does not exhibit a sign reversal in the entire ranges of magnetic fields (1–9 T) and temperatures (13–16 K).

3.2. Experimental procedure

3.2.1. Thin film fabrication

A 350-nm-thick BaFe₂As₂:Co epitaxial film was grown directly on an insulating (La,Sr)(Al,Ta)O₃ (001) single-crystal substrate by pulsed laser deposition (PLD)

without a buffer layer. The second harmonic (the wavelength = 532 nm) of a neodymium-doped yttrium aluminum garnet laser²⁶ and a polycrystalline disk of Ba(Fe_{0.92}Co_{0.08})₂As₂¹³ were used as the excitation source and the PLD target, respectively. Detailed growth conditions and film quality are reported in the literature.^{13,14} The transition width ΔT_c of ρ_{xx} (~1 K) and the transport J_c at 4 K (2.4 MA/cm²) under a self-field of the resulting film were comparable to those in previous papers.^{13,14}

3.2.2. Mixed-state Hall effect measurements

To examine the mixed-state Hall effect, the film was patterned into an eight-terminal Hall bar structure by photolithography and Ar ion milling. To minimize the contact resistance, a Au film was formed on the contact electrode pads using a lift-off process.²⁷ ρ_{xx} and ρ_{xy} were measured by applying a dc current at a density of 5 kA/cm² using two measurement modes: (i) a T sweep mode with a fixed H and (ii) a H sweep mode with a fixed T . Cancelling the offset effects using the relation $\rho_{xy} = (\rho_{xy}^+ - \rho_{xy}^-)/2$, where ρ_{xy}^+ and ρ_{xy}^- were measured under inverted magnetic fields, the net ρ_{xy} values were extracted. The measurement limit of the system was ~125 nV due to fluctuations in T/H and the digital voltmeter. Thus, the reliability was for $\rho_{xy} > 5.0 \times 10^{-9}$ Ωcm and $\rho_{xx} > 1.4 \times 10^{-10}$ Ωcm . Magnetic fields were applied parallel to the c -axis of the film and varied up to 9 T.

3.3. Results

3.3.1. Mixed-state Hall effect measurements with T sweep and H sweep

Figure 3 - 1 (a) and (b) show the T sweep results of ρ_{xx} and ρ_{xy} under fixed magnetic fields varied up to 9 T, respectively. As H increases, ΔT_c broadens along with shifts in T_c^{onset} and T_c^{zero} toward lower temperatures. As discussed later, this broadening originates from the presence of a vortex liquid state.¹⁰ The negative ρ_{xy} Fig. 1(b) indicates that the majority of charge carriers are electrons, which is consistent with aliovalent ion doping, i.e., the substitution of Co^{3+} with Fe^{2+} sites. The Hall coefficient at 25 K is $-1.7 \times 10^{-3} \text{ cm}^3/\text{C}$, which is comparable to those reported for single crystals with the same doping level as the present PLD target disk,²⁸ and implies that the Co dopant concentration in the film is almost the same as that of the PLD target disk.²⁹

Figure 3 - 1 (c) and (d) show the H sweep results at temperatures from 13 to 16 K for ρ_{xx} and ρ_{xy} , respectively. Due to its high $H_{c2} \geq 50 \text{ T}$,² superconductivity remains at 13–16 K even when high magnetic fields up to 9 T are applied. Similar to observations in MgB_2 films, neither the T nor H sweep results exhibit a Hall sign reversal.²⁰ However, these observations sharply contrast most cuprates such as $\text{YBa}_2\text{Cu}_3\text{O}_{7-\delta}$ (YBCO), $\text{Bi}_2\text{Sr}_2\text{Ca}_2\text{Cu}_3\text{O}_{10}$ (BSCCO), and $\text{HgSr}_2\text{CaCuO}_{6-\delta}$,^{15,19,23} in which the sign of ρ_{xy} changes from positive to negative near the superconducting transition.

Figure 3 - 2 replots the T sweep results of Figs. 1 (a, b) in terms of the scaling behavior between ρ_{xy} and ρ_{xx} . Throughout the entire mixed-state region, ρ_{xy} and ρ_{xx} follow the relation $\rho_{xy} = A\rho_{xx}^\beta$ very well. The β values are extracted from the slopes of the double logarithmic plots by a least squares fit (the resulting standard errors σ_e are < 0.008 , except for 1 T, which is $\sigma_e = 0.03$). All the β values are similar and definitely less

than 2.0; they are between 1.7–1.8 and independent of the applied magnetic field up to at least 9 T. These β values are lower than those reported for Ba(Fe_{1-x}Co_x)₂As₂ single crystals with $\beta = 3.0$ – 3.4 for $x = 0.08$ and $\beta = 2.0 \pm 0.2$ for $x = 0.10$,³⁰ but are comparable to those of YBCO epitaxial films with strong pinning centers.¹⁵ Similar β behaviors with magnetic fields (i.e., no variation with H) are also observed in BSCCO single crystals¹⁷ and MgB₂ films,²⁰ in which weak pinning centers are introduced. However, in those two films, the β values are close to 2.0. The above behavior for a Ba(Fe_{1-x}Co_x)₂As₂ film, in which a small and constant β is maintained under various magnetic fields, is generally reported for superconductors with strong pinning centers such as twinned YBCO epitaxial films,¹⁵ irradiated YBCO single crystals,¹⁸ and irradiated Tl₂Ba₂CaCu₂O₈ films.^{16,31}

Figure 3 - 3 replots the H sweep results of Figure 3 - 1 (c, d) in terms of the scaling behavior between ρ_{xy} and ρ_{xx} . Similar to the T sweep results, most of the data follow the power scaling law. However, the β values between the T and the H sweeps clearly differ. Unlike the T sweep results (Figure 3 - 2), the β value increases from 1.8 to 2.0 as the T increases from 13 to 16 K. According to the above discussion for Fig. 2, this result suggests that the pinning mechanism changes as T increases.

3.3.2. Summary of anomalous Hall scaling with large vortex phase diagram

Table 3 - 1 summarizes the scaling results of the T and the H sweeps. For the T sweep, the scaling behavior shows low β values (1.7–1.8), which are independent of magnetic fields at least up to 9 T. In contrast, the β value changes from 1.8 to 2.0 as T increases in the H sweep. Wang *et al.*²⁵ proposed a unified theory based on the normal

core model³² by taking both the backflow currents and thermal fluctuations into account. According to the Wang's theory for systems with strong pinnings, the pinning effect becomes dominant and the scaling behavior changes from $\beta \sim 2.0$ to ~ 1.5 , indicating that a reduced β corresponds to the weakening of the pinning strength. In fact, the β values of most cuprate superconductors exhibiting strong pinning are 1.0–1.8, which are considerably less than 2.0.^{15,16,18,19}

Based on the Wang's theory,²⁵ used experimental results with $\beta = 1.7$ –1.82 indicate that strong pinning centers effectively work for the T sweep in the entire H region examined in this study. The strong pinning centers are also effective for the H sweep only in the low T (< 14 K) region, but the pinning strength rapidly weakens as T increases and approaches T_c . Maierov *et al.* observed a similar behavior in the angular dependence of J_c ;¹⁰ i.e., strong c -axis pinning remains under high magnetic fields but weakens as T increases.

On the other hand, the BaFe₂As₂:Co epitaxial film displays an anomalous scaling behavior (i.e., different β values are observed in the T and the H sweeps even for the same T and the H conditions). Figure 4 (a) shows the vortex phase diagram of the BaFe₂As₂:Co epitaxial film normalized by H_{c2} and T_c , while Figure 3 - 4 (b) compares the vortex phase diagrams of other superconductors. The irreversibility line H_{irr} , [defined by $\rho(T, H) = 0.01\rho_N$, where ρ_N denotes the normal state resistivity at 25K (dotted lines)] and H_{c2} [defined $\rho(T, H) = 0.90\rho_N$ (dashed lines)] are obtained from Figs. 1(a) and (c). The horizontal and vertical lines indicate the T sweep and the H sweep trajectories, respectively. The corresponding β values are indicated on the left (for H sweep) and right (for T sweep). The two $\beta(T, H)$ values obtained by the T sweep and

the H sweep are similar, 1.7–1.8 in the relatively low T and high H region, as indicated by the dashed square area. By contrast, the two $\beta(T, H)$ values clearly differ between the T sweep and the H sweep even at the same T and H in the high T and low H region, as indicated by the solid square area. This behavior has not been observed in other superconductors. Because this difference is observed at the same T and H and depends on the sweep history, it originates from a hysteresis phenomenon probably due to the dynamics of the vortices.

I also like to note that the normalized vortex phase diagram of the BaFe₂As₂:Co film has a wider vortex liquid region than those of YBCO and MgB₂. Although the H_{c2} lines are similar for all three, the H_{irr} line of the BaFe₂As₂ film extends to the lower T (i.e., to lower H) region [Figure 3 - 4 (b)]. The width of the vortex liquid phase is narrower for a BaFe₂As₂:Co single crystal, indicating that the vortex liquid phase in the BaFe₂As₂:Co film is wider due to the extrinsic disorder introduced during the thin-film growth process.

3.4. Discussion

This phenomenon where the β values depend on the measurement history shows that the vortex penetration process affects the vortex dynamics in BaFe₂As₂:Co epitaxial films, especially at a relatively high T and a low H . Figure 3 - 5 illustrates the proposed vortices penetration model. A low T and zero H condition in Figure 3 - 5 (a) is start to describe. U denotes the effective pinning potential. N_v and N_p denote the numbers of penetrated vortices and pinning centers, respectively. For the T sweep, H is initially applied at a low T , and then T is swept to higher values. For the H sweep, T is initially

adjusted while maintaining the zero H , and then H is swept to higher values. First, we considered the case of high H (i.e., the final $N_v \gg N_p$) and a relatively low T (b), which corresponds to the dashed squares in Figure 3 - 4 (a). The short and long vertical arrows denote pinned vortices and unpinned vortices, respectively. For the T sweep, when a high H (i.e., $N_v \gg N_p$) is applied at a low T (upper left), a large portion of the vortices spills over from the pinning centers. The pinned vortices are maintained at a high T , while the vortices unpinned in the strong pinning centers are mobile (upper right). For the H sweep, the effective pinning force weakens at higher T (lower left). Then vortices are introduced at the high T , where most of the pinning centers are filled due to the condition $N_v \gg N_p$, and the extra vortices that spill over from the pinning centers are mobile (lower right). Thus, the difference in the T and H sweep data is small. The condition of low H (the final $N_v \sim N_p$) and high T , which corresponds to the solid square area in Figure 3 - 4 (a), provides a different result. For the T sweep, the pinning centers trap the penetrated vortices upon applying H . All the penetrated vortices are effectively trapped at the pinning centers at low T because the effective pinning force is sufficiently strong (upper left), and their positions are stabilized and maintained even at a high T (upper left). Consequently, a strong pinning condition with $\beta < 2.0$ is produced. By contrast, for the H sweep, the effective pinning force weakens at high T (lower left), and vortices are penetrated at the high T with a weak pinning force. This leads to a large thermal fluctuation at high temperatures near T_c . Consequently, fewer vortices are trapped by the pinning centers, and the vortices are mobile (lower right), giving rise to a weak pinning condition with $\beta \sim 2.0$.

This model explains well the observation that the $\beta(T, H)$ value at the same T and H condition depends on the measurement history for a BaFe₂As₂:Co epitaxial film, e.g.,

the T sweep or the H sweep. This phenomenon may occur in other superconductors, but has only been observed in a BaFe₂As₂:Co epitaxial film. The above model indicates that the difference of the β values between in the T and H sweep data occurs for the condition $N_v < N_p$, which suggests that the BaFe₂As₂:Co epitaxial film has high-density pinning centers. In MgB₂ and YBCO films without artificial pinning centers, it is estimated that their dominant intrinsic pinning centers are planar defects (i.e., grain boundaries and twin boundaries) due to the scaling behaviors of their normalized pinning force and transmission electron microscopy image.^{33–36} On the other hand, the scaling behaviors of their normalized pinning force and magnetic Bitter decoration indicate that BaFe₂As₂:Co has intrinsic pinning centers^{2,37} and extrinsic c -axis pinning centers exist in BaFe₂As₂:Co epitaxial film.¹⁰ The F_p maximum position of BaFe₂As₂:Co epitaxial film is about $0.4 H/H_{irr}$ ⁷, indicating that origin of the pinning is not purely the collective pinning and includes the strong core pinning. This mechanism is similar to the case of columnar BaFeO₂ pinning centers³⁸ in a BaFe₂As₂:Co epitaxial film grown using SrTiO₃ buffer layer. These experimental results indicate the existence of a dense vortex-pinning structure in a BaFe₂As₂:Co epitaxial film; these conditions give a larger N_p than those of other superconductors. Furthermore, because the width of the vortex liquid phase is larger in a BaFe₂As₂:Co epitaxial film than that of the single crystal, the BaFe₂As₂:Co epitaxial film has additional extrinsic pinning centers besides the intrinsic ones in the single crystal. Thus, the distinct scaling behaviors in the BaFe₂As₂:Co epitaxial film at a relatively high T and in a low H should originate from the high-density pinning structure, which consists of the intrinsic and the extrinsic pinning centers.

Unlike cuprate superconductors exhibiting $1.0 < \beta < 2.0$,^{15, 16, 18, 19} the sign of ρ_{xy} in

this study does not reverse in either the T or the H sweep results. Wang's theory²⁵ predicts that the scaling behavior exhibiting $\beta < 2.0$ occurs after a sign reversal, which is inconsistent with the present results. Therefore, we would like to discuss the sign reversal based on the Hall conductivity, which is defined as $\sigma_{xy} = \rho_{xy}/(\rho_{xy}^2 + \rho_{xx}^2)$, because a general argument of vortex dynamics indicates σ_{xy} is insensitive to disorder effects.^{24,31} Indeed, for cuprates, the sign reversal is clearly observed in σ_{xy} .^{39,40} Figure 3 - 6 replots Figure 3 - 1 in terms of σ_{xy} . The H and the T sweep results substantiate that σ_{xy} tends to diverge to a large negative value and sign reversal is not detected. Matsuda *et al.*³⁹ and Nagaoka *et al.*⁴⁰ have experimentally suggested that the sign of ρ_{xy} depends on the doping level in most cuprate superconductors; i.e., a sign reversal occurs in an underdoped regime but diminishes in overdoped ones. Kopnin *et al.*⁴¹ and Dorsey⁴² have also discussed the Hall anomaly based on a microscopic approach and proposed theories of a mixed-state Hall effect based on a time-dependent Ginzburg-Landau model; they postulate that the sign reversal depends on the gradient of the density of states at the Fermi surface. According to these experimental and theoretical results, researching the doping concentration dependence may provide a definitive conclusion on the Hall sign reversal in high- J_c BaFe₂As₂:Co epitaxial films because this study employed a slightly overdoped sample.¹⁴

3.5. Conclusion

The transport properties in a mixed-state of a high- J_c BaFe₂As₂:Co epitaxial film was investigated. The scaling behavior in the T sweep measurements shows constant β values less than 2.0 under magnetic fields up to 9 T. On the other hand, the β values clearly increase from 1.8 to 2.0 in the H sweep measurements as T increases from 13 to

16 K. These results indicate that strong pinning centers trap the vortices introduced at low temperatures, but some of the vortices introduced at high temperatures are not trapped and that pinning weakens at higher temperatures near the normal state. In the entire H and T ranges examined in this study, the sign does not reverse. These distinct scaling behaviors, which sharply contrast cuprates and MgB₂, can be explained by the high-density c -axis pinning centers in a BaFe₂As₂:Co epitaxial film, which are consistent with wider vortex liquid phase.

References

- ¹ T. Katase, Y. Ishimaru, A. Tsukamoto, H. Hiramatsu, T. Kamiya, K. Tanabe, and H. Hosono, *Nature Communications* **2**, 409 (2011).
- ² A. Yamamoto, J. Jaroszynski, C. Tarantini, L. Balicas, J. Jiang, A. Gurevich, D.C. Larbalestier, R. Jin, A.S. Sefat, M.A. McGuire, B.C. Sales, D.K. Christen, and D. Mandrus, *Applied Physics Letters* **94**, 062511 (2009).
- ³ K. Togano, A. Matsumoto, and H. Kumakura, *Applied Physics Express* **4**, 043101 (2011).
- ⁴ J.D. Weiss, C. Tarantini, J. Jiang, F. Kametani, A.A. Polyanskii, D.C. Larbalestier, and E.E. Hellstrom, *Nature Materials* **11**, 682 (2012).
- ⁵ Y. Ma, *Superconductor Science and Technology* **25**, 113001 (2012).
- ⁶ K. Iida, J. Hänisch, S. Trommler, V. Matias, S. Haindl, F. Kurth, I.L. del Pozo, R. Hühne, M. Kidszun, J. Engelmann, L. Schultz, and B. Holzapfel, *Applied Physics Express* **4**, 013103 (2011).
- ⁷ T. Katase, H. Hiramatsu, V. Matias, C. Sheehan, Y. Ishimaru, T. Kamiya, K. Tanabe, and H. Hosono, *Applied Physics Letters* **98**, 242510 (2011).
- ⁸ R. Prozorov, N. Ni, M.A. Tanatar, V.G. Kogan, R.T. Gordon, C. Martin, E.C. Blomberg, P. Proumapan, J.Q. Yan, S.L. Bud'ko, and P.C. Canfield, *Phys. Rev. B* **78**, 224506 (2008).
- ⁹ Y. Nakajima, Y. Tsuchiya, T. Taen, T. Tamegai, S. Okayasu, and M. Sasase, *Phys. Rev. B* **80**, 012510 (2009).
- ¹⁰ B. Maiorov, T. Katase, S.A. Baily, H. Hiramatsu, T.G. Holesinger, H. Hosono, and L. Civale, *Superconductor Science and Technology* **24**, 055007 (2011).
- ¹¹ T. Thersleff, K. Iida, S. Haindl, M. Kidszun, D. Pohl, A. Hartmann, F. Kurth, J. Hänisch, R. Hühne, B. Rellinghaus, L. Schultz, and B. Holzapfel, *Applied Physics Letters* **97**, 022506 (2010).
- ¹² S. Lee, J. Jiang, Y. Zhang, C.W. Bark, J.D. Weiss, C. Tarantini, C.T. Nelson, H.W. Jang, C.M. Folkman, S.H. Baek, A. Polyanskii, D. Abaimov, A. Yamamoto, J.W. Park, X.Q. Pan, E.E. Hellstrom, D.C. Larbalestier, and C.B. Eom, *Nature Materials* **9**, 397 (2010).
- ¹³ T. Katase, H. Hiramatsu, T. Kamiya, and H. Hosono, *Applied Physics Express* **3**, 063101 (2010).
- ¹⁴ T. Katase, H. Hiramatsu, T. Kamiya, and H. Hosono, *Superconductor Science and Technology* **25**, 084015 (2012).
- ¹⁵ J. Luo, T.P. Orlando, J.M. Graybeal, X.D. Wu, and R. Muenchausen, *Phys. Rev. Lett.*

68, 690 (1992).

¹⁶ R.C. Budhani, S.H. Liou, and Z.X. Cai, Phys. Rev. Lett. **71**, 621 (1993).

¹⁷ A.V. Samoilov, Phys. Rev. Lett. **71**, 617 (1993).

¹⁸ W.N. Kang, D.H. Kim, S.Y. Shim, J.H. Park, T.S. Hahn, S.S. Choi, W.C. Lee, J.D. Hettinger, K.E. Gray, and B. Glagola, Phys. Rev. Lett. **76**, 2993 (1996).

¹⁹ W.N. Kang, B.W. Kang, Q.Y. Chen, J.Z. Wu, S.H. Yun, A. Gapud, J.Z. Qu, W.K. Chu, D.K. Christen, R. Kerchner, and C.W. Chu, Phys. Rev. B **59**, R9031 (1999).

²⁰ W.N. Kang, H.-J. Kim, E.-M. Choi, H.J. Kim, K.H.P. Kim, and S.-I. Lee, Phys. Rev. B **65**, 184520 (2002).

²¹ M. Galffy and E. Zirngiebl, Solid State Communications **68**, 929 (1988).

²² S.J. Hagen, C.J. Lobb, R.L. Greene, M.G. Forrester, and J.H. Kang, Phys. Rev. B **41**, 11630 (1990).

²³ Y. Iye, S. Nakamura, and T. Tamegai, Physica C: Superconductivity **159**, 616 (1989).

²⁴ V.M. Vinokur, V.B. Geshkenbein, M.V. Feigel'man, and G. Blatter, Phys. Rev. Lett. **71**, 1242 (1993).

²⁵ Z.D. Wang, J. Dong, and C.S. Ting, Phys. Rev. Lett. **72**, 3875 (1994).

²⁶ H. Hiramatsu, T. Katase, T. Kamiya, M. Hirano, and H. Hosono, Applied Physics Express **1**, 101702 (2008).

²⁷ W.N. Kang, H.-J. Kim, E.-M. Choi, H.J. Kim, K.H.P. Kim, H.S. Lee, and S.-I. Lee, Phys. Rev. B **65**, 134508 (2002).

²⁸ L. Fang, H. Luo, P. Cheng, Z. Wang, Y. Jia, G. Mu, B. Shen, I.I. Mazin, L. Shan, C. Ren, and H.-H. Wen, Phys. Rev. B **80**, 140508 (2009).

²⁹ H. Hiramatsu, T. Katase, Y. Ishimaru, A. Tsukamoto, T. Kamiya, K. Tanabe, and H. Hosono, Materials Science and Engineering: B **177**, 515 (2012).

³⁰ L.M. Wang, U.-C. Sou, H.C. Yang, L.J. Chang, C.-M. Cheng, K.-D. Tsuei, Y. Su, T. Wolf, and P. Adelman, Phys. Rev. B **83**, 134506 (2011).

³¹ A.V. Samoilov, A. Legris, F. Rullier-Albenque, P. Lejay, S. Bouffard, Z.G. Ivanov, and L.-G. Johansson, Phys. Rev. Lett. **74**, 2351 (1995).

³² J. Bardeen and M.J. Stephen, Phys. Rev. **140**, A1197 (1965).

³³ D. Dew-Hughes, Philosophical Magazine **30**, 293 (1974).

³⁴ D.C. Larbalestier, L.D. Cooley, M.O. Rikel, A.A. Polyanskii, J. Jiang, S. Patnaik, X.Y. Cai, D.M. Feldmann, A. Gurevich, A.A. Squitieri, M.T. Naus, C.B. Eom, E.E. Hellstrom, R.J. Cava, K.A. Regan, N. Rogado, M.A. Hayward, T. He, J.S. Slusky, P. Khalifah, K. Inumaru, and M. Haas, Nature **410**, 186 (2001).

³⁵ B. Roas, L. Schultz, and G. Saemann-Ischenko, Phys. Rev. Lett. **64**, 479 (1990).

³⁶ T. Nishizaki, T. Aomine, I. Fujii, K. Yamamoto, S. Yoshii, T. Terashima, and Y. Bando,

Physica C: Superconductivity **181**, 223 (1991).

³⁷ S. Demirdiř, C.J. van der Beek, Y. Fasano, N.R. Cejas Bolecek, H. Pastoriza, D. Colson, and F. Rullier-Albenque, Phys. Rev. B **84**, 094517 (2011).

³⁸ C. Tarantini, S. Lee, Y. Zhang, J. Jiang, C.W. Bark, J.D. Weiss, A. Polyanskii, C.T. Nelson, H.W. Jang, C.M. Folkman, S.H. Baek, X.Q. Pan, A. Gurevich, E.E. Hellstrom, C.B. Eom, and D.C. Larbalestier, Applied Physics Letters **96**, 142510 (2010).

³⁹ Y. Matsuda, T. Nagaoka, G. Suzuki, K. Kumagai, M. Suzuki, M. Machida, M. Sera, M. Hiroi, and N. Kobayashi, Phys. Rev. B **52**, R15749 (1995).

⁴⁰ T. Nagaoka, Y. Matsuda, H. Obara, A. Sawa, T. Terashima, I. Chong, M. Takano, and M. Suzuki, Phys. Rev. Lett. **80**, 3594 (1998).

⁴¹ N.B. Kopnin, B.I. Ivlev, and V.A. Kalatsky, Journal of Low Temperature Physics **90**, 1 (1993).

⁴² A.T. Dorsey, Phys. Rev. B **46**, 8376 (1992).

Table 3 - 1. Summary of the mixed-state Hall effect of a BaFe₂As₂:Co epitaxial film for T and H sweep modes.

Sweep variable	Temperature	Magnetic field
Fixed parameter	Magnetic field	Temperature
Range	1 → 9 T	13 → 16 K
β value	constant	monotonically increase
	1.7–1.8	1.8 → 2.0
Sign reversal		Not detected

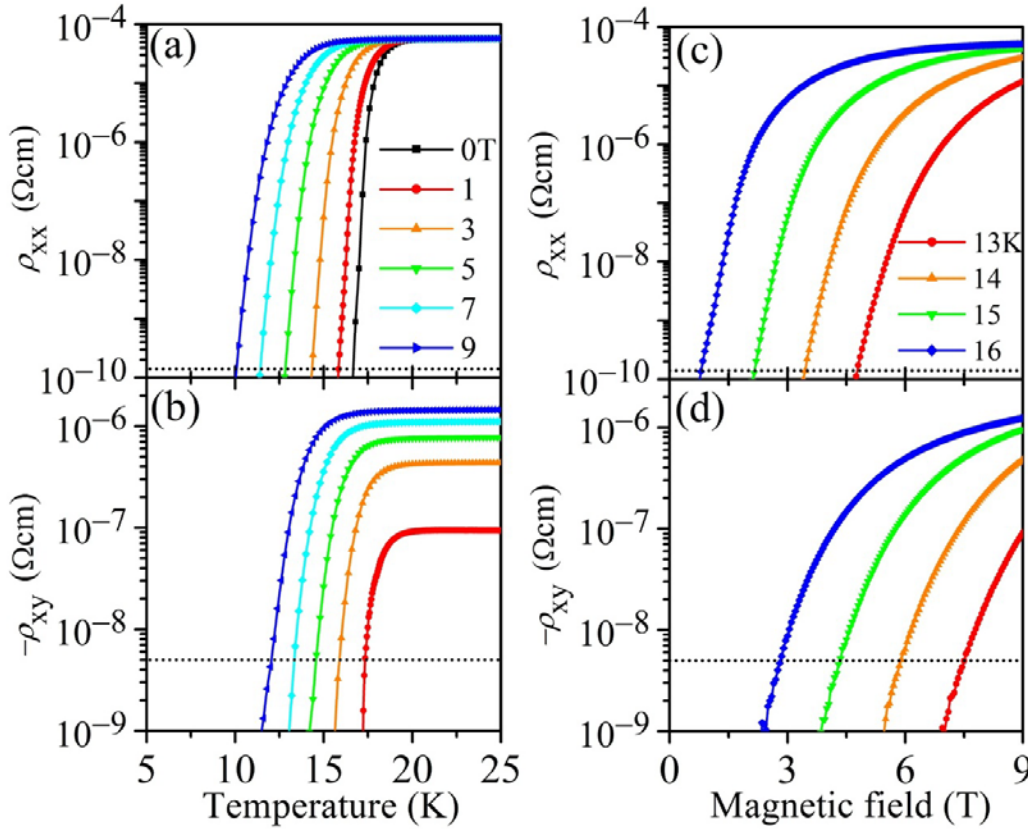


Figure 3 - 1 (a), (b) T sweep and (c), (d) H sweep results of ρ_{xx} and ρ_{xy} of a BaFe₂As₂:Co epitaxial film. Measurements were performed under fixed magnetic fields between 0 and 9 T (a), (b) and at fixed temperatures between 13 and 16 K (c), (d). Horizontal dotted lines show the measurement limits.

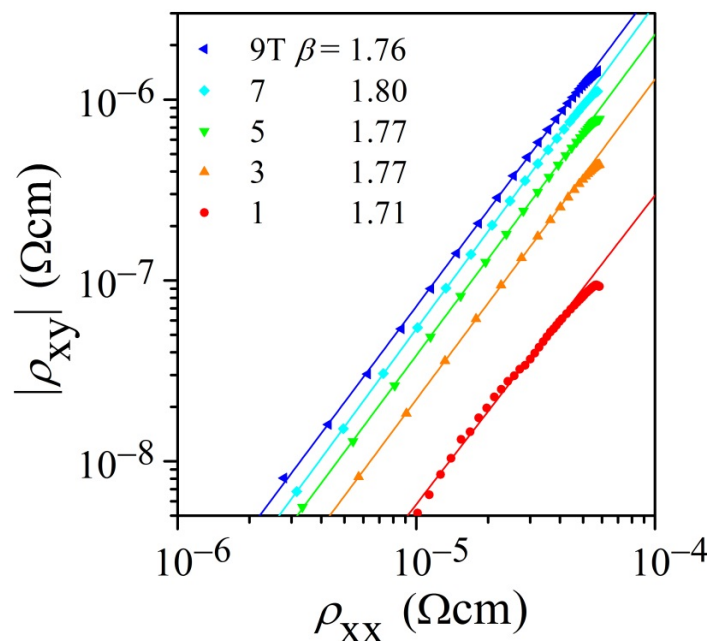


Figure 3 - 2. T sweep scaling behavior between ρ_{xy} and ρ_{xx} under fixed magnetic fields varied from 1 to 9 T. Solid lines show fitted results using the relation $\rho_{xy} = A\rho_{xx}^{\beta}$. Magnetic fields and the β values are shown on top left.

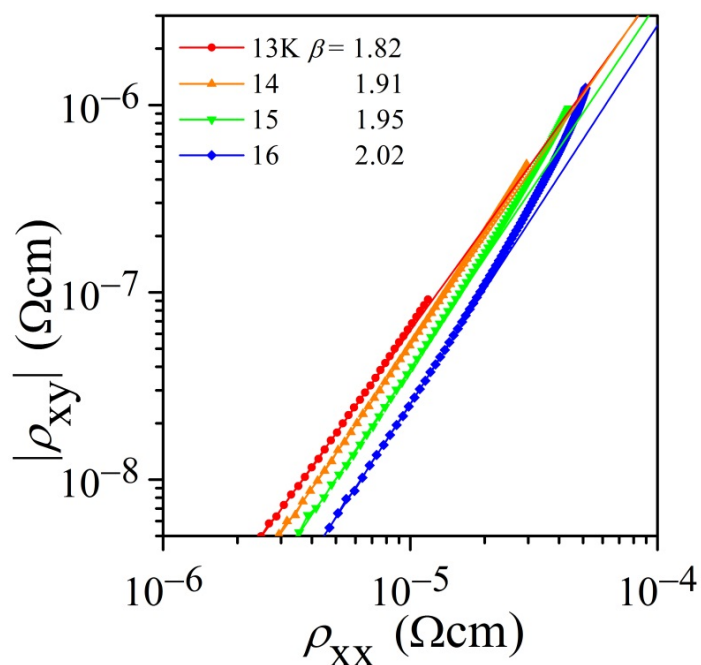


Figure 3 - 3. H sweep scaling behavior between ρ_{xy} and ρ_{xx} at fixed temperatures varied from 13 to 16 K. Solid lines are fitted results. Measurement temperatures and the β values are shown on top left.

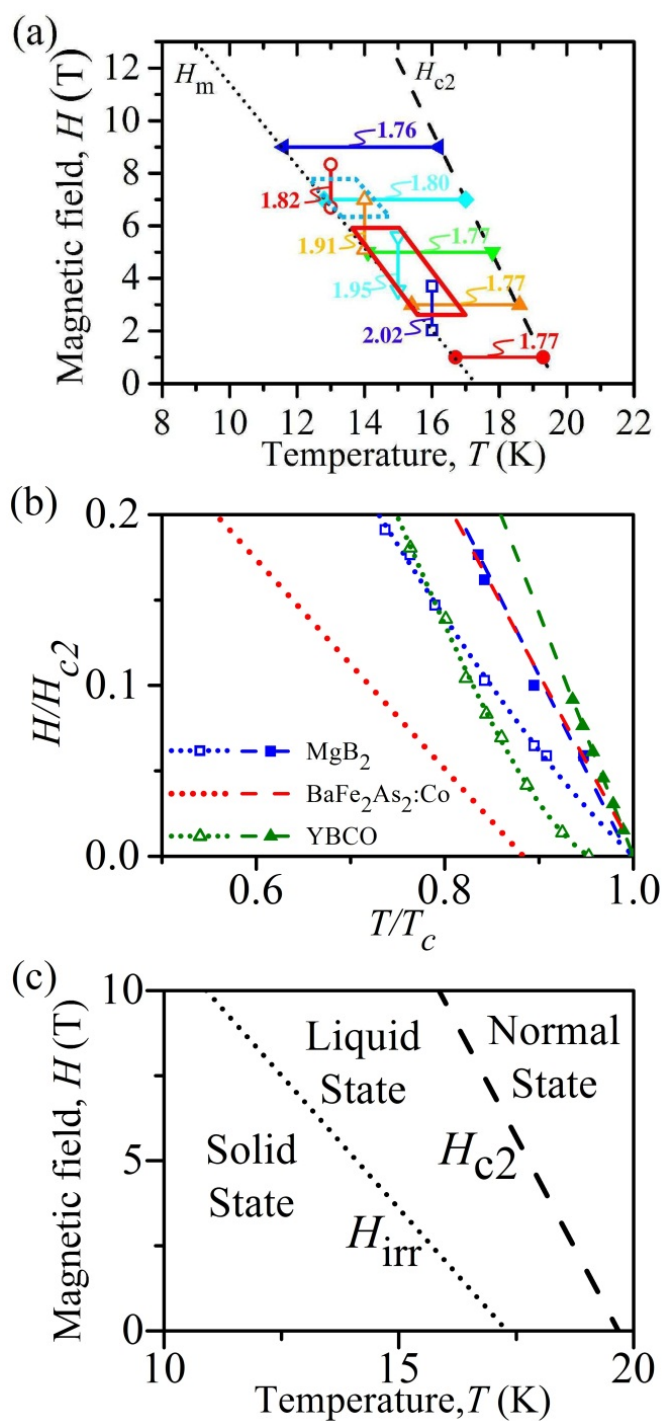


Figure 3 - 4. Vortex phase diagrams of (a) BaFe₂As₂:Co epitaxial film and (b) BaFe₂As₂:Co epitaxial film with YBCO^{22,52} and MgB₂⁵³ normalized by H_{c2} and T_c . Dotted and dashed lines indicate the irreversibility lines (H_{irr}) and H_{c2} , respectively, which are schematically shown in (c) as a general vortex diagram. (a) Vertical and horizontal lines show the results of the T sweep (taken from Fig. 3) and the H sweep measurements (taken from Fig. 4), respectively.

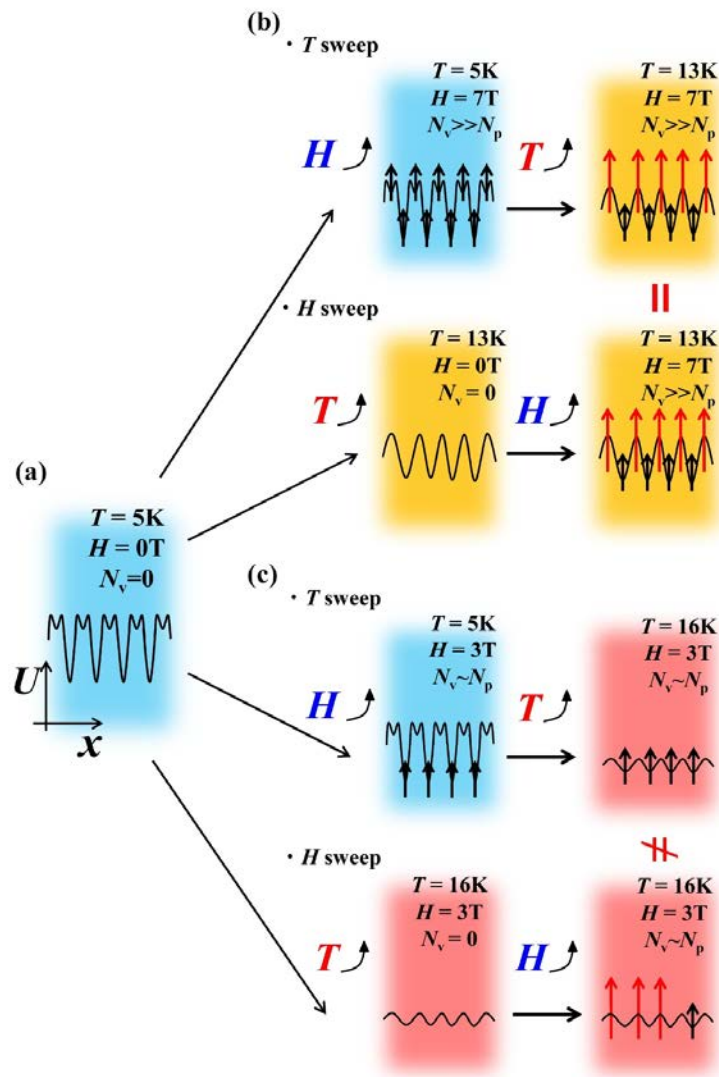


Figure 3 - 5. Vortex-penetration processes under various conditions for the T sweep (H is increased and then T is increased) and H sweep (T is increased and then H is increased) processes. U denotes the effective pinning potential. N_v and N_p denote the numbers of penetrated vortices and strong pinning centers, respectively. Short and long vertical arrows denote pinned vortices and unpinned vortices, respectively. (a) Initial state at low T (e.g., 5 K) and $H = 0$ ($N_v = 0$). (b) Final condition corresponds to a high H (i.e., the final $N_v \gg N_p$) and a relatively low T . For the T sweep, the strong pinning centers are filled with vortices, and many extra vortices spill over upon applying high H (upper left). Pinned vortices are maintained at higher T but extra vortices are mobile (upper right). For the H sweep, the effective pinning force weakens at higher T (lower left); then vortices are introduced and most of the pinning centers are filled due to the condition $N_v \gg N_p$, and the extra vortices are mobile (lower right). This final situation is the same as the T sweep case. (c) Final condition corresponds to low H (the final $N_v \sim N_p$) and high T . For the T sweep, the penetrated

vortices are trapped by the pinning centers upon applying H (upper left). These trapped vortices are maintained at high T (upper right), giving a strong pinning condition with $\beta < 2.0$. For the H sweep, effective pinning force weakens at high T (lower left); then vortices are introduced, but many vortices are not trapped and remain mobile (lower right), giving rise to a weak pinning condition with $\beta \sim 2.0$. The final state differs from the T sweep case.

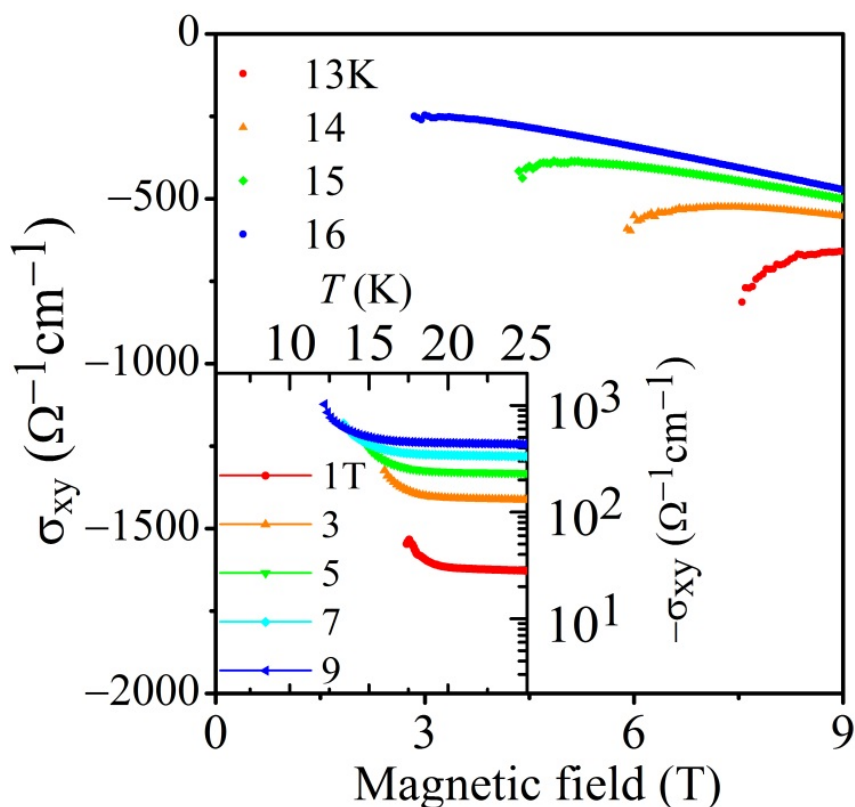


Figure 3 - 6. H dependence of the Hall conductivity $\sigma_{xy} = \rho_{xy}/(\rho_{xy}^2 + \rho_{xx}^2)$ at 13–16 K. Inset shows T dependence of σ_{xy} under 1–9 T.

Chapter 4: Anisotropic pressure effects on superconducting properties of cobalt-doped BaFe₂As₂ epitaxial films

4.1. Introduction

Since the early stage of researches on iron-based superconductors¹, it has been known that applying external pressures is an effective way to enhance their critical temperatures (T_c)^{2,3}; e.g., T_c of 1111-type LaFeAsO_{0.89}F_{0.11} and 11-type Fe_{1.01}Se are drastically enhanced from 27 to 43 K² and from 8.5 to 35.7 K⁴, respectively. Additionally, it is reported that a double-dome-shaped superconducting phase diagram of LaFeAsO_{1-x}H_x⁵ is merged into an one-dome-shaped one under 6 GPa and its maximum T_c reaches 52 K, which is almost the same as those (55 K) of the highest- T_c -family, 1111-type SmFeAsO_{1-x}F_x⁶ and SmFeAsO_{1-x}H_x⁷. This result indicates that applying high pressures is an attractive way not only to enhance T_c but also to control it in iron-based superconductors.

On the other hand, 122-type AFe_2As_2 ($A = Ca, Sr, Ba$), which is the most promising materials for applications in iron-based superconductors⁸, are very sensitive to the direction of the pressure⁹. According to the results of the comparison of pressure apparatus and pressure medium^{3,10}, the pressurizing along c -axis is very effective for inducing the superconductivity in parent material AFe_2As_2 and it is understood in terms of the stability of tetragonal structure. However, T_c of optimally and over-doped 122-type BaFe₂As₂ does not largely increase under high pressure (~ 1 K increase or decrease)¹¹⁻¹⁴. According to the results of thermal expansion and heat capacity

measurements ¹⁵ [i.e., Ehrenfest relationship: $dT_c / dP_i = V_m \Delta \alpha_{Ti} / (\Delta C_p / T_c)$ for second-order phase transitions. Here, P_i is pressure along i direction, V_m is molar volume, $\Delta \alpha_{Ti}$ is the jump in the thermal expansion coefficient (α_T) along i direction and ΔC_p is the specific-heat jump], the anisotropic pressure along a -axis is effective for enhancing its T_c but that along c -axis decreases T_c , which is contrary to the undoped parent material case; i.e., applying external pressures to undoped parents emerged superconductivity ¹⁶. However, applying strong anisotropic pressure and controlling its direction exactly are very difficult in the case of bulk samples because of the obtained sample shapes (e.g. plate like single crystals) and configuration of high pressure apparatus.

On the other hand, in the case of thin films, the anisotropic pressure can be easily generated by epitaxial strain utilizing lattice mismatch between films and substrates and it is well-known effective technique to enhance the T_c in cuprates ^{17,18}. For cobalt-doped BaFe₂As₂ epitaxial films, it has also been reported that the ratios of a - and c -axes lengths can be controlled by epitaxial strain and their T_c strongly depend on the c/a ratios ^{19,20}. However, types of substrates which can be used are limited because the epitaxial films cannot be grown if we employ substrates with large in-plane lattice mismatches. Therefore, other ways are necessary to induce stronger anisotropic pressures and enhance their T_c .

To overcome this issue (i.e., applying stronger anisotropic pressures), we propose a guiding principle concept utilizing differences in thermal expansion coefficients (α_T) and compressibilities (α_P) between films and substrates as well as in-plane lattice mismatches. Figure 1 summarizes the concept. I utilize heterostructure interfaces

between epitaxial films and single-crystal substrates to realize this concept. As we mentioned above, epitaxial strain is induced by the lattice mismatch between film and substrate. When the lateral lattice parameter of film (a^{Film}) is larger than that of substrate ($a^{\text{Sub.}}$), the compressive strain is induced [Figure 1 (a) Right panel]. On the other hand, tensile strain is induced in the case of $a^{\text{Film}} < a^{\text{Sub.}}$ [Fig. 1 (a) Left panel]. In addition, the differences of α_T and α_P induce the anisotropic strain. When a substrate has larger α_T and α_P than those of a film [Fig. 1 (b)], the film is strongly compressed along the lateral direction (i.e., along the in-plane direction) in cooling process caused by larger shrinkage of substrate and the shrinkage along the normal to the plane is suppressed by Poisson's effect. Moreover, hydrostatic pressure also makes the anisotropic pressure in the heterointerface. When the hydrostatic pressure is applied to the thin films, the anisotropic pressures can be induced at the hetero-interface because of the differences in the α_P between film and substrate. On the other hand, the opposite variation of the thin film occurs when the substrate has smaller α_T and α_P [Fig. 1 (c)]. Finally, anisotropic pressure is induced in the cooling process from room temperature to low temperature utilizing differences in α_T . Thus, we can apply complex and effectively strong anisotropic external pressures originating from lattice mismatches, and differences in α_T and α_P between films and substrates.

In this study, we selected 150 – 200 nm-thick 122-type optimally cobalt-doped BaFe₂As₂ (Ba122:Co) epitaxial films, an iron-based superconductor with a bulk T_c of 22 K²¹, because T_c of the optimally doped Ba122:Co is robust to the hydrostatic pressure^{11,12} but sensitive to the anisotropic pressure^{19,20}. According to the results of thermal expansion and heat capacity measurements¹⁵, the anisotropic pressure along a -axis is effective for enhancing its T_c but that along c -axis decreases T_c and hydrostatic pressure

slightly decrease its T_c summarizing the these pressure effects ($dT_c/dP_{\text{hydrostatic}} = 2dT_c/dP_a + dT_c/dP_c = -0.9(3)$ K/GPa). These mean that we can examine effects of anisotropic external pressures on T_c by applying based on our concept. To realize our concept, four kinds of single-crystal substrates were selected; two kinds of fluoride substrates (CaF₂ and BaF₂) with large α_T and α_P and two kinds of oxide substrates [MgO and (La,Sr)(Ar,Ta)O₃ (LSAT)] with small α_T and α_P than those of Ba122:Co (The substrates' structural and physical parameters are summarized in Table 1). To utilize the lattice mismatch, two kinds of substrates which have $a^{\text{Sub.}} < a^{\text{Film}}$ (CaF₂ and LSAT) and $a^{\text{Sub.}} > a^{\text{Film}}$ (BaF₂, MgO) are mixed in each kind (fluoride and oxide). To examine the pressure effects generated by thermal expansion, structural parameters of films are examined with increasing temperature and it is clearly shown that the crystal structures of thin films are strongly affected by thermal expansion of the substrates. Applying the hydrostatic pressure to the films, $T_c(3\text{GPa}) - T_c(0)$ is proportional to the compressibility of substrates. These results also indicate that the anisotropic pressure was induced obeying with mentioned concept and it is consistent with the Ehrenfest relationship. To discuss the dominant parameters of superconductivity, the relationship of Hall coefficients and T_c is investigated under high pressure.

4.2. Experimental procedure

4.2.1. Thin film fabrication and structure characterization

BaFe₂As₂:Co epitaxial films were fabricated on (001)-oriented cubic CaF₂, BaF₂, MgO and LSAT single-crystal substrates by PLD method. The substrates' structural and physical parameters are listed in Table 1. The second harmonics (the wavelength = 532 nm) of a neodymium-doped yttrium aluminum garnet laser and a polycrystalline disks

of Ba(Fe_{0.92}Co_{0.08})₂As₂ were used as the excitation source and the PLD targets, respectively. Detailed growth conditions are reported in refs ^{22,23}. Structural parameters and crystallinity are examined by high resolution (HR) XRD apparatus [radiation: Cu K α ₁ monochromated by Ge (220) crystals] at room temperature. To determine the lattice parameters at high temperature up to 500 °C, a dome-type hot stage (Anton Paar, DHS 1100) was used as a XRD sample stage under a vacuum condition $\sim 1 \times 10^{-2}$ Pa.

4.2.2. Electrical transport measurements under ambient and high pressure

Thin films were patterned as a Hall bar structure using photolithography and Ar milling technique. After the Hall-bar fabrication process, Au electrode pads were formed by DC-sputtering and lift-off process. To measure the longitudinal electrical resistivity ρ (ρ_{xx}) under ambient pressure, $\rho - T$ measurements were performed with constant current along a -axis of films by a four-probe method using a physical property measurement system (PPMS). Temperature dependence of transverse Hall resistivity (ρ_{xy}) was also measured using the four-probe technique. External magnetic fields up to 9 T were applied parallel to the c -axis. In the case of high pressure measurements, Daphne 7474 oil and a piston-cylinder-type high-pressure cell were employed as a liquid pressure medium and a high pressure apparatus, respectively to obtain the hydrostatic external pressure ²⁴. The hydrostatic pressures of 0 – 3.5 GPa were applied in this study. For the pressure calibration in the high-pressure cell, ρ_{xx} of a Sn wire in the same high-pressure cell was measured and the absolute values of applied pressures were determined by T_c of Sn. A Cernox thermometer was directly mounted at the bottom of the high pressure cell to calibrate the actual measurement temperature because there is a small difference between temperature of the high pressure cell and that of PPMS mainly

caused by a large heat capacity of the high pressure cell. In order to decrease the difference, we slowly swept the measurement temperatures at 0.5 K/min so as to control the temperature difference less than 0.1 K around the superconducting transition.

4.3. Results

4.3.1. Structural parameters of the films

Wide range X-ray diffraction (XRD) patterns [Supplemental figure 2 (a) and (b)] exhibited clear $00l$ diffractions for out-of-plane and $h00$ diffractions for in-plane with small peak of non-oriented Fe and/or Fe-Co alloy particles [H.sato APL Supple (2014)]. According to the tetragonal lattice of Ba122:Co, clear four-fold symmetric peaks were observed in in-plane ϕ scans [Supplemental figure 2 (c – f)]. These data indicate that all of the BaFe₂As₂:Co thin films heteroepitaxially grow on the all substrates with the heteroepitaxial relationship of $[001]\text{Ba122:Co} \parallel [001]$ substrates for out-of-plane and $[100]\text{Ba122:Co} \parallel [100]\text{MgO,LSAT}$ or $[100]\text{Ba122:Co} \parallel [110]\text{CaF}_2,\text{BaF}_2$ for in-plane. This epitaxial relationship can be explained by lattice mismatching for in-plane as summarized in Table 1. Figures 2 (a) and (b) show the magnified patterns around 400 and 004 peaks of Ba122:Co epitaxial films on each substrate, respectively. 400 peaks of BaFe₂As₂:Co epitaxial films on MgO and LSAT were observed at almost the same 2θ angle with each other and at lower 2θ angle than that of a single crystal²¹; while those of BaF₂ and CaF₂ were observed at higher 2θ angle than those of films on oxide substrates and a single crystal²¹, indicating that the a -axes of Ba122:Co epitaxial films on BaF₂ and CaF₂ are compressed and those on MgO and LSAT are expanded. It should be note that BaF₂ has larger lateral lattice parameter ($a/\sqrt{2} = 4.38$) than that of a single crystal with the same chemical composition Ba(Fe_{0.92}Co_{0.08})₂As₂ single crystal ($a =$

3.9639)²¹ but the thin film has shorter *a*-axis; i.e., compressed, not tensile. This phenomenon cannot be explained only by epitaxial strain and should be originated from the large lattice variation in cooling process from growth temperature (GT) to room temperature (RT) caused by large α_T of substrate (see Supplemental table 1 and figure 1). This phenomenon is also observed in the case of FeSe thin film on CaF₂²⁵. In addition, similar opposite strain effect was observed also in the films on LSAT with shorter *a*-axis ($a = 3.87$). In this case, the origin seems to be the smaller shrinkage of substrate in cooling process from GT to RT and/or thin reaction layer between BaFe₂As₂:Co and LSAT²⁶. It should be note that CaF₂ and LSAT have almost same lattice mismatch at room temperature but the films on CaF₂ are most compressed ($\sim -1.6\%$: same variation which is induced by 4.2 GPa hydrostatic pressure along in-plane direction among 4 kinds of substrates because of the combination of negative lattice mismatch and larger shrinkage of substrate in cooling process from GT to RT. These results indicate that utilizing the differences of thermal expansion become powerful tool to control the structure of thin film combined with epitaxial strain. Also for out-of-plane, 004 peaks of BaFe₂As₂:Co epitaxial films on MgO and LSAT were observed at almost the same 2θ angle with each other but those of CaF₂ and BaF₂ were observed at lower 2θ angle, indicating that *c*-axis of those on CaF₂ and BaF₂ are expanded compared with those on MgO and LSAT and Ba(Fe_{0.92}Co_{0.08})₂As₂ single crystal. These results are summarized in Figure 2 (c). Upper left shaded area indicates that *a*-axis is compressed and *c*-axis is expanded. Lower right shaded area indicates *a*-axis expanded and *c*-axis is compressed. The plotted points obey the linear scaling of solid line in Fig. 2 (c), implying that change in lattice parameters is proportionate to Poisson's ratio and it is not caused by Co doping (i.e. structure changes in obedience to different trend)

4.3.2. Investigations on strain effects using high temperature XRD

In order to examine how the structural changes of substrates affect to the structure of the thin films, high temperature (HT) XRD measurements were performed at 30–500 °C because Ba122:Co films start being decomposed at ≥ 600 °C under a vacuum atmosphere ($\sim 10^{-2}$ Pa). Figures 2 (d) and (e) shows the a -axis and c -axis lengths of BaFe₂As₂:Co thin films on each substrate at high temperature, respectively with those of bulk Ba122:Co. Table 2 shows the summary of α_T of the films and substrates. In the case of thin films on fluoride substrates with larger α_T , a -axis lengths of the films increase rapidly with increasing temperature and a -axis α_T (α_{Ta}) becomes extremely larger than that of Ba122:Co single crystal²⁷. To maintain the cell volumes, c -axis α (α_{Tc}) becomes smaller values. On the other hand, a -axes of the films on oxide substrates gently changes with increasing temperature because smaller difference in α_T between the film and oxide substrates (see Table 2). It should be note that α_{Ta} of the film on CaF₂ is larger than α_{Tc} . In the case of BaFe₂As₂:Co single crystal, α_{Tc} is about 3 times larger than α_{Ta} ^{15,27}; i.e., anisotropy of α_T (i.e., $\alpha_{Ta} / \alpha_{Tc}$) of the film on CaF₂ is opposite compared with that of single crystal. This would be one of the reasons of the unusual physical properties of BaFe₂As₂:Co on CaF₂ as discussed in the next section.

4.3.3. Electrical transport properties under ambient pressure: the unique characteristics of strained films on CaF₂

First, we performed temperature dependence resistivity (ρ - T) measurements to check strain effects from substrates on T_c at ambient pressure. Figures 3 (a) and (b) shows the $\rho - T$ curves of BaFe₂As₂:Co thin films on each substrate and magnified figure of $\rho - T$ curves around superconducting transition, respectively. The origin of the

high normal state ρ in CaF₂ sample would be the electron/magnetic scattering, which will be discussed later. T_c of the films on CaF₂, BaF₂, MgO and LSAT are 19, 25, 19 and 21 K, respectively. It should be noted that T_c of the film on BaF₂ exhibited higher than that of single crystal ($T_c = 22$ K) and slightly higher than maximum T_c of the Ba122:Co films (24.5 K) reported in Ref 19. In addition, the film on CaF₂ exhibited upturn like behavior at $T^{\text{upturn}} \sim 80$ K (see the vertical arrow in Fig. 3a), similar to that of (Ba_{1-x}RE_x)Fe₂As₂ ($RE = \text{La, Ce, Pr, Nd}$)^{28,29}. To examine the magnetic properties, magnetoresistance ($MR = 100 \times [\rho(H) - \rho(0)] / \rho(0)$) is measured in all films. Different from a BaFe₂As₂:Co single crystal³⁰, the film on CaF₂ exhibits negative MR [Figure 3 (c)] in contrast to the other samples which exhibit weak positive MR similar to that observed in a single crystal [Supplemental figure 2]. In addition, the film on CaF₂ exhibit anomalous behavior also in ρ_{xy} . Figure 3 (d) show ρ_{xy} as a function of the magnetic field and temperature for the film on CaF₂. At lower temperature than T^{upturn} , ρ_{xy} rapidly increase to the positive value in low magnetic field region (± 0.3 T). As reported previously³¹, anomalous Hall effects (AHE) of a BaFe₂As₂:Co film are observed caused by magnetic impurities³² and/or intrinsic properties of the electron doped BaFe₂As₂ [La doped BaFe₂As₂ also exhibits AHE around low magnetic field²⁸ but the isovalent doped BaFe₂As₂ (Phosphorous-doped BaFe₂As₂) does not exhibit AHE (Supplemental Figure 4)]. However, these AHE is continuously suppressed with decreasing temperature in contrast to AHE in BaFe₂As₂:Co. Therefore, the large enhancement of AHE in BaFe₂As₂:Co thin film on CaF₂ is totally different from those. Summarizing the unique properties of the BaFe₂As₂:Co thin film on CaF₂, it exhibits (i) upturn like behavior in $\rho - T$ curve, (ii) negative MR and (iii) large enhancement of AHE in lower than T^{upturn} . These results imply that BaFe₂As₂:Co thin film on CaF₂

would have another magnetic fluctuation or ordering.

4.3.4. Electrical transport properties under high pressures

Next, high pressure effects were examined using piston-cylinder-type high pressure cell. Figure 4 (b) and (c) show the $\rho - T$ curves of BaFe₂As₂:Co thin films on MgO and LSAT, respectively. In the case of films on oxide substrates, normal state ρ and T_c continuously decrease ~ 4 K from that in ambient pressure with increasing external pressures up to ~ 3 GPa. These trend are also observed in K and P optimally and over-doped BaFe₂As₂ system under high pressures^{13,14} but they are different from that of La-doped BaFe₂As₂²⁸.

As shown in Figure 3 (a), BaFe₂As₂:Co thin films on CaF₂ exhibits upturn like behavior unlike those on other substrates. Figure 5 show $\rho - T$ curves under high pressure of BaFe₂As₂:Co thin films on CaF₂. Applying the pressure, upturn like behavior is suppressed and it completely diminishes at 3.3GPa (Fig. 5(a)). The upturn like behavior of $\rho - T$ can be explained by electron scattering which caused either by carrier localization with disorder scattering^{33,34}. Thus, these results indicate that the pressure suppresses electron scattering in the BaFe₂As₂:Co thin film on CaF₂. In this experiment, all of the films include small amount of non-oriented Fe and/or Fe-Co alloy particles in the matrix of film³⁵. The amount of impurities and the crystalline qualities are almost the same among all of the films. Therefore, the electron scattering cannot be explained by extrinsic effects such as magnetic impurities and crystallinities of the films. Inset of figure 5 (b) shows the pressure dependence of MR at 30 K. MR under high pressure exhibited almost the same trend as that in ambient pressure [Fig. 3(c)]. These results indicate that the external pressure does not work to suppress the magnetic

ordering. As a results, the upturn behavior of BaFe₂As₂:Co thin films on CaF₂ does not originate from its magnetic scattering and would be caused by carrier localization. In fact, the carrier density increases with applying high pressure as we mentioned below.

In contrast to the other samples, T_c of the film on BaF₂ increased under high pressure up to 3.4 GPa [Figure 6] from 25 to 27 K at 3.4 GPa. $T_c(P) - T_c(0)$ is higher than that of a single crystal under high pressures¹¹ i.e. is this maximum T_c is highest in optimally doped Ba122:Co. ΔT_c is almost same among all pressure region, which means there is no inhomogeneity of the pressure and increase of T_c is clearly originated from pressure unlike bulk experiments which shows broadening of superconducting transitions¹¹. This result show the opposite direction of predicted one from the experiments of thermal expansion measurements ($dT_c/dP_{\text{hydrostatic}} = -0.9$ K) [F. Hardy et al., PRL 102, 187004 (2009)].

4.4. Discussion

Figure 7 (a) and (b) summarizes the changes in T_c under high pressures. T_c of the films on CaF₂, MgO, and LSAT continuously decreased but that on CaF₂ shows the gentler decay against the pressure compared with those of MgO and LSAT. Consequently, only T_c of the film on BaF₂ increased. Figure 7 (b) show the relationship between the α_P of substrates and $T_c(3\text{GPa}) - T_c(0)$. The α_P of LSAT is not reported, to our knowledge, but we can easily speculate that it is close to oxide substrates such as STO and LAO (the α_P of SrTiO₃ is $5.67 \cdot 10^{-3}$ GPa³⁶ and that of LaAlO₃ is $5.65 \cdot 10^{-3}$ GPa)³⁷. Thus, we plot it as $\alpha_P(\text{LSAT}) = 5.6 \cdot 10^{-3}$ GPa in Fig. 6 (c). It is noteworthy that $T_c(3\text{GPa}) - T_c(0)$ is proportional to the α_P of substrates. As shown in Fig 1. the crystal structure of the thin film is strongly affected by the structural changes of the substrates.

In fact, that is strongly affected by thermal expansion of substrate in temperature variation. Therefore, the differences in the α_P of substrates make the anisotropic pressure in pressure variation as we proposed in Fig. 1 and it is proved that this concept is very powerful technique for inducing anisotropic pressures. This results is also consistent with the Ehrenfest relationship ($dT_c/dP_a = + 3.1$ K/GPa, $dT_c/dP_c = - 7.1$ K/GPa. P_a : pressure along a-axis, P_c : pressure along c-axis) ¹⁵.

However, what is the dominant parameter to determine the T_c in BaFe₂As₂? This is the long-time-unresolved problem, especially the relationship between the carrier density and structure because of the difficulties of the Hall measurements under high pressure. To discuss the dominant parameters of superconductivity of BaFe₂As₂, we also examined the Hall effects of BaFe₂As₂:Co thin films on BaF₂, CaF₂ and MgO under high pressure. Figures 8 (a) – (c) show the results of ρ_{xy} as a function of the magnetic field at 30 K. The slopes of ρ_{xy} decrease with increasing the pressure in all films. These results indicate carrier density of BaFe₂As₂:Co thin films increase with increasing the pressure. Figure 8 (d) – (f) show the temperature dependence of R_H . As mentioned before, normal state ρ of the films on CaF₂ is much higher than those of others [Fig. 3(a)] and its ρ_{xy} show the enhancement of AHE at low temperature. Therefore, the R_H of BaFe₂As₂:Co thin films on CaF₂ is determined using linear region under high magnetic field. $|R_H|$ of all the films increase with decreasing the temperature but they decrease with increasing the pressure at low temperature. To examine the relationship between T_c and carrier density, T_c is plotted as a function of R_H in Figure 8 (d). In the case of single crystal of BaFe₂As₂:Co, clear correlation between T_c and R_H is reported as shown in Figure 8 (e) ³⁸. However, there is no significant correlation between R_H and T_c in BaFe₂As₂:Co films [Fig.8 (d)]. The region from $R_H = - 2.0$ to $- 1.0$ corresponds to the

over-doped region in BaFe₂As₂:Co single-crystal. According to the small MR of the films on MgO and BaF₂ and LSAT in supplemental Fig. 3, these films are speculated to belong in the optimal – over-doped region. However, T_c of the film on BaF₂ increased regardless of the increase in R_H (i.e., carrier density). These results indicate that the carrier density is not dominant parameter determining T_c in BaFe₂As₂:Co films and difference in the local structure induced by anisotropic pressures is a possible origin of increase/decrease in T_c .

4.5. Conclusion

In summary, we proposed the concept to induce the anisotropic pressure utilizing the differences of α_T and the α_P between BaFe₂As₂:Co and substrates with epitaxial strain. Affected from substrates, as-grown films have the strained structures. According to the results of HT-XRD, it is clearly shown that the crystal structures of thin films are affected by the change of structure of substrates. BaFe₂As₂:Co epitaxial films on CaF₂ exhibit unique properties such as (i) upturn like behavior in $\rho - T$ curve, (ii) negative MR and (iii) large enhancement of AHE. According to the results of high pressure experiments, $T_c(3\text{GPa}) - T_c(0)$ is proportional to the α_P of substrates and T_c of BaFe₂As₂:Co thin films on BaF₂ largely increased compared with the single-crystal. This would be the reason why strongest anisotropic pressure is applied to the film. These results are also consistent with the Ehrenfest relationship derived from thermal expansion and heat capacity measurements. The Hall effects of BaFe₂As₂:Co thin films also examined to discuss the dominant parameters of superconductivity but there is no significant relationship between R_H and T_c . These results indicate that the carrier density is not dominant parameter determining T_c in BaFe₂As₂:Co and the local structure of

BaFe₂As₂:Co would control the increase/decrease of T_c .

References

- ¹ Y. Kamihara, T. Watanabe, M. Hirano, and H. Hosono, *J. Am. Chem. Soc.* **130**, 3296 (2008).
- ² H. Takahashi, K. Igawa, K. Arii, Y. Kamihara, M. Hirano, and H. Hosono, *Nature* **453**, 376 (2008).
- ³ A.S. Sefat, *Rep. Prog. Phys.* **74**, 124502 (2011).
- ⁴ S. Medvedev, T.M. McQueen, I.A. Troyan, T. Palasyuk, M.I. Erements, R.J. Cava, S. Naghavi, F. Casper, V. Ksenofontov, G. Wortmann, and C. Felser, *Nat. Mater.* **8**, 630 (2009).
- ⁵ S. Iimura, S. Matsuishi, H. Sato, T. Hanna, Y. Muraba, S.W. Kim, J.E. Kim, M. Takata, and H. Hosono, *Nat. Commun.* **3**, 943 (2012).
- ⁶ R. Zhi-An, L. Wei, Y. Jie, Y. Wei, S. Xiao-Li, Zheng-Cai, C. Guang-Can, D. Xiao-Li, S. Li-Ling, Zhou Fang, and Z. Zhong-Xian, *Chin. Phys. Lett.* **25**, 2215 (2008).
- ⁷ T. Hanna, Y. Muraba, S. Matsuishi, N. Igawa, K. Kodama, S. Shamoto, and H. Hosono, *Phys. Rev. B* **84**, 024521 (2011).
- ⁸ K. Tanabe and H. Hosono, *Jpn. J. Appl. Phys.* **51**, 010005 (2012).
- ⁹ J. Paglione and R.L. Greene, *Nat. Phys.* **6**, 645 (2010).
- ¹⁰ T. Yamazaki, N. Takeshita, R. Kobayashi, H. Fukazawa, Y. Kohori, K. Kihou, C.-H. Lee, H. Kito, A. Iyo, and H. Eisaki, *Phys. Rev. B* **81**, 224511 (2010).
- ¹¹ K. Ahilan, F.L. Ning, T. Imai, A.S. Sefat, M.A. McGuire, B.C. Sales, and D. Mandrus, *Phys. Rev. B* **79**, 214520 (2009).
- ¹² S. Drotziger, P. Schweiss, K. Grube, T. Wolf, P. Adelmann, C. Meingast, and H. v. Löhneysen, *J. Phys. Soc. Jpn.* **79**, 124705 (2010).
- ¹³ L. E. Klintberg, S. K. Goh, S. Kasahara, Y. Nakai, K. Ishida, M. Sutherland, T. Shibauchi, Y. Matsuda, and T. Terashima, *J. Phys. Soc. Jpn.* **79**, 123706 (2010).
- ¹⁴ M.S. Torikachvili, S.L. Bud'ko, N. Ni, and P.C. Canfield, *Phys. Rev. B* **78**, 104527 (2008).
- ¹⁵ F. Hardy, P. Adelmann, T. Wolf, H. v. Löhneysen, and C. Meingast, *Phys. Rev. Lett.* **102**, 187004 (2009).
- ¹⁶ F. Ishikawa, N. Eguchi, M. Kodama, K. Fujimaki, M. Einaga, A. Ohmura, A. Nakayama, A. Mitsuda, and Y. Yamada, *Phys. Rev. B* **79**, 172506 (2009).

- ¹⁷ H. Sato and M. Naito, *Phys. C Supercond.* **274**, 221 (1997).
- ¹⁸ J.-P. Locquet, J. Perret, J. Fompeyrine, E. Mächler, J.W. Seo, and G. Van Tendeloo, *Nature* **394**, 453 (1998).
- ¹⁹ K. Iida, J. Hänisch, R. Hühne, F. Kurth, M. Kidszun, S. Haindl, J. Werner, L. Schultz, and B. Holzapfel, *Appl. Phys. Lett.* **95**, 192501 (2009).
- ²⁰ F. Kurth, E. Reich, J. Hänisch, A. Ichinose, I. Tsukada, R. Hühne, S. Trommler, J. Engelmann, L. Schultz, B. Holzapfel, and K. Iida, *Appl. Phys. Lett.* **102**, 142601 (2013).
- ²¹ A.S. Sefat, R. Jin, M.A. McGuire, B.C. Sales, D.J. Singh, and D. Mandrus, *Phys. Rev. Lett.* **101**, 117004 (2008).
- ²² T. Katase, H. Hiramatsu, T. Kamiya, and H. Hosono, *Appl. Phys. Express* **3**, 063101 (2010).
- ²³ T. Katase, H. Hiramatsu, T. Kamiya, and H. Hosono, *Supercond. Sci. Technol.* **25**, 084015 (2012).
- ²⁴ K. Murata, K. Yokogawa, H. Yoshino, S. Klotz, P. Munsch, A. Irizawa, M. Nishiyama, K. Iizuka, T. Nanba, T. Okada, Y. Shiraga, and S. Aoyama, *Rev. Sci. Instrum.* **79**, 085101 (2008).
- ²⁵ I. Tsukada, M. Hanawa, T. Akiike, F. Nabeshima, Y. Imai, A. Ichinose, S. Komiya, T. Hikage, T. Kawaguchi, H. Ikuta, and A. Maeda, *Appl. Phys. Express* **4**, 053101 (2011).
- ²⁶ H. Hiramatsu, H. Sato, T. Katase, T. Kamiya, and H. Hosono, *Appl. Phys. Lett.* **104**, 172602 (2014).
- ²⁷ M.S. da Luz, J.J. Neumeier, R.K. Bollinger, A.S. Sefat, M.A. McGuire, R. Jin, B.C. Sales, and D. Mandrus, *Phys. Rev. B* **79**, 214505 (2009).
- ²⁸ T. Katase, S. Iimura, H. Hiramatsu, T. Kamiya, and H. Hosono, *Phys. Rev. B* **85**, 140516 (2012).
- ²⁹ T. Katase, H. Hiramatsu, T. Kamiya, and H. Hosono, *New J. Phys.* **15**, 073019 (2013).
- ³⁰ H.-H. Kuo, J.-H. Chu, S.C. Riggs, L. Yu, P.L. McMahon, K. De Greve, Y. Yamamoto, J.G. Analytis, and I.R. Fisher, *Phys. Rev. B* **84**, 054540 (2011).
- ³¹ S. Mohan, T. Taen, H. Yagyuda, Y. Nakajima, T. Tamegai, T. Katase, H. Hiramatsu, and H. Hosono, *Supercond. Sci. Technol.* **23**, 105016 (2010).
- ³² Y. Shiomi, Y. Onose, and Y. Tokura, *Phys. Rev. B* **79**, 100404 (2009).
- ³³ P.A. Lee and T.V. Ramakrishnan, *Rev. Mod. Phys.* **57**, 287 (1985).
- ³⁴ H. Alloul, J. Bobroff, M. Gabay, and P.J. Hirschfeld, *Rev. Mod. Phys.* **81**, 45 (2009).

³⁵ H. Sato, H. Hiramatsu, T. Kamiya, and H. Hosono, *Appl. Phys. Lett.* **104**, 182603 (2014).

³⁶ R.O. Bell and G. Rupprecht, *Phys. Rev.* **129**, 90 (1963).

³⁷ J. Zhao, N.L. Ross, and R.J. Angel, *J. Phys. Condens. Matter* **16**, 8763 (2004).

³⁸ L. Fang, H. Luo, P. Cheng, Z. Wang, Y. Jia, G. Mu, B. Shen, I.I. Mazin, L. Shan, C. Ren, and H.-H. Wen, *Phys. Rev. B* **80**, 140508 (2009).

Table 4 - 1. The structural and physical parameters of single-crystal substrates. Lattice mismatches of oxide substrates (MgO and LSAT) and those of fluoride substrates (BaF₂ and CaF₂) are calculated by $(a^{\text{Sub.}} - a^{\text{Ba122:Co}}) / a^{\text{Ba122:Co}}$ and $(a^{\text{Sub.}/\sqrt{2}} - a^{\text{Ba122:Co}}) / a^{\text{Ba122:Co}}$, respectively.

Substrate	BaF ₂	MgO	LSAT	CaF ₂
Lattice parameter at 300 K (Å)	6.196	4.21	3.87	5.46
	4.38 ($a/\sqrt{2}$)			3.86 ($a/\sqrt{2}$)
Lattice mismatch with Ba122:Co (%)	+10.5	+6.21	-2.37	-2.62
α_P (10^{-3} GPa^{-1})	17.6	6.50	5.68	11.6
α_T ($10^{-6}/\text{K}$)	18.3	10.3	8.2	18.9

Table 4 - 2 . Thermal expansion coefficients α_T of BaFe₂As₂:Co films obtained from Fig. 2(c). The α_T of single crystal is taken from ref**[M. S. da Luz et al., PRB 79, 214505(2009)]

Substrate	BaF ₂	MgO	Single crystal	LSAT	CaF ₂
α_T of substrate	18.3	10.3	—	8.2	18.9
α_{T_a} at 300 K ($10^{-6}/\text{K}$)	17.0	10.2	8.21	7.56	18.9
α_{T_c} at 300 K ($10^{-6}/\text{K}$)	19.8	26.9	24.6	29.9	15.5

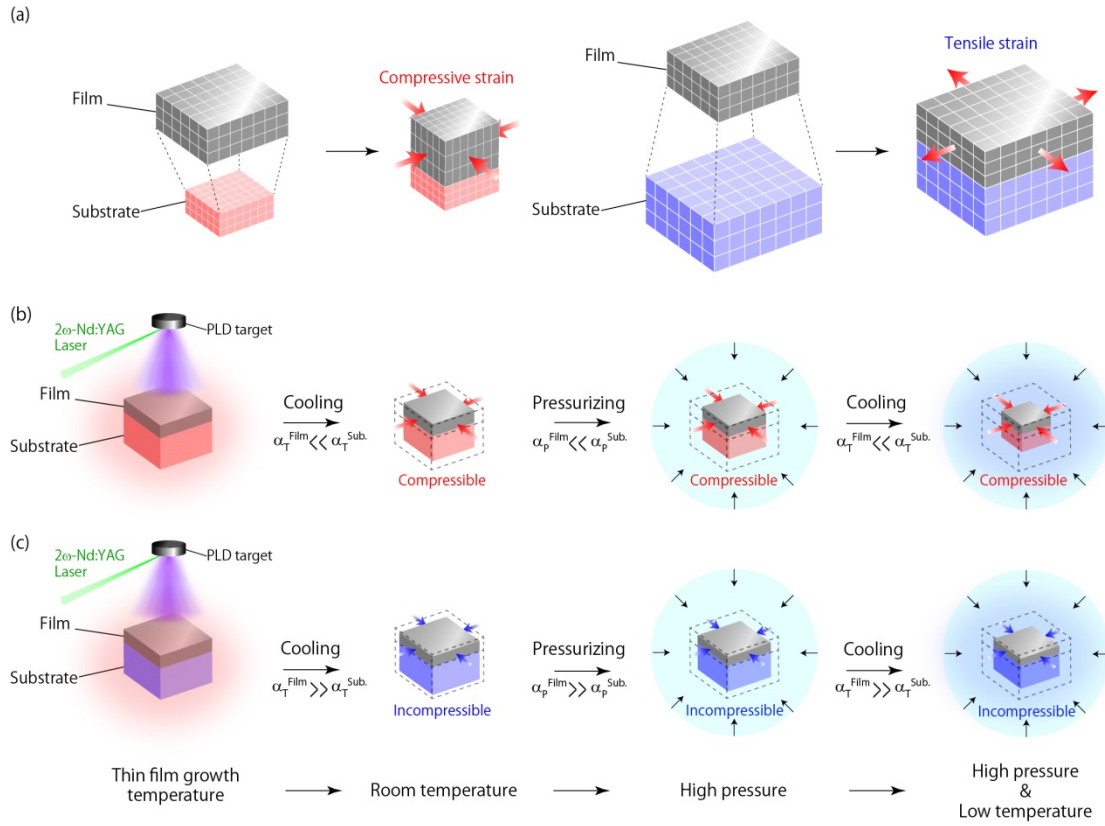


Fig. 1. Strain engineering utilizing heterointerface. (a) Epitaxial strain is induced by the lattice mismatch between film and substrate. When the lateral lattice parameter of film (a^{Film}) is larger than that of substrate ($a^{\text{Sub.}}$), the compressive strain induced (Right figure). On the other hand, tensile strain is induced in the case of $a^{\text{Film}} < a^{\text{Sub.}}$ (Left figure). In addition, the anisotropic pressure induced by the variation of environment because of the differences of thermal expansion coefficient (α_T) and compressibility (α_p) in heterointerface. When the substrate has larger α_T and α_p than those of the film, the lateral compressive strain induced by cooling and pressurizing process is more compressible than that in bulk (b). On the other hand, that is more incompressible than that in bulk when the substrate has smaller α_T and α_p than those of the film (c).

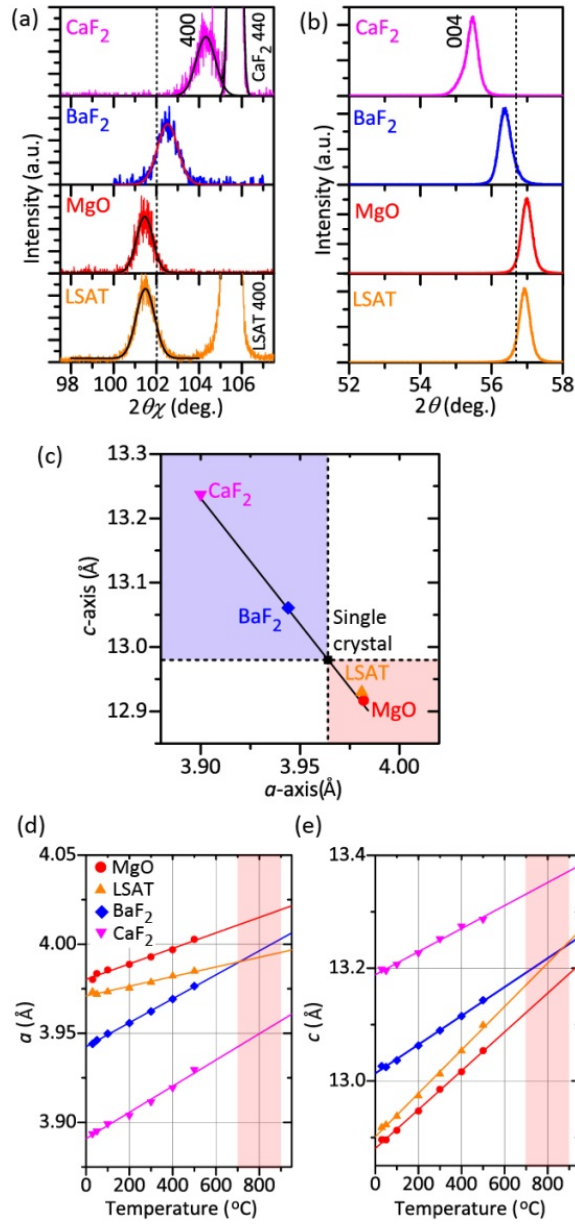


Fig. 2. XRD patterns and structural parameters of BaFe₂As₂:Co thin films on oxide and fluoride single-crystal substrates. (a) In-plane ϕ -coupled $2\theta_\chi$ patterns around 400 diffractions at room temperature. Solid lines are results of deconvolution. (b) Out-of-plan ω -coupled 2θ patterns around 004 diffractions at room temperature. (c) Summary of lattice parameters calculated from (a) and (b). Vertical dotted lines in (a) – (b) indicates the peak position of a single crystal taken from ref ** [A. S. Sefat et al., PRL (2008)]. Upper left shaded area indicates a -axis is compressed and c -axis is expanded. Lower right shaded area indicates a -axis expanded and c -axis is compressed. (d, e) Temperature dependence of lattice parameters of the films. The shaded temperature regions correspond to the epitaxial growth windows. Solid lines are fitted lines from RT to 500 °C as the guide to the eye.

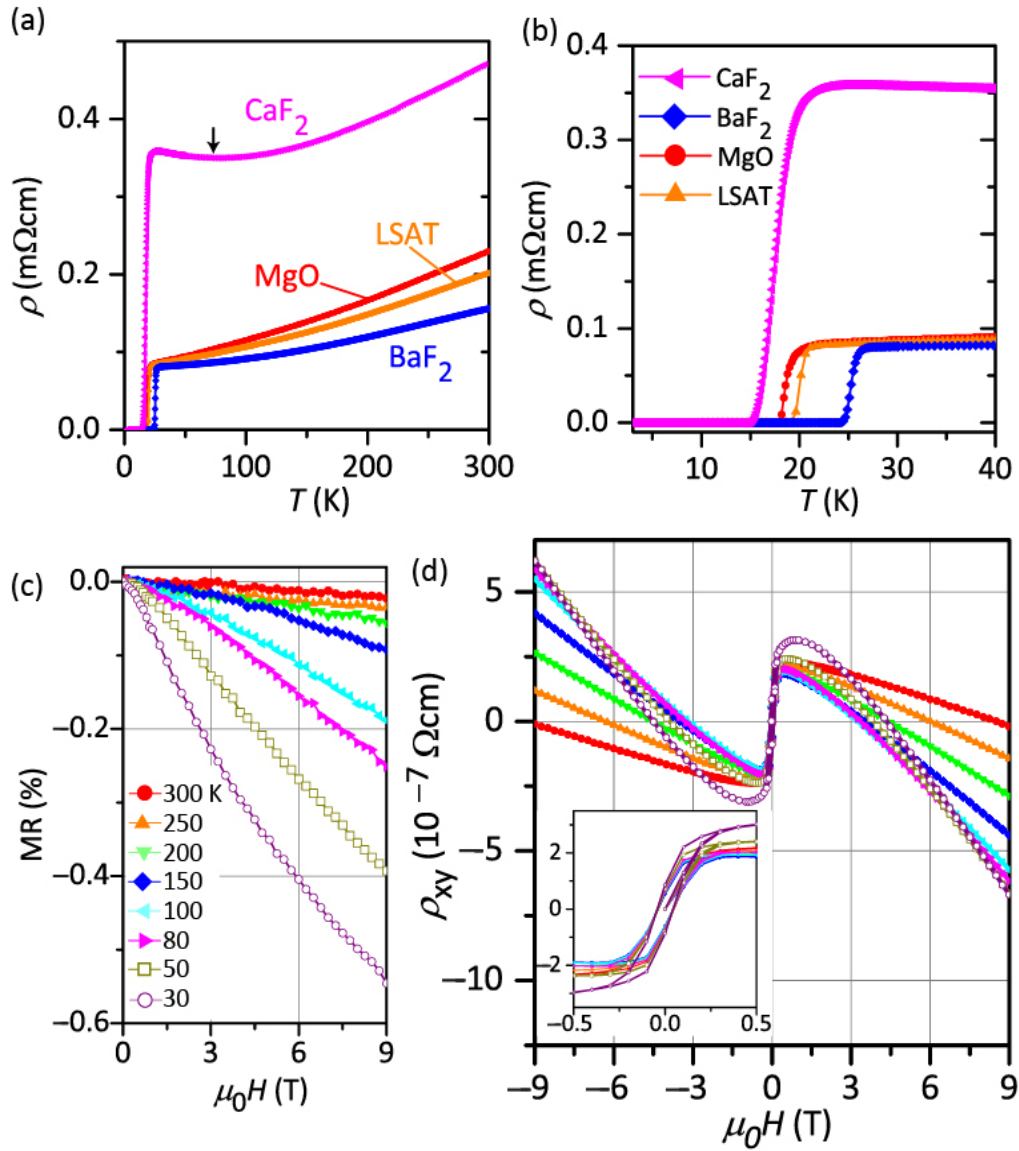


Fig. 3. Transport properties of $\text{BaFe}_2\text{As}_2:\text{Co}$ thin films under ambient pressure. (a) $\rho - T$ curves. The vertical arrow indicates T^{upturn} in the film on CaF_2 . (b) Magnified figure of (a) around superconducting transition. (c) Magnetoresistance MR as a function of the magnetic field for the film on CaF_2 . (d) Hall resistivity as a function of the magnetic field and temperature for the film on CaF_2 . Inset of figure (d) shows the magnified figure in low magnetic field region. The symbols are the same as those in (c).

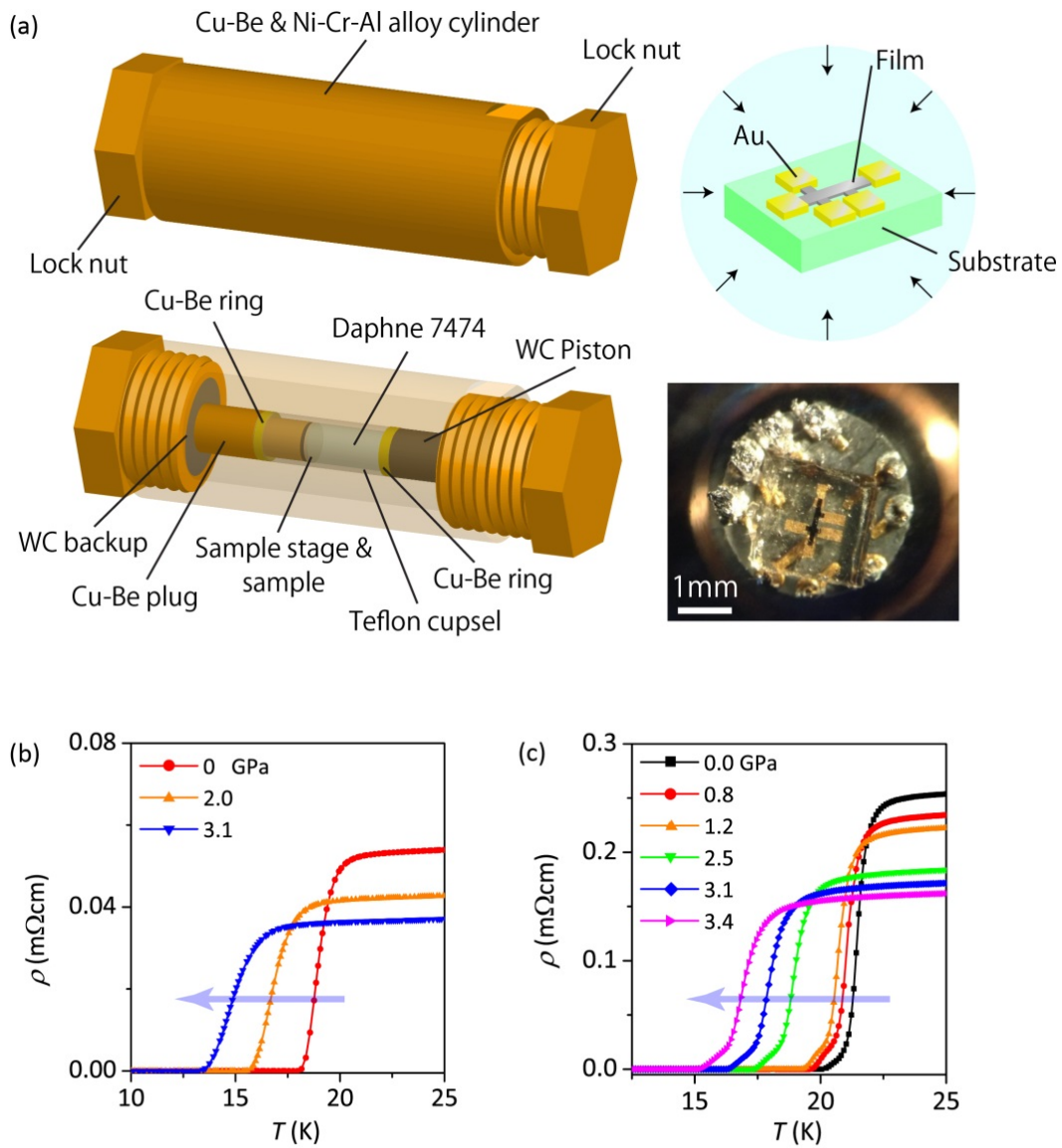


Fig. 4. Temperature dependence of resistivity of BaFe₂As₂:Co thin films on oxide substrates under high pressure. (a) Schematic images of piston-cylinder type high pressure cell (left panels) and sample images and picture (right panels). Thin films are patterned as Hall bar and mounted on the Cu-Be plug with Sn manometer. (b) Temperature dependence of resistivity of the film on MgO, (c) the film on LSAT.

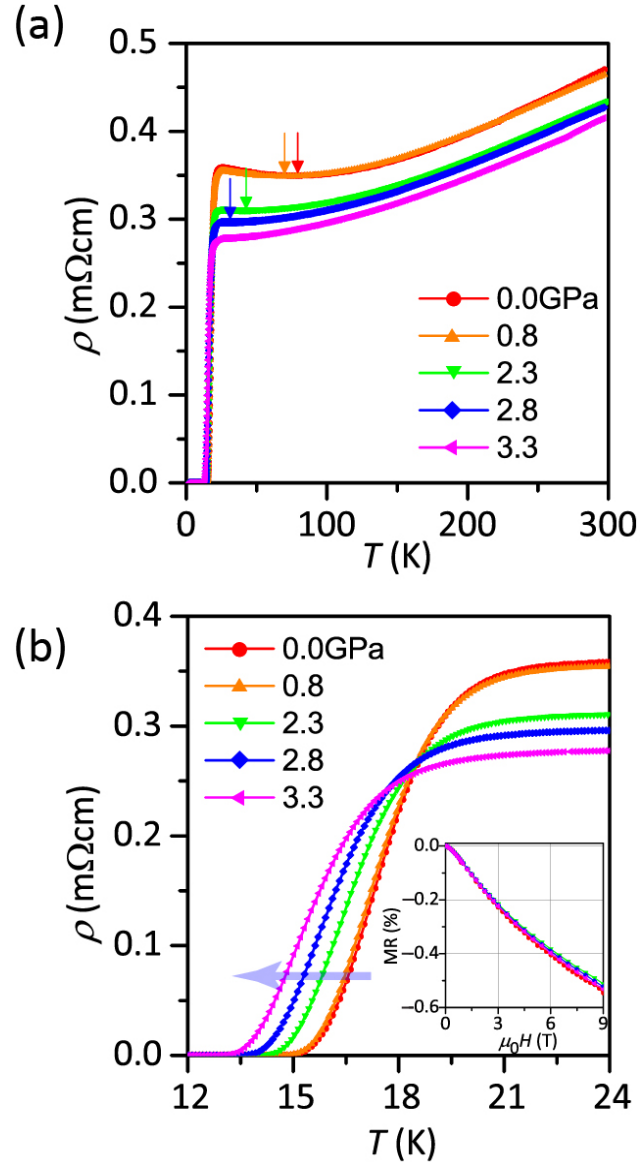


Fig. 5. Temperature dependence of resistivity under high pressure of BaFe₂As₂:Co thin films on CaF₂. Vertical arrows in (a) indicate T^{upturn} . Inset of (b) is magnetic field dependence of magnetoresistance MR under high pressures up to 3.3 GPa at 30 K

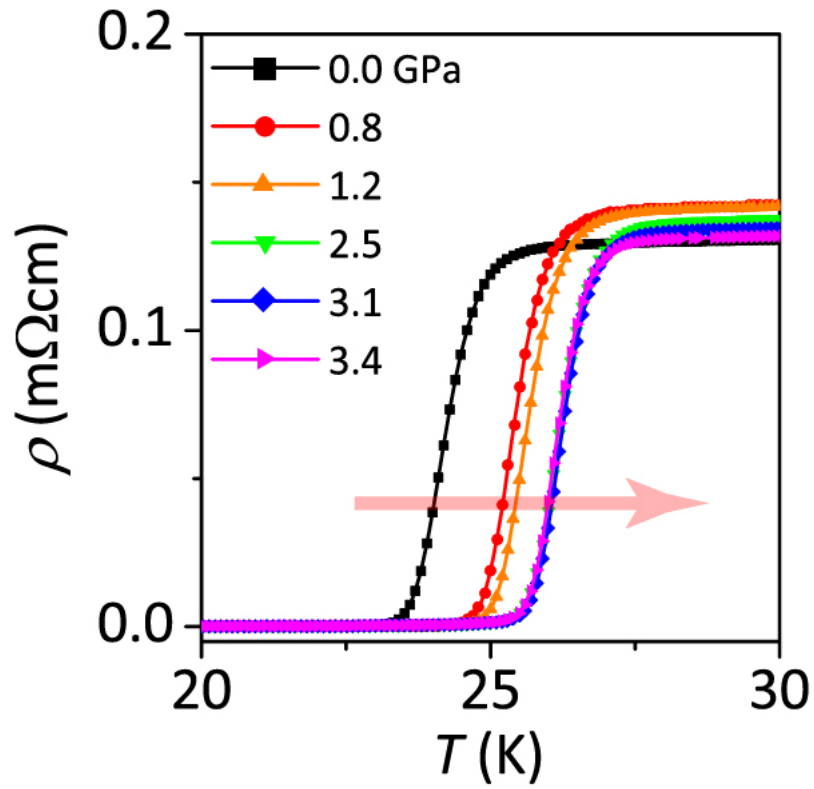


Fig. 6. Temperature dependence of resistivity under high pressure of Ba122:Co thin films on BaF₂

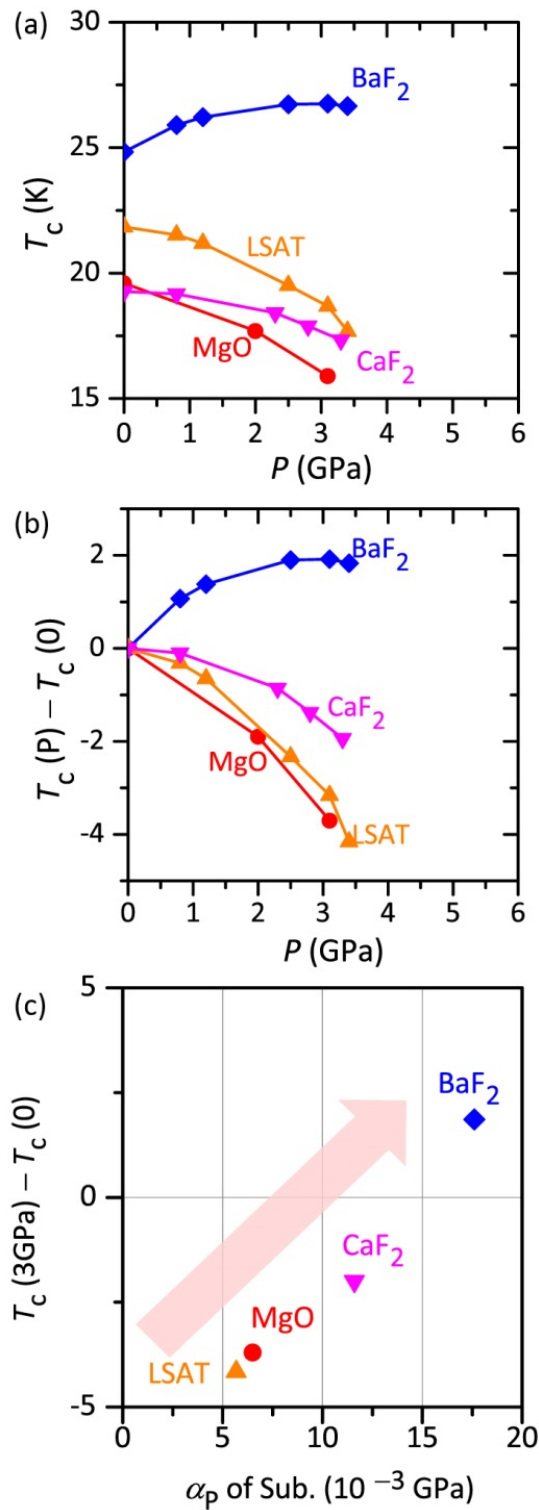


Fig. 7. Summary of the pressure effects on superconducting properties of Ba122:Co films. (a) pressure dependence of T_c . (b) The difference of T_c as a function of the pressure. (c) The difference of T_c as a function of the compressibility of substrate. In this figure, we use α_p of STO as that of LSAT.

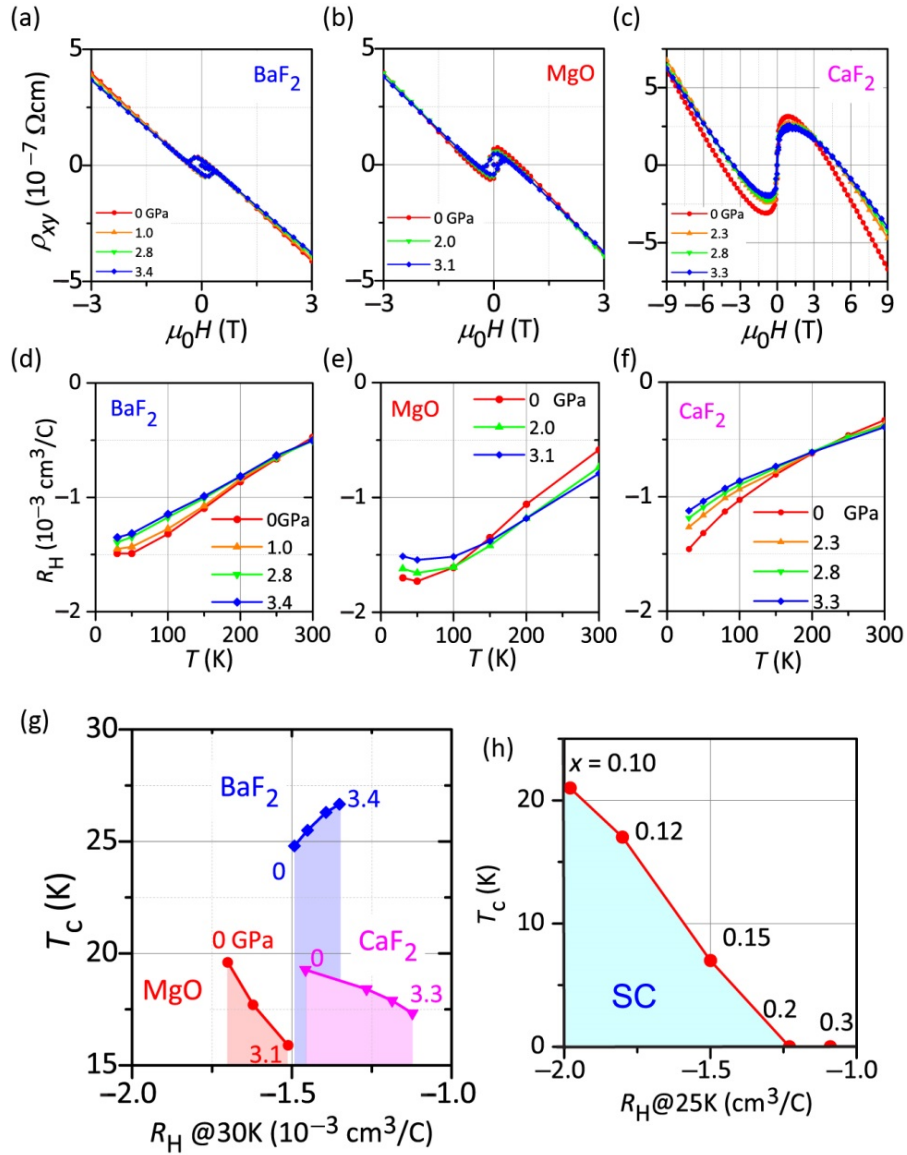
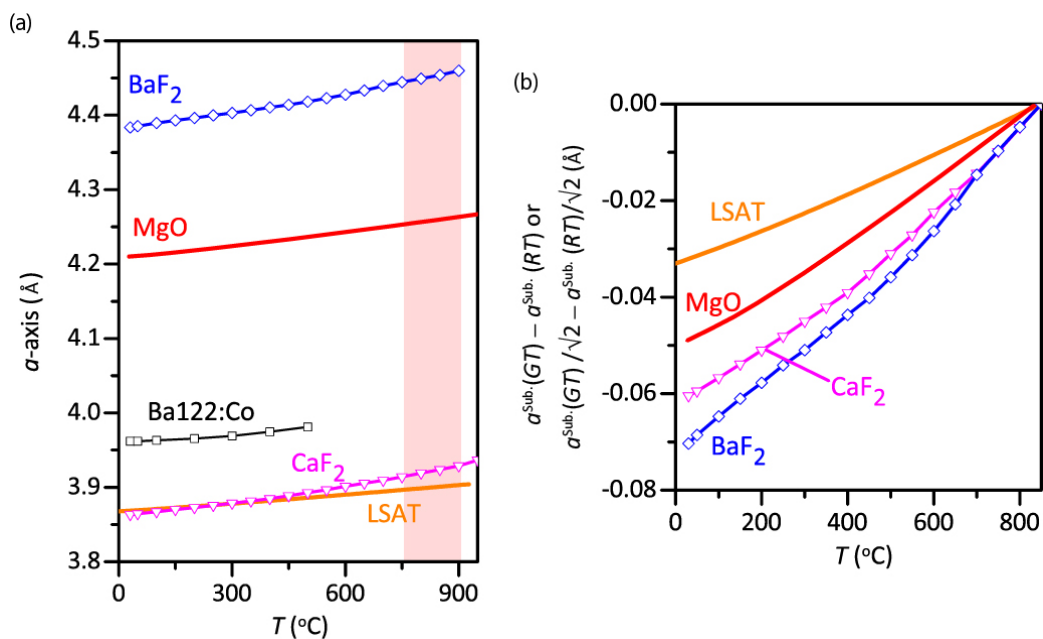


Fig. 8. Hall effect measurements of BaFe₂As₂:Co thin films on BaF₂, MgO and CaF₂ under the high pressure. (a) – (c) Hall resistivity (ρ_{xy}) as a function of the magnetic field. (d) – (f) Temperature dependence of the Hall coefficient (R_H). (g) The relationship between T_c and R_H at 30K. The shaded areas correspond to the superconducting region. (h) Relationship between T_c and R_H in the case of BaFe₂As₂:Co single crystal at 25 K. All of data is taken from ref [L. Fang et al., Phys. Rev. B 80, 140508(R) (2009)]. In this figure only R_H value of $x = 0.10$ is observed at 30K, not 25 K.

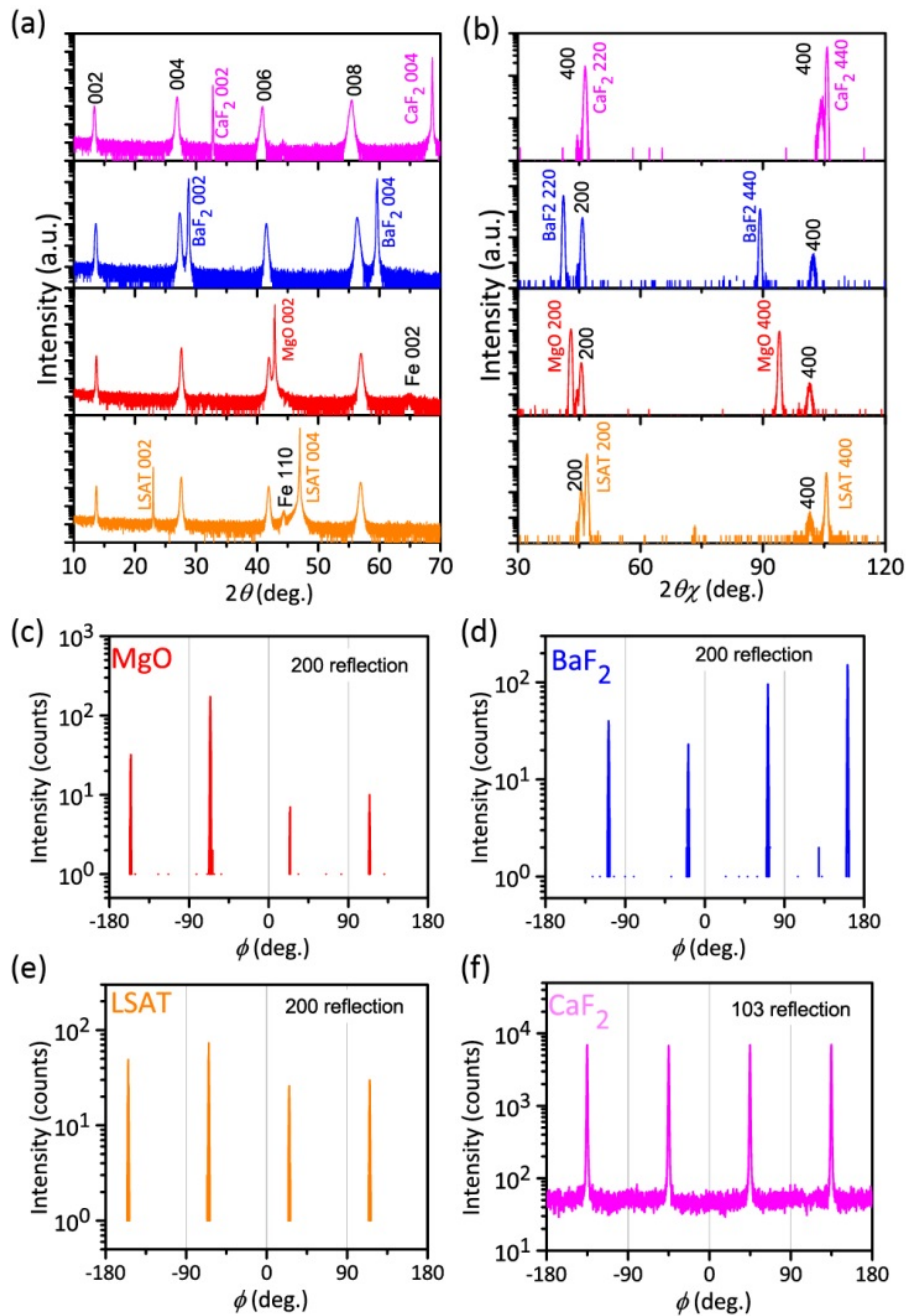
Supplemental information

Supplimental Table 1. The structural and physical parameters of single-crystal substrates and Ba122:Co. Lattice mismatches of oxide substrates (MgO and LSAT) and those of fluoride substrates (BaF₂ and CaF₂) are calculated by $(a^{\text{Sub.}} - a^{\text{Ba122:Co}}) / a^{\text{Ba122:Co}}$ and $(a^{\text{Sub.}/\sqrt{2}} - a^{\text{Ba122:Co}}) / a^{\text{Ba122:Co}}$, respectively. Here, GT, RT and LT are growth temperature (~1123 K), room temperature (~300 K) and low temperature. $a(P)$ and $a/\sqrt{2}(P)$ are simplistically calculated by $a(P) = a(0\text{GPa}) \times (1 + \alpha_P \times P)$.

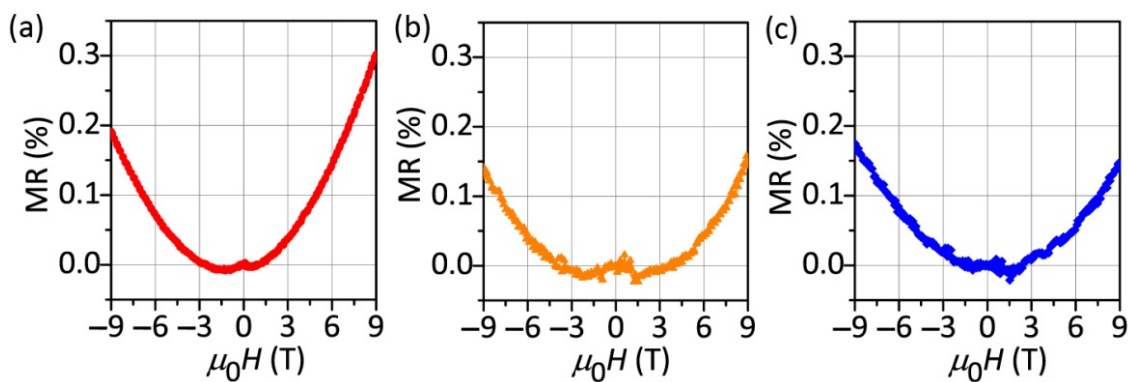
Substrate	BaF ₂	MgO	Ba122:Co	LSAT	CaF ₂
Structural parameters at RT					
α_T at RT ($10^{-6}/\text{K}$)	18.3	10.3	8.21(α_T^{ab})	8.2	18.9
$a(\text{RT})$ or $a/\sqrt{2}(\text{RT})$ (Å)	6.196	4.210	3.964	3.868	5.4527
	4.38 ($a/\sqrt{2}$)				3.856 ($a/\sqrt{2}$)
Lattice mismatch with Ba122:Co (%)	10.5	6.21	—	-2.42	-2.62
Epitaxial strain direction	Tensile	Tensile	—	Compressive	Compressive
Structural parameters at GT					
Lattice parameter at GT (Å)	4.47	4.26	—	3.90	3.94
Epitaxial strain at GT	Tensile	Tensile	—	Compressive	Compressive
Cooling process (GT→RT)					
α_T at GT ($10^{-6}/\text{K}$)	25.6	15.5	—	10.8	27
$a(\text{GT}) - a(\text{RT})$ (Å) or $a/\sqrt{2}(\text{GT}) - a/\sqrt{2}(\text{RT})$ (Å)	-0.071	-0.049	—	-0.032	-0.060
Pressurizing process					
α_P at RT (10^{-3}GPa^{-1})	17.6	6.5	15 (anisotropic)	5.68	11.6
$a(3\text{GPa}) - a(0\text{GPa})$ or $a/\sqrt{2}(3\text{GPa}) - a/\sqrt{2}(0\text{GPa})$ (Å)	-0.079	-0.028	-0.044	-0.022	-0.045
In-plane pressure effect	Compressible	Incompressible	—	Incompressible	Compressible
Cooling process (RT→LT)					
α_T at RT ($10^{-6}/\text{K}$)	18.3	10.3	8.21(α_T^{ab})	8.2	18.9
$a(\text{LT}) - a(\text{RT})$ or $a/\sqrt{2}(\text{LT}) - a/\sqrt{2}(\text{RT})$ (Å)	-0.0150 (at 30K)	-0.007 (at 77K)	-0.0063 (at 30 K)	-0.0055 (at 15K)	-0.0125 (at 6K)
thermal expansion strain	Compressible	Compressible	—	Incompressible	Compressible



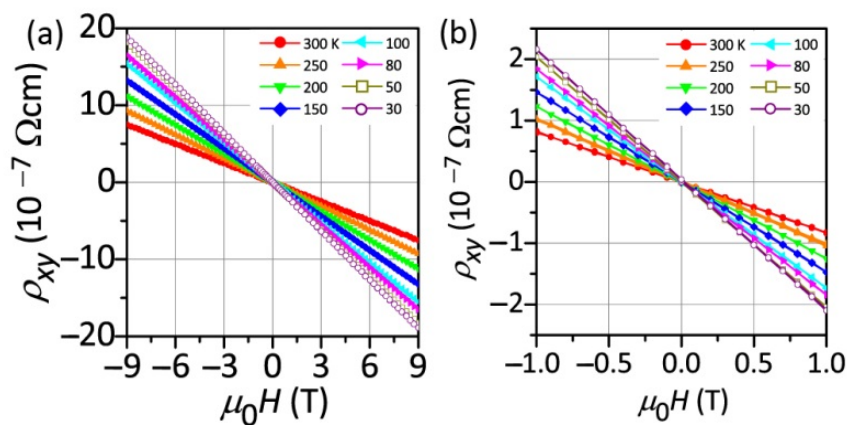
Supplemental Figure 1. (a) Temperature dependence of lattice parameters of the substrates and bulk Ba122:Co. (b) the variation of lattice parameters of substrates ($a^{\text{Sub.}}$ or $a^{\text{Sub.}}/\sqrt{2}$) when the temperature change from growth temperature (GT) to room temperature (RT)



Supplemental Figure 2. HR-XRD data of BaFe₂As₂:Co thin films. Wide range scan data of BaFe₂As₂:Co thin films show the clear 00l diffractions in out-of-plane (a) and *h*00 diffractions in in-plane (b) with small peak of non-oriented Fe and/or Fe-Co alloy particles. According to the tetragonal lattice of BaFe₂As₂:Co, clear four-fold symmetric peaks are observed in φ scan (c – f). BaFe₂As₂:Co on CaF₂ has very close *a*-axis value; therefore 103 reflection is used to confirm the four-fold symmetry of tetragonal lattice.



Supplemental Figure 3. Magnetoresistance MR as a function of the magnetic field for BaFe₂As₂:Co thin film on MgO (a), LSAT (b) and BaF₂ (c). the asymmetry of MR is caused by effects of Hall resistivity because those MR signal are small and they are same order as Hall resistivity.



Supplemental Figure 4. (a) Hall resistivity of BaFe₂(As,P)₂ as a function of magnetic field and temperature. (b) Magnified images around low magnetic field.

Chapter 5: Unusual pressure effects on the superconductivity of indirectly electron-doped (Ba_{1-x}La_x)Fe₂As₂ epitaxial films

5.1. Introduction

Since the first report on an iron-based superconductor,¹ it has been recognized that applying external pressure is one of the predominant ways to enhance the superconducting critical temperature (T_c).^{2,3} An iron pnictide BaFe₂As₂ has a layered crystal structure composed of alternating stacks of alkaline earth ($A = \text{Ba, Sr, and Ca}$) and FeAs layers, called a “122-type structure,” as shown in Figure 5 - 1. Undoped BaFe₂As₂ is an antiferromagnetic metal and does not exhibit a superconducting transition under an ambient pressure.⁴ However, it exhibits superconductivity with a T_c up to 34 K by applying external pressures of 1–3 GPa,^{5,6} along with suppression of the antiferromagnetism. This crystal structure has two major doping sites that can induce superconductivity under an ambient pressure. Substitution with a different transition metal at the Fe site is called “direct doping” and substitution with a different ion at the A or As site is called “indirect doping.” This is because the Fermi level is mainly formed of Fe 3d orbitals. So far, pressure effects on the superconductivity of BaFe₂As₂ single crystals have been examined for Co doping (direct electron doping at the Fe sites),⁷ K doping (indirect hole doping at the Ba sites),^{8–10} and P doping (indirect isovalent doping at the As sites)¹¹ for wide ranges of doping concentrations. For the series of Co-, K-, and P-doped BaFe₂As₂ crystals, the T_c was only enhanced in the underdoped regions and never in the optimally doped and overdoped regions. This result is consistent with experimental results, showing that an external pressure significantly affected the

superconductivity in the underdoped regions. It had very little effect in the overdoped region where the magnetic instability was completely suppressed.¹²

Indirect doping in 122-type AFe₂As₂ was reported with only hole doping (K at the A sites) and isovalent doping (P at the As sites), but not with electron doping, and the T_c was limited to 38 K.¹³ More recently, high T_c values up to 49 K (Ref. 14) were demonstrated in indirectly electron-doped [rare earth (R) metals at the A sites] 122-type CaFe₂As₂ single crystals grown using a flux method.¹⁵ The reported T_c is the highest among the 122-type AFe₂As₂ series. On the other hand, we recently succeeded in indirect R - (electron) doping ($R = \text{La-Nd}$) at the Ba sites in 122-type BaFe₂As₂ using a film growth process. This was thermodynamically unstable under an ambient pressure and demonstrated bulk superconductivity with a maximum $T_c = 22$ K with La doping.^{16,17} This unstable phase was stabilized using the highly nonequilibrium nature of the thin film growth via a vapor phase. The maximum T_c of the (Ba_{1-x}R_x)Fe₂As₂ films was much lower than that of the R -doped CaFe₂As₂ single crystals. According to the scenario of the above R -doped CaFe₂As₂ crystals (smaller R doping such as Pr led to a higher T_c), we expected that the external pressure would induce lattice shrinkage, similar to the R -doped CaFe₂As₂, and then enhance the T_c of the (Ba_{1-x}La_x)Fe₂As₂ epitaxial films.

In this study we have examined the pressure effects up to 3.5 GPa on the superconductivity of indirectly electron-doped 122-type (Ba_{1-x}La_x)Fe₂As₂ epitaxial films with a wide range of x values from the underdoped ($x = 0.08$) to the heavily overdoped regions ($x = 0.30$). This is different from the previously reported results on other doped modes of the 122-type AFe₂As₂. The (Ba_{1-x}La_x)Fe₂As₂ films exhibited a large enhancement of the T_c , as well as narrowing of the transition width, in the wide

doping region from the underdoped to the optimally doped and overdoped regions. This distinct characteristic is discussed in relation to the changes in the electron transport properties.

5.2. Experimental procedure

5.2.1. Thin film fabrication and patterning of the films

Here, 200-nm-thick epitaxial films of (Ba_{1-x}La_x)Fe₂As₂ with $x = 0.08, 0.09, 0.13, 0.18, 0.21,$ and 0.30 were prepared on MgO (001) single-crystal substrates by pulsed laser deposition. Details on the procedures and sample quality are reported in Ref. 16. Each film was patterned in a six-terminal Hall-bar structure using photolithography and Ar ion milling, followed by the formation of Au electrode pads using sputtering and a lift-off process.

5.2.2. Electrical transport measurements under high pressures

High-pressure experiments were performed using a piston-cylinder-type high-pressure cell. The Hall-bar samples were introduced into a Teflon cell together with a liquid-pressure-transmitting medium (Daphne oil 7474), which solidifies at 3.7 GPa at room temperature.¹⁸ Thus, hydrostatic external pressures of 0–3.5 GPa were applied in this study. The pressure in the cell was calibrated using the measured T_c of 99.99 % pure Sn wires, located in the vicinity of the sample. A Cernox thermometer, attached to the body of the cell, was used to determine the sample temperature (T). The electrical resistivity ρ (ρ_{xx}) and Hall resistivity ρ_{xy} were measured using the four-probe technique. The electrical current flowed along the a axis in the film plane. Magnetic fields up to 9 T were applied parallel to the c axis, normal to the film plane. After the

pressure was released we confirmed that the T_c , ρ_{xx} , and ρ_{xy} recovered the initial ambient state, guaranteeing no pressure-induced degradation of the films.

5.3. Results and discussion

5.3.1. Electron transport properties under ambient pressure

Before showing the results of high pressure effects, the electron transport properties of (Ba_{1-x}La_x)Fe₂As₂ epitaxial films are characterized at ambient pressure. Electronic phase diagram of (Ba_{1-x}La_x)Fe₂As₂ epitaxial films summarized in Figure 5 - 2 (a) using the data from Ref ¹⁶. In this study, we investigated the whole range of doping concentration from under- to over doping. For a quantitative discussion of the mobile carrier density under ambient pressure and high pressure, we should assess whether we can apply the Hall effect relation $N_e = 1/(e \times |R_H|)$ (where R_H is Hall coefficient, N_e is the mobile carrier density and e is the elementary electric charge) to BaFe₂As₂ because BaFe₂As₂ has a complex Fermi surface composed of three hole bands and two electron bands. In the case of directly electron-doped (Co-doped) BaFe₂As₂, it has been reported that the hole contribution to the carrier transport was negligible and the above relation provides reasonable N_e at low T in most of the doping regions.¹⁹ In Figure 5 - 2 (b), we measured R_H at $P = 0$ GPa and estimated the values of N_e per Fe site (N_e/Fe) using the equation $N_e/Fe = 1/(e \times |R_H|) / V/4$, where V is the unit cell volume containing four Fe atoms for (Ba_{1-x}La_x)Fe₂As₂ epitaxial films. Figure 5 - 2 (c) shows that the normalized N_e/Fe [plotting against $x/2$ for (Ba_{1-x}La_x)Fe₂As₂ and x for Ba(Fe_{1-x}Co_x)₂As₂ (Ref. ²⁰)] follows the same relationship between the directly Co-doped and the indirectly La-doped BaFe₂As₂. This result supports the idea that the same conclusion can be applied also for (Ba_{1-x}La_x)Fe₂As₂. Therefore, we directly estimated N_e as $1/(e \times |R_H|)$.

5.3.2. Electron transport properties under high pressures

Figure 5 - 3 (a) shows the ρ - T curves of the optimally doped (Ba_{0.87}La_{0.13})Fe₂As₂ epitaxial film measured under external pressures up to $P = 3.2$ GPa. The ρ at the normal state monotonically decreased and the T_c shifted toward higher T as P increased. The ρ - T_c curves in the wide T range up to 200 K are explained well with a simple linear law of $\rho^{\text{fit}} = AT^n + \rho_0$ with the exponent $n = 1$, where ρ_0 is the residual resistivity [see the solid straight lines for the fitting results in Figure 5 - 3 (a)]. For $P = 0$ GPa, the ρ - T_c curve followed the linear relation well into the high- T region, but deviated, showing an upturn at T lower than $T_{\text{min}} = 120$ K [the solid triangle of the ρ - T curve at 0 GPa in Figure 5 - 3 (a)]. With an increase in P the deviations from the linear relations became smaller and the T_{min} shifted to lower T . The upturn in ρ is attributed to electron scattering by the La dopants, as recently discussed in Ref. 17. Compared with the results of indirectly Co-doped films, which do not exhibit any resistivity upturn, the amount of the Fe impurity phase and the crystalline qualities are almost the same in both the La- and Co-doped films.^{16,21} Therefore, the electron scattering cannot be explained by external effects such as Fe impurity and different crystalline qualities. In addition, the La-doped film did not show any magnetoresistance, which implies that the electron scattering with the La dopants cannot be explained by magnetic scattering and should be attributed to disordering of the charges at the (Ba,La) sites.¹⁷ This result indicates that the electron scattering was significantly suppressed by applying P . This will be further discussed below. The P dependences of the onset of T_c [$T_c^{\text{onset}}(P)$] and the superconducting transition width [$\Delta T_c(P)$] (defined by $\Delta T_c = T_c^{\text{onset}} - T_c^{\text{zero}}$) are summarized in Figure 5 - 3 (b) and (c), respectively. The T_c^{onset} was extremely sensitive

to P and increased from 22.6 to 30.3K at 2.8 GPa, leveling off at $P = 3.2$ GPa. I also confirmed that when a magnetic field was applied at $P = 3.2$ GPa, the superconducting transition became broader and T_c decreased, further supporting the superconductivity [Figure 5 - 3 (d)]. With an increase in P , the ΔT_c also narrowed from 3.4 to 1.4K, along with the enhancement of T_c . It should be noted that all the data previously reported on Co-, K-, and P-doped BaFe₂As₂ crystals⁷⁻¹² indicated that T_c large enhancement was observed only in the underdoped region and never in the optimally doped region.

Figure 5 - 4 (a)–(e) and Figure 5 - 5 (a)–(e) show the ρ - T curves for the underdoped ($x = 0.08$ and 0.09), the overdoped ($x = 0.18$ and 0.21), and the heavily overdoped ($x = 0.30$) epitaxial films under various pressures in the wider T range and magnified range around T_c . Upon applying P , the normal-state ρ for both the underdoped and the overdoped films decreased and all of their T_c^{onset} shifted to higher T . On the other hand, although the heavily overdoped film also exhibited a decrease in ρ , it did not transit to a superconducting phase for P up to 3.5 GPa. Figure 5 - 5 (f) summarizes the pressure effects on $T_c^{\text{onset}}(P)$ for the underdoped and the overdoped films and the inset represents the change in $\Delta T_c(P)$. For the underdoped film with $x = 0.08$, a clear saturation of T_c^{onset} was not observed up to 3.4 GPa, while the films with a higher x exhibited saturation of the T_c^{onset} at $P \sim 3$ GPa. Since the film with $x = 0.08$ showed a resistivity anomaly at $P = 0$ GPa in Figure 5 - 4 (a), caused by the coexistence of the magnetic order, the suppression of the resistivity anomaly with pressure contributed to the enhancement of T_c in the higher P region over 3 GPa via suppression of the magnetic order and reduction of electron scattering.

Figure 5 - 6 (a) outlines the electronic phase diagram plotting the maximum T_c^{onset} (T_c^{max}) under high pressures in comparison with the T_c^{onset} at $P = 0$ GPa. The

superconducting dome became larger with a higher T_c^{onset} upon application of a higher P . It should be noted that an increase in T_c^{onset} with pressure was observed for all films. The highest enhancement factor [Figure 5 - 6 (b)], defined by $T_c(P)/T_c(0)$, was obtained for the underdoped film with $x = 0.08$ (2.7 at $P = 3.4$ GPa) and the lowest enhancement factor for the optimally doped film with $x = 0.13$ was 1.4 at 3.2 GPa. The larger enhancement for the underdoped film originated from the existence of a magnetic instability at $P = 0$ GPa. The $T_c(P)/T_c(0)$ value became smaller as x increased and was a minimum for the optimal value of $x = 0.13$. Almost the same $T_c(P)/T_c(0)$ values were obtained between the underdoped film with $x = 0.09$ and the overdoped film with $x = 0.21$. For the other 122-type BaFe₂As₂ crystals, such as those that were Co, K, and P doped,⁷⁻¹² the $T_c(P)/T_c(0)$ were nearly one or less than one [Figure 5 - 6 (b)]. Compared with the pressure phase diagrams of the other 122-type BaFe₂As₂ crystals [Figure 5 - 6 (c)], the widening of the phase diagram toward the higher T_c region under pressure over the whole doping region was a unique feature, observed only in the indirectly electron doped (Ba_{1-x}La_x)Fe₂As₂ epitaxial films among the 122-type AFe₂As₂. Here we should point out that, although the epitaxial films are affected by uniaxial pressures originating from epitaxial strain, differences of thermal expansion and compressibility as discussed in chapter 4, this is not essential for the present results. To discuss these effects, we examined the pressure effects on the T_c^{onset} for the optimally doped Ba(Fe_{1-x}Co_x)₂As₂ epitaxial films²¹ grown on MgO (001) single crystals (in chapter 4) and compared them with that of the (Ba_{1-x}La_x)Fe₂As₂ films. The former film had in-plane lattice mismatches (-6.2 ± 0.3 %) similar to those (-5.9 %) of the (Ba_{1-x}La_x)Fe₂As₂/MgO films. Irrespective of the large epitaxial strains, the T_c decreased and was not enhanced for both of the samples. Similarly, optimally doped (Ba_{1-x}K_x)Fe₂As₂ films exhibited a

pressure effect on the T_c^{onset} but it was quite small.²² These results suggest that the T_c enhancement in the (Ba_{1-x}La_x)Fe₂As₂ epitaxial films did not originate from anisotropic pressure from substrates but from the external hydrostatic pressure.

Figure 5 - 7 (a)–(c) show the T dependences of the R_H for the underdoped ($x = 0.08$), the optimally doped ($x = 0.13$), and the overdoped ($x = 0.21$) epitaxial films at different pressures. The R_H values were all negative and their absolute values ($|R_H|$) increased with decreasing T for all of the films. With an increasing P , the R_H values at high T were almost unchanged, while the $|R_H|$ values decreased at low T , giving a smaller T dependence under a higher P . This result implies that the P induced more mobile carriers at lower T . As we mentioned above, we directly estimated N_e as $1/(e \times |R_H|)$ for a quantitative discussion of the mobile carrier density. Pressure dependences of the N_e at 35 K is summarized in Figure 5 - 7 (d). N_e at 35 K gradually increased with P for all of the films. The relationships between the estimated N_e and T_c^{onset} for the three kinds of films from the underdoped to the overdoped regions are superimposed in the inset of Figure 5 - 7 (d). The $x = 0.21$ film exhibited a $T_c^{\text{onset}} - N_e$ curve that was very different from those of the other films. A universal relation such as a domelike single $T_c^{\text{onset}} - N_e$ relation was not observed. This trend implies that the T_c^{onset} of the (Ba_{1-x}La_x)Fe₂As₂ epitaxial films under a high pressure was not determined just by N_e . The estimated Hall mobilities (μ) were independent of pressure, shown in the insets of Figure 5 - 7 (a)–(c). These results indicate that P increases N_e but does not affect the mobility and does not disturb the carrier transport. This consideration is consistent with the indirect La doping at the Ba sites in BaFe₂As₂. I considered that the reduction of electron scattering and the increase in N_e induced by P would be a plausible origin for the T_c enhancement because a large enhancement of $T_{\text{onset}}T_c$ shows a good correlation with the suppression of the ρ

upturn [shown in Figure 5 - 3 (a) and Figure 5 - 4 (a)] and the increase in N_e at low T (shown in Figure 5 - 7).

5.4. Conclusion

In summary, we observed a unique pressure phase diagram in indirectly electron-doped 122-type (Ba_{1-x}La_x)Fe₂As₂ epitaxial films. The enhancement of T_c in all of the doping regions along with narrowing of ΔT_c was associated with the reduction of electron scattering and the increase in the carrier density caused by lattice shrinkage, which optimizes its crystal and electronic structure to achieve higher T_c and sharper ΔT_c in (Ba_{1-x}La_x)Fe₂As₂ films.

References

- ¹ Y. Kamihara, T. Watanabe, M. Hirano, and H. Hosono, *J. Am. Chem. Soc.* **130**, 3296 (2008).
- ² H. Takahashi, K. Igawa, K. Arii, Y. Kamihara, M. Hirano, and H. Hosono, *Nature* **453**, 376 (2008).
- ³ A.S. Sefat, *Rep. Prog. Phys.* **74**, 124502 (2011).
- ⁴ M. Rotter, M. Tegel, D. Johrendt, I. Schellenberg, W. Hermes, and R. Pöttgen, *Phys. Rev. B* **78**, 020503 (2008).
- ⁵ F. Ishikawa, N. Eguchi, M. Kodama, K. Fujimaki, M. Einaga, A. Ohmura, A. Nakayama, A. Mitsuda, and Y. Yamada, *Phys. Rev. B* **79**, 172506 (2009).
- ⁶ A. Mani, N. Ghosh, S. Paulraj, A. Bharathi, and C.S. Sundar, *EPL Europhys. Lett.* **87**, 17004 (2009).
- ⁷ E. Colombier, M.S. Torikachvili, N. Ni, A. Thaler, S.L. Bud'ko, and P.C. Canfield, *Supercond. Sci. Technol.* **23**, 054003 (2010).
- ⁸ M.S. Torikachvili, S.L. Bud'ko, N. Ni, and P.C. Canfield, *Phys. Rev. B* **78**, 104527 (2008).
- ⁹ T. Yamazaki, N. Takeshita, K. Kondo, R. Kobayashi, Y. Yamada, H. Fukazawa, Y. Kohori, P.M. Shirage, K. Kihou, H. Kito, H. Eisaki, and A. Iyo, *J. Phys. Conf. Ser.* **215**, 012041 (2010).
- ¹⁰ E. Hassinger, G. Gredat, F. Valade, S.R. de Cotret, A. Juneau-Fecteau, J.-P. Reid, H. Kim, M.A. Tanatar, R. Prozorov, B. Shen, H.-H. Wen, N. Doiron-Leyraud, and L. Taillefer, *Phys. Rev. B* **86**, 140502 (2012).
- ¹¹ L. E. Klintberg, S. K. Goh, S. Kasahara, Y. Nakai, K. Ishida, M. Sutherland, T. Shibauchi, Y. Matsuda, and T. Terashima, *J. Phys. Soc. Jpn.* **79**, 123706 (2010).
- ¹² K. Ahilan, F.L. Ning, T. Imai, A.S. Sefat, M.A. McGuire, B.C. Sales, and D. Mandrus, *Phys. Rev. B* **79**, 214520 (2009).
- ¹³ M. Rotter, M. Tegel, and D. Johrendt, *Phys. Rev. Lett.* **101**, 107006 (2008).
- ¹⁴ B. Lv, L. Deng, M. Gooch, F. Wei, Y. Sun, J.K. Meen, Y.-Y. Xue, B. Lorenz, and C.-W. Chu, *Proc. Natl. Acad. Sci.* **108**, 15705 (2011).
- ¹⁵ S.R. Saha, N.P. Butch, T. Drye, J. Magill, S. Ziemak, K. Kirshenbaum, P.Y. Zavalij, J.W. Lynn, and J. Paglione, *Phys. Rev. B* **85**, 024525 (2012).
- ¹⁶ T. Katase, S. Iimura, H. Hiramatsu, T. Kamiya, and H. Hosono, *Phys. Rev. B* **85**, 140516 (2012).
- ¹⁷ T. Katase, H. Hiramatsu, T. Kamiya, and H. Hosono, *New J. Phys.* **15**, 073019 (2013).

- ¹⁸ K. Murata, K. Yokogawa, H. Yoshino, S. Klotz, P. Munsch, A. Irizawa, M. Nishiyama, K. Iizuka, T. Nanba, T. Okada, Y. Shiraga, and S. Aoyama, *Rev. Sci. Instrum.* **79**, 085101 (2008).
- ¹⁹ F. Rullier-Albenque, D. Colson, A. Forget, and H. Alloul, *Phys. Rev. Lett.* **103**, 057001 (2009).
- ²⁰ A. Olariu, F. Rullier-Albenque, D. Colson, and A. Forget, *Phys. Rev. B* **83**, 054518 (2011).
- ²¹ T. Katase, H. Hiramatsu, T. Kamiya, and H. Hosono, *Supercond. Sci. Technol.* **25**, 084015 (2012).
- ²² E. Park, N.H. Lee, W.N. Kang, and T. Park, *Appl. Phys. Lett.* **101**, 042601 (2012).

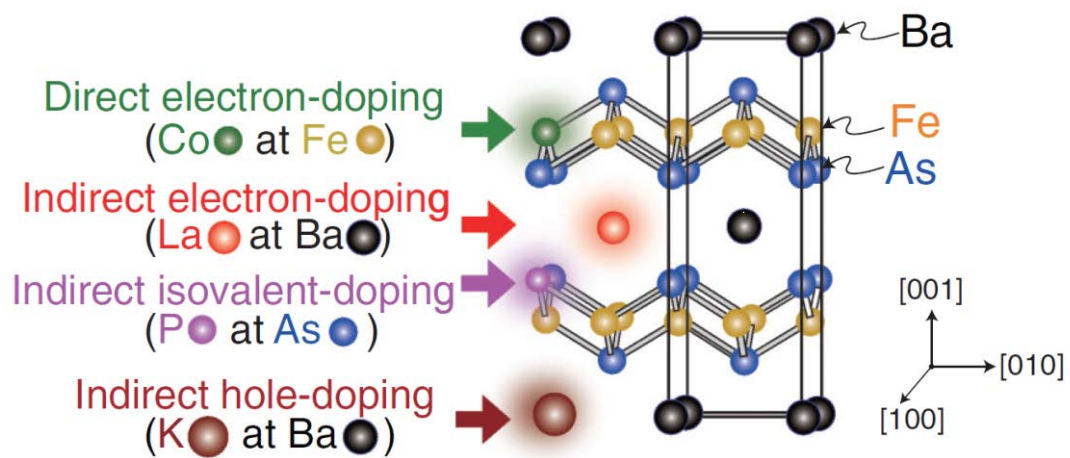


Figure 5 - 1. Crystal structure and doping modes of the layered 122-type BaFe_2As_2 . Solid lines show a unit cell. The doping sites that induce superconductivity are categorized into two modes. One is “indirect doping” for doping at sites other than the Fe sites, and the other is “direct doping” for doping at the Fe sites.

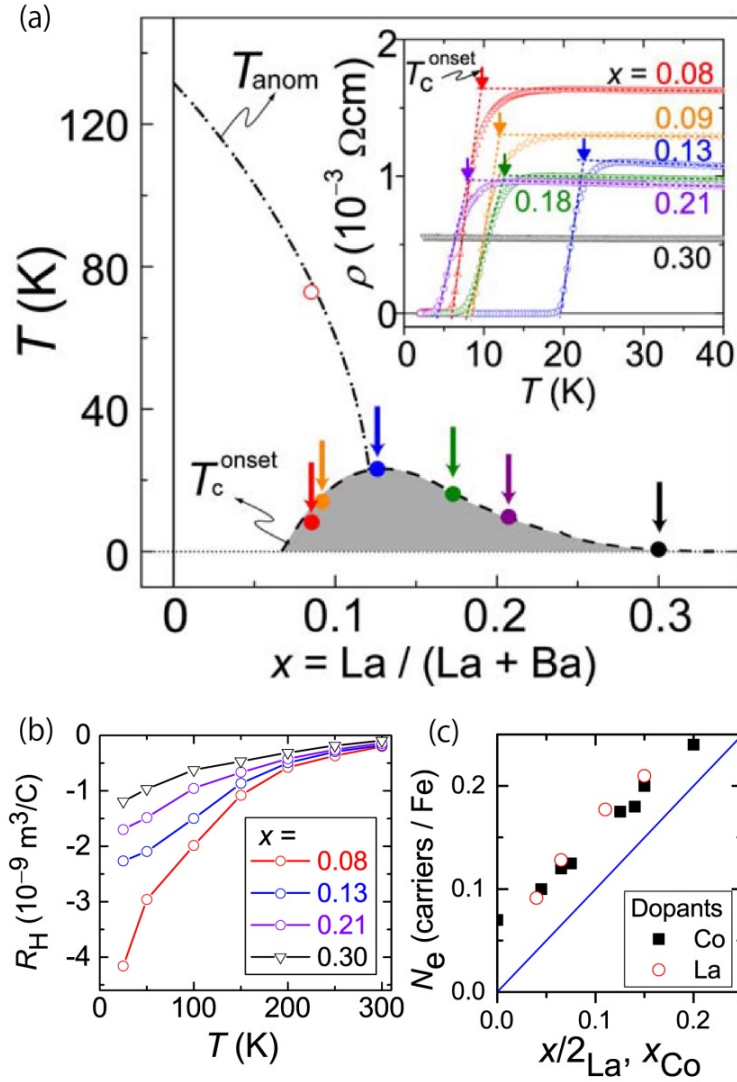


Figure 5 - 2 The electron transport properties of $(\text{Ba}_{1-x}\text{La}_x)\text{Fe}_2\text{As}_2$ epitaxial films at ambient pressure. (a) Electronic phase diagram of $(\text{Ba}_{1-x}\text{La}_x)\text{Fe}_2\text{As}_2$ epitaxial films under an ambient pressure. The arrows indicate the positions of the T_c^{onset} for the $(\text{Ba}_{1-x}\text{La}_x)\text{Fe}_2\text{As}_2$ epitaxial films with $x = 0.08, 0.09, 0.13, 0.18, 0.21,$ and 0.30 . The inset shows the ρ - T curves of these films. (b) Temperature dependence of the Hall coefficient R_H under an ambient pressure. The circles, diamonds, squares and triangles represent the R_H of $(\text{Ba}_{1-x}\text{La}_x)\text{Fe}_2\text{As}_2$ epitaxial films with $x = 0.08, 0.13, 0.21,$ and $0.30,$ respectively. (c) Doping concentration dependences of carrier density (N_e). The previously reported $N_e - x$ data for $\text{Ba}(\text{Fe}_{1-x}\text{Co}_x)_2\text{As}_2$ single crystals are superimposed.

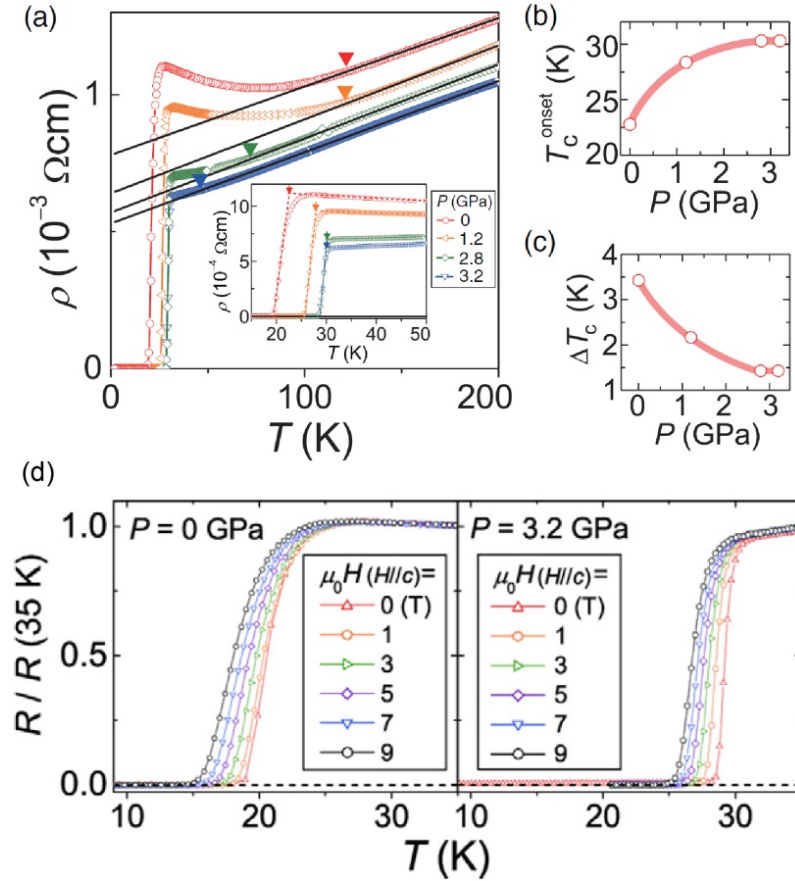


Figure 5 - 3 Pressure effects on the superconductivity of the optimally doped $(\text{Ba}_{0.87}\text{La}_{0.13})\text{Fe}_2\text{As}_2$ epitaxial films. (a) ρ - T curves were measured under various pressures from an ambient pressure up to $P = 3.2$ GPa. The solid lines are the fitting results to the power law, $\rho^{\text{fit}} = AT^n + \rho_0$, with $n = 1$. The solid triangles indicate the positions of T_{min} . An expanded view of the ρ - T curves at low $T \leq 50$ K is shown in the inset. The arrows indicate the positions of T_c^{onset} . Summary of the variation of (b) T_c^{onset} and (c) ΔT_c against pressure. (d) Magnetic field (H) dependence of the ρ - T curves for the optimally doped $(\text{Ba}_{0.87}\text{La}_{0.13})\text{Fe}_2\text{As}_2$ epitaxial film under an ambient pressure (left panel) and a high pressure of 3.2 GPa (right panel). Magnetic fields up to 9 T were applied parallel to the c -axis

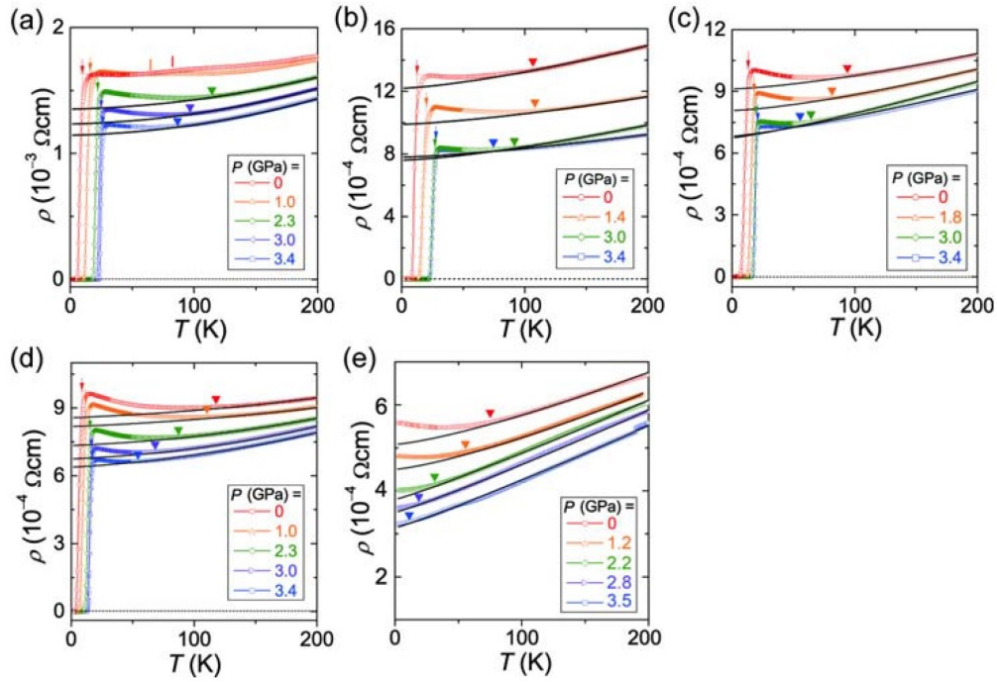


Figure 5 - 4 ρ - T curves measured under various pressures for $(\text{Ba}_{1-x}\text{La}_x)\text{Fe}_2\text{As}_2$ epitaxial films that are under-doped [(a) $x = 0.08$ and (b) 0.09], over-doped [(c) $x = 0.18$ and (d) 0.21], and heavily over-doped [(e) $x = 0.30$]. The arrows and the triangles indicate the positions of T_c^{onset} and T_{min} , respectively. The vertical lines in (a) indicate the positions of the resistivity anomaly temperature. The applied pressures are indicated in each panel. The expanded views near T_c are shown in Figure 5 - 5(a - e).

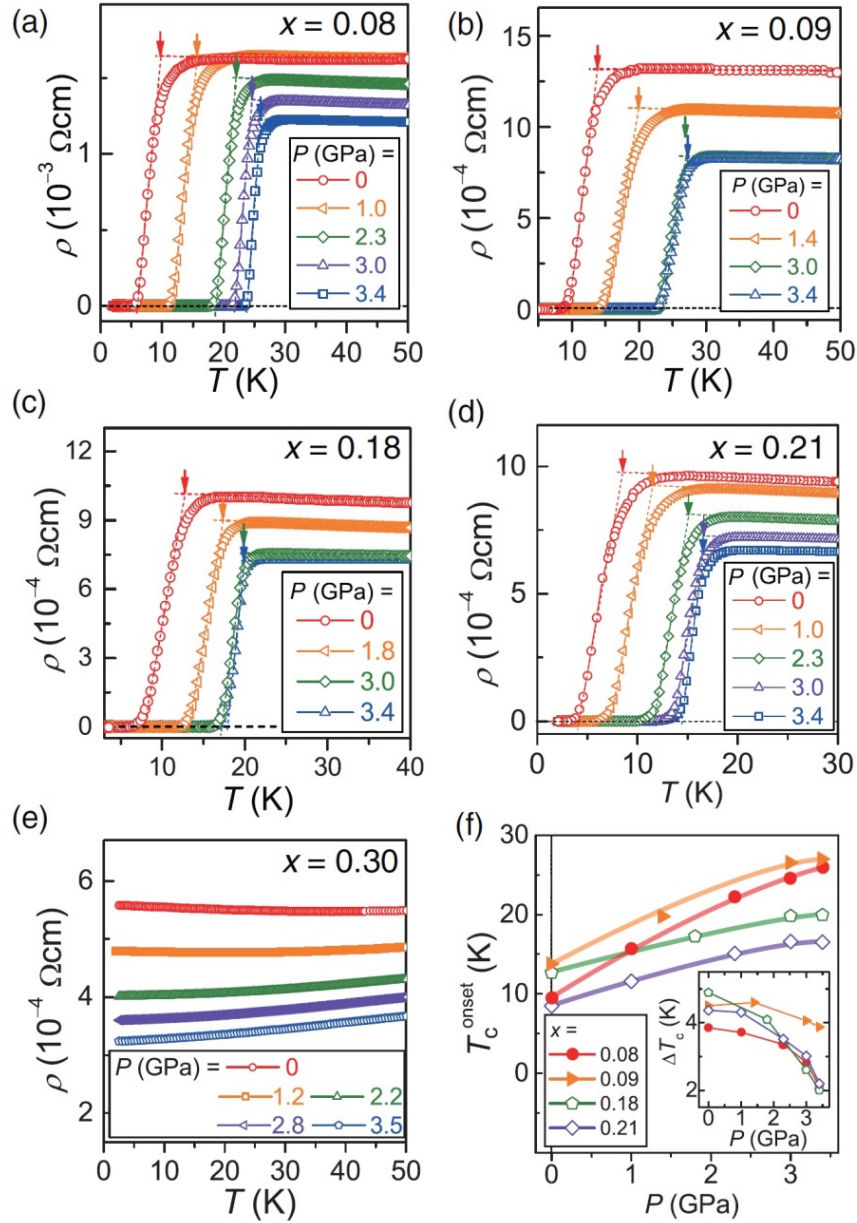


Figure 5 - 5 (a)–(e) ρ - T curves measured under various pressures for $(\text{Ba}_{1-x}\text{La}_x)\text{Fe}_2\text{As}_2$ epitaxial films that are underdoped [(a) $x = 0.08$ and (b) 0.09], overdoped [(c) $x = 0.18$ and (d) 0.21], and heavily overdoped [(e) $x = 0.30$]. The arrows indicate the positions of T_c^{onset} . The applied pressures are indicated in each panel. (f) Pressure dependences of T_c^{onset} [$T_c(P)$] for the underdoped and overdoped films. The inset shows the changes in ΔT_c [$\Delta T_c(P)$] as a function of P . Open and solid symbols represent $T_c(P)$ and $\Delta T_c(P)$ for underdoped and overdoped films, respectively.

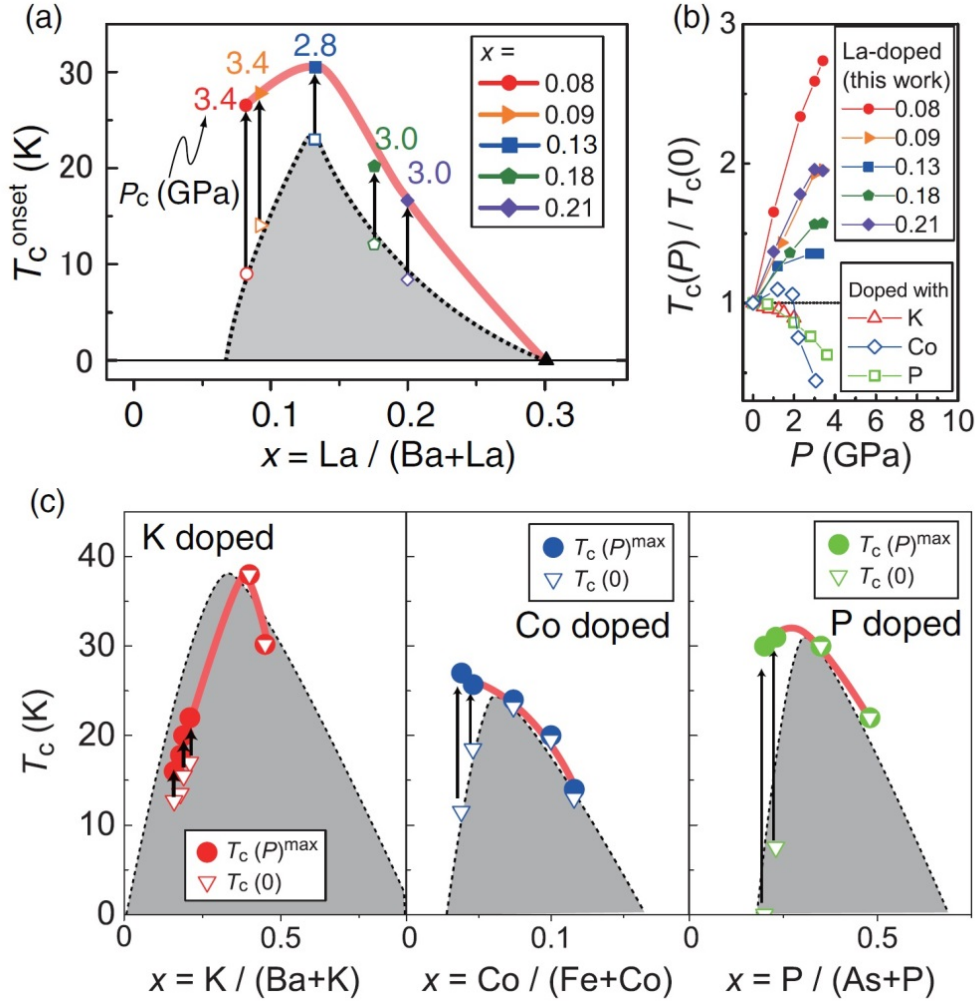


Figure 5 - 6 (a) High-pressure electronic phase diagram of $(\text{Ba}_{1-x}\text{La}_x)\text{Fe}_2\text{As}_2$ epitaxial films in comparison with that under an ambient pressure. Solid and open symbols show the maximum T_c^{onset} (T_c^{max}) obtained under high pressures and those under an ambient pressure, respectively. The critical pressures (P_c), where T_c^{max} was obtained, are indicated in the figure. (b) Enhancement factors defined by $T_c(P)/T_c(0)$ as a function of P for $(\text{Ba}_{1-x}\text{La}_x)\text{Fe}_2\text{As}_2$ epitaxial films. Those of the optimally, K(indirect hole)-, P (indirect isovalent)-, and Co (direct electron)-doped BaFe_2As_2 single crystals are shown for comparison (Refs. 7,8, and 11). (c) Pressure phase diagrams of $(\text{Ba}_{1-x}\text{K}_x)\text{Fe}_2\text{As}_2$ (indirect hole-doped), $\text{BaFe}_2(\text{As}_{1-x}\text{P}_x)_2$ (indirect isovalent-doped), and $\text{Ba}(\text{Fe}_{1-x}\text{Co}_x)_2\text{As}_2$ (direct electron-doped) single crystals (Refs. 7–11). Typical electronic phase diagrams under an ambient pressure are shown by the dark areas. Solid and open symbols indicate T_c^{max} under external pressures [$T_c(P)^{\text{max}}$] and T_c at 0 GPa, respectively.

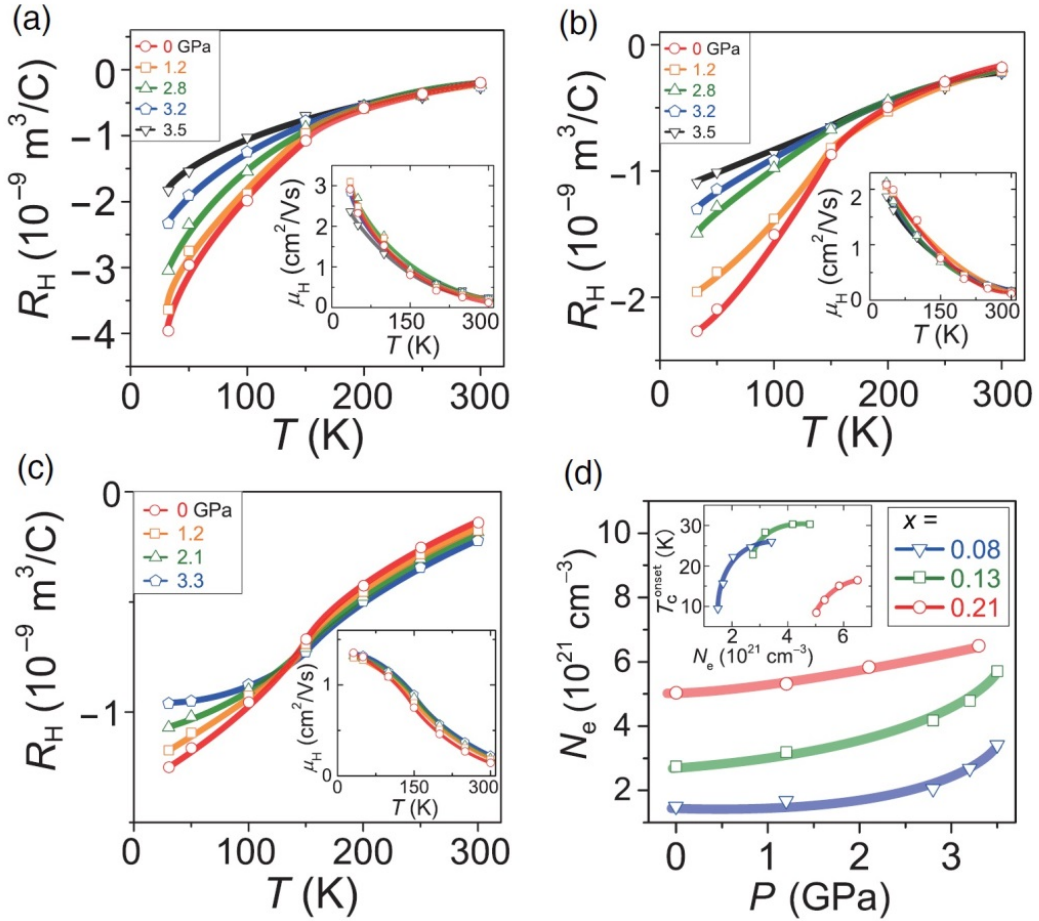


Figure 5 - 7 (a)–(c) Temperature dependence of the Hall coefficients (R_H) for $(\text{Ba}_{1-x}\text{La}_x)\text{Fe}_2\text{As}_2$ epitaxial films with $x = 0.08$ [(a) underdoped], $x = 0.13$ [(b) optimally doped], and $x = 0.21$ [(c) overdoped] under high pressures. The applied pressures are indicated on the upper left of each panel. The inset shows the temperature dependence of the Hall mobilities (μ_H) under various pressures. (d) Pressure dependences of the carrier density (N_e) at 35 K. The relationship between T_c^{onset} and N_e is summarized in the inset.

Chapter 6: Heteroepitaxial growth of phosphorus-doped BaFe₂As₂ thin films

6.1. Introduction

As compared to Ba(Fe_{1-x}Co_x)₂As₂ (BaFe₂As₂:Co), 122-type BaFe₂(As_{1-x}P_x)₂ (BaFe₂As₂:P) exhibits a higher T_c (~31 K) and a comparable γ ¹. In addition, it was recently reported² that BaFe₂As₂:P epitaxial films have a very high J_c of 10 MA/cm², which is two to three times greater than that of BaFe₂As₂:Co^{3,4}. Unfortunately, the decay rate of J_c for a BaFe₂As₂:P epitaxial film under a magnetic field¹ is greater than that of a BaFe₂As₂:Co epitaxial film⁵. This observation is attributed to the weak vortex pinning in BaFe₂As₂:P because an isovalent P dopant is not thought to work as an effective pinning center^{6,7}. This characteristic contrasts sharply with BaFe₂As₂:Co, in which the disorder of aliovalent Co dopants in the Fe layers works as intrinsic vortex pinning centers. Therefore, to exploit the advantages of BaFe₂As₂:P films, it is vital to enhance their vortex pinning so that a high J_c can be maintained under high magnetic fields.

Another important issue for wire/tape applications is the anisotropy of J_c . Since high- T_c superconductors such as cuprates and 1111-type iron-based superconductors have distinct layered structures, H_{c2} with $H // ab$ is higher than H_{c2} with $H // c$ because of their electronic anisotropy; their J_c properties also reflect this intrinsic crystallographic anisotropy. Therefore, introducing pinning centers along the c -axis is a practical way to reduce their anisotropy.^{8,9} Heavy-ion irradiation experiments have clarified the attractive properties of iron-based superconductors, which are totally

different from cuprates; introducing a high density of nanosize columnar defects does not degrade T_c until the dose-matching field becomes 21 T, which indicates the excellent potential of iron-based superconductors for high-field applications.^[16] Although these results revealed the high potential of iron-based superconductors if pinning centers as structural defects are introduced, it is difficult to apply to large-scale superconducting wires and tapes. Therefore, a simple fabrication process, which controls the shape, size, and density of defects, is more practical than introducing artificial pinning centers.

To introduce the vortex pinning centers, the choice of the substrate and buffer layer has been discussed in iron-based superconductor thin films. Lee et al.³ successfully fabricated high-performance Ba(Fe,Co)₂As₂ epitaxial films on mixed-perovskite type (La,Sr)(Al,Ta)O₃ (LSAT) using a thin SrTiO₃ (STO) buffer layer. In this film, 2–3 nm diameter BaFeO₂ rods were produced by diffusion of oxygen from the STO buffer layer¹⁰. They worked as strong c -axis pinning centers, resulting in high critical current densities (J_c) under high magnetic fields¹¹. Iida et al.¹² employed an Fe buffer layer. This film had no pinning centers along the c -axis and exhibited a vortex pinning anisotropy similarly to that of single crystals. On the other hand, Katase et al. succeeded in fabricating Ba(Fe,Co)₂As₂ epitaxial films directly on LSAT and MgO (001) single-crystal substrates without buffer layers by optimizing the growth condition^{4,13,14}. These films exhibited strong vortex pinning along the c -axis^{15,16}, which is comparable to those of the above films employing the buffer layers, originating from vertical defects in the films. However, their vortex pinning properties depended largely on the substrates. The films on LSAT exhibited strong c -axis pinning at 4 K and 15 T that also worked effectively even at ~10 K and 12 T¹⁵. While in the case of MgO substrates¹⁶, the c -axis

pinning centers did not work above 5 T.

In this study, we fabricated BaFe₂As₂:P epitaxial films on MgO (001) [BaFe₂As₂:P/MgO] and LSAT (001) [BaFe₂As₂:P/LSAT] substrates and characterized their crystallinities, microstructures and electron transport properties. I obtained BaFe₂As₂:P epitaxial films grown by high-temperature pulsed-laser deposition (PLD) at 1050 °C, which is about 200 °C higher than that of BaFe₂As₂:Co¹⁴. Compared with these crystallinity, BaFe₂As₂:P/LSAT has poor crystallinity than that of BaFe₂As₂:P/MgO because of the reaction layer between film and substrate. The vortex pinning properties are discussed in chapter 7.

6.2. Experimental procedure

6.2.1. Thin film fabrication

BaFe₂As₂:P films of 150–200 nm thickness were grown on MgO (001) and LSAT (001) single-crystal substrates by PLD. Optimally P-doped polycrystalline BaFe₂(As_{0.7}P_{0.3})₂ disks were used as the PLD targets, which were synthesized by a solid-state reaction of BaAs + 0.4Fe₂As + 0.6Fe₂P → BaFe₂(As_{0.7}P_{0.3})₂ at 930 °C for 16 h in a sealed Ar-filled stainless-steel tube. The pulsed-laser excitation source was the second harmonic of an Nd:YAG laser (wavelength = 532 nm, repetition rate = 10 Hz, laser fluence ~ 3 J/cm²). The base pressure of the growth chamber was approximately 5 × 10⁻⁷ Pa. Instead of a halogen-lamp heater,¹⁴ A semiconductor infrared laser diode was used (wavelength = 975 nm, maximum power = 300 W) to achieve high substrate temperatures (T_s) up to 1400 °C. The T_s was calibrated by an *ex-situ* measurement using a thermocouple connected to a substrate directly. To heat the substrate, a Mo plate was

tightly contacted to the backside of the substrate and heated by focused infrared light, which provided uniform T_s over the substrate. First, in order to find the epitaxial growth condition, we employed MgO substrates and varied T_s from 700 to 1300 °C by maintaining similar growth rates of ~ 3 Å/s, which is almost the same as that used for the epitaxial growth of BaFe₂As₂:Co.¹⁴

6.2.2. Characterization

To determine the crystalline phases and the small amount of impurity phases, θ -coupled 2θ -scan x-ray diffraction measurements (XRD, anode radiation: Cu $K\alpha$) were performed with a high-power conventional XRD apparatus. The crystallinity of the epitaxial films was characterized on the basis of full widths at half maximum (FWHM) of the out-of-plane (2θ -fixed ω scans) rocking curves ($\Delta\omega$) of 002 diffraction and the in-plane ($2\theta_\chi$ -fixed ϕ scans) rocking curves ($\Delta\phi$) of 200 diffraction with a high-resolution XRD apparatus [HR-XRD, Cu $K\alpha_1$ monochromated by Ge (220)]. The chemical composition was determined from electron-probe microanalyzer (EPMA). For quantitative analyses, we employed the atomic number, absorption, fluorescence (ZAF) correction method using the following standard samples; BaTiO₃ for Ba, Fe for Fe, LaAs for As, and InP for P, which provided reasonable results as will be shown later (for a BaFe₂As₂:P film grown at an optimum $T_s \sim 1050$ °C, Ba: Fe: (As + P) = 1: 2.1 : 2.0).

The surface morphology was observed with an atomic force microscope (AFM). Cross-sectional microstructural images were obtained by scanning transmission electron microscopy (STEM). The variation in chemical composition around defects was measured using energy-dispersive x-ray spectroscopy (EDXS) with a spatial resolution

of about 1 nm. These characterizations were performed at room temperature.

Temperature (T) dependence of electrical resistivity (ρ) was measured by the four-probe method using Au electrodes with a physical property measurement system.

6.3. Results and discussion

6.3.1. Optimization of growth temperature

At first, growth temperature was optimized using MgO substrates. Figure 6 - 1 (a) summarizes the relationship between the growth condition (T_s and laser fluence) and crystallographic orientation of BaFe₂As₂:P thin films grown at growth rates of ~ 3 Å/s. When $T_s \leq 950$ °C [“Random oriented” region: triangles in Figure 6 - 1 (a) and lower XRD pattern in Figure 6 - 1 (b)], the films were preferentially oriented along the c -axis along with a smaller portion of nonoriented BaFe₂As₂:P crystallites and Fe impurities appeared. When T_s was increased to 1100 °C [“Epitaxial” region: circles in Figure 6 - 1 (a)], epitaxial BaFe₂As₂:P films were obtained; that is, only $00l$ diffractions were observed out of plane [middle row of Figure 6 - 1 (b)], and due to the tetragonal lattice, a clear four-fold symmetry was observed in the in-plane ϕ scan [Figure 6 - 1 (c)]. At $T_s \geq 1100$ °C [“ $00l$ & $hh0$ ” region, squares in Figure 6 - 1 (a) and the top XRD pattern in Fig. 1(b)], $00l$ and $hh0$ preferential orientations were observed, which is similar to that observed for high- T_s growth of BaFe₂As₂:Co.¹⁴ A weak Fe 002 peak is observed in the XRD patterns. Figure 6 - 1 (c) and (d) show the cross-section STEM image of BaFe₂As₂:P/MgO and EDX results. I confirmed that impurity Fe particles segregated in the bulk regions of the films, not at the film–substrate interface, sharply different from the result of BaFe₂As₂:Co films grown by PLD using a KrF excimer laser¹⁷. In the latter report, the Fe impurity is epitaxially grown at the interface. However, similar

segregation in the bulk region is observed also in BaFe₂As₂:Co epitaxial films fabricated using a Nd:YAG laser as an excitation source.

Based on these results, we concluded that the optimum T_s for epitaxial growth of BaFe₂As₂:P is ~1050 °C. The chemical composition of the film, as determined by EPMA, was Ba: Fe: As: P = 19.7: 41.5: 30.3: 8.5 [i.e., P/(As + P) = 22%], indicating that the P doping level was lower than the nominal composition of the PLD target [P/(As + P) = 30%]. The lattice parameters of the film were $a = 3.95 \text{ \AA}$ and $c = 12.830 \text{ \AA}$, which differ slightly from those of a single crystal with the same chemical composition ($a = 3.94 \text{ \AA}$ and $c = 12.89 \text{ \AA}$)¹⁸. This result implies that a tensile strain in the ab plane is introduced into the epitaxial film because of the larger in-plane lattice parameter of the MgO substrate ($a = 4.21 \text{ \AA}$)¹⁹.

The surface morphology of the film grown at the optimum T_s , as observed by AFM, shows that the film grows via spiral-island growth and has a smooth surface with the step height corresponding to half of the c -axis length Figure 6 - 1 (f)]. Note that there are few droplets and pit structures, although these are often observed in BaFe₂As₂:Co epitaxial films²⁰. These results would originate from the higher T_s growth (1050 °C) than that of BaFe₂As₂:Co epitaxial films (800–850 °C),¹⁴ which promotes the migration of deposition precursors and reconstruction of their structure at the growing surface. Such an atomically flat surface would be useful for future applications such as multilayer junction devices.

6.3.2. Fabrication on LSAT substrates and characterization

As we mentioned above, optimal growth condition is founded (i.e. optimum T_s is

~1050 °C). Therefore, we also fabricated BaFe₂As₂:P films on LSAT substrates using optimized condition. Figure 5 - 3 (a) shows a θ -coupled 2θ XRD pattern of the BaFe₂As₂:P/LSAT. Clear $00l$ peaks of BaFe₂As₂:P were observed along with the 110 reflection of impurity Fe ($2\theta = 65$ degree) which is also observed in the matrix region of BaFe₂As₂:P/MgO. It should be noted that an unassigned peak in ~ 23 degree is observed. It will be discussed later with the data of STEM-EDX. Figure 5 - 3 (b) shows an in-plane HR-XRD pattern of ϕ -coupled $2\theta/\chi$ scan. Only $h00$ peaks of BaFe₂As₂:P were observed with $h00$ peaks of LSAT. Fig. 1 (c) shows the XRD pattern of in-plane ϕ -scan ($2\theta/\chi$ -fixed ϕ -scans). Four-fold symmetry was observed due to the tetragonal lattice of BaFe₂As₂:P. These results indicate that the thin film grew heteroepitaxially on the LSAT substrate with the relationship of $[001]$ BaFe₂As₂:P \parallel $[001]$ LSAT for out-of-plane and $[100]$ BaFe₂As₂:P \parallel $[100]$ LSAT for in-plane. The chemical composition of the BaFe₂As₂:P/LSAT determined by EPMA was Ba : Fe : As : P = 21.2 : 40.6 : 28.3 : 9.9 in atomic ratio. It gives the P/(P+As) ratio of 0.26, which is close to but slightly higher than that of BaFe₂As₂:P/MgO [P/(P+As) = 0.22]. This small difference becomes one of the origin of the differences of the T_c between BaFe₂As₂:P/MgO and BaFe₂As₂:P/LSAT discussed later.

Lattice parameters of the BaFe₂As₂:P/LSAT were $a = 3.96$ Å, $c = 12.806$ Å, and $c/a = 3.23$, which are different from those of a single crystal BaFe₂(As_{1-x}P_x)₂ with a similar chemical composition ($x = 0.2 - 0.4$, $c/a \sim 3.27$)¹⁸. This result indicates that a tensile strain in the a - b plane remained in the BaFe₂As₂:P/LSAT, which is the same trend as the case of the BaFe₂As₂:P/MgO ($a = 3.95$ Å, $c = 12.830$ Å, and $c/a = 3.25$), and the larger c/a ratio of the BaFe₂As₂:P/LSAT indicates that it had a stronger lattice strain than BaFe₂As₂:P/MgO. This stronger tensile strain could be another origin of the higher T_c of

the BaFe₂As₂:P/LSAT¹⁹ discussed later. The lattice parameter of MgO (4.21 Å) is larger than that of BaFe₂As₂:P; therefore, it would be natural to consider that the tensile strain in the *a-b* plane is induced. However, it is expected that the strain should be reversed (i.e., compressive) by considering only the in-plane lattice mismatch because the in-plane lattice parameter of LSAT (3.86 Å) is smaller than that of the BaFe₂As₂:P. This contradiction suggests that the in-plane lattice mismatch is not the origin of the tensile strain in the BaFe₂As₂:P/LSAT. As we discussed in chapter 4, the differences of thermal expansion coefficients should be the one of the origin of this discrepancy.

Next, we compared the crystallinity of the BaFe₂As₂:P/LSAT with that of the BaFe₂As₂:P/MgO. Figure 6 - 1 (d) and (e) show the normalized rocking curves of the 004 and 200 reflections, respectively. In the case of BaFe₂As₂:P/MgO, the FWHMs of $\Delta\omega$ and $\Delta\phi$ were 0.6 degrees. On the other hand, when the films were grown on LSAT substrates, the FWHMs of $\Delta\omega$ and $\Delta\phi$ were 1.1 and 1.5 degrees, respectively. The in-plane lattice mismatch $[(a_{\text{substrate}} - a_{\text{Ba122:P}})/a_{\text{Ba122:P}}]$, where $a_{\text{Ba122:P}}$ is *a*-axis length of the single crystal with the same chemical composition] between BaFe₂As₂:P and LSAT ($a = 3.86$ Å) is smaller (- 1.8 %) than that between BaFe₂As₂:P and MgO ($a = 4.21$ Å) (+ 6.9 %), but the crystallinity of BaFe₂As₂:P/LSAT was poorer than that of BaFe₂As₂:P/MgO. This result suggests the presence of a larger number of defects than for BaFe₂As₂:P/MgO and/or a chemical reaction between LSAT and BaFe₂As₂:P, similar to the case of Ba(Fe,Co)₂As₂ on LSAT [chapter 2].

To investigate the shapes and the chemical composition of the defects in the BaFe₂As₂:P/LSAT, we performed cross-sectional STEM, HR-TEM, and EDX observations. Figure 5 - 4 (a) and (b) show a wide cross-sectional bright-field STEM

image of BaFe₂As₂:P/LSAT and its magnified image, respectively. As shown in Figure 5 - 4 (a), many vertical defects along the *c*-axis were observed. They appear to start growing from the heterointerface throughout to the film surface, and are slightly tilted from the normal direction to the substrate surface. Such tilted boundaries would be introduced by lateral growth of crystallites. Therefore, these results suggest that most of the defects in the BaFe₂As₂:P/LSAT are domain boundaries nucleated at the onset of film growth, which is similar to the case of the BaFe₂As₂:P/MgO grown at a higher growth rate (discussed in chapter 7).

Figure 5 - 4 (c) shows the results of a STEM-EDX line scan along the horizontal line in Figure 5 - 4 (b). The chemical composition of the defects is the same as that in the bulk region of the film, and the oxygen concentration in the film is lower than the detection limit of the STEM-EDX measurement. These results also support that these defects are domain boundaries and are not oxygen-related impurities as reported for BaFeO₂ introduced from a STO buffer layer¹⁰.

The poorer crystallinity of the BaFe₂As₂:P/LSAT shown in Figure 6 - 1 (d) and (e) originates from these many domain boundaries in the BaFe₂As₂:P/LSAT. The thicknesses of the domain boundary region appear to be ~ 4 nm, but these values are unclear because the domain boundaries are not parallel to the electron-beam incident direction. However, a few nanometers are comparable in size to twice the coherence length of BaFe₂As₂:P¹; therefore, we expect that these boundaries work as two-dimensional strong vortex pinning centers. Most of the defects in BaFe₂As₂:P/LSAT started from the heterointerface and grew through to the film surface. Because these defects have large pinning areas, it is expected that they more strongly

pin the vortices than the small defects such as point-like defects⁵ and columnar defects¹⁰.

I also found a reaction layer at the heterointerface between the BaFe₂As₂:P and the LSAT. As shown in Figure 5 - 4 (d), the reaction layer is a crystalline phase with a thickness of ~ 5 nm. Figure 5 - 4 (e) shows the results of STEM-EDX around the interface. As shown in the right panel of Figure 5 - 4 (e), the Ba concentration has peaks at the interface, and the La signal also shows a smaller but similar peak at the interface. The concentrations of Fe and As decrease monotonically from the film to the substrate through the reaction layer, while the P concentration is almost constant in the reaction layer. Large amounts of oxygen were detected in the reaction layer. Thus, the reaction layer mainly consists of Ba, La, P and O. Judging from these results, La-doped barium phosphate or apatite is a possible candidate for the reaction layer. Recently, Adachi et al.²¹ reported that the reaction layer at the interface between BaFe₂Fe₂:P and LSAT is Ba₅(PO₄)₃OH, determined by XRD 2θ - ψ mapping. From our XRD data (Fig. 1(a)), the unassigned impurity peak indicated by the asterisk was observed around $2\theta = 21.1$ degrees, which is reasonably assigned to the 111 diffraction of Ba₅(PO₄)₃OH ($2\theta = 20.94$ degrees)²². This small difference in the 2θ angles can be explained by the difference in the ion radii between La (116 pm) and Ba (142 pm)²³. Thus, we concluded that the reaction layer in our films is La-doped Ba₅(PO₄)₃OH. This reaction layer would be an origin of the tensile strain, the poor crystallinity, and the generation of domain boundaries in the present BaFe₂As₂:P/LSAT.

6.3.3. Electron transport properties of the films on MgO and LSAT

Finally, electron transport properties are discussed. As shown in Figure 6 - 4 (a), BaFe₂As₂:P/LSAT exhibited its $T_c = 28.5$ K, which is slightly higher than that of BaFe₂As₂:P/MgO ($T_c = 26.5$ K). The P/(P+As) ratio of the BaFe₂As₂:P/LSAT determined by EPMA was 0.26, which is close to but slightly higher than that of the BaFe₂As₂:P/MgO [P/(P+As) = 0.22]. This result would be consistent with a higher T_c (28.5 K) of the BaFe₂As₂:P/LSAT than that of the BaFe₂As₂:P/MgO (26.5 K) because the doping level of the BaFe₂As₂:P/LSAT is closer to the optimum value for bulk BaFe₂As₂:P [P/(P+As) = 0.33, $T_c = 31$ K¹⁸] than that of the BaFe₂As₂:P/MgO. This result is also consistent with the behavior of normal state resistivity [Figure 6 - 4 (b)]. Moreover, BaFe₂As₂:P/LSAT had a stronger tensile strain than BaFe₂As₂:P/MgO as discussed before. These results are consistent with electron transport properties of BaFe₂As₂:P/MgO and BaFe₂As₂:P/LSAT.

6.4. Conclusion

I fabricated BaFe₂As₂:P/MgO and BaFe₂As₂:P/LSAT and characterized their crystallinities, microstructures and electron transport properties. Optimizing the growth temperature, we concluded that the optimum T_s for epitaxial growth of BaFe₂As₂:P is ~1050 °C, which is about 200 °C higher than that of BaFe₂As₂:Co. Comparing those physical properties, the BaFe₂As₂:P/LSAT had poorer crystallinity, larger in-plane tensile strain, and a larger density of domain boundaries, which would be caused by a thin reaction layer between the BaFe₂As₂:P film and the LSAT substrate. Because of slightly higher doping level and strong tensile strain caused by reaction layer and/or small thermal expansion coefficients of LSAT substrate, T_c of BaFe₂As₂:P/LSAT is

slightly higher than BaFe₂As₂:P/MgO. These results of crystallinity, defects and electron transport properties should affect to the vortex pinning properties and referred to the fabrication process of superconducting tape in chapter 8.

References

- ¹ M. Miura, S. Adachi, T. Shimode, K. Wada, A. Takemori, N. Chikumoto, K. Nakao, and K. Tanabe, *Appl. Phys. Express* **6**, 093101 (2013).
- ² A. Sakagami, T. Kawaguchi, M. Tabuchi, T. Ujihara, Y. Takeda, and H. Ikuta, *Phys. C Supercond.* **494**, 181 (2013).
- ³ S. Lee, J. Jiang, Y. Zhang, C.W. Bark, J.D. Weiss, C. Tarantini, C.T. Nelson, H.W. Jang, C.M. Folkman, S.H. Baek, A. Polyanskii, D. Abraimov, A. Yamamoto, J.W. Park, X.Q. Pan, E.E. Hellstrom, D.C. Larbalestier, and C.B. Eom, *Nat. Mater.* **9**, 397 (2010).
- ⁴ T. Katase, H. Hiramatsu, T. Kamiya, and H. Hosono, *Appl. Phys. Express* **3**, 063101 (2010).
- ⁵ B. Maiorov, T. Katase, I.O. Usov, M. Weigand, L. Civale, H. Hiramatsu, and H. Hosono, *Phys. Rev. B* **86**, 094513 (2012).
- ⁶ C.J. van der Beek, M. Konczykowski, S. Kasahara, T. Terashima, R. Okazaki, T. Shibauchi, and Y. Matsuda, *Phys. Rev. Lett.* **105**, 267002 (2010).
- ⁷ S. Demirdiř, Y. Fasano, S. Kasahara, T. Terashima, T. Shibauchi, Y. Matsuda, M. Konczykowski, H. Pastoriza, and C.J. van der Beek, *Phys. Rev. B* **87**, 094506 (2013).
- ⁸ J.L. MacManus-Driscoll, S.R. Foltyn, Q.X. Jia, H. Wang, A. Serquis, L. Civale, B. Maiorov, M.E. Hawley, M.P. Maley, and D.E. Peterson, *Nat. Mater.* **3**, 439 (2004).
- ⁹ K. Matsumoto and P. Mele, *Supercond. Sci. Technol.* **23**, 014001 (2010).
- ¹⁰ Y. Zhang, C.T. Nelson, S. Lee, J. Jiang, C.W. Bark, J.D. Weiss, C. Tarantini, C.M. Folkman, S.-H. Baek, E.E. Hellstrom, D.C. Larbalestier, C.-B. Eom, and X. Pan, *Appl. Phys. Lett.* **98**, 042509 (2011).
- ¹¹ C. Tarantini, S. Lee, Y. Zhang, J. Jiang, C.W. Bark, J.D. Weiss, A. Polyanskii, C.T. Nelson, H.W. Jang, C.M. Folkman, S.H. Baek, X.Q. Pan, A. Gurevich, E.E. Hellstrom, C.B. Eom, and D.C. Larbalestier, *Appl. Phys. Lett.* **96**, 142510 (2010).
- ¹² T. Thersleff, K. Iida, S. Haindl, M. Kidszun, D. Pohl, A. Hartmann, F. Kurth, J. Hänisch, R. Hühne, B. Rellinghaus, L. Schultz, and B. Holzapfel, *Appl. Phys. Lett.* **97**, 022506 (2010).
- ¹³ H. Hiramatsu, T. Katase, Y. Ishimaru, A. Tsukamoto, T. Kamiya, K. Tanabe, and H. Hosono, *Mater. Sci. Eng. B* **177**, 515 (2012).
- ¹⁴ T. Katase, H. Hiramatsu, T. Kamiya, and H. Hosono, *Supercond. Sci. Technol.* **25**, 084015 (2012).
- ¹⁵ B. Maiorov, T. Katase, S.A. Baily, H. Hiramatsu, T.G. Holesinger, H. Hosono, and L. Civale, *Supercond. Sci. Technol.* **24**, 055007 (2011).

- ¹⁶ S. Mohan, T. Taen, H. Yagyuda, Y. Nakajima, T. Tamegai, T. Katase, H. Hiramatsu, and H. Hosono, *Phys. C Supercond.* **471**, 1181 (2011).
- ¹⁷ K. Iida, J. Hänisch, T. Thersleff, F. Kurth, M. Kieszun, S. Haindl, R. Hühne, L. Schultz, and B. Holzapfel, *Phys. Rev. B* **81**, 100507 (2010).
- ¹⁸ S. Kasahara, T. Shibauchi, K. Hashimoto, K. Ikada, S. Tonegawa, R. Okazaki, H. Shishido, H. Ikeda, H. Takeya, K. Hirata, T. Terashima, and Y. Matsuda, *Phys. Rev. B* **81**, 184519 (2010).
- ¹⁹ T. Kawaguchi, A. Sakagami, Y. Mori, M. Tabuchi, T. Ujihara, Y. Takeda, and H. Ikuta, *Supercond. Sci. Technol.* **27**, 065005 (2014).
- ²⁰ T. Katase, H. Hiramatsu, H. Yanagi, T. Kamiya, M. Hirano, and H. Hosono, *Solid State Commun.* **149**, 2121 (2009).
- ²¹ S. Adachi, T. Shimode, Y. Murai, N. Chikumoto, and K. Tanabe, *Phys. C Supercond.* **502**, 31 (2014).
- ²² C.-J. Duan, X.-Y. Wu, W. Liu, H.-H. Chen, X.-X. Yang, and J.-T. Zhao, *J. Alloys Compd.* **396**, 86 (2005).
- ²³ R.D. Shannon, *Acta Crystallogr. Sect. A* **32**, 751 (1976).

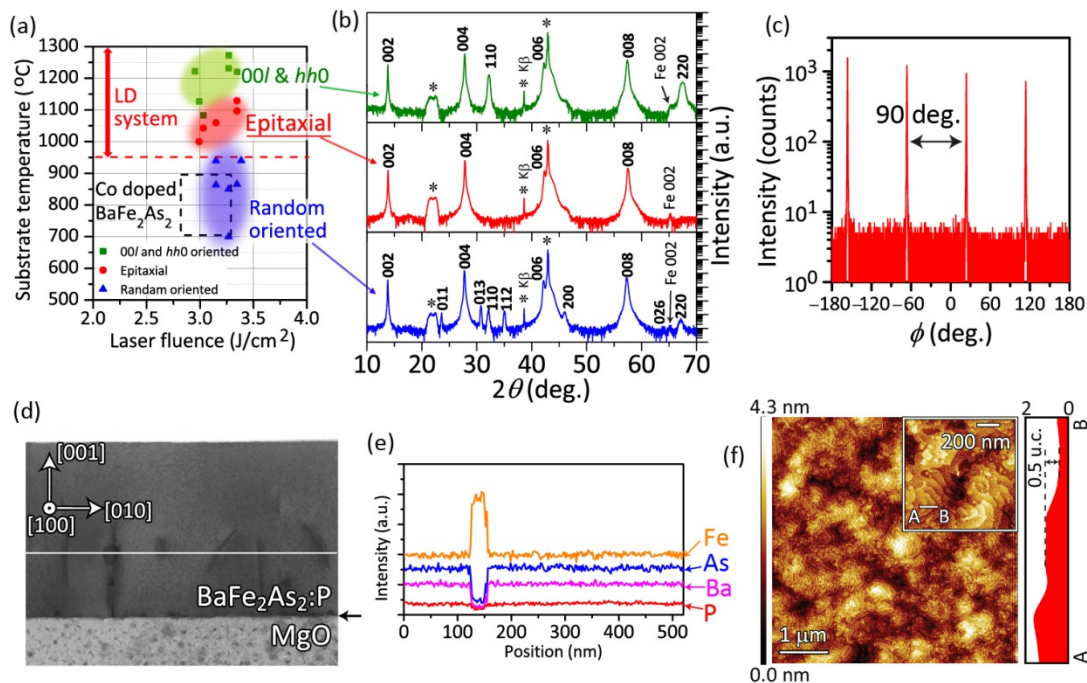


Figure 6 - 1. Growth of $BaFe_2As_2:P$ films and structural and electrical properties of the epitaxial film. (a) Relationship between growth condition (substrate temperature T_s and laser fluence) and crystallographic orientation of $BaFe_2As_2:P$ films. Three regions with different orientation structures obtained with different T_s values are shown. The dashed square region shows the optimum condition for epitaxial growth of $BaFe_2As_2:Co$.^[17] (b) Typical XRD patterns, measured in Bragg-Brentano configuration, of $BaFe_2As_2:P$ thin films for the three T_s regions in panel (a). (c) In-plane ϕ scan of the 200 diffractions of the $BaFe_2As_2:P$ thin film grown at the optimum T_s . (d) Cross-sectional bright-field STEM images of $BaFe_2As_2:P$ epitaxial films. Horizontal arrows indicate the heterointerfaces between the films and MgO substrates. (e) the results of EDXS line-scans along the white horizontal lines in panels (d) (f) AFM scan showing surface morphology of $BaFe_2As_2:P$ film grown at the optimum T_s . Upper-right inset shows a magnified image. A cross-sectional profile along the horizontal line A-B in the inset is shown to the right (“0.5 u.c.” denotes the half size of the c -axis unit-cell length).

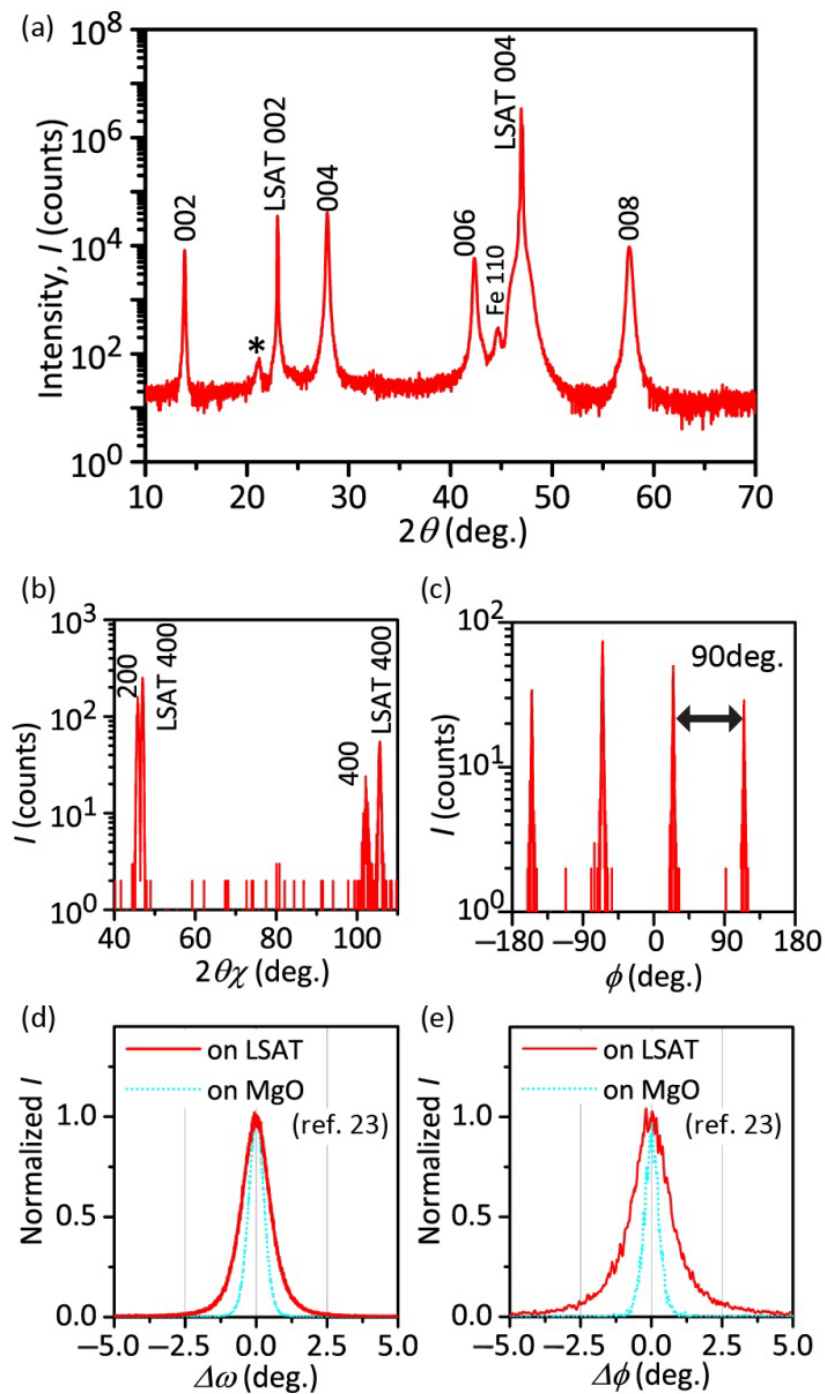


Figure 6 - 2 XRD patterns of a BaFe₂As₂:P film on a MgO and LSAT (001) substrate. (a) θ -coupled 2θ pattern. The asterisk shows a peak position of an impurity phase. (b, c) Normalized rocking curves of the out-of-plane 004 (b) and the in-plane 200 reflections (c).

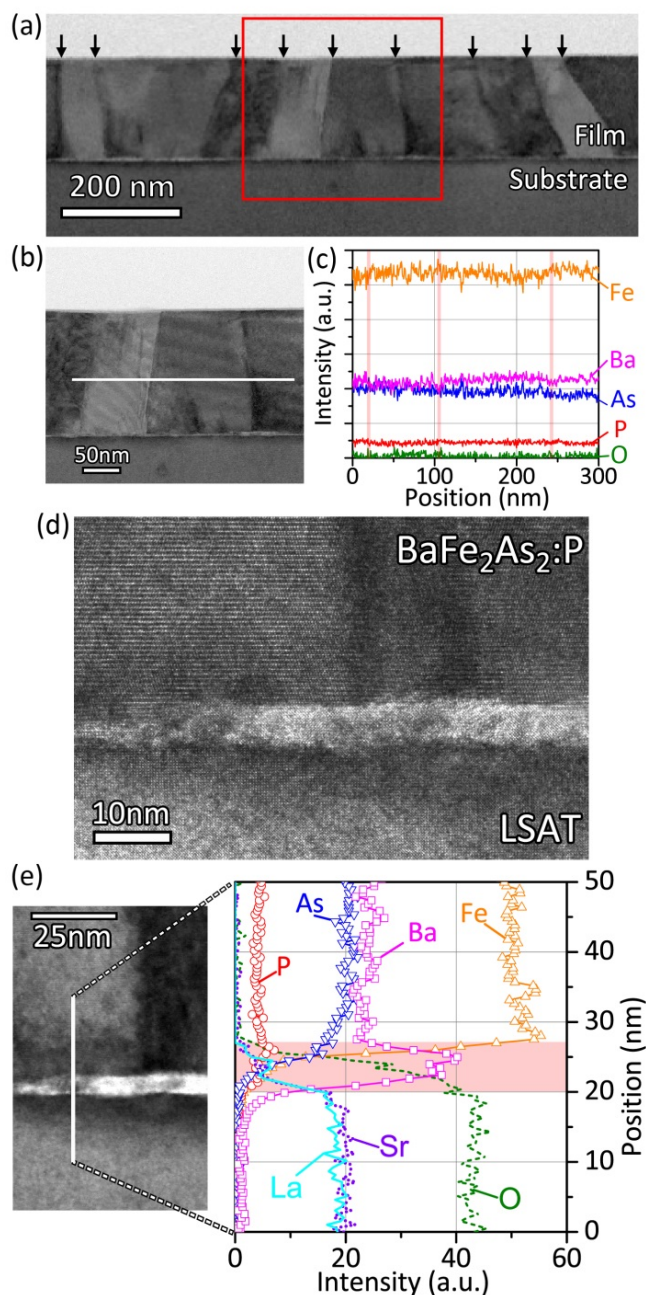


Figure 6 - 3 Microstructure and chemical composition of a $BaFe_2As_2:P$ epitaxial film on a LSAT (001) substrate. The incident direction of the electron beam is $BaFe_2As_2:P$ [100]. (a) Cross-sectional bright-field STEM image. Vertical arrows show the vertical defects. (b) Magnified image of the square region in Fig (a). (c) STEM-EDX line scan along the horizontal line shown in Fig. (b). The vertical lines correspond to the positions of the vertical defects. (d) HR-TEM image at the interface between the $BaFe_2As_2:P$ film and LSAT substrate. (e) Left panel shows STEM image at the interface. Right panel shows the results of STEM-EDX line scan along the vertical line shown in the left panel. The shaded region corresponds to the interfacial layer.

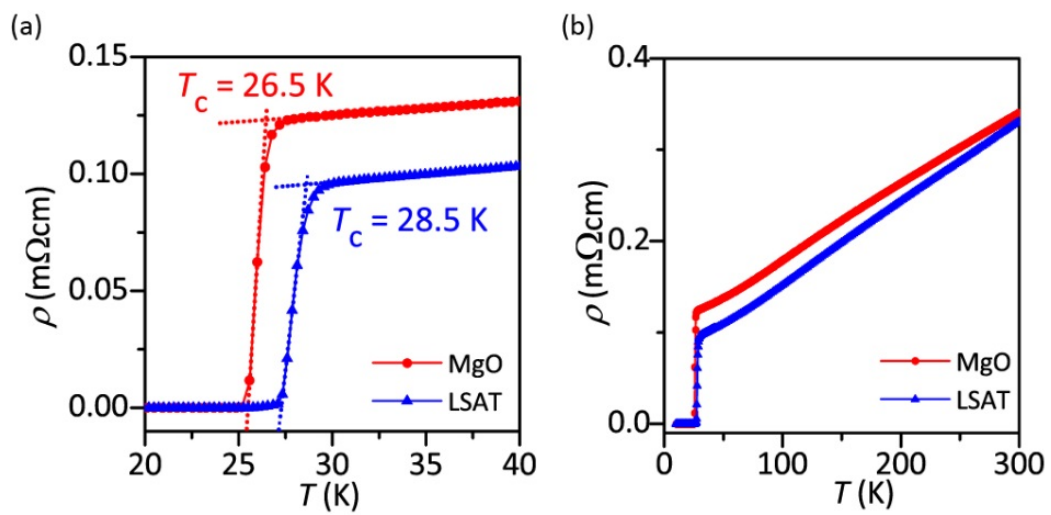


Figure 6 - 4 Temperature dependence of resistivity (ρ) of BaFe₂As₂/P/MgO and BaFe₂As₂/P/LSAT.
(a) magnified figure around T_c (b) wide range ρ - T curves.

Chapter 7: High critical-current density with less anisotropy in phosphorus-doped BaFe₂As₂ epitaxial thin films

7.1. Introduction

As we mentioned in chapter 6, BaFe₂(As_{1-x}P_x)₂ (BaFe₂As₂:P) exhibits (i) a higher T_c (~31 K) and a (ii) small anisotropy ($\gamma = 1-2$)¹ and (iii) high self-field critical current density ($J_c \sim 10 \text{ MA/cm}^2$)² which is two to three times greater than that of BaFe₂As₂:Co^{3,4} but it also has weak intrinsic pinning because an isovalent P dopant is not thought to work as an effective pinning center^{6,7}. Therefore, to exploit the advantages of BaFe₂As₂:P films, it is vital to enhance their vortex pinning so that a high J_c can be maintained under high magnetic fields.

In this chapter, vortex pinning properties of BaFe₂As₂:P epitaxial films on MgO and LSAT are characterized and examined the growth rate dependence of the anisotropy of vortex pinning properties of BaFe₂As₂:P epitaxial films. After the optimization, a high-self-field J_c of 7 MA/cm² was obtained for BaFe₂As₂:P epitaxial films and a high J_c of over 1 MA/cm² was maintained even with an applied magnetic field of 9 T. This J_c value at 9 T is the highest value obtained so far for iron-based superconductor thin films.

7.2. Experimental procedure

7.2.1. Thin film fabrication

Thin film fabrication and characterization process was noted in chapter 6. In this

chapter, the growth rate was varied from 2.1 to 3.9 Å/s by changing the substrate–target distance with fixed substrate temperature ~ 1050 °C.

7.2.2. Characterization of microstructure and transport J_c

To discuss the microstructures of films grown at different growth rate, cross-sectional microstructures were observed by scanning transmission electron microscopy (STEM) and high-resolution transmission electron microscopy (HR-TEM). Chemical compositions at a heterointerface and of defects were evaluated by energy-dispersive x-ray spectroscopy (EDX) with a spatial resolution of ~ 1 nm. To examine the transport properties of J_c , the films were patterned into microbridges by photolithography and an Ar milling process. The transport J_c was determined from voltage–current curves with the criterion of 1 μV/cm under an external magnetic field (H) of up to 9 T. The angle θ_H of the applied H was varied from –30 to 120° (0 and 90° corresponding to $H // c$ -axis normal to the film surface and $H // ab$ plane, respectively).

7.3. Results and discussion

7.3.1. Comparison of the J_c properties of the films on MgO with those on LSAT

To discuss the vortex pinning properties, we examined the magnetic field dependences of J_c at 4 K and 12 K (Figure 7 - 1). The J_c^{self} of BaFe₂As₂:P/LSAT was 5.0 MA/cm² at 4 K and 2.8 MA/cm² at 12 K. On the other hand, J_c^{self} of BaFe₂As₂:P/MgO was 6.7 MA/cm² at 4 K and 3.5 MA/cm² at 12 K. These differences in J_c^{self} originated from the difference in crystallinity as observed in chapter 6. It should be noted that the anisotropy of the J_c of BaFe₂As₂:P/LSAT in the high field region is totally different from that of BaFe₂As₂:P/MgO. The difference between J_c under $H // ab$ (closed

symbols) and $H // c$ (open symbols) of BaFe₂As₂:P/LSAT are much smaller than that of BaFe₂As₂:P/MgO. These results imply that the pinning centers along the c -axis of BaFe₂As₂:P/LSAT work better than that of BaFe₂As₂:P/MgO under high magnetic fields. The lower panels of Figure 7 - 1 (a) and (b) show the magnetic field dependences of the pinning force (F_p) at 12 K. As shown by arrows, the peak positions of F_p under $H // c$ ($F_p^{H//c}$) of BaFe₂As₂:P/LSAT (~ 7 T) was higher than that of BaFe₂As₂:P/MgO (~ 5 T). This result also implies that the pinning centers along the c -axis of BaFe₂As₂:P/LSAT work better than that of BaFe₂As₂:P/MgO under high magnetic fields, although the absolute value of F_p^c of BaFe₂As₂:P/LSAT (15 GN/m³ at 7 T) was slightly lower than that of BaFe₂As₂:P/MgO (17 GN/m³ at 5 T) because of the differences in J_c^{self} .

Figure 5 - 2 (a) and (b) show the angular dependence of the transport J_c of the BaFe₂As₂:P/MgO and the BaFe₂As₂:P/LSAT under several magnetic fields at 12 K. In common with two films, the J_c peak at $\theta_H = 90^\circ$ ($H // ab$ plane) became larger with increasing magnetic field. This J_c peak at 90° originates from the intrinsic property of BaFe₂As₂:P with a layered structure and an anisotropic electronic state. On the other hand, another broad peak was observed around $\theta_H = 0^\circ$ ($H // c$ axis). It should be noted that extrinsic vortex pinning centers along the c -axis were successfully introduced in the BaFe₂As₂:P/MgO and BaFe₂As₂:P/LSAT similar to the case of BaFe₂As₂:Co/MgO and consistent with the result of the microstructure observation in chapter 6.

Figure 5 - 2 (c) compares the angular dependence of the transport J_c of the BaFe₂As₂:P/MgO with that of the BaFe₂As₂:P/LSAT. The anisotropies of J_c were almost the same at 12 K and 3 T, while the absolute values of J_c were totally different from each other. The J_c at 3 T of the BaFe₂As₂:P/LSAT is smaller than that of the

BaFe₂As₂:P/MgO. This difference was attributed to the differences in J_c^{self} because J_c^{self} of the BaFe₂As₂:P/LSAT at 12 K was smaller than that of the BaFe₂As₂:P/MgO. However, at 9 T, the anisotropy of J_c was drastically changed between LSAT and MgO. Focusing on the J_c around $\theta_H = 0^\circ$ at 9 T, the J_c peak was observed in the BaFe₂As₂:P/LSAT but almost disappeared in the BaFe₂As₂:P/MgO. The peak position was shifted slightly from $\theta_H = 0^\circ$ due mainly to the tilted defects working as pinning centers (see the cross-section STEM image in chapter 6). These results indicate that BaFe₂As₂:P/LSAT has stronger pinning centers along the c -axis than that of the BaFe₂As₂:P/MgO. Consequently, the J_c anisotropy of the BaFe₂As₂:P/LSAT under high magnetic field seems to be slightly better than that of the BaFe₂As₂:P/MgO. However, these results imply that there is a trade-off between J_c^{self} and vortex pinning forces of the BaFe₂As₂:P epitaxial films because crystallinity and defect density dominate J_c^{self} and vortex pinning forces, respectively. That is, in order to realize the best performance, it is necessary to tune the growth condition of BaFe₂As₂:P.

7.3.2. Growth rate dependence of vortex pinning properties

As we mentioned above, BaFe₂As₂:P/LSAT show the potential capability for the high field application but the absolute value of J_c is smaller than that of BaFe₂As₂:P/MgO. Therefore, we discuss the growth rate dependence of crystallinity and vortex pinning properties in transport J_c using MgO substrates. The growth rate was varied with the T_s held at the optimum $T_s = 1050^\circ\text{C}$. As seen in Figure 5 - 3 (a), the rocking-curve FWHMs of $\Delta\omega$ and $\Delta\phi$ remain almost constant at $\sim 0.5^\circ$ for a growth rate ranging from 2.1 to 3.9 Å/s. This trend is different from that for BaFe₂As₂:Co epitaxial films (see chapter 2), where low growth rates such as 2.1 Å/s led to large $\Delta\omega$ and $\Delta\phi$ (FWHM \sim

1°). In addition, the chemical composition of BaFe₂As₂:P do not depends on the growth rate [Figure 5 - 3 (b)]. This finding means that BaFe₂As₂:P films may be grown over a wider range of growth rates, a result that is also attributed to the higher optimum T_s .

There is no significant difference on crystallinity when the growth rate was varied, but attractive results are observed in the anisotropy of the vortex pinning properties. For several growth rates, Figure 5 - 3 (c) shows angular dependence of J_c for BaFe₂As₂:P epitaxial films grown at the optimum T_s . The data show that J_c increases with decreasing growth rate over the entire range of θ_H . This result is attributed to the improvement in the self-field J_c ; namely, at 12 K, the self-field J_c increased from 2.70 to 5.14 MA/cm² as the growth rate decreased from 3.9 to 2.2 Å/s. All the films exhibit intrinsic J_c peaks at $\theta_H = 90^\circ$ ($H // ab$), which is in agreement with the results for the film grown at the higher growth rate of 5.0 Å/s.^[7] The present films, however, exhibit additional J_c peaks at $\theta_H = 0^\circ$ ($H // c$). The value of J_c at $\theta_H = 0^\circ$ ($J_c^{H//c}$) increases with decreasing growth rate, then it exceeds J_c at $\theta_H = 90^\circ$ ($J_c^{H//ab}$) at the growth rate of 2.2 Å/s. These results indicate that vortex-pinning centers along the c -axis are introduced into BaFe₂As₂:P epitaxial films when these films are grown at a lower growth rate. Note that the J_c peak at $\theta_H = 0^\circ$ becomes larger and sharper upon decreasing the growth rate, which averages out the angle dependence of J_c and contributes to the highly isotropic property. These results indicate that the vortex-pinning properties and anisotropy of BaFe₂As₂:P epitaxial films can be controlled by tuning the growth rate.

7.3.3. J_c properties of optimized epitaxial films and comparison with other films

Figure 5 - 4 (a) compares the dependence of $J_c^{H//ab}$ (closed symbols) and $J_c^{H//c}$ (open symbols) at 4 K for BaFe₂As₂:P epitaxial film grown at the optimum T_s (1050 °C) and

growth rate (2.2 Å/s) with what is found for other iron-based superconductor epitaxial films exhibiting high J_c . The self-field J_c of the optimally grown BaFe₂As₂:P epitaxial film was over 7 MA/cm², which is comparable to the best results recently reported,⁴ and a high $J_c^{H//ab}$ of over 1 MA/cm² was maintained even at 9 T. It would be noteworthy the value of $J_c^{H//ab}$ obtained at 9 T = 1.1 MA/cm² (corresponding to a pinning force of 99 GN/m³) is the highest obtained for iron-based superconductor thin films, as shown in Fig. 3(a).⁵⁻¹¹ Moreover, at 9 T, $J_c^{H//c}$ is 0.8 MA/cm² and the pinning force is 72 GN/m³. These values are higher than the previously reported ones, including those for 122-type compounds [e.g., BaFe₂As₂:P films with artificial pinning centers created by BaZrO₃ nanoparticles⁵ and oxygen-rich BaFe₂As₂/BaFe₂As₂:Co superlattice (SL) films⁷] and conventional alloy superconducting wires (Nb-Ti,¹² Nb₃Sn,¹³ and MgB₂¹⁴).

Figure 5 - 4 (b) compares the J_c anisotropy of the BaFe₂As₂:P epitaxial film with the J_c of other 122-type films^{5,7,8,15} in similar ranges of H and T . The BaFe₂As₂:P epitaxial film obtained in this study exhibited a lower anisotropy than those of BaFe₂As₂:P¹⁵ and BaFe₂As₂:Co/Fe buffer.⁸ Moreover, the anisotropy obtained is much lower than that of the SL thin films,⁷ and is comparable to that of the BaFe₂As₂:P films with artificial pinning centers created by BaZrO₃ nanoparticles.⁵

7.3.4. Microstructure analysis and mechanism of isotropic vortex pinning

As discussed above, the strong vortex pinning and the isotropic J_c properties were achieved by decreasing the growth rate for the BaFe₂As₂:P epitaxial films. Therefore, we investigate the origin of the pinning centers by microstructure analysis. Figure 5 - 5 (a) and (b) show cross-sectional bright-field STEM images of BaFe₂As₂:P epitaxial films grown at 2.2 and 3.9 Å/s, respectively. Although small island structures (~ 20 nm

in lateral size) rich in oxygen are periodically found at the heterointerface in the film grown at 2.2 Å/s, as indicated by the slanted black arrows, sharp heterointerfaces without a reaction layer were observed throughout the region. Other planar or line defects in the *ab* plane, such as stacking faults, were not detected. However, as indicated by the vertical white arrows in Figure 5 - 5, many vertical defects, which occur at a higher density compared with that found for BaFe₂As₂:Co films,¹⁶ are observed in the STEM images. The number of defects did not significantly differ between the BaFe₂As₂:P films grown at 2.2 Å/s and 3.9 Å/s, but the shape and microstructure of the defects did differ. Most of the defects in the film grown at 2.2 Å/s start appearing at midthickness and are oriented parallel to the *c*-axis, which would be assigned to vertical dislocations. However, most of the defects in the film grown at 3.9 Å/s originate at the heterointerface just at the substrate surface and are tilted with respect to the *c*-axis. Such defects could be induced by lateral growth of the epitaxial domains. These results suggest that the defects in the film grown at 3.9 Å/s are domain boundaries that initiate at the onset of film growth. This difference in the structure of the defects would correspond to the results of Figure 5 - 3 (c): against a magnetic field with $\theta_H = 0^\circ$, the vertical dislocations would pin vortices more strongly than the tilted domain boundaries, resulting in the sharper peak near $\theta_H = 0^\circ$ for films grown at 2.2 Å/s and the broad peak near $\theta_H = 90^\circ$ for films grown at 3.9 Å/s.

The STEM-EDXS line scans [Figure 5 - 5 (c) and d)] show that the chemical composition of the defects is the same as that of the matrix region in the film and that the impurity oxygen concentration in the thin film is less than the detection limit of EDXS. I performed the EDXS line scans for six other vertical dislocations and nine domain boundaries, and obtained the same results. These results indicate that the defects

are not an impurity phase such as BaFeO₂,¹⁷ but may be edge or threading dislocations and/or domain boundaries. The defect sizes are estimated to be ~ 4 nm laterally and roughly double of the superconducting coherence length in the *ab* plane of BaFe₂As₂:P at 4 K,¹⁵ which is consistent because such size defects effectively serve as vortex-pinning centers.

7.4. Conclusion

In summary, BaFe₂As₂:P epitaxial films are fabricated and their vortex pinning properties was compared. The poor crystallinity and the generation of domain boundaries in the BaFe₂As₂:P/LSAT lead to a decrease in the J_c^{self} and strong vortex pinning along the *c*-axis under high magnetic fields. These results imply that there is a trade-off between J_c^{self} and vortex pinning forces of the BaFe₂As₂:P epitaxial films because crystallinity and defect density dominate J_c^{self} and vortex pinning forces, respectively. Decreasing the growth rate, a high-self-field J_c of 7 MA/cm² was obtained for BaFe₂As₂:P epitaxial films and a high J_c of over 1 MA/cm² was maintained even with an applied magnetic field of 9 T. This J_c value at 9 T is the highest value obtained so far for iron-based superconductor thin films. In addition, a highly isotropic high J_c performance was obtained by decreasing the film growth rate, which introduced vertical dislocations along the *c*-axis that served as strong vortex-pinning centers.

References

- ¹ J.L. MacManus-Driscoll, S.R. Foltyn, Q.X. Jia, H. Wang, A. Serquis, L. Civale, B. Maiorov, M.E. Hawley, M.P. Maley, and D.E. Peterson, *Nat. Mater.* **3**, 439 (2004).
- ² K. Matsumoto and P. Mele, *Supercond. Sci. Technol.* **23**, 014001 (2010).
- ³ L. Fang, Y. Jia, C. Chaparro, G. Sheet, H. Claus, M.A. Kirk, A.E. Koshelev, U. Welp, G.W. Crabtree, W.K. Kwok, S. Zhu, H.F. Hu, J.M. Zuo, H.-H. Wen, and B. Shen, *Appl. Phys. Lett.* **101**, 012601 (2012).
- ⁴ A. Sakagami, T. Kawaguchi, M. Tabuchi, T. Ujihara, Y. Takeda, and H. Ikuta, *Phys. C Supercond.* **494**, 181 (2013).
- ⁵ M. Miura, B. Maiorov, T. Kato, T. Shimode, K. Wada, S. Adachi, and K. Tanabe, *Nat. Commun.* **4**, 2499 (2013).
- ⁶ K. Iida, J. Hänisch, T. Thersleff, F. Kurth, M. Kidszun, S. Haindl, R. Hühne, L. Schultz, and B. Holzapfel, *Phys. Rev. B* **81**, 100507 (2010).
- ⁷ S. Lee, C. Tarantini, P. Gao, J. Jiang, J.D. Weiss, F. Kametani, C.M. Folkman, Y. Zhang, X.Q. Pan, E.E. Hellstrom, D.C. Larbalestier, and C.B. Eom, *Nat. Mater.* **12**, 392 (2013).
- ⁸ K. Iida, S. Haindl, T. Thersleff, J. Hänisch, F. Kurth, M. Kidszun, R. Hühne, I. Mönch, L. Schultz, B. Holzapfel, and R. Heller, *Appl. Phys. Lett.* **97**, 172507 (2010).
- ⁹ S. Trommler, J. Hänisch, V. Matias, R. Hühne, E. Reich, K. Iida, S. Haindl, L. Schultz, and B. Holzapfel, *Supercond. Sci. Technol.* **25**, 084019 (2012).
- ¹⁰ V. Braccini, S. Kawale, E. Reich, E. Bellingeri, L. Pellegrino, A. Sala, M. Putti, K. Higashikawa, T. Kiss, B. Holzapfel, and C. Ferdeghini, *Appl. Phys. Lett.* **103**, 172601 (2013).
- ¹¹ H. Hiramatsu, T. Katase, Y. Ishimaru, A. Tsukamoto, T. Kamiya, K. Tanabe, and H. Hosono, *Mater. Sci. Eng. B* **177**, 515 (2012).
- ¹² L.D. Cooley, P.J. Lee, and D.C. Larbalestier, *Phys. Rev. B* **53**, 6638 (1996).
- ¹³ A. Godeke, *Supercond. Sci. Technol.* **19**, R68 (2006).
- ¹⁴ C.G. Zhuang, S. Meng, H. Yang, Y. Jia, H.H. Wen, X.X. Xi, Q.R. Feng, and Z.Z. Gan, *Supercond. Sci. Technol.* **21**, 082002 (2008).
- ¹⁵ M. Miura, S. Adachi, T. Shimode, K. Wada, A. Takemori, N. Chikumoto, K. Nakao, and K. Tanabe, *Appl. Phys. Express* **6**, 093101 (2013).
- ¹⁶ H. Sato, T. Katase, W.N. Kang, H. Hiramatsu, T. Kamiya, and H. Hosono, *Phys. Rev. B* **87**, 064504 (2013).
- ¹⁷ Y. Zhang, C.T. Nelson, S. Lee, J. Jiang, C.W. Bark, J.D. Weiss, C. Tarantini, C.M.

Folkman, S.-H. Baek, E.E. Hellstrom, D.C. Larbalestier, C.-B. Eom, and X. Pan, Appl. Phys. Lett. **98**, 042509 (2011).

¹⁸ K. Iida, J. Hänisch, C. Tarantini, F. Kurth, J. Jaroszynski, S. Ueda, M. Naito, A. Ichinose, I. Tsukada, E. Reich, V. Grinenko, L. Schultz, and B. Holzapfel, Sci. Rep. **3**, (2013).

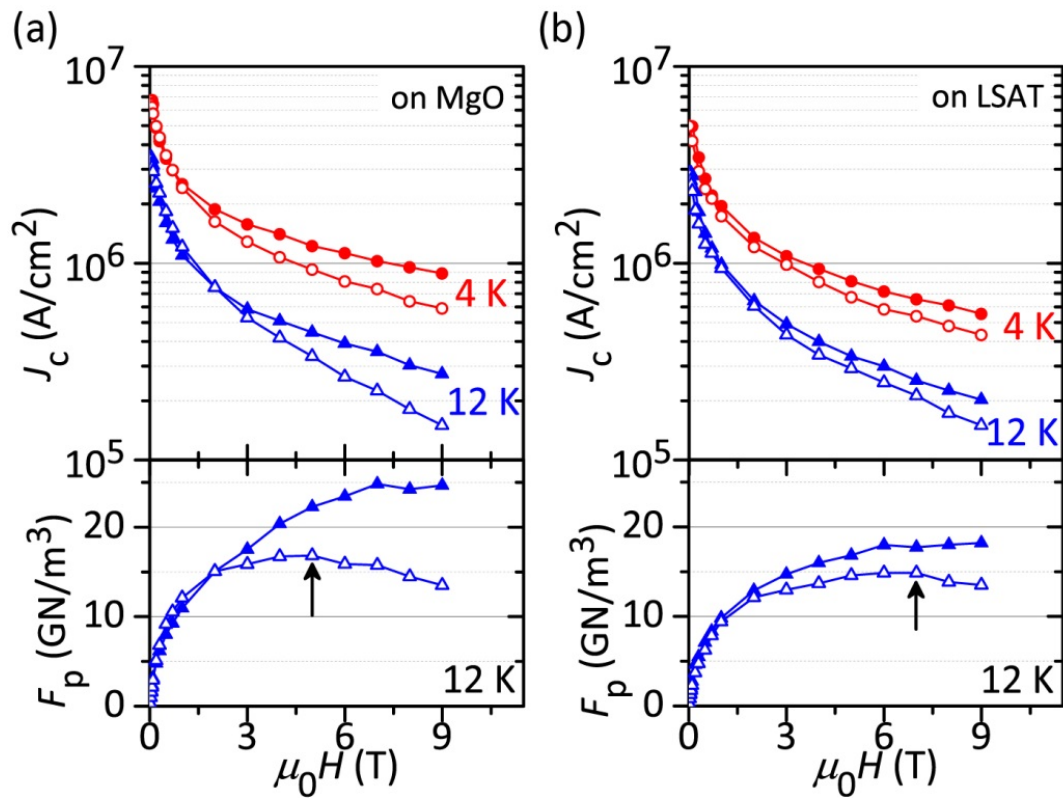


Figure 7 - 1. External magnetic field dependence of J_c (upper panels) and F_p (bottom panels) for BaFe₂As₂:P epitaxial films on MgO (a) and on LSAT (b) substrates. Closed and open symbols indicate the J_c and F_p obtained under $H // a-b$ plane and $H // c$ -axis, respectively.

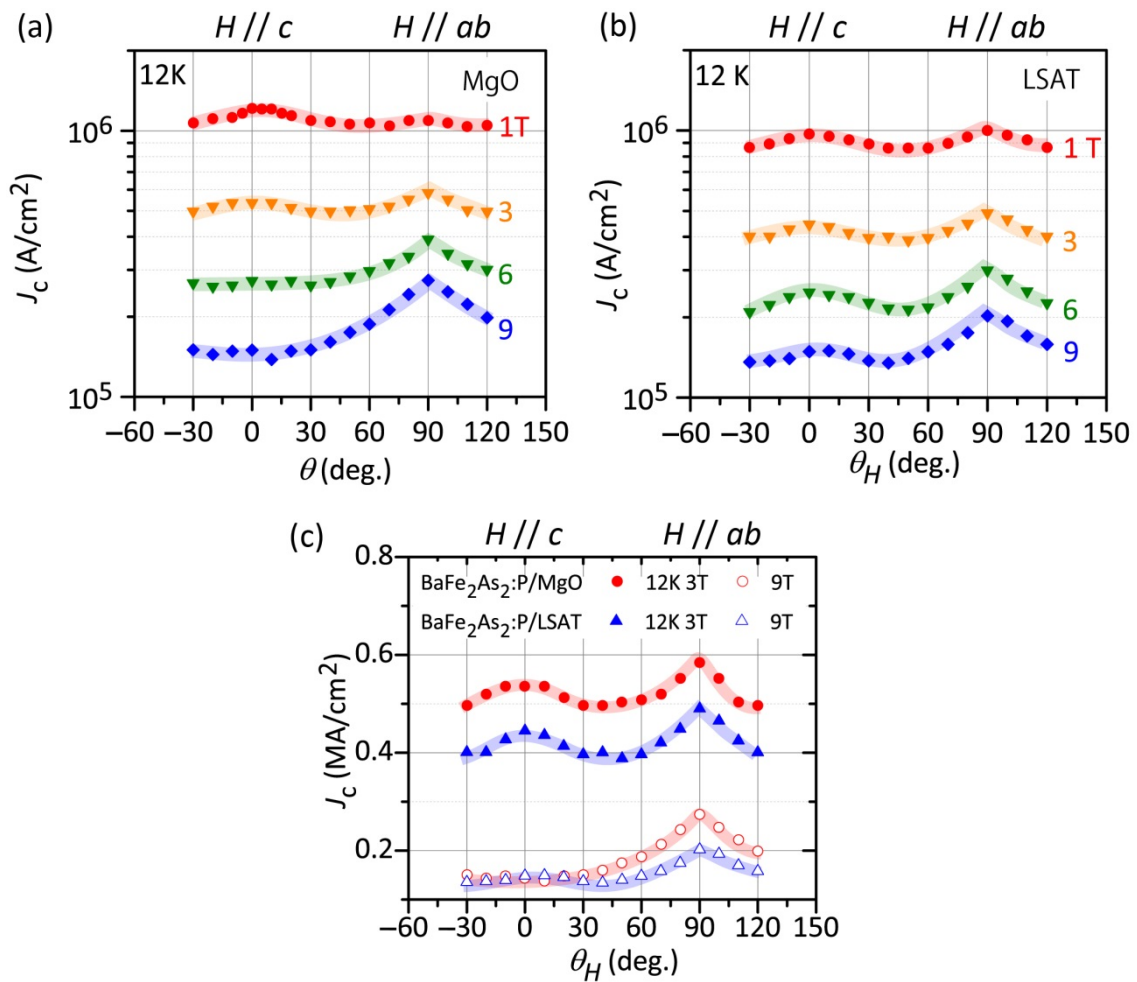


Figure 7 - 2 Critical current density J_c as a function of applied magnetic-field angle θ_H for BaFe₂As₂:P epitaxial films (a) on MgO and (b) on LSAT at 12 K. Measured at 1 – 9 T. (c) Data at 3 and 9 T for BaAs₂Fe₂:P on LSAT are compared with those on MgO

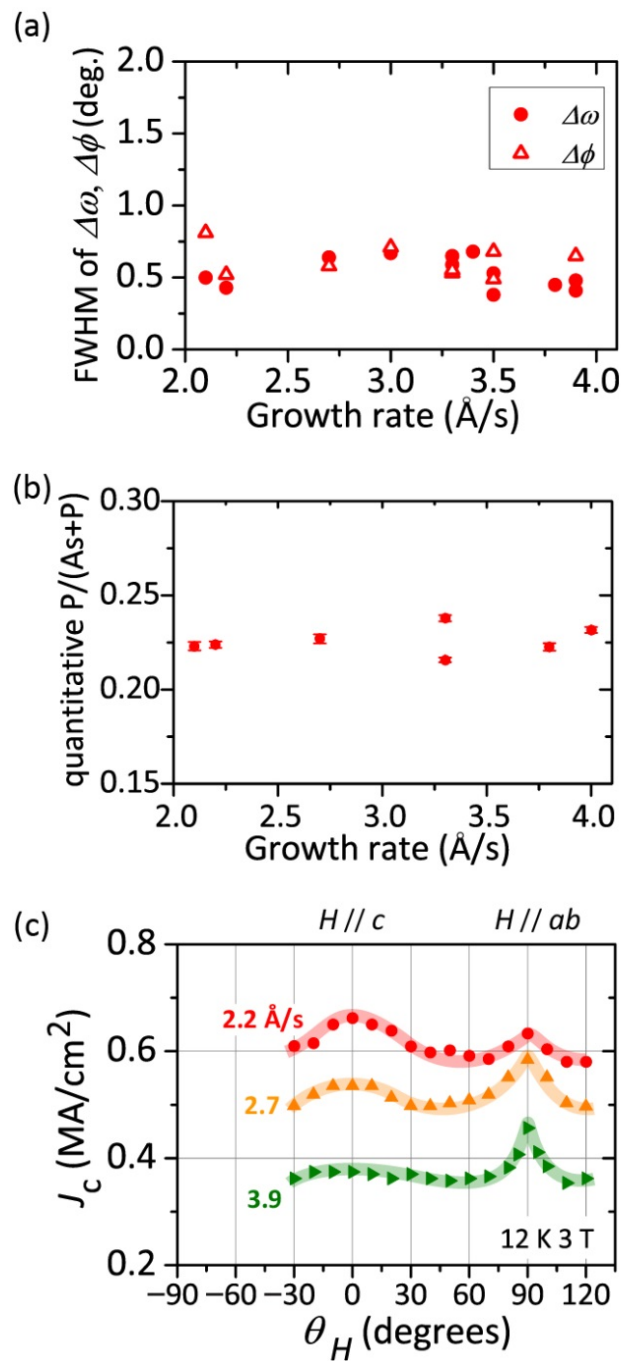


Figure 7 - 3 Growth rate dependence of crystallinity, chemical composition and vortex pinning property. (a) Dependence of FWHM of $\Delta\omega$ and $\Delta\phi$ on growth rate of BaFe_2As_2 :P films grown at the optimum T_s . (b) Quantitative P concentration of thin films grown at the various growth rate. (c) Critical current density J_c as a function of angle of applied magnetic field θ_H for BaFe_2As_2 :P epitaxial films grown at three growth rates, with $\mu_0H = 3\text{ T}$ and $T = 12\text{ K}$.

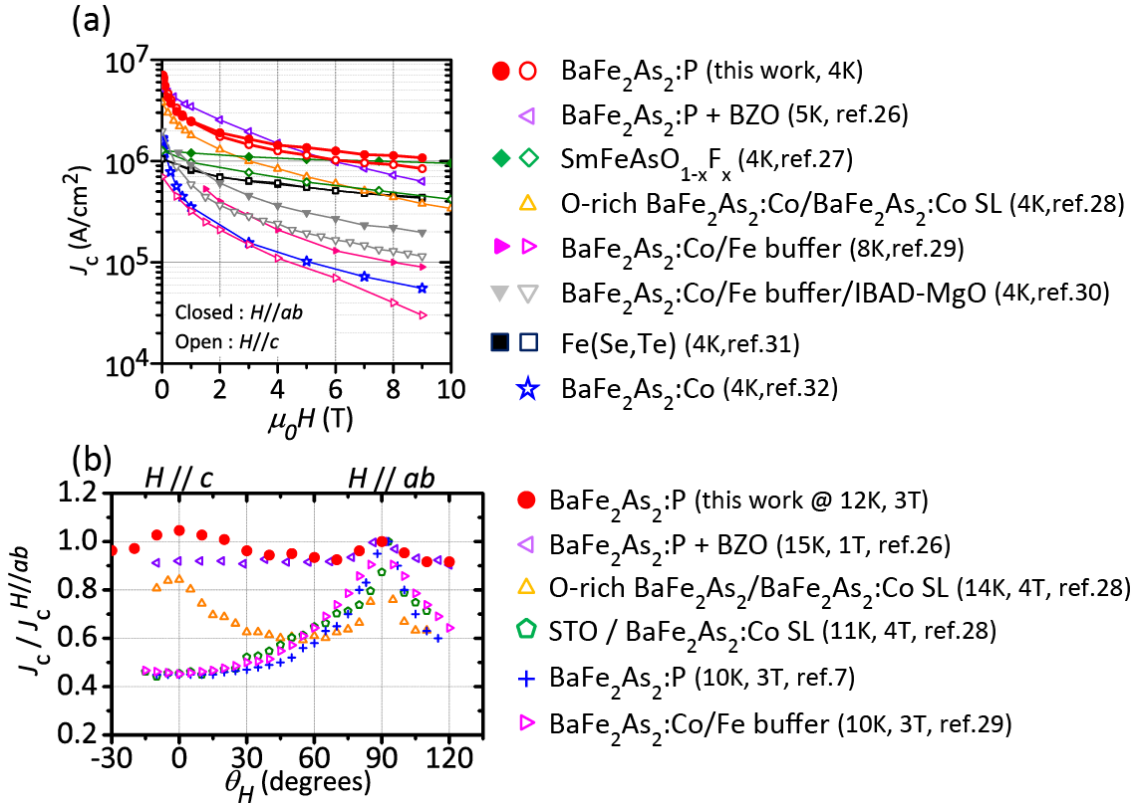


Figure 7 - 4 (a) Critical current density J_c as a function of magnetic-field H for BaFe₂As₂:P epitaxial film grown at the optimum T_s (1050 °C) and growth rate (2.2 Å/s) (circles). Open and closed symbols show the data obtained by applying $H // c$ and $H // ab$, respectively. (b) Dependence of J_c (normalized to $J_c^{H//ab}$) on angle of external magnetic field θ_H for BaFe₂As₂:P epitaxial film at 12 K and 3 T (circles). Also shown for comparison are the data for BaFe₂As₂:P + 3 mol% BaZrO₃ nanoparticles (left-pointing triangles),⁵ SmFeAsO_{1-x}F_x (diamonds),¹⁸ O-rich BaFe₂As₂/BaFe₂As₂:Co superlattice (SL) (triangles),⁷ STO/BaFe₂As₂:Co SL (pentagons),⁷ BaFe₂As₂:Co/Fe buffer (right-pointing triangles),^[29] BaFe₂As₂:P (crosses),¹⁵ BaFe₂As₂:Co/Fe/IBAD-MgO (inverse triangles),⁹ Fe(Se,Te) (squares).¹⁰ and BaFe₂As₂:Co (stars).¹¹

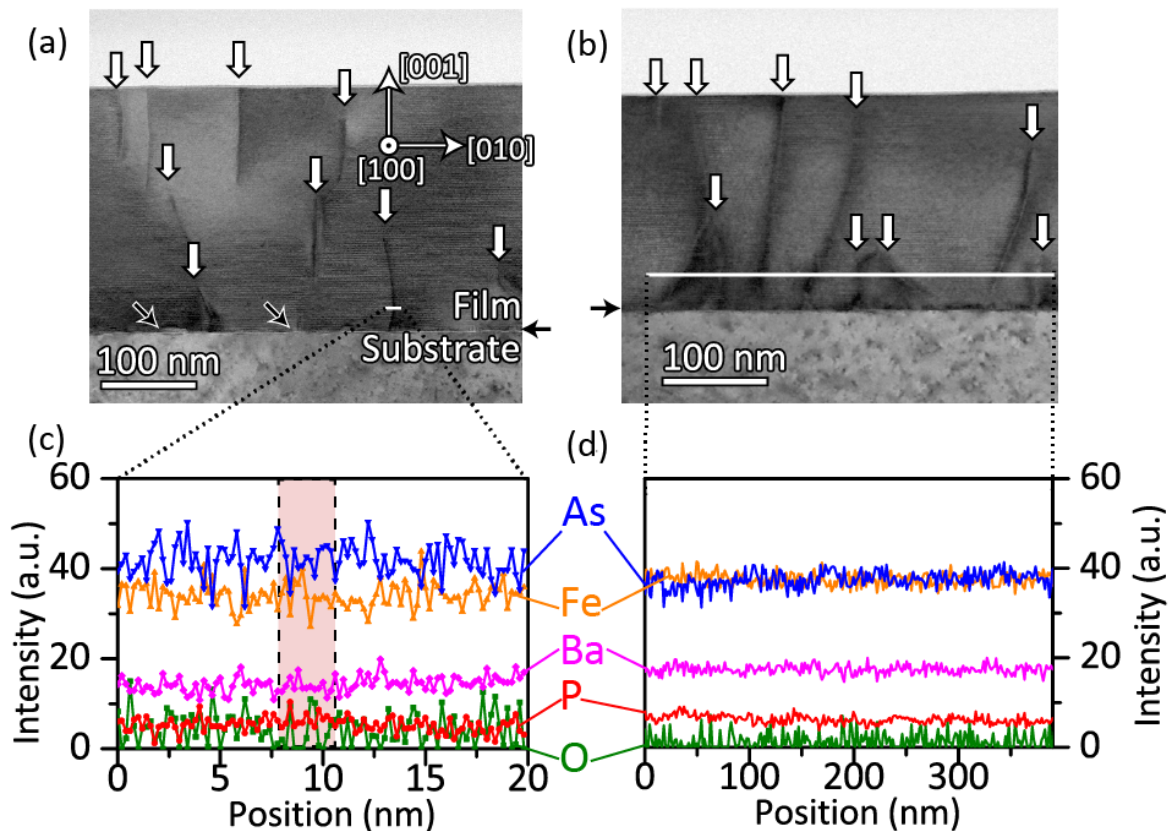


Figure 7 - 5 Cross-sectional bright-field STEM images of BaFe₂As₂:P epitaxial films grown at the growth rates (a) 2.2 Å/s and (b) 3.9 Å/s. The horizontal black arrow on the side of each figure indicates the heterointerface between the substrate and the BaFe₂As₂:P epitaxial film. The vertical white arrows indicate the vertical defects, and the slanted black arrows indicate oxygen-rich island structures. Panels (c) and (d) show the results of an STEM-EDXS line scan along the horizontal line shown in panels (a) and (b), respectively. The dashed shaded region in panel (c) corresponds to the vertical defect in panel (a).

Chapter 8: Isotropic J_c properties of phosphorus-doped BaFe₂As₂ films on practical tape-substrates: Toward future applications to coated conductors

8.1. Introduction

To obtain the high-performance coated conductor of REBa₂Cu₃O_{7- δ} (REBCO, RE = rare earth), misorientation angle of MgO layer ($\Delta\phi_{\text{MgO}}$) of practical tape substrates should be lower than 5°. However, as it was mentioned in chapter 1, iron-based superconductors have great potential for high magnetic field applications such as superconducting wires and tapes due to their good grain boundary properties¹, large upper critical magnetic fields over 50 T and small anisotropy factors². In fact, Katase et al.³ successfully fabricated the same-quality Ba(Fe_{1-x}Co_x)₂As₂ films on roughly aligned tape substrate ($\Delta\phi_{\text{MgO}} = 7^\circ$). In chapters 6 and 7, BaFe₂(As_{1-x}P_x)₂ epitaxial films successfully fabricated and they exhibit high J_c . Optimizing the growth rate, c -axis oriented vortex pinning centers were successfully introduced and their isotropy of J_c and self-field J_c are improved. As a result, these films exhibit the highest J_c over 1 MA/cm² at 9 T among iron-based superconductor thin films reported so far.

In this study, we fabricated BaFe₂(As_{1-x}P_x)₂ film on practical tape-substrate [i.e. IBAD-MgO buffered metal-tape substrates (IBAD substrate, Figure 8 - 1)] by pulsed laser deposition and characterized their crystallinities, doping concentration dependence of electron transport properties and misorientation-angle ($\Delta\phi_{\text{MgO}}$) dependence of J_c properties.

8.2. Experimental procedure

8.2.1. Thin film fabrication on IBAD substrates

BaFe₂(As_{1-x}P_x)₂ films of 150–200 nm thickness were grown on IBAD substrates (made by iBeam Materials, Inc.. Detail growth condition is described in ref⁴) by PLD. Optimally P-doped polycrystalline BaFe₂(As_{0.7}P_{0.3})₂ disks were used as the PLD targets at first to optimize the growth condition of thin film. After the optimization of the growth temperature, BaFe₂(As_{1-x}P_x)₂ ($x = 0.35, 0.40$ and 0.45) targets were employed as the PLD target to discuss and improve the properties. The pulsed-laser excitation source was the second harmonic of an Nd:YAG laser (wavelength = 532 nm, repetition rate = 10 Hz, laser fluence ~ 3 J/cm²). The base pressure of the growth chamber was approximately 5×10^{-7} Pa. To heat the IBAD-substrate uniformly, a thicker Mo plate (thickness is 1 mm) was tightly contacted to the backside of the IBAD-substrate and heated by focused infrared light. First, we varied T_s from 500 to 1300 °C by maintaining similar growth rates of ~ 2.2 Å/s, which is almost the same growth rate optimized for the epitaxial growth of BaFe₂(As_{1-x}P_x)₂ (detail was mentioned in chapter 6). After finding the optimum T_s , doping concentration and $\Delta\phi_{\text{MgO}}$ were varied with fixed growth condition. In this study, IBAD-sbustrates with $\Delta\phi_{\text{MgO}} = 4^\circ$ and 8° were used.

8.2.2. Characterization

To determine the crystalline phases and the small amount of impurity phases, θ -coupled 2θ -scan XRD measurements were performed with a high-power conventional XRD apparatus. The crystallinity of the epitaxial films was characterized on the basis of FWHM of the out-of-plane rocking curves ($\Delta\omega$) of 002 diffraction and the in-plane rocking curves ($\Delta\phi$) of 200 diffraction with a high-resolution XRD

apparatus [HR-XRD]. The chemical composition was determined from electron-probe microanalyzer (EPMA). For quantitative analyses, we employed the ZAF correction method which was also used to evaluate the chemical composition of BaFe₂(As_{1-x}P_x)₂ epitaxial films on single-crystal substrates [detail measurement condition is described in chapter 6]. To avoid the matrix effect from hastelloy-metal-tape, acceleration voltage of electron beam was adjusted with monitoring the spectrum of Ni-K α [Figure 8 - 2 (a) and (b)] because a hastelloy consist of Ni-based alloy.

To examine the transport properties, the films were patterned into microbridges by photolithography and an Ar milling process [Figure 8 - 2 (c)]. Temperature (T) dependence of electrical resistivity (ρ) was measured by the four-probe method with a physical property measurement system. The transport J_c was determined from voltage–current curves with the criterion of 1 μ V/cm under an external magnetic field (H) of up to 9 T. The angle θ_H of the applied H was varied from -30 to 120° (0 and 90° corresponding to $H // c$ -axis normal to the film surface and $H // ab$ plane, respectively).

8.3. Results and discussion

8.3.1. Optimization of growth temperature and structural characterization

Figure 8 - 3 show the summary of growth condition of BaFe₂(As_{1-x}P_x)₂ epitaxial films on IBAD-substrate by using BaFe₂(As_{0.7}P_{0.3})₂ disks as the PLD target. Figure 3 (a) show the relationship between growth temperature, c -axis and chemical composition. When $T_s \leq 1000$ °C [“Random oriented” region in Figure 8 - 3 (a) and lower 2 XRD pattern in Figure 8 - 3 (b)], the films were nonoriented or preferentially oriented along the c -axis along with a smaller portion of nonoriented BaFe₂As₂:P crystallites. In XRD

patterns, the diffraction peak of MgO layer and halo peak of a-Y₂O₃ were observed with the diffractions from BaFe₂(As_{1-x}P_x)₂ crystallites. When T_s was increased to 1050 °C [“Epitaxial” region in Figure 8 - 3 (a) and middle XRD pattern in Figure 3 (b)], epitaxial BaFe₂As₂:P films were obtained; that is, only 00 l diffractions were observed out of plane. It should be note that halo peak of a-Y₂O₃ were diminished and the diffractions of crystal Y₂O₃ were observed $T_s > 1000^\circ\text{C}$. These results indicate that the a-Y₂O₃ layer start to crystallize over 1000°C and it should be paid attention to the deterioration with the crystallization of a-Y₂O₃ layer (e.g. crystallinity and roughness). At $T_s \geq 1250$ °C [“00 l & $hh0$ ” region Fugure 3 (a) and upper XRD pattern in Figure 8 - 3 (b)], 00 l and $hh0$ preferential orientations were observed. These trend is same as in the case of BaFe₂(As_{1-x}P_x)₂ (see chapter 6) and Ba(Fe_{1-x}Co_x)₂As₂ epitaxial films⁵ on single crystal MgO (SC-MgO).

Increasing the T_s , BaFe₂(As_{1-x}P_x)₂ film structure exhibit the shrinkage of c -axis and chemical composition of the film slightly increase (~ 1%). In the epitaxial region, x become 0.21 – 0.22, which is lower than that of the nominal composition of bulk target. According to the results of single crystal of BaFe₂(As_{1-x}P_x)₂, the chemical composition changes of ~ 1 % does not reasonable to change the lattice parameters from 12.93 to 12.83 (if the same shrinkage is generated by only doping concentration, it should be changed from 15 % to 33 %). Therefore, the origin of the the shrinkage of c -axis is epitaxial strain with improvement of the crystallinity and epitaxy. In fact, the lattice parameters have strain structure (i.e. expanded along a -axis and compressed along c -axis) as discussed later.

The chemical composition of the BaFe₂(As_{1-x}P_x)₂ film on IBAD-substrates analyzed by EPMA. The proportion of the (As+P)/Ba ~ 1.7. Compared with

BaFe₂(As_{1-x}P_x)₂ films on SC-MgO and single-crystal LSAT, which have stoichiometric chemical composition, the chemical composition of the BaFe₂(As_{1-x}P_x)₂ on IBAD is not stoichiometric. The origin of this properties are still unclear but there are possible origin: oxygen diffusion from IBAD-substrates and chemical reaction as described in chapter 2 and 6.

8.3.2. Comparison of the electron transport properties between BaFe₂(As_{0.78}P_{0.22})₂ films on IBAD-substrate and those on MgO single-crystal substrates

Figure 8 - 4 (a) show the out-of-plane HR-XRD pattern of BaFe₂(As_{0.78}P_{0.22})₂ epitaxial film on IBAD-substrate. Symmetric *00l* diffractions are observed with the diffraction of MgO, Y₂O₃ and hastelloy. Figure 8 - 4 (b) show the ϕ scan of 103 diffraction of BaFe₂(As_{0.78}P_{0.22})₂ and 202 diffraction of MgO. Clear 4-fold symmetric peaks of BaFe₂(As_{0.78}P_{0.22})₂ 103 and MgO 202 observed in ϕ same position. This result indicate that BaFe₂(As_{0.78}P_{0.22})₂ was epitaxially grown on MgO with cube-on-cube configuration (i.e. the relationship of [001] BaFe₂As₂:P || [001] MgO for out-of-plane and [100] BaFe₂As₂:P || [100] MgO for in-plane).

Next, the crystallinity of the BaFe₂(As_{0.78}P_{0.22})₂ is compared with that of the BaFe₂(As_{0.78}P_{0.22})₂ on SC-MgO. Figure 8 - 4 (c) and (d) show the normalized rocking curves of the 004 and 200 reflections, respectively. In the case of BaFe₂(As_{0.78}P_{0.22})₂ on SC-MgO, the FWHMs of $\Delta\omega$ and $\Delta\phi$ were 0.6 degrees. On the other hand, when the films were grown on IBAD-substrates, the FWHMs of $\Delta\omega$ and $\Delta\phi$ were 1.3 and 2.9 degrees, respectively. The degradation of the crystallinity is caused by the larger $\Delta\phi_{\text{MgO}}$ of IBAD-substrate than that of SC-MgO. It should be note that $\Delta\phi$ of BaFe₂(As_{0.78}P_{0.22})₂ is almost same as $\Delta\phi_{\text{MgO}}$. In the case of the fabrication of Ba(Fe,Co)₂As₂ on IBAD-substrates³, the $\Delta\phi$ of BaFe₂(As_{0.78}P_{0.22})₂ is smaller than $\Delta\phi_{\text{MgO}}$, which would be

originated from self-epitaxy effect. This means that BaFe₂(As_{0.78}P_{0.22})₂ has low reduction rate of $\Delta\phi$ as a function of the thickness or crystal Y₂O₃ layer generated by high temperature growth deteriorates the crystallinity of top layer.

Figure 8 - 4 (e) indicated the summary of the lattice parameters of BaFe₂(As_{0.78}P_{0.22})₂ single crystal, BaFe₂(As_{0.78}P_{0.22})₂ epitaxial films on SC-MgO and that on IBAD-substrate. As it discussed in chapter 6, the thin film has strained structure caused by the lattice mismatch. In the case of MgO substrates, MgO has larger lateral lattice parameter than that of BaFe₂(As_{0.78}P_{0.22})₂. Therefore, BaFe₂(As_{0.78}P_{0.22})₂ has expanded structure along *ab*-plane caused by the tensile strain. Compared the lattice parameters of BaFe₂(As_{0.78}P_{0.22})₂ on IBAD-substrates and SC-MgO, BaFe₂(As_{0.78}P_{0.22})₂ on IBAD-substrates has more relaxed structure than that on SC-MgO. This is consistent of the poor crystallinity of BaFe₂(As_{0.78}P_{0.22})₂ and one of the reason of lower T_c of BaFe₂(As_{0.78}P_{0.22})₂ on IBAD-substrates as discussed later.

Figure 8 - 5 (a) shows $\rho - T$ curves of BaFe₂(As_{0.78}P_{0.22})₂ on IBAD-substrates and SC-MgO. It should be note that T_c^{zero} of BaFe₂(As_{0.78}P_{0.22})₂ on IBAD-substrate (~ 21 K) is lower than that of film on SC-MgO (~ 25 K). As shown in Figure 8 - 4 (e), BaFe₂(As_{0.78}P_{0.22})₂ on IBAD-substrate has more relaxed structure than that of BaFe₂(As_{0.78}P_{0.22})₂ on SC-MgO. It is reported that the tensile strain induces the decrease of the optimal doping concentration and shift the superconducting dome to lower doping region from $\sim 33\%$ to $\sim 25\%$. In the case of BaFe₂(As_{0.78}P_{0.22})₂ on SC-MgO, the films were strongly strained caused by their high crystallinity and T_c becomes higher than that of the BaFe₂(As_{0.78}P_{0.22})₂ single crystal though the doping concentration was under-doped region as the bulk. Therefore, the reduction of the T_c caused by the weaker tensile strain and doping concentration should be increased to increase their T_c .

Figure 8 - 5 (b) show the transport J_c of BaFe₂(As_{0.78}P_{0.22})₂ on IBAD-substrate as a function of magnetic field. Reflecting the lower T_c , the self-field J_c (J_c^{self}) is lower than that of single crystal. Moreover, the difference of the J_c^{self} between 4 K and 12 K [$J_c^{\text{self}}(12\text{K}) / J_c^{\text{self}}(4\text{K}) = 0.54$] is considerably larger than that of BaFe₂(As_{0.78}P_{0.22})₂ on SC-MgO [$J_c^{\text{self}}(12\text{K}) / J_c^{\text{self}}(4\text{K}) = 0.18$]. This rapid decay of J_c^{self} is observed around T_c in the case of the Ba(Fe,Co)₂As₂ epitaxial films⁶. These results indicate the doping concentration should be increased to improve their J_c .

8.3.3. Optimization of the phosphorous concentration

Next, the doping concentration is optimized by using the variation of the bulk target of BaFe₂(As_{1-x}P_x)₂ ($x = 0.35, 0.40$ and 0.45). Figure 8 - 6 (a) show the results of the chemical composition analysis of BaFe₂(As_{1-x}P_x)₂ epitaxial films. Increasing the nominal composition, the doping concentration of film continuously increase. These results are clear evidence that the doping concentration can be controlled by target composition. Figure 8 - 6 (b) and (c) show the ρ - T curves of BaFe₂(As_{1-x}P_x)₂ film on IBAD-substrate as a function of the doping concentration x . As shown Figure 8 - 6 (b), BaFe₂(As_{1-x}P_x)₂ with $x = 0.28$ show the highest T_c zero at 22.4 K. $\rho(T) / \rho(300\text{K})$ show the continuous decay rate with the increase of x . These trend is totally same as the bulk BaFe₂(As_{1-x}P_x)₂.

Figure 8 - 7 (a - d) show the transport J_c of BaFe₂(As_{1-x}P_x)₂ epitaxial films on IBAD-substrate as a function of magnetic field. With increase its T_c , BaFe₂(As_{1-x}P_x)₂ with $x = 0.28$ exhibits the small difference of the J_c^{self} between 4 K and 12 K [$J_c^{\text{self}}(12\text{K}) / J_c^{\text{self}}(4\text{K})$] and J_c drastically increase at low magnetic field at 12 K with increasing of J_c^{self} . In addition, the J_c at $H // ab$ and $H // c$ is very close to each other at optimally

doped sample. This trend is consistent with the anisotropy factor of BaFe₂(As_{1-x}P_x)₂⁷ but these kinds of almost same J_c values in $H // ab$ and $H // c$ cannot be understood only by the intrinsic pinning anisotropy of the BaFe₂(As_{1-x}P_x)₂. Therefore, the pinning centers along c -axis and/or point-like pinning centers⁸ should be introduced into the film. Figure 8 - 7 (e) and (f) show the angular dependence of J_c of BaFe₂(As_{0.72}P_{0.28})₂. As shown here, J_c of BaFe₂(As_{0.72}P_{0.28})₂ is isotropic and the anisotropy of J_c is much lower than that of that of the SL thin films,⁹ and is comparable to that of the BaFe₂(As_{1-x}P_x)₂ films with artificial pinning centers created by BaZrO₃ nanoparticles¹⁰ and BaFe₂(As_{0.78}P_{0.22})₂ films on SC-MgO in optimized condition. J_c peaks are observed in $H // ab$ ($\theta_H = 90^\circ$) and $H // c$ ($\theta_H = 0^\circ$). The peak around $H // ab$ is originated from the intrinsic pinning center which is generated by the layered crystal structure of iron-based superconductors (chapter 1). On the other hand, the peak around $H // c$ is originated from extrinsic pinning centers. In the case of the BaFe₂(As_{1-x}P_x)₂, vertical dislocations and domain boundaries work as the extrinsic strong pinning centers. As it was mentioned above, the BaFe₂(As_{0.72}P_{0.28})₂ exhibits the comparable anisotropy with BaFe₂As₂:P films on SC-MgO. These results indicate that the pinning properties have been successfully controlled by growth condition even in the fabrication of BaFe₂(As_{1-x}P_x)₂ films on IBAD-substrates.

8.3.4. Fabrication and characterization of “roughly aligned” BaFe₂(As_{1-x}P_x)₂ films : Attractive properties for the practical application

Figure 8 - 8 shows the results of the XRD of BaFe₂(As_{1-x}P_x)₂ film on roughly aligned IBAD-MgO substrate. I could confirm c -axis orientation of BaFe₂(As_{1-x}P_x)₂ film on roughly aligned substrate with small domains which did not grow epitaxially (i.e. the small peaks of 112 diffraction were observed). In Figure 8 - 8 (b), the thin film

exhibit the 4 fold symmetric peaks in ϕ scan, therefore BaFe₂(As_{1-x}P_x)₂ films successfully grown on roughly aligned IBAD-MgO substrate epitaxially but the in-plane orientation becomes quite worse. Compared the crystallinities of two kinds of films on different IBAD substrates, BaFe₂(As_{1-x}P_x)₂ on roughly aligned substrate exhibits very wide rocking curve [Figure 8 - 8 (c) and (d)], especially in in-plane direction reflecting the poor crystallinity of IBAD substrates. As it mentioned above, the self-epitaxy effect are not observed in the case of the fabrication of BaFe₂(As_{1-x}P_x)₂ films on IBAD substrates.

Figure 8 - 9 (a) show the transport J_c of BaFe₂(As_{0.78}P_{0.22})₂ on roughly aligned IBAD-substrate as a function of magnetic field. It should be note that J_c of BaFe₂(As_{0.78}P_{0.22})₂ on roughly aligned IBAD-substrate exhibits higher J_c than the film on well-aligned IBAD-substrates ($\Delta\phi_{\text{MgO}} = 4^\circ$). J_c^{self} is almost same at 4 K and 12 K but the J_c of BaFe₂(As_{0.78}P_{0.22})₂ on roughly aligned IBAD-substrate show the strong vortex pinning at high magnetic field region with small anisotropy. Figure 8 - 9 (b) and (c) show the angular dependence of J_c at 4 K and 12 K. J_c peaks are observed in $H // ab$ ($\theta_H = 90^\circ$) and $H // c$ ($\theta_H = 0^\circ$). However, compared with these of BaFe₂(As_{0.78}P_{0.22})₂ on well-aligned IBAD-substrates, the peaks in $H // c$ still remain at 9T. these results indicate that the strong vortex pinning is introduced in the film on roughly aligned IBAD-substrate. These results are silimar to the vortex pinning properties of BaFe₂(As_{1-x}P_x)₂ on LSAT substrates. In the case of BaFe₂(As_{1-x}P_x)₂ on LSAT, many amount of domain boundaries are observed and they work as the strong vortex pinning centers. As it shown in Figure 8 - 8 (d), BaFe₂(As_{0.78}P_{0.22})₂ on well-aligned IBAD-substrates have poor crystallinity ($\Delta\phi \sim 8^\circ$) and it is easily estimated that there are many domain boundaries in the films. Therefore, these kinds of many domain

boundaries would work as the strong pinning centers in $BaFe_2(As_{0.78}P_{0.22})_2$ films on roughly aligned IBAD-substrates. These results indicate that this materials is robust to the deterioration of the crystallinity and promising for the future applications.

8.4. Conclusion

The fabrication of $BaFe_2(As_{1-x}P_x)_2$ films on IBAD-substrates has been demonstrated to show the potential for the practical applications. $BaFe_2(As_{1-x}P_x)_2$ epitaxial films were fabricated on IBAD-substrates and. Compared with the films on single crystal substrates, the films on IBAD-substrates has relaxed structure caused by the poor crystallinity and the optimal doping level is close to that of bulk $BaFe_2(As_{1-x}P_x)_2$ in terms of T_c . Utilizing the fabrication technique which is well-established in the case of the fabrication on single-crystal substrates, $BaFe_2(As_{1-x}P_x)_2$ epitaxial films exhibit the isotropic J_c properties ($J_c^{\min}/J_c^{\max} = 0.88$), which is most isotropic J_c performance in 122 type thin films. $BaFe_2(As,P)_2$ epitaxial films have been also fabricated on roughly aligned IBAD-substrates ($\Delta\phi_{MgO} = 8^\circ$) and they exhibits strong vortex pinning properties and higher J_c properties than that of $BaFe_2(As_{1-x}P_x)_2$ epitaxial films on aligned IBAD-substrates ($\Delta\phi_{MgO} = 4^\circ$). These results indicate that this material is robust to the deterioration of the crystallinity and promising for the future applications.

References

- ¹ T. Katase, Y. Ishimaru, A. Tsukamoto, H. Hiramatsu, T. Kamiya, K. Tanabe, and H. Hosono, *Nat. Commun.* **2**, 409 (2011).
- ² A. Yamamoto, J. Jaroszynski, C. Tarantini, L. Balicas, J. Jiang, A. Gurevich, D.C. Larbalestier, R. Jin, A.S. Sefat, M.A. McGuire, B.C. Sales, D.K. Christen, and D. Mandrus, *Appl. Phys. Lett.* **94**, 062511 (2009).
- ³ T. Katase, H. Hiramatsu, V. Matias, C. Sheehan, Y. Ishimaru, T. Kamiya, K. Tanabe, and H. Hosono, *Appl. Phys. Lett.* **98**, 242510 (2011).
- ⁴ C. Sheehan, Y. Jung, T. Holesinger, D.M. Feldmann, C. Edney, J.F. Ihlefeld, P.G. Clem, and V. Matias, *Appl. Phys. Lett.* **98**, 071907 (2011).
- ⁵ T. Katase, H. Hiramatsu, T. Kamiya, and H. Hosono, *Supercond. Sci. Technol.* **25**, 084015 (2012).
- ⁶ T. Katase, H. Hiramatsu, T. Kamiya, and H. Hosono, *Appl. Phys. Express* **3**, 063101 (2010).
- ⁷ M. Miura, S. Adachi, T. Shimode, K. Wada, A. Takemori, N. Chikumoto, K. Nakao, and K. Tanabe, *Appl. Phys. Express* **6**, 093101 (2013).
- ⁸ B. Maiorov, T. Katase, I.O. Usov, M. Weigand, L. Civale, H. Hiramatsu, and H. Hosono, *Phys. Rev. B* **86**, 094513 (2012).
- ⁹ S. Lee, C. Tarantini, P. Gao, J. Jiang, J.D. Weiss, F. Kametani, C.M. Folkman, Y. Zhang, X.Q. Pan, E.E. Hellstrom, D.C. Larbalestier, and C.B. Eom, *Nat. Mater.* **12**, 392 (2013).
- ¹⁰ M. Miura, B. Maiorov, T. Kato, T. Shimode, K. Wada, S. Adachi, and K. Tanabe, *Nat. Commun.* **4**, 2499 (2013).
- ¹¹ S. Kasahara, T. Shibauchi, K. Hashimoto, K. Ikada, S. Tonegawa, R. Okazaki, H. Shishido, H. Ikeda, H. Takeya, K. Hirata, T. Terashima, and Y. Matsuda, *Phys. Rev. B* **81**, 184519 (2010).

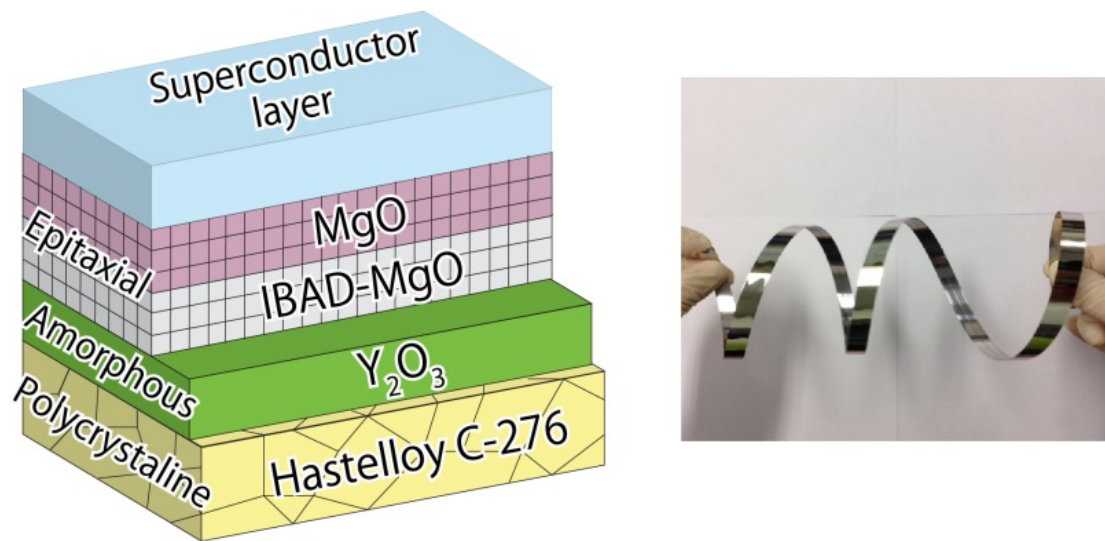


Figure 8 - 1 The images of practical tape substrate. (a) Schematic image of the cross-section of ion-beam-assisted-deposition-MgO buffered metal-tape-substrates (IBAD-substrate). (b) the picture of IBAD-substrate.

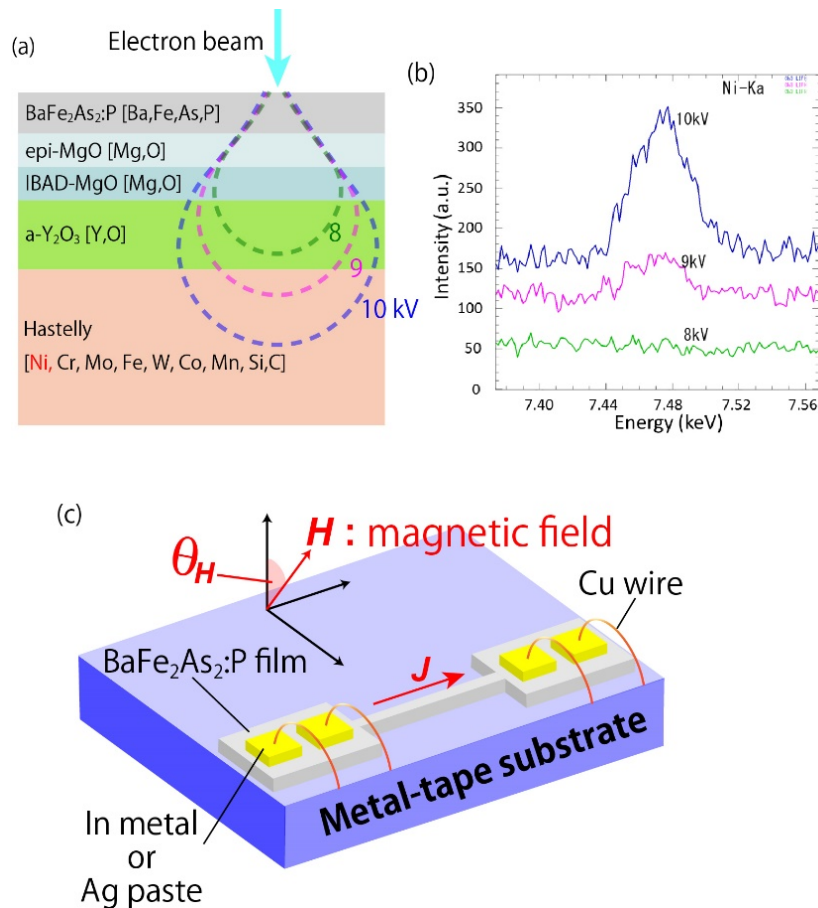


Figure 8 - 2. Chemical composition analysis and transport measurements of $BaFe_2(As_{1-x}P_x)_2$ epitaxial films on IBAD substrates (a) A Schematic image of the cross-section of $BaFe_2(As_{1-x}P_x)_2$ on IBAD substrate. Inside of the brackets indicate the elements which consist each layer. Dashed lines indicate the penetration area of electron beam. To avoid the matrix effects from hastelloy, acceleration voltage was decided at 8kV. (b) the acceleration voltage dependence of Ni-K α peak. (c) schematic image of $BaFe_2(As_{1-x}P_x)_2$ microbridge. The angle θ_H of the applied H was varied from -30 to 120° (0 and 90° corresponding to $H // c$ -axis normal to the film surface and $H // ab$ plane, respectively)

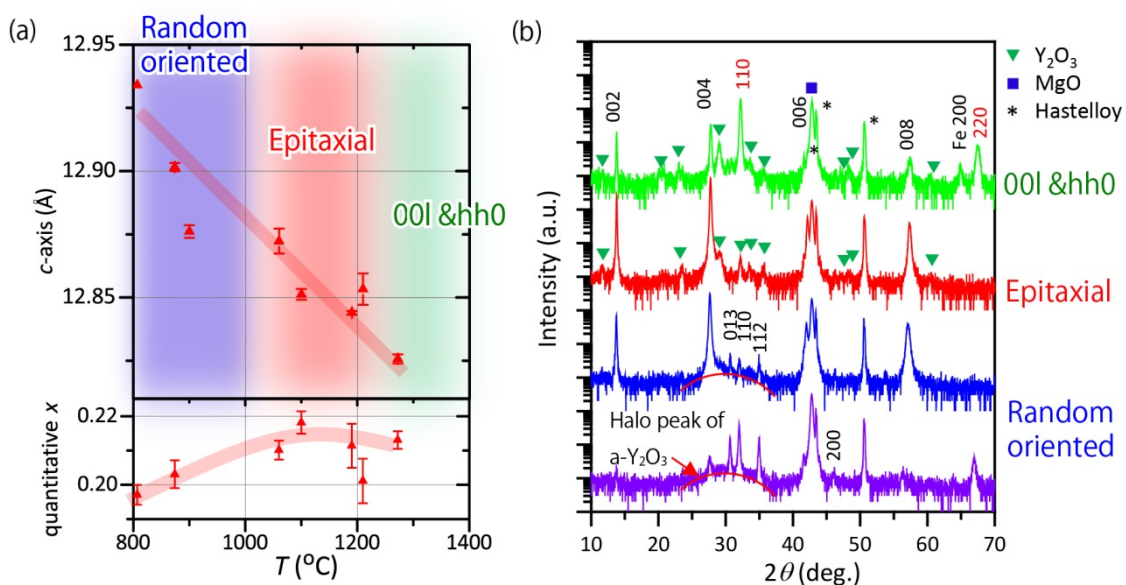


Figure 8 - 3 Growth condition of $BaFe_2(As_{0.78}P_{0.22})_2$ epitaxial films on IBAD-substrates. (a) Relationship between growth condition (substrate temperature T_s , c -axis length and doping concentration). Crystallographic orientation of $BaFe_2As_2:P$ films are also shown. Three regions with different orientation structures obtained with different T_s values are shown. (b) Typical XRD patterns, measured in Bragg–Brentano configuration, of $BaFe_2As_2:P$ thin films for the three T_s regions in panel (a). In $T_s > 1000$ °C, a - Y_2O_3 start to crystallize.

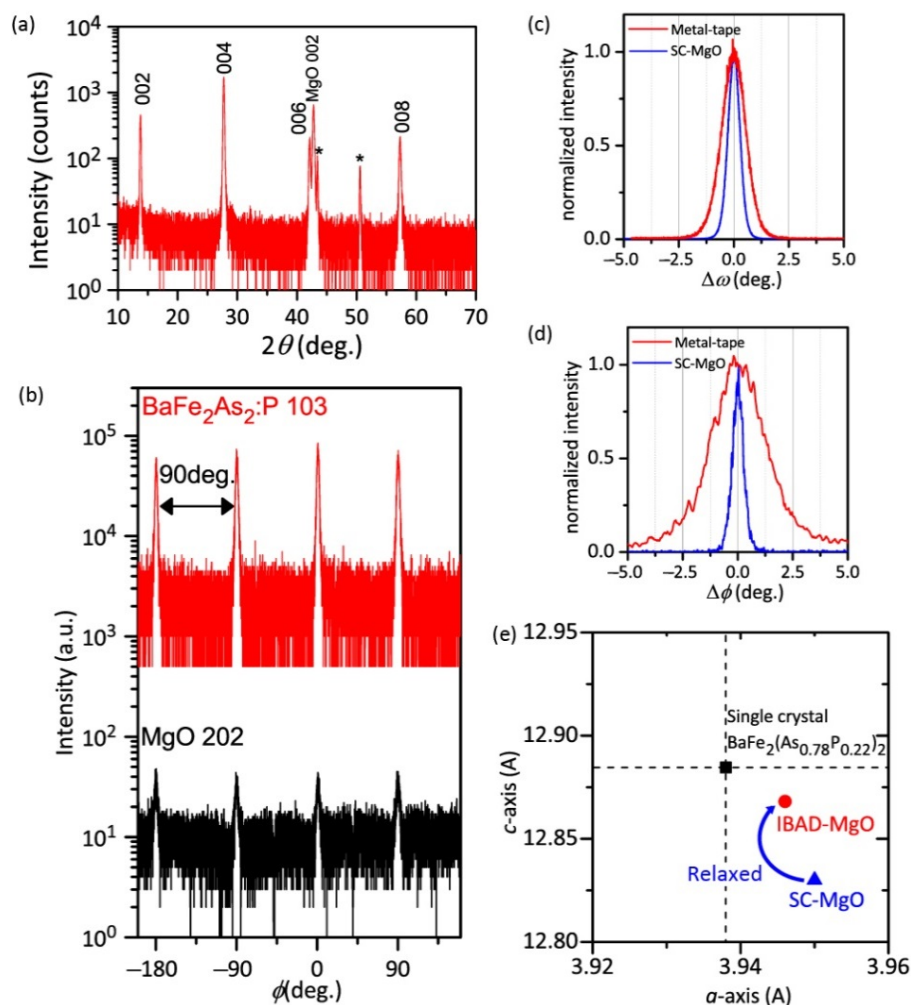


Figure 8 - 4. XRD patterns and structural parameters of $BaFe_2(As_{0.78}P_{0.22})_2$ epitaxial films on IBAD-substrates. (a) Out-of-plane ω -coupled 2θ patterns. (b) ϕ scan of 103 diffraction of $BaFe_2(As_{0.78}P_{0.22})_2$ and 202 diffraction of MgO. (c, d) Normalized rocking curves of the out-of-plane 004 (c) and the in-plane 200 reflections (d). For comparison, the rocking curves of $BaFe_2(As_{0.78}P_{0.22})_2$ epitaxial film on single-crystal MgO (SC-MgO) is referred from chapter 6. (e) Comparison of lattice parameters with those of $BaFe_2(As_{0.78}P_{0.22})_2$ epitaxial film on SC-MgO. Dotted lines indicates the lattice parameters of a single crystal $BaFe_2(As_{0.78}P_{0.22})_2$ taken from ref ¹¹.

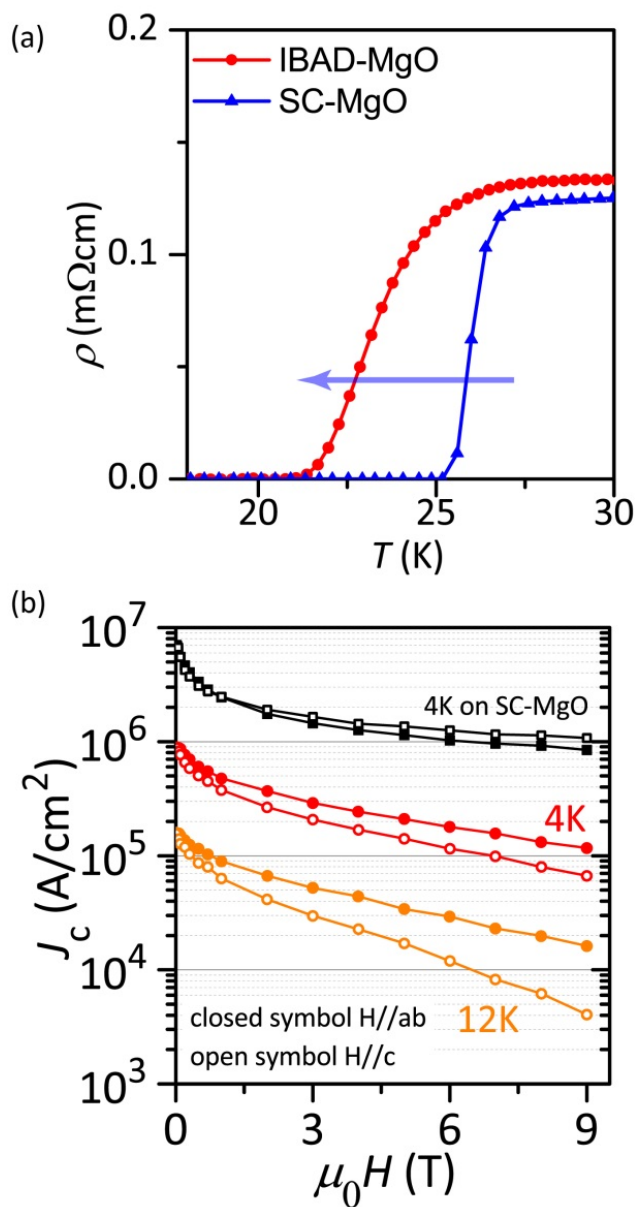


Figure 8 - 5. Comparison of the electron properties between $BaFe_2(As_{0.78}P_{0.22})_2$ on IBAD-substrate and that on single-crystal MgO substrate SC-MgO (a) Temperature dependence of resistivity ρ of $BaFe_2(As_{0.78}P_{0.22})_2$ film on IBAD-substrate and $BaFe_2(As_{0.78}P_{0.22})_2$ film on SC-MgO. (a) magnified figure around T_c (b) wide range ρ - T curves. (b) Transport J_c of $BaFe_2(As_{0.78}P_{0.22})_2$ on IBAD-substrate and that on SC-MgO as a function of magnetic field.

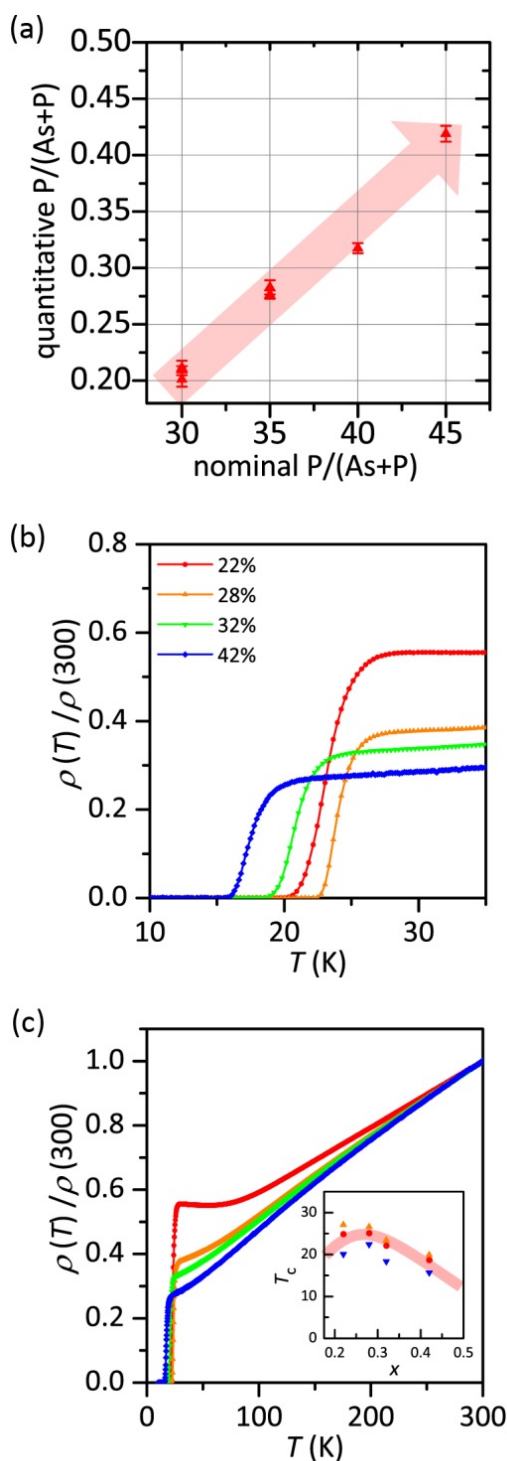


Figure 8 - 6. Doping concentration dependence of structural parameters and T_c . (a) Chemical composition analysis using EPMA. (b,c) Temperature dependence of resistivity ρ of $BaFe_2(As_{1-x}P_x)_2$ film on IBAD-substrate as a function of the doping concentration x . (b) magnified image around T_c . (c) Wide range : 10 – 300 K. Inset figure of (c) is phase diagram of $BaFe_2(As_{1-x}P_x)_2$. Circles, triangles and reversed triangles indicate T_c , T_c onset and T_c zero.

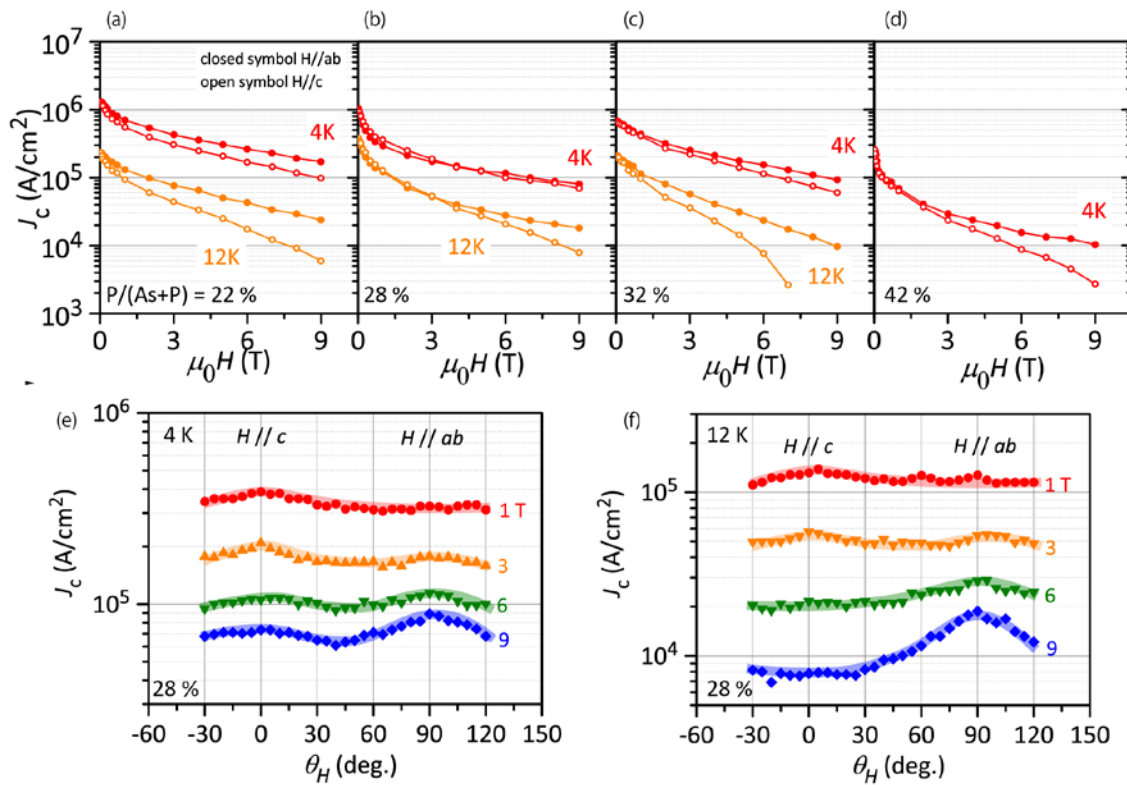


Figure 8 - 7. Doping concentration dependence of transport J_c . J_c of $P/(P+As) = 0.22$ (a), 0.28 (b), 0.32 (c) and 0.42 (d) as a function of magnetic field. (e, f) angular dependence of J_c of optimally-doped $BaFe_2(As_{1-x}P_x)_2$ film on IBAD-substrate at 4 K (e) and 12 K (f)

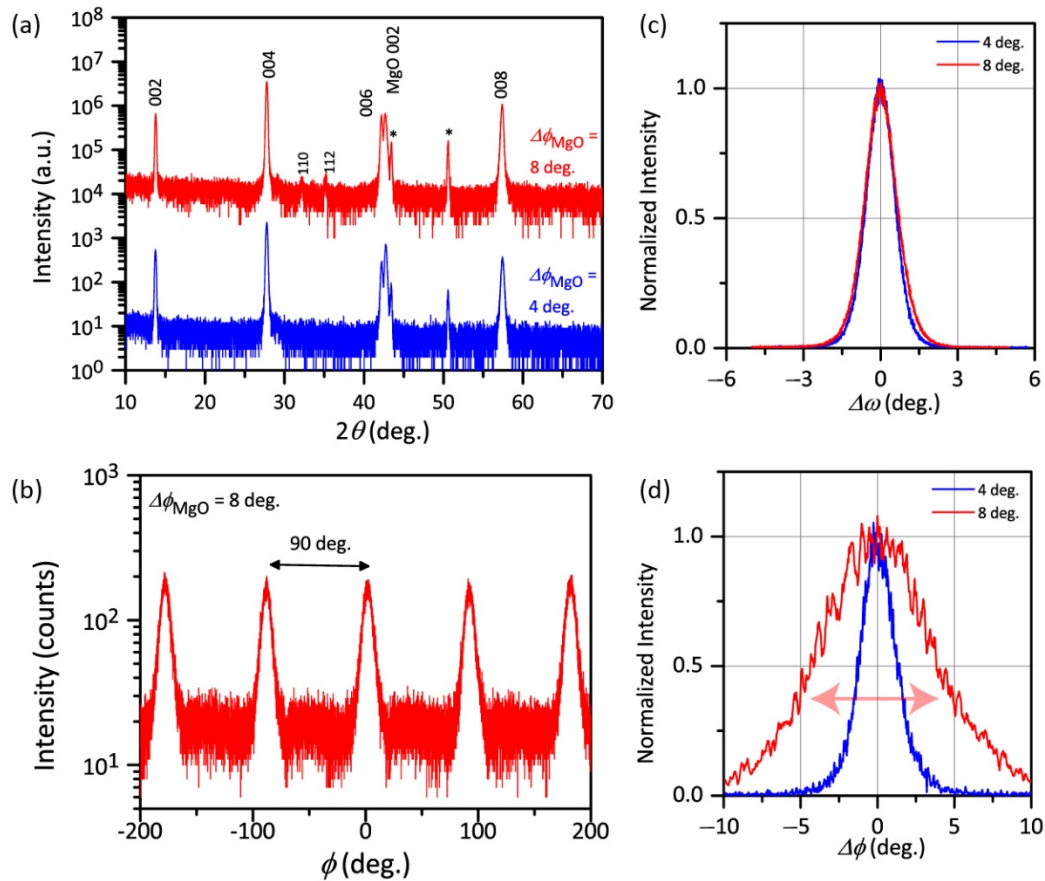


Figure 8 - 8. XRD patterns and structural parameters of $BaFe_2(As_{0.72}P_{0.28})_2$ epitaxial films on IBAD-substrates with $\Delta\phi_{MgO} = 8^\circ$. (a) Out-of-plan ω -coupled 2θ patterns. (b) ϕ scan of 103 diffraction of $BaFe_2(As_{0.72}P_{0.28})_2$. (c, d) Normalized rocking curves of the out-of-plane 004 (b) and the in-plane 200 reflections (c). For comparison, the rocking curves of $BaFe_2(As_{0.72}P_{0.28})_2$ epitaxial film on IBAD-substrate with $\Delta\phi_{MgO} = 4^\circ$ is plotted.

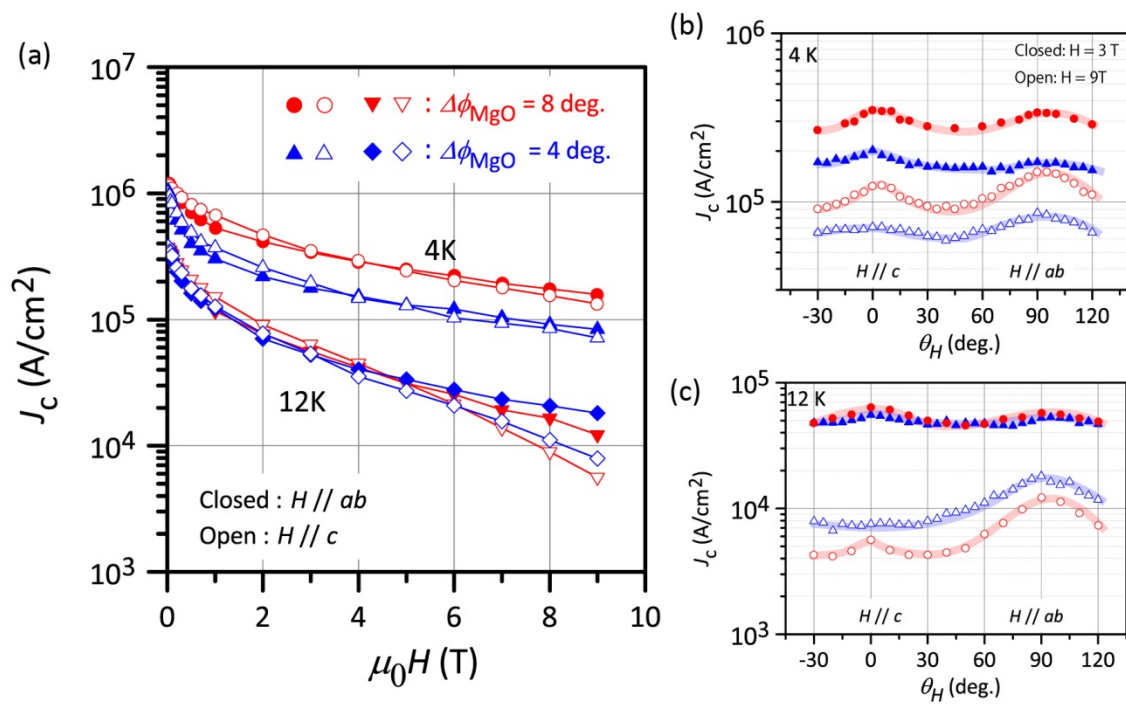


Figure 8 - 9. Misorientation angle dependence of transport J_c of $BaFe_2(As_{0.72}P_{0.28})_2$ on IBAD-substrates with $\Delta\phi_{MgO} = 4^\circ$ and 8° (a) Transport J_c as a function of magnetic field. (b, c) Angular dependence of J_c at 4 K (b) and 12 K (c)

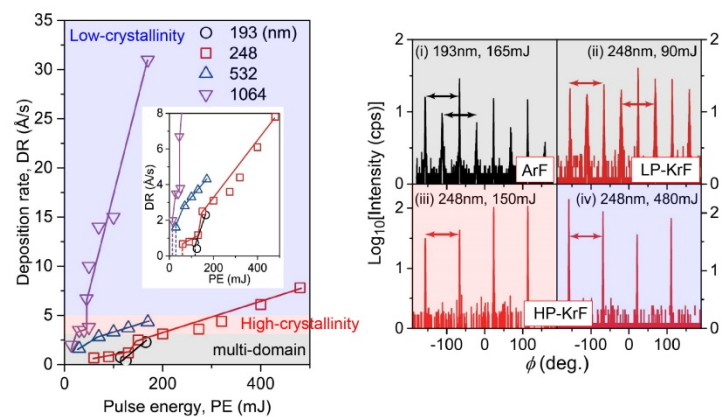
Chapter 9: General conclusion

I found the important parameters for epitaxial growth of many types of the 122-type iron-based superconductors to realize high performance and to discussed/clarified mechanism of their unique superconducting properties such as vortex pinning, and proposed a new design concept to enhance their T_c and J_c by utilizing the anisotropic pressure and microstructure engineering. As a result, I achieved the highest J_c and the most isotropic J_c on practically applied metal-tape substrates as well as single-crystal substrates among iron-based superconductors to date.

Each chapter is summarized as follows:

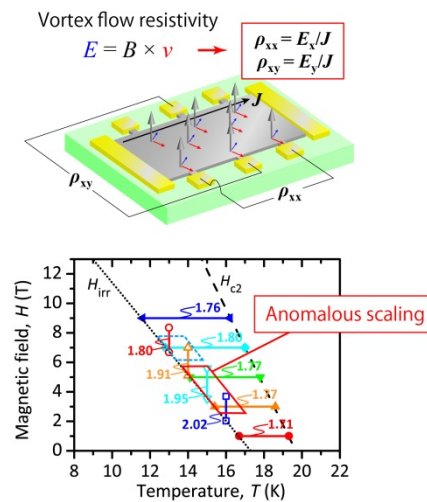
In chapter 2, $\text{Ba}(\text{Fe},\text{Co})_2\text{As}_2$ films were epitaxially grown by PLD and examined how the laser wavelength and pulse energy affected their growth by using four different excitation wavelengths. It was found that the optimal deposition rate does not depend on the type of laser (i.e., wavelength). This study also explains why the Nd:YAG laser is better for producing high- J_c $\text{Ba}(\text{Fe},\text{Co})_2\text{As}_2$ films with high crystallinity at a low laser power, and will improve the

fabrication of other iron-based superconductor films such as REFeAsO (RE : rare earth), $\text{BaFe}_2(\text{As},\text{P})_2$, and other types of superconductors.



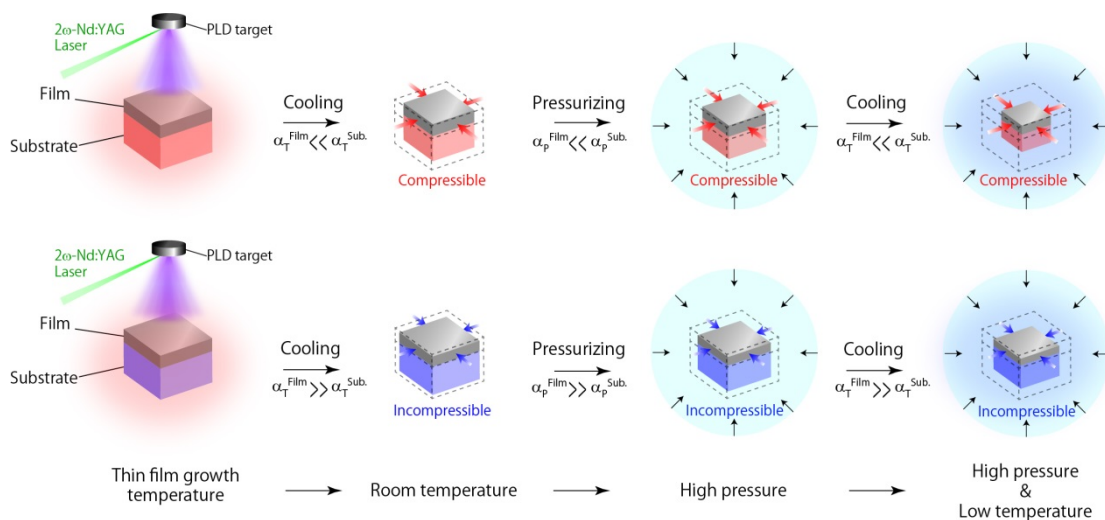
In chapter 3, the transport properties in a mixed state of a high- J_c $\text{Ba}(\text{Fe},\text{Co})_2\text{As}_2$

epitaxial film were investigated to understand the vortex pinning mechanism of $\text{Ba}(\text{Fe},\text{Co})_2\text{As}_2$. The $\rho_{xy} = A\rho_{xx}^\beta$ scaling behavior in the T sweep measurements shows constant β values less than 2.0 under magnetic fields up to 9 T. On the other hand, the β values clearly increase from 1.8 to 2.0 in the H sweep measurements as T increases from



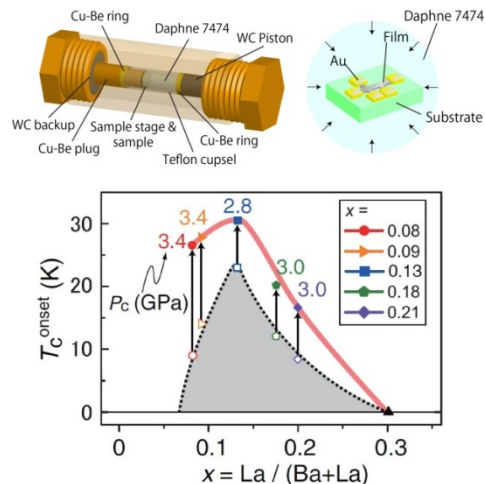
13 to 16 K. These results indicate that strong pinning centers trap the vortices introduced at low temperatures, but some of the vortices introduced at high temperatures are not trapped and that pinning weakens at higher temperatures near the normal state. These distinct scaling behaviors, which sharply contrast cuprates and MgB_2 , can be explained by the high-density intrinsic and extrinsic pinning centers in a $\text{Ba}(\text{Fe},\text{Co})_2\text{As}_2$ epitaxial film, which are consistent with wider vortex liquid phase.

In chapter 4, a novel design concept to induce the anisotropic pressure was proposed utilizing the differences in thermal expansion coefficients (α_T) and the compressibility (α_P) between $\text{Ba}(\text{Fe},\text{Co})_2\text{As}_2$ and substrates with epitaxial strain.



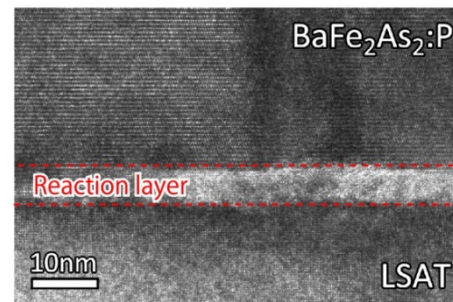
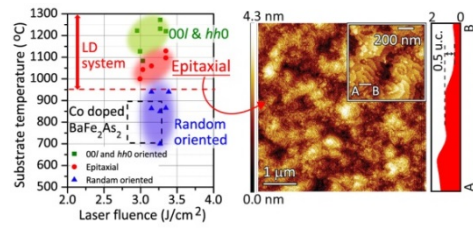
Affected from differences of α_T , as-grown films on fluoride substrates have more strained structures than those of films on oxide substrates. According to the results of high pressure experiments, $T_c(3\text{GPa}) - T_c(0)$ is proportional to the α_P of substrates and T_c of $\text{Ba}(\text{Fe},\text{Co})_2\text{As}_2$ thin films on BaF_2 enhanced compared with that of the single crystal. This would be the reason why the strongest anisotropic pressure is applied to the film by using the most compressible substrate (i.e., BaF_2) among four kinds of substrates examined. These results are also consistent with the Ehrenfest relationship derived from thermal expansion and heat capacity measurements. The Hall effects of $\text{Ba}(\text{Fe},\text{Co})_2\text{As}_2$ thin films also examined to discuss the dominant parameters of superconductivity but there is no significant relationship between R_H and T_c . These results indicate that the carrier density is not dominant parameter determining T_c in $\text{Ba}(\text{Fe},\text{Co})_2\text{As}_2$ and the local structure of $\text{Ba}(\text{Fe},\text{Co})_2\text{As}_2$ would determine T_c .

In chapter 5, a unique pressure phase diagram was observed in indirectly electron-doped 122-type $(\text{Ba},\text{La})\text{Fe}_2\text{As}_2$ epitaxial films, which is the non-equilibrium phase realized by PLD. The enhancement of T_c in all of the doping regions along with narrowing of ΔT_c was associated with the reduction of electron scattering and the increase in the carrier density caused by lattice shrinkage, which optimizes its crystal and electronic structure to achieve higher T_c and sharper ΔT_c in $(\text{Ba}_{1-x}\text{La}_x)\text{Fe}_2\text{As}_2$ films.

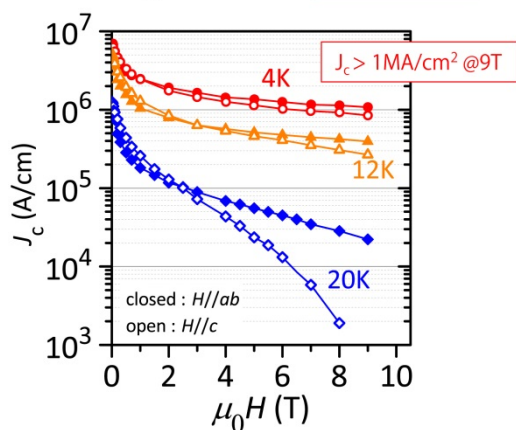
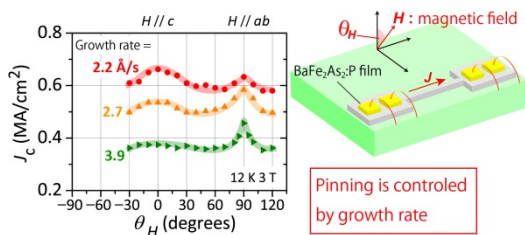


In chapter 6, isovalent-doped $\text{BaFe}_2(\text{As},\text{P})_2$ epitaxial films, whose bulks have higher T_c than electron-doped $\text{Ba}(\text{Fe},\text{Co})_2\text{As}_2$ and $(\text{Ba},\text{La})\text{Fe}_2\text{As}_2$ discussed above, were

fabricated on MgO (001) [BaFe₂As₂:P/MgO] and LSAT (001) [BaFe₂As₂:P/LSAT] substrates. I found, by developing a new substrate heating system using a high power laser diode, that the high temperature growth condition (1050 °C, 200°C higher than that of Ba(Fe,Co)₂As₂) is necessary for obtaining high-quality BaFe₂As₂:P epitaxial films. Compared with these crystallinity, BaFe₂As₂:P/LSAT has poor crystallinity than that of BaFe₂As₂:P/MgO because of the reaction layer between film and substrate.



In chapter 7, vortex pinning properties of BaFe₂(As,P)₂ epitaxial films on MgO and LSAT were examined. The poor crystallinity and the generation of domain boundaries in the BaFe₂As₂:P/LSAT lead to a decrease in the J_c^{self} and strong vortex pinning along the *c*-axis under high magnetic fields. These results imply that there is a trade-off relationship between J_c^{self} and vortex pinning forces of the BaFe₂(As,P)₂

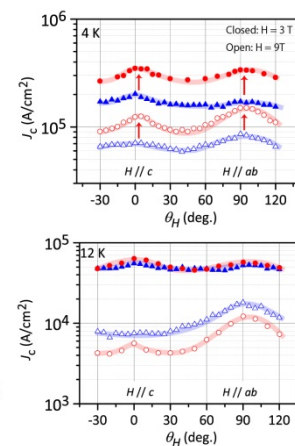
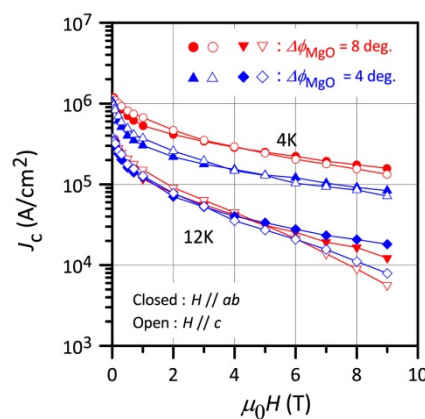
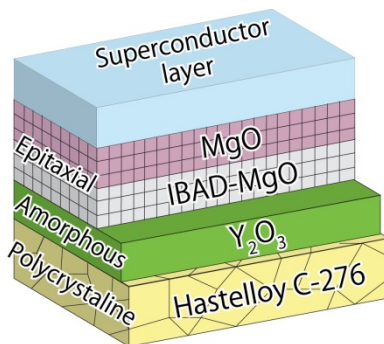


epitaxial films because crystallinity and defect density dominate J_c^{self} and vortex pinning forces, respectively. Decreasing the growth rate, a high self-field J_c of 7 MA/cm² was obtained for BaFe₂(As,P)₂ epitaxial films and a high J_c of over 1 MA/cm² was maintained even with an applied magnetic field of 9 T. This J_c value at 9 T is the highest value obtained so far for iron-based

superconductor thin films. In addition, a highly isotropic high- J_c performance was obtained by decreasing the film growth rate, which was explained that vertical dislocations along the c -axis are introduced with the decrease in the growth rate and they are served as strong vortex-pinning centers.

In chapter 8, the fabrication of $\text{BaFe}_2(\text{As,P})_2$ films on IBAD metal-tape substrates, which is usually used for commercially available superconductor tapes, was demonstrated to show the potential for future practical application. Compared with the films on single-crystal substrates, the films on IBAD-substrates has a relaxed structure caused by the poor crystallinity and the optimal doping level is close to that of bulk $\text{BaFe}_2(\text{As}_{1-x}\text{P}_x)_2$ in terms of T_c . Utilizing the fabrication technique which is well-optimized for single-crystal substrates, $\text{BaFe}_2(\text{As,P})_2$ epitaxial films exhibited the isotropic J_c properties ($J_c^{\min}/J_c^{\max} = 0.88$), which is the most isotropic J_c performance in 122-type thin films.

$\text{BaFe}_2(\text{As,P})_2$ epitaxial films was also fabricated on roughly aligned IBAD-substrates ($\Delta\phi_{\text{MgO}} = 8^\circ$) and they exhibited strong vortex pinning properties and higher J_c properties than that of $\text{BaFe}_2(\text{As,P})_2$ epitaxial films on more exactly aligned IBAD-substrates ($\Delta\phi_{\text{MgO}} = 4^\circ$). These results indicate



that this material is robust to the deterioration of the crystallinity and promising for the future applications.

Acknowledgments

This study was carried out in *Hosono, Kamiya, Hiramatsu & Matsuishi Laboratory* at the Tokyo Institute of Technology from April 2011 to March 2016. Numerous people have contributed to this study.

First of all, I would like to express gratitude to Prof. **Hideo Hosono** for his advice and continuous encouragement. Also, I would like to express my sincere thanks to Prof. **Toshio Kamiya**, Associate Prof. **Hidenori Hiramatsu** and Associate Prof. **Satoru Matsuishi** for their kind guidance, discussions, and important suggestions. I learned a lot from them such as a sense of materials research.

I am indebted to Prof. **Satoru Fujitsu**, Prof. **Hideya Kumomi**, Prof. **Toshiharu Yokoyama**, Associate Prof. **Masaaki Kitano**, Associate Prof. **Tomofumi Tada**, Associate Prof. **Sung Wng Kim** (currently at Sungkyunkwan university), Associate Prof. **Hiroshi Mizoguchi**, Assistant Prof. **Yoshitake Toda**, Assistant Prof. **Fuji Funabiki**, Assistant Prof. **Soshi Imura**, Assistant Prof. **Keisuke Ide**, Dr. **Takayoshi Katase**, Dr. **Gihun Ryu** (currently at *Max Planck Institute*), Dr. **Dong Hee Lee** (currently at Samsung Electronics Co., Ltd), Dr. **Kyeongmi Lee** (currently at Qualcomm MEMS Technologies, Inc.), Dr. **Kimoon Lee** (currently at Kunsan National University), Dr. **Hechang Lei** (currently at Renmin University of China), Dr. **Ran Fanyong**, Dr. **Zhang Xiao**, Dr. **Yangfan Lu**, Dr. **Min Liao**, Dr. **Katsumi Abe** (currently at Samsung Electronics Co., Ltd.), Dr. **Taku hanna**, Dr. **Yoshinori Muraba**, Dr. **Sehoon Jeong** (currently at Samsung Electronics Co., Ltd.) and Dr. **Joonho Ban** for their kind help and suggestions.

I also would like to thank, Mr. **Yudai Tomota**, Mr. **Junghwan Kim**, Mr. **Nobuhiro Nakamura**, Mr. **Takuya Maruyama**, Mr. **Sang Won Park**, Mr. **Takaya Miyase**, Mr. **Masataka Taniguchi**, Mr. **Shogo Matsuda**, Mr. **Kyohei Ishikawa**, Mr. **Takeshi Inoue**, Mr. **Norihiko Miyokawa**, Mr. **Kota Hanzawa**, Mr. **Taisuke Hatakeyama** and other members of the *Hosono, Kamiya, Hiramatsu & Matsuishi Laboratory*.

Further I am indebted to Assistant Prof. **Kosuke Matsuzaki** (at Susaki Lab.) for helping me to use thin film experimental apparatus and Mr. **Yuji Kondo** for helping me to analyze the chemical composition. I would like to acknowledge Secretaries Ms. **Kanako Ochiai**, Ms. **Mayumi Nakano**, and Ms. **Hanae Murayama** for their kind helps to my research works.

Finally, I express appreciation to my family and friends.

March 2016

Hikaru Sato

Publication List

Papers included in this thesis

1. **H. Sato**, T. Katase, W. N. Kang, H. Hiramatsu, T. Kamiya, and H. Hosono
“Anomalous scaling behavior in a mixed-state Hall effect of a cobalt-doped BaFe₂As₂ epitaxial film with a high critical current density over 1 MA/cm²”
Physical Review B **87**, pp. 064504-1–064504-7 (2013).
2. **H. Sato**, H. Hiramatsu, T. Kamiya, and H. Hosono
“High critical-current density with less anisotropy in BaFe₂(As,P)₂ epitaxial thin films: Effect of intentionally grown *c*-axis vortex-pinning centers”
Applied Physics Letters **104**, pp. 182603-1–182603-5 (2014).
3. **H. Sato**, H. Hiramatsu, T. Kamiya, and H. Hosono
“Vortex Pinning Properties of Phosphorous-Doped BaFe₂As₂ Epitaxial Films: Comparison between (La,Sr)(Al,Ta)O₃ and MgO Substrates”
IEEE Transactions on Applied Superconductivity **25**, pp. 7500305-1–7500305-5 (2015).
4. **H. Sato**, H. Hiramatsu, T. Kamiya, and H. Hosono
“Anisotropic pressure effects on superconducting properties of cobalt-doped BaFe₂As₂ epitaxial films utilizing the differences in thermal expansion coefficients and compressibilities”
Submitted to Nature Materials.
5. **H. Sato**, H. Hiramatsu, T. Kamiya, and H. Hosono
“Isotropic *J_c* properties of phosphorus-doped BaFe₂As₂ films on IBAD MgO tape substrates”
Submitted to Nature Communications.
6. **H. Sato**, H. Hiramatsu, T. Kamiya, and H. Hosono
“Optimization of growth parameters for phosphorus-doped BaFe₂As₂ films on IBAD-MgO metal-tape substrates”
To be submitted.
7. T. Katase, **H. Sato**, H. Hiramatsu, T. Kamiya, and H. Hosono
“Unusual pressure effects on the superconductivity of indirectly electron-doped (Ba_{1-x}La_x)Fe₂As₂ epitaxial films”
Physical Review B **88**, pp. 140503(R)-1–140503(R)-5 (2013).
8. H. Hiramatsu, **H. Sato**, T. Katase, T. Kamiya, and H. Hosono
“Critical factor for epitaxial growth of cobalt-doped BaFe₂As₂ films by pulsed laser deposition”
Applied Physics Letters **104**, pp. 172602-1–172602-5 (2014).

Other Papers

1. S. Iimura, S. Matsuishi, **H. Sato**, T. Hanna, Y. Muraba, S. W. Kim, J. E. Kim, M. Takata, and H. Hosono
“Two-dome structure in electron-doped iron arsenide superconductors”
Nature Communications **3**, pp. 943-1–943-6 (2012).
2. H. Hiramatsu, S. Matsuda, **H. Sato**, T. Kamiya, and H. Hosono

- “Growth of *c*-Axis-Oriented Superconducting KFe₂As₂ Thin Films”
ACS Applied Materials & Interfaces **6**, pp. 14293–14301 (2014).
3. Y. Wang, **H. Sato**, Y. Toda, S. Ueda, H. Hiramatsu, and H. Hosono
"SnAs with the NaCl-type Structure: Type-I Superconductivity and Single Valence State of Sn"
Chemistry of Materials **26**, pp. 7209–7213 (2014).
 4. K. Hanzawa, **H. Sato**, H. Hiramatsu, T. Kamiya, and H. Hosono
"Electric field-induced superconducting transition of an insulating FeSe thin film at 31 K"
Submitted to Proceedings of the National Academy of Sciences of the United States of America (under the second review process).
 5. Y. Hinuma, T. Hatakeyama, Y. Kumagai, L. A. Burton, **H. Sato**, Y. Muraba, S. Iimura, H. Hiramatsu, I. Tanaka, H. Hosono, and F. Oba
“Discovery of earth-abundant nitride semiconductors by computational screening and high-pressure synthesis”
Submitted to Nature Communications (under the second review process).
 6. T. Hatakeyama, **H. Sato**, H. Hiramatsu, T. Kamiya, and H. Hosono
"Heteroepitaxial Growth of KFe₂As₂ Thin Films by Solid-Phase Epitaxy in Strictly Controlled Atmosphere for Alkali Metal Elements"
Submitted to Chemistry of Materials.

Presentation List

International Presentations

Invited

1. **H. Sato**, H. Hiramatsu, T. Kamiya, and H. Hosono
“Thin film growth and superconductivity of layered iron-pnictides”
Collective Quantum Seminar at Tübingen University (CQ seminar), Tübingen, Germany,
August 31, 2015

Oral

1. **H. Sato**, T. Katase, W. N. Kang, H. Hiramatsu, T. Kamiya, and H. Hosono
“Scaling of Mixed-State Hall Effect in Optimally Cobalt-Doped BaFe₂As₂ Epitaxial Films”
Applied Superconductivity Conference (ASC 2012), Portland, USA, October 7–12, 2012
2. **H. Sato**, H. Hiramatsu, T. Kamiya, and H. Hosono
“Heteroepitaxial growth and superconductivity of Fe-based superconductor P-doped BaFe₂As₂ epitaxial film”
The 7th International Conference on the Science and Technology for Advance Ceramics (STAC-7), Yokohama, Japan, June 19–21, 2013
3. **H. Sato**, H. Hiramatsu, T. Kamiya, and H. Hosono
“Strong vortex pinning and isotropic critical current properties of iron-based superconductor BaFe₂(As,P)₂ epitaxial film”
The 12th Asia Pacific Physics Conference (APPC 12), Chiba, Japan, July 14–19, 2013
4. **H. Sato**, H. Hiramatsu, T. Kamiya, and H. Hosono
“Heteroepitaxial Growth of Mn-Based Layered Oxypnictides with ZrCuSiAs Structure by Pulsed Laser Deposition”
The 8th International Conference on the Science and Technology for Advanced Ceramics (STAC-8), Yokohama, Japan, June 25–27, 2014
5. **H. Sato**, H. Hiramatsu, T. Kamiya, and H. Hosono
“Strong vortex pinning and isotropic critical current density in BaFe₂(As,P)₂ epitaxial films grown by pulsed laser deposition”
Applied Superconductivity Conference 2014 (ASC 2014), Charlotte, USA, August 10–15, 2014
6. **H. Sato**, H. Hiramatsu, T. Kamiya, and H. Hosono
“Isotropic J_c properties of P-doped BaFe₂As₂ films on IBAD MgO tape substrates”
The European Society for Applied Superconductivity 2015 (EUCAS 2015), Lyon, France,
September 6–10, 2015
7. **H. Sato**, H. Hiramatsu, T. Kamiya, and H. Hosono
“Superconductivity properties of phosphorus-doped BaFe₂As₂ films on IBAD-MgO buffered metal tape substrates”
The 9th International Conference on the Science and Technology for Advanced Ceramics

(STAC-9), Tukuba, Japan, October 19–21, 2015

Poster

1. **H. Sato**, T. Katase, H. Hiramatsu, T. Kamiya, and H. Hosono
“Pressure effects on superconducting properties of 122-type iron pnictide epitaxial films on several substrates”
26th International Symposium on Superconductivity (ISS 2013), Tokyo, Japan, November 18–20, 2013
2. **H. Sato**, H. Hiramatsu, T. Kamiya, and H. Hosono
“Isotropic High Critical Current Density Realized by Strong Vortex Pinning in BaFe₂(As,P)₂ Epitaxial Films”
International Workshop on Novel Superconductors and Super Materials 2013 (NS² 2013), Tokyo, Japan, November 21–22, 2013
3. **H. Sato**, H. Hiramatsu, T. Kamiya, and H. Hosono
“Unusual pressure effects on superconducting properties of cobalt-doped BaFe₂As₂ epitaxial films”
Materials and Mechanisms of Superconductivity 2015 (M²S 2015), Geneva, Switzerland, August 23–28, 2015

Domestic Presentations

Invited

1. **佐藤 光**, 平松 秀典, 神谷 利夫, 細野 秀雄
「講演奨励賞受賞記念講演: 高 J_c BaFe₂(As,P)₂ 薄膜のヘテロエピタキシャル成長と等方的な磁束ピンニング特性」
『第 61 回応用物理学会春季学術講演会』(2014/3/17~3/20, 神奈川)

Oral

1. **佐藤 光**, 片瀬 貴義, ワン ナン カン, 平松 秀典, 神谷 利夫, 細野 秀雄
「高 J_c BaFe₂As₂:Co エピタキシャル薄膜における特異なホールスケールリング」
『第 73 回応用物理学会秋季学術講演会』(2012/9/11~9/14, 愛媛)
2. **佐藤 光**, 平松 秀典, 神谷 利夫, 細野 秀雄
「高 J_c BaFe₂(As,P)₂ 薄膜のヘテロエピタキシャル成長と等方的な磁束ピンニング特性」
『第 74 回応用物理学会秋季学術講演会』(2013/9/16~9/20, 京都)
3. **佐藤 光**, 平松 秀典, 神谷 利夫, 細野 秀雄
「Co 添加 BaFe₂As₂ エピタキシャル薄膜における特異な圧力効果」
『第 62 回応用物理学会春季学術講演会』(2015/3/11~3/14, 神奈川)

4. **佐藤 光**, 平松 秀典, 神谷 利夫, 細野 秀雄
「PLD 法による IBAD-MgO 基板上への P 添加 BaFe₂As₂ 薄膜成長」
『第 76 回応用物理学会秋季学術講演会』(2015/9/13~9/16, 愛知)
5. **佐藤 光**, 平松 秀典, 神谷 利夫, 細野 秀雄
「金属テープ基板上への BaFe₂(As,P)₂ 薄膜の PLD 成長とその等方的な臨界電流特性」
『第 157 回金属学会秋季講演大会』(2015/9/16~9/18, 福岡)
6. **佐藤 光**, 平松 秀典, 神谷 利夫, 細野 秀雄
「複数の単結晶基板上に作製した鉄系超伝導体 P ドープ BaFe₂As₂ エピタキシャル薄膜の臨界電流特性」
『第 54 回セラミックス基礎科学討論会』(2016/1/7~1/8, 佐賀)

Award

JSAP 35th Young Scientist Presentation Award (第 35 回 応用物理学会講演奨励賞)
「高 J_c BaFe₂(As,P)₂ 薄膜のヘテロエピタキシャル成長と等方的な磁束ピンニング特性」

Biography

Date of birth: 30th November 1988.

Education

Mar. 2011: Bachelor from Department of Physics, Kyushu University, Japan.

Mar. 2013: Master from Department of Materials Science & Engineering, Tokyo
Institute of Technology, Japan